UNIVERSITÄT ZU LÜBECK

From the Institute for Cardiogenetics

of the University of Lübeck

Interim Director: Prof. Dr. med. Malte Spielmann

High-content Screen for Cardiovascular Modulators in Zebrafish (*Danio rerio*)

Dissertation

for Fulfillment of Requirements

for the Doctoral Degree of the University of Lübeck

from the Department of Natural Sciences

Submitted by

Viviana Luisa Vedder

from Lübeck, Germany

Lübeck, 2024

First Referee:	Prof. Dr. Malte Spielmann
Second Referee:	Prof. Dr. Stefan Schulte-Merker
Date of oral examination:	20.01.2025
Approved for printing:	Lübeck, 28.01.2025

Table of Content

List of Tables

List of Figures

List of Figures

List of Figures

List of Figures

List of Figures

Abbreviations and Units

Table 1: Abbreviations and Units Used in this Study

Abbreviation	*Meaning*
°C	Degree Celsius
Å	Ångström
µl	Microliter
µM	Micromolar
µm	Micrometer
18s	18s ribosomal RNA
2^-ΔΔCT	Relative gene expression
AA	Amino Acid
aEF	Atrial Ejection Fraction
AF	Atrial Flutter
AF1-2	Activation Function Domain 1-2
AFib	Atrial Fibrillation
AJ	Adherens Junction
AncGR2	Ancestral glucocorticoid receptor 2
ANG1	Angiopoietin-1
ANG2	Angiopoietin-2
AP	Alkaline phosphatase
ARCHS4	All RNA-seq and CHIP-Seq Sample Search Space
AUROC	Area under the Receiver Operating Characteristic
AVB	Atrioventricular block
AVC	Atrioventricular canal
AVI	Audio video interleave
AVN	Atrioventricular node
BA	*Bulbus arteriosus*
BBC3	BCL2-binding component 3
BCI	*5,5-dibromo-4,4,-dichloro indigo*
BCIP	5-bromo-4-chloro-3-indolyl phosphate
BF	Brightfield
bp	Base Pair
bps	Beats per second
BSA	Bovine Serum Albumin
Cα	Carbon alpha
Ca^{2+}	Calcium
CCD	Conserved Domain Database
CCS	Cardiac Conduction System
CDH5	Vascular endothelial cadherin 5
cDNA	Complimentary DNA
CHB	Congenital Heart Blocks

CHD	Congenital Heart Disease
CI	Confidence Interval
CM	Cardiomyocytes
cm	Centimeter
CRISPR/Cas 9	Clustered regularly interspaced short palindromic repeats / CRISPR-associated protein-9 nuclease
CTs	Threshold cycles
CV	Cardinal vein
CVD	Cardiovascular disease
CZI	Zeiss integrated software RAW data format
DA	Dorsal aorta
DART	Developmental and reproductive toxicity
DBD	DNA Binding Domain
ddH2O	Double-distilled water
DIG	Digoxigenin
DIOPT	Drosophila RNAi Screening Center Integrative Ortholog Prediction Tool
DLAV	Dorsal longitudinal anastomotic vessel
DLL4	Delta-like 4
DNA	Deoxyribonucleic acid
DNase	Deoxyribonuclease
dpf	Days post fertilization
DTT	Dithiothreitol
DV	Dorsal Vein
e.g.	For example
EC	Endothelial cell
ECVAM	European Centre for Validation of Alternative Methods
EDTA	Ethylenediaminetetraacetic Acid
EF	Ejection Fraction
eGFP	Enhanced Green Fluorescence Protein
EMA	European Medicines Agency
EMB	Fraunhofer Institute for Marine Biology
ENCODE	Encyclopedia of DNA Elements
ENU	N-ethyl-N-nitrosourea
EtOH	Ethanol
EZRC	European Zebrafish Resource Center
f/s	Frames per Second
FASTA	Text-based format for representing nucleotide sequences or amino acid sequences

FDA	Food and Drug Administration
FFT	Fast Fourier Transformation
FHF	First Heart Field
FKBP51	Immunophilin FK506-Binding Protein 51
fli1a	Fli-1 proto-oncogene
GC	Glucocorticoid
GCL	Retinal ganglion Cell Layer
GECIs	Genetically Encoded Ca2+ Indicators
GIF	Graphics Interchange Format
GJ	Gap Junctions
GPCR	G-coupled protein receptors
GR	Glucocorticoid receptor NR3C1
GRE	Glucocorticoid Response Elements
GUI	Graphical user interface
h	Hour
H	Histamine
HCl	Hydrochloride
HeLa	Immortalized human cell line named after Henrietta Lacks
HF	Heart Failure
HKG	Housekeeping Gene
HMG-CoA	3-hydroxy-3-methylglutaryl-CoA
hpf	Hours post fertilization
HR	Heart Rate
HRH1-4	Histaminergic Receptor H1-4
HS	Heart Size
IFD	Induced Fit Docking
IFT	Inflow Tract
INL	Inner Nuclear Layer
IPL	Inner Plexiform Layer
ISH	*In situ* hybridization
ISV	Intersegmental vessel
IVT	*In vitro* transcription
JPEG	*Joint Photographic Experts Group – file format*
kcal	*Kilocalorie*
KD	Knockdown
Kdr	Kdra; VEGFR2
Kdrl	Kinase insert domain receptor-like, VEGFR4; Kdrb
KO	Knockout
l	Liter
LBD	Ligand-Binding Domain
LDL	Low-Density Lipoprotein
LED	Light-Emitting Diode

LPM	Lateral Plate Mesoderm
M	Molar
MARRVEL2	Model organism Aggregated Resources for Rare Variant ExpLoration
max	Maximum
MeOH	Methanol
meta-MQAP	meta–Model Quality Assessment Program
mg	Milligram
min	Minute
MLV-RT	Moloney Murine Leukemia Virus - Reverse Transcriptase
MM	Mammalian micro-mass test
mm	Millimeter
MO	Morpholino
MoA	Mode of Action
MP4	MPEG-4 advanced video coding
MR	Mineralcorticoid receptor
mRNA	messenger RNA
myh6	Atrial myosin heavy chain
myl7	Myosin light chain polypeptide 7
N/A	Not applicable
NBT	Nitro blue tetrazolium
NCBI	National Center for Biotechnology Information
ng	Nanogram
NIH	National Institutes of Health
NMR	Nuclear Magnetic Resonance
NSAID	Non-Steroidal Anti-Inflammatory Drug
NR3C1 & GR	Glucocorticoid Receptor 1
NTD	N-terminal transactivation domain
NTMT	NaCl, Tris-HCl, magnesium chloride, Tween
NTPs	Ribonucleoside Triphosphates
O/N	Over Night
OFT	Outflow tract
ONL	Outer nuclear layer
OPLS	Optimized Potentials for Liquid Simulations
PBS	Phosphate-Buffered Saline
PBST	Phosphate-buffered saline with Tween
PCR	Polymerase chain reaction
PDB	Protein Data Bank
PDGFRβ	Platelet-derived growth factor receptor β

PDL	Prestwick Drug Library
pdx1	Insulin promoter factor 1
PFA	Paraformaldehyde
PIGF	Placental growth factor
PNG	Portable network graphic
PPN	Peripheral Purkinje network
Prehyb	Prehybridization buffer
PTU	N-Phenylthiourea
PTU-EW	0.003% PTU in Egg Water
RMSD	Root Mean Square Deviation
RNA	Ribonucleic acid
RNase	Ribonuclease
ROC	Receiver Operating Characteristic
ROI	Region of interest
ROS	Reactive Oxygen Species
RPE	Retinal Pigmented Epithelium
rpm	Revolutions per Minute
RT	Room Temperature
RTK	Receptor tyrosine kinase
RT-qPCR	Quantitative real-time polymerase chain reaction
s	Second
SAN	Sinoatrial node
scRNA-seq	Single cell RNA-sequencing
SD	Standard Deviation
SDF	Structured Data File
SHF	Second Heart Field
SSC	Saline-Sodium Citrate
TAE	Tris-Acetate-EDTA
TALEN	Transcription Activator-Like Effector Nuclease
Tb	Terabytes
TBE	Tris-borate-EDTA
TIE2	Endothelial receptor tyrosine kinase-2
TIF	Tagged image format
TIFF	Tagged image file format
Tg	Transgene
TrxR	Thioredoxin Reductase
U	Unit
UGP	Urogenital Pore
UNG	Uracil-DNA Glycosidase
UV	Ultraviolet
V	Volt
vdW	van der Waals
vEF	Ventricular Ejection Fraction
VEGF	Vascular endothelial growth factor

VEGFR	Vascular Endothelial Growth Factor Receptor
vmhc	Ventricle Myosin Heavy Chain
VSMC	Vascular smooth muscle cell
W	Weeks
WEC	Whole Embryo Culture test
WHO	World Health Organization
WISH	Whole-mount *In Situ* Hybridization
wnt	Wingless-related integration site
WT	Wildtype
XP	Extra Precision

Table 2: Compound Abbreviations

Compound Abbreviations	
AAH	Azelastine hydrochloride
ATO	*Atorvastatin*
AZS	Azlocillin sodium salt
BEC	Beclomethasone dipropionate
BZY	Benzydamine hydrochloride
CCP	Clocortolone pivalate
CHCl	Chloropyramine hydrochloride
CHX	Cycloheximide
CLO	Clobetasol propionate
CPS	Cephalotin sodium salt
DMSO	Dimethyl sulfoxide
DPH	Diphenylpyraline hydrochloride
FCA	Fluocinolone acetonide
FCP	Fluticasone propionate
FMP	Flumethasone pivalate
IOP	Iopanoic acid
IPT	Ifenpro dil tartrate
MBEH	Monobenzone
MP	Methapyrilene hydrochloride
NAS	Nalidixic acid sodium salt
NZ	Niridazole
NaCl	Sodium chloride
OXB	Oxibendazole
P5	Pregnenolone
PEN	Pentamidine isethionate
PI	Pimozide
PP	Pyrvinium pamoate
PRC	Prednicarbate
SuM	Sunitinib malate
TRP	Tripelennamine hydrochloride
HOD	Homochlorcyclizine dihydrochloride

Nomenclature

The nomenclature used in this study is based on Trends in Genetics, “Genetic Nomenclature Guide” (1998) (1); Genetic methods: conventions for naming zebrafish genes in The Zebrafish Book from Mullins (1995) (2) and the ZFIN Zebrafish Nomenclature Conventions (zfin.org; latest update: 2019; accessed 24/03/2022) (3).

Table 3: Organism-Specific Nomenclature

Organism	*Gene*	*Protein*
Human	*NR3C1*	NR3C1
Mouse	*Nr3c1*	NR3C1
Zebrafish	*nr3c1*	Nr3c1

1 Abstract

Over the past two decades, cardiovascular diseases (CVDs) have remained the leading cause of death worldwide. Among these diseases, congenital heart disease is the most common type of human birth defect, affecting 1 in 100 live-born infants. It is crucial to identify new therapeutic targets and treatments for CVDs. Zebrafish are a suitable model for this task, as they can provide new insights into CVDs. Further, their small size and translucency make them an ideal model for high-content drug screenings.

In this study, a phenotype-based high-content screening approach in zebrafish was established to identify cardiovascular modulators. Utilizing the ‘Acquifer Imaging Machine‘, 1,280 compounds of the Prestwick Chemical Library were screened for angiogenesis and heartbeat phenotypes. The previously established type III receptor tyrosine kinase inhibitor sunitinib malate, which inhibits angiogenesis in zebrafish, was used as a positive control. Additionally, the competitive 3-hydroxy-3-methylglutaryl-CoA (HMG-CoA) inhibitor atorvastatin, which was previously shown to cause severe heart phenotypes in zebrafish, served as a positive control for heart rate (HR) and heart morphology. HR was selected as a screening phenotype under the assumption that morphological and functional changes in the heart during development would result in altered HR.

In search of angiogenesis modulators, blood vessel diameters of treated fish were measured for 320 of the 1,280 tested compounds. Application of different filters for known toxicities, previously published results and unknown targets, led to the identification of 11 promising hit compounds. Three of these compounds, namely desonide, oxibendazole, and azlocillin sodium salt, directly targeted angiogenesis by significantly reducing the diameter of intersegmental vessels. The remaining nine compounds affected the diameter of the dorsal aorta and/or dorsal vein.

Of the 134 compounds significantly altering HR, 21 compounds repeatedly induced significant HR alterations in two different transgenic zebrafish lines. In this study, two main target clusters were identified for HR modulators: the histaminergic receptor H1 (HRH1) and the glucocorticoid receptor (NR3C1). While HRH1 is commonly associated with allergic reactions, it has also been linked to CVDs. All antagonistic hit compounds targeting HRH1 caused significant bradycardia with moderate to severe dose-dependent teratogenicity. *In situ* hybridization for various *hrh* probes revealed that *hrh1* was the only detectable *hrh* in the heart at 3 days post fertilization (dpf), indicating its involvement in heart development. Additionally, the heart analysis tool *pyHeart4Fish* showed chamber-specific effects of HRH1 antagonists. Collectively, the data suggests that *hrh1*

plays a role in heart contractility and heart size. However, further investigation on the mechanism of action is necessary to comprehend how Hrh1 is involved in cardiogenesis and what long-term effects HRH1 antagonists can have on the developing embryo to determine drug safety for pregnant women.

NR3C1 is a ligand-activated transcription factor known to be involved in inflammation, metabolism, and stress response. In this study involving zebrafish larvae, a group of six NR3C1 agonists was found to significantly increase HR at 48 hours post fertilization. While previous research had identified *nr3c1*'s involvement in heart development in zebrafish, its role in arrhythmias remained unclear. Here, expression of *nr3c1* was detected in the larval heart at 5 dpf using *in situ* hybridization. Further analysis using *pyHeart4Fish* revealed that NR3C1 agonists induced chamber-specific phenotypes, including atrioventricular block. A homology model of zebrafish Nr3c1 was also developed, which suggested that the agonists known to bind in humans may also bind in zebrafish. These findings support the use of zebrafish as a screening model for cardiovascular phenotypes and highlight the potential role of nr3c1 in CVDs.

2 Zusammenfassung (German)

In den vergangenen zwei Jahrzehnten waren Herz-Kreislauf-Erkrankungen (CVDs) weltweit die häufigste Todesursache. Unter CVDs sind angeborene Herzkrankheiten die häufigste Art von Geburtsfehlern beim Menschen: 1 von 100 Lebendgeborenen ist davon betroffen. Daher ist es von größter Bedeutung, neue therapeutische Zielgene und Behandlungen für CVDs zu identifizieren. Zebrafische haben sich als geeignetes Modell für diese Aufgabe erwiesen, da sie neue Erkenntnisse über Herz-Kreislauf-Erkrankungen liefern können. Ihre geringe Größe und Lichtdurchlässigkeit machen sie zu einem idealen Modell für High-Content-Screenings.

In dieser Studie wurde ein phänotypbasierter High-Content-Screening-Ansatz in Zebrafischen entwickelt, um kardiovaskuläre Modulatoren zu identifizieren. Unter Verwendung der 'Acquifer Imaging Machine' wurden 1.280 Verbindungen aus der Prestwick Chemical Library auf Angiogenese- und Herzschlag-Phänotypen untersucht. Der bereits etablierte Typ-III-Rezeptor-Tyrosinkinase-Inhibitor Sunitinib-Malat, der die Angiogenese im Zebrafisch hemmt, wurde als Positivkontrolle verwendet. Darüber hinaus diente der kompetitive 3-Hydroxy-3-Methylglutaryl-CoA (HMG-CoA)-Inhibitor Atorvastatin, von dem zuvor gezeigt wurde, dass er bei Zebrafischen schwere Herzphänotypen verursacht, als Positivkontrolle für Herzfrequenz (HR) und Herzmorphologie. Die HR wurde unter der Annahme als Screening-Phänotyp ausgewählt, dass morphologische und funktionelle Veränderungen im Herzen während der Entwicklung zu einer veränderten HR führen würden. Von den 134 Verbindungen, die die HR signifikant veränderten, lösten 21 Verbindungen wiederholt signifikante HR-Veränderungen in zwei verschiedenen transgenen Zebrafischlinien aus und wurden daher als valide Hits angesehen.

Auf der Suche nach Angiogenese Modulatoren wurden die Blutgefäßdurchmesser von behandelten Fischen für 320 der 1.280 getesteten Substanzen gemessen. Die Anwendung verschiedener Kriterien für z.B. bekannte Toxizitäten, bereits veröffentlichte Ergebnisse und unbekannte Zielmoleküle führte zur Identifizierung von 11 vielversprechenden Substanzen. Drei dieser Substanzen, Desonid, Oxibendazol und Azlocillin-Natriumsalz, wirkten direkt auf die Angiogenese, indem sie den Durchmesser der intersegmentalen Gefäße deutlich verringerten. Die übrigen neun Substanzen beeinflussten den Durchmesser der dorsalen Aorta und/oder der dorsalen Vene.

In dieser Studie wurden zwei Hauptzielgruppen für HR Modulatoren identifiziert: der histaminerge Rezeptor H1 (HRH1) und der Glucocorticoid Rezeptor (NR3C1). HRH1 wird allgemein mit allergischen Reaktionen assoziiert, steht aber auch mit CVDs in Verbindung. Interessanterweise verringerten alle Wirkstoffe, die auf HRH1 abzielten, die HR signifikant. Die *in situ*-Hybridisierung

für verschiedene *hrh*-Sonden ergab, dass *hrh1* das einzige nachweisbare der getesteten *hrh* im Herzen 3 Tage nach Befruchtung (dpf) war, was auf seine Beteiligung an der Herzentwicklung hinweist. Darüber hinaus zeigte das Herzanalysetool *pyHeart4Fish* kammerspezifische Wirkungen von HRH1-Antagonisten auf. Insgesamt deuten die Daten darauf hin, dass *hrh1* eine Rolle bei der Herzkontraktilität und Herzgröße spielt. Allerdings sind weitere Untersuchungen zum Wirkmechanismus erforderlich, um zu verstehen, wie Hrh1 an der Kardiogenese beteiligt ist und welche langfristigen Auswirkungen HRH1-Antagonisten auf den sich entwickelnden Embryo haben können, um die Arzneimittelsicherheit für schwangere Frauen zu bestimmen.

NR3C1 ist ein Liganden-aktivierter Transkriptionsfaktor, von dem bekannt ist, dass er an Entzündungen, Stoffwechsel und Stressreaktionen beteiligt ist. In dieser Studie mit Zebrafischlarven wurde festgestellt, dass eine Gruppe von sechs NR3C1-Agonisten die Herzfrequenz bei 48 h nach Befruchtung deutlich erhöht. Während frühere Forschungen die Beteiligung von *nr3c1* an der Herzentwicklung bei Zebrafischen identifiziert hatten, blieb seine Rolle bei Herzrhythmusstörungen unklar. Hier wurde die Expression von *nr3c1* im larvalen Herzen bei 5 dpf mittels *in situ*-Hybridisierung nachgewiesen. Weitere Analysen mit *pyHeart4Fish* ergaben außerdem, dass NR3C1-Agonisten kammerspezifische Phänotypen, einschließlich eines atrioventrikulären Blocks, induzieren. Des Weiteren wurde ein Homologie Modell des Zebrafisch-Nr3c1 entwickelt, das darauf hindeutet, dass die Agonisten, von denen bekannt ist, dass sie beim Menschen binden, auch im Zebrafisch binden können. Diese Ergebnisse unterstützen die Verwendung von Zebrafischen als Screening-Modell für kardiovaskuläre Phänotypen und unterstreichen die potenzielle Rolle von *nr3c1* bei CVDs.

3 Introduction

Cardiovascular diseases (CVDs) have been among the leading causes of death worldwide for almost two decades (4). According to the World Health Organization (WHO), congenital heart diseases (CHDs) are the most common human birth defect (5). CHDs lead to premature pregnancy termination in 5-10% of the cases. Additionally, 1 in 100 live-born infants is affected by CHD (6). This count includes immune-mediated atrioventricular blocks (AVBs), which are among the leading causes of congenital heart blocks (CHBs). One in 15.000-22.000 live-born infants is affected by CHBs (7,8). Irregularities and mutations in genes responsible for heart chamber formation and/or function are associated with CHDs, can lead to severe insufficiencies, and sooner rather than later early death (9). Therefore, it is essential to understand disease mechanisms better and to find and implement new treatment options for CVDs to reach Sustainable Development Goal 3 and achieve a 33% reduction in premature mortality caused by non-communicable diseases by 2030 (10,11).

3.1 Heart Development and Function

One of the first structures to form during early vertebrate organogenesis is the heart. After the two bilateral heart fields of the precardiac mesoderm are formed during gastrulation, the two epithelial layers fuse to form the primary heart tube (12) (Figure 1 A). This tube consists of the inner endocardium and the outer myocardium. Between both layers, an acellular matrix, the cardiac jelly, is located (12). As development progresses, the tube is divided longitudinally into two chambers, the atrium and the ventricle. At the 7-10-somite stage, a single pacemaker area is established at the inflow tract (IFT) (13). This process determines the polarity of the vertebrate heart, characterized by the atrium's location at the IFT, where dominant pacemaker activity is observed, facilitating unidirectional blood flow (14). The dominant pacemaker is the sinoatrial node (SAN), sending electrical impulses resulting in cardiac contraction. Together with the atrioventricular node (AVN), the SAN is part of the slow cardiac conduction system (CCS). SAN and AVN derive from the slow-conducting myocardium of the IFT, respectively, atrioventricular canal (AVC), which divides the atrium and ventricle (14). The AVN is connected to the His bundle, also known as AV-bundle (15), and together they are responsible for conduction from the atrium to the ventricle (Figure 1 B) (16).

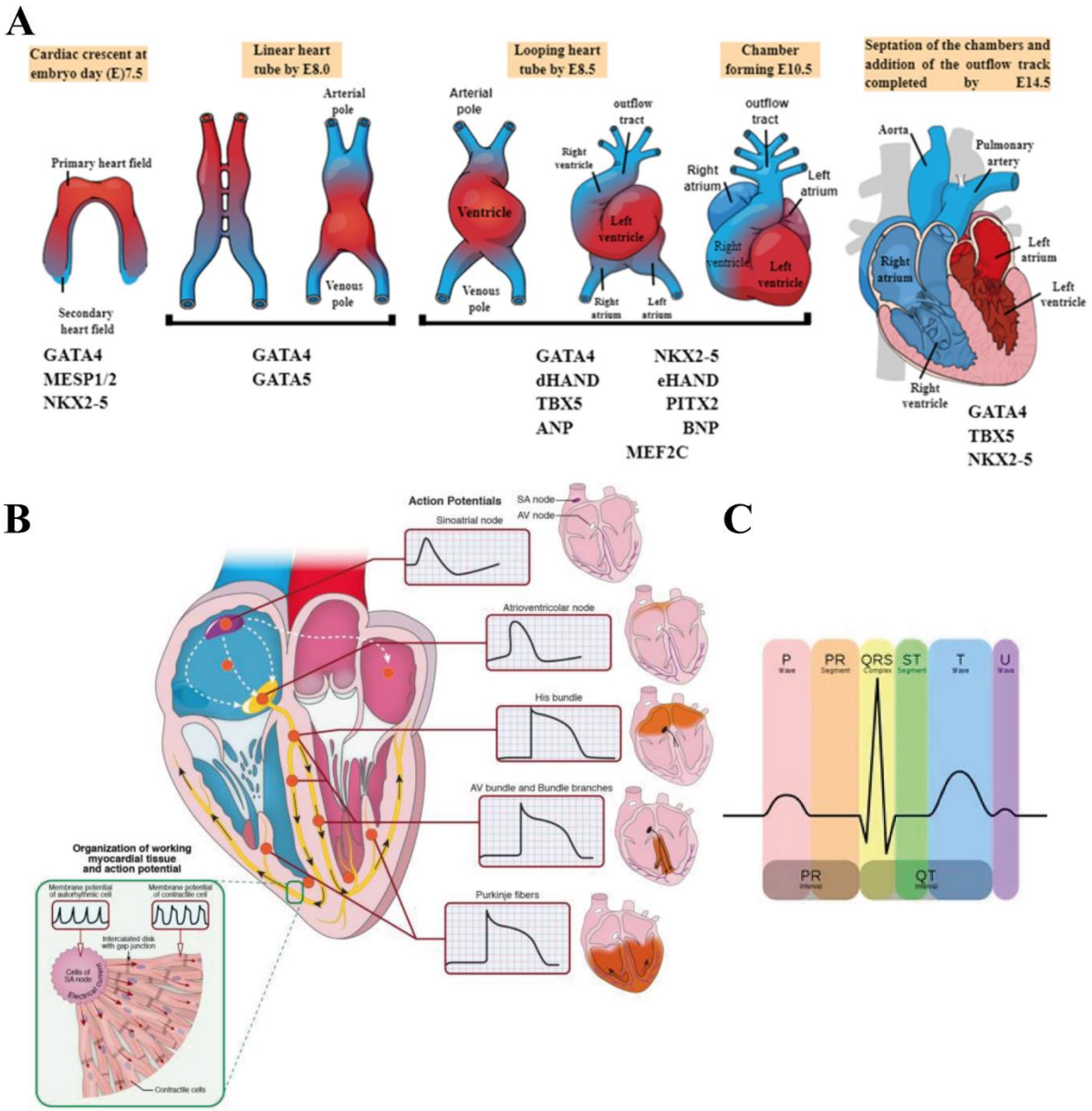

Figure 1: Mammalian Heart Development

Overview of human embryonic heart development. **A**, Mammalian cardiogenesis can be divided into the following stages: primitive heart tube, heart tube linearization, cardiac looping, chamber formation, and cardiac septation. At the inflow tract a single pacemaker area develops as early as ~E8-E9.5. **B**, In the mature mammalian heart the sinoatrial node generates electrical impulses, that spread through atrioventricular node to the His-Purkinje network and lead to contraction of the heart chambers. **C**, De- and repolarization can be traced via non-invasive ECG measurements. (E) embryonic days of gestation. This figure was adapted with permission from **A** Hussen *et al.* (17), **B** Iop *et al.* (18) and **C** Cardarilli *et al.* (19).

While the single atrium and ventricle present the basic blueprint for a teleost heart, additional looping and partitioning form the mammalian four-chambered heart. In this maturation and looping process, the cardiac jelly disappears from the atria and ventricles, but it accumulates in the AVC

and the outflow tract (OFT) (12). The AVC and OFT cardiac jelly matures into the endocardial cushions. The endocardial cushions are required for proper fusions during looping and thereby, for healthy morphogenesis of the heart (20). Abnormalities in cushion formation lead to dysmorphogenesis of the heart in mice (21–23). At this point, it is worth mentioning that the heart is not completely developed at birth (15). Therefore, genetic and environmental factors can still affect its development.

3.1.1 Electrophysiological Conduction

As previously described, the CCS generates and transmits electrical impulses required for coordinated heart contraction (24,25). Electrical impulses originating from SAN spread across the atrial myocardium before being delayed by the AVN in the AVC (Figure 1 B). In addition to the delay, AVN cells have a relatively long refractory period and depend on the conduction velocity, which limits excitation frequency. Thereby, the maximum (max) number of impulses within a certain timeframe is limited, creating a filter for high atrial frequencies (26). This limited excitation frequency protects the ventricle from high atrial frequencies such as atrial tachycardia and atrial fibrillation (AFib) (27). Furthermore, experiments have shown that the AVN possesses inherent automaticity, but it cannot replace the SAN sufficiently (24,28). After a delay at the AVN, the electrical impulses move rapidly across the fast CCS of the ventricle via bundle branches and the peripheral Purkinje network (PPN) (14,24,25,29,30). Purkinje cells are specialized myocytes of the CCS (31) (Figure 1 B). This impulse conduction would not be possible without conductance gap junctions (GJs) that transfer depolarizing action potentials from one cytoplasm to another throughout the myocardium (24,32) (Figure 1 A & C). GJs are composed of six membrane-bound connexin proteins that form a hemichannel. They display electrophysiological properties and different ion and second messenger permeabilities (32). The low abundance of GJs and expression of low to ultralow conductance GJs in SAN and AVN explains these tissues' slow conduction and conduction delay (32,33).

3.2 Arrhythmias and Atrial Fibrillation

The CCS generates and transmits electrical impulses required for coordinated heart contraction (24,25). Defects in the CCS can be grouped into 3 classes according to Chi *et al*. (2008): Class I (24 hours post fertilization (hpf)): Initial organized cardiac conduction; Class II (36-48 hpf): Development of atrioventricular delay; Class III (72-96 hpf): Development of peripheral cardiac conduction (25). Any deviations in this complex system can lead to CVDs such as tachycardia, bradycardia and other arrhythmias (34). One of the more commonly known arrhythmias is the AVB.

It can be congenital (CHB) and be caused by CAD, fibrosis, sclerosis, medications and others. AVBs can be separated into three categories: first-degree, second-degree (Mobitz type 1 or 2), and third-degree. The first-degree AVB is more common and displays a delay in transmission of the electrophysiological impulse and may lead to bradycardia. It usually does not require treatment (35). The second-degree AVB (Mobitz type 1 or 2) is more severe as the AVN does not conduct all impulses. In this case, the atria will contract more often than the ventricles, but overall, patients display a slower heartbeat (36). Mobitz type 1 occurs within the AVN and can lead to the ventricles skipping a beat (35,37). Mobitz type 2 originates from a block of the CCS downstream of the AVN in the His-bundle or the bundle branches (37–39). Therefore, this type of AVB is likely to progress to the third degree of AVB (35). The third-degree is the most severe case, that can lead to a complete heart block, where the AVN will not conduct any electrical impulses to the ventricles (40). In this case, the inherent automaticity of the AVN can create its own current in the ventricles (41,42). Atria and ventricles will contract entirely out of synch while also displaying bradycardia. An artificial pacemaker is the most common treatment for second-degree Mobitz type 2 and third-degree AVB (36,40,43).

Another common arrhythmia is the atrial flutter (AF). AF presents as a chamber-specific disorder, where the atrium develops tachycardia with a regular frequency. While AF does not cause symptoms in patients, it is associated with an increased risk for CVDs. AF is very similar to AFib, however, AFib causes irregular heartbeats. A canine study demonstrated that AF causes a linear functional block in the right atrial wall between the *venae cavae*. A decrease in the length of this linear block leads to the conversion of the AF to an AFib (44). Invasive electrophysiological studies in humans later confirmed these findings at the *crista terminalis* (45,46). Furthermore, it was discovered that this linear block is more likely to develop into a conduction block when AFib cycle lengths are shorter (46). While both conditions could be without acute symptoms for patients, AF and AFib may cause or be a consequence of heart failure (HF), and both are associated with increased morbidity and mortality (47–49). Both arrhythmias are usually treated with anti-arrhythmic drugs or catheter ablation of small areas of the heart tissue (50–53).

3.3 Angiogenesis, a Risk Factor for CVDs

Vasculogenesis is a process that forms primary blood vessels in the absence of pre-existing vessels (54,55). In this process, angioblasts differentiate into endothelial cells (ECs) and migrate and merge, forming EC cords (57). Within the EC cords a central vascular lumen forms, while the cords become ensheathed by vascular smooth muscle cells (VSMCs), forming the primary vasculature in the developing embryo (55–57).

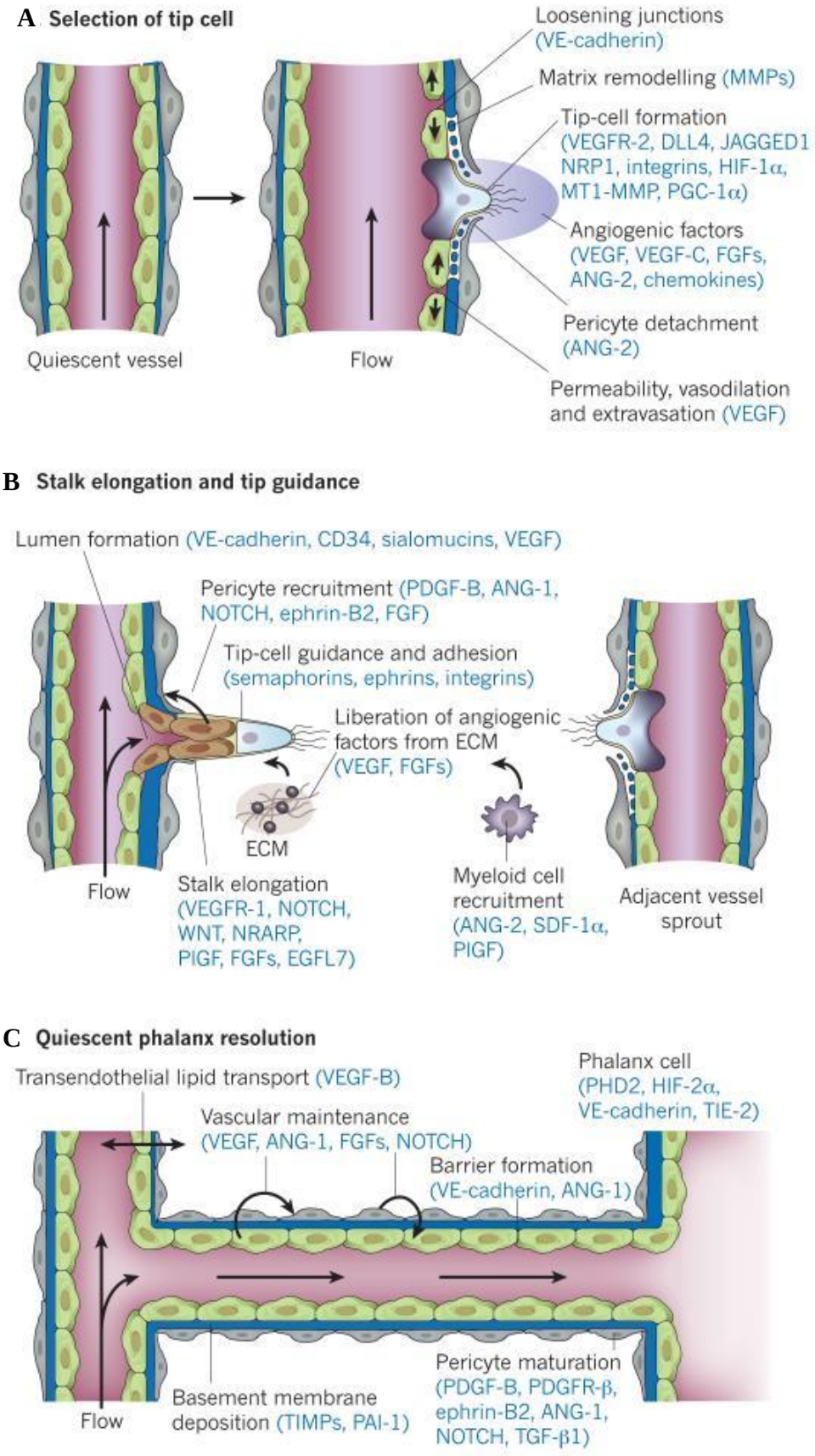

Figure 2: Molecular Mechanisms of Angiogenic Sprouting

Overview of key players involved in angiogenic sprouting. **A**, Stimulation of quiescent phalanx cells with angiogenic factors results in their detachment. Matrix remodeling, endothelial cell (EC) junction loosening and finally, EC dilation leads to tip cell formation. **B**, In response to guidance signals, tip cells adhere to the extracellular matrix (ECM) and migrate. Stalk cells form a lumen and recruit pericytes to stabilize the new vessel. **C**, Following vessel fusion and stabilization, a lumen develops to allow blood flow, integrating the new vessel into the vascular system. This figure was adapted with permission from Carmeliet and Jain (2011) (License: 5471971425317) (56).

Angiogenesis, defined as secondary vessel formation from pre-existing vessels, is a highly conserved process involved in embryogenesis, growth and wound healing (58). Therefore, errors in this integral process during early development or later in life can contribute to a variety of diseases, such as rheumatoid arthritis, cancer and atherosclerosis (59).

Mature vessels are lined with quiescent phalanx cells, and ECs ensheathed by pericytes. EC proliferation is suppressed by pericytes, which ensures cell survival via vascular endothelial growth factor (VEGF) and angiopoietin-1 (ANG1) (56). The EC VEGF high-affinity receptor 1 (VEGFR1), regulated by VEGFA, VEGFB and placental growth factor (PIGF) (60), is a negative regulator of angiogenesis that acts as a decoy receptor for VEGF (61,62). Angiogenic signals, such as ANG2, VEGFA, VEGFC and chemokines, induce pericyte detachment from phalanx cells (56). ANG2 is abundantly expressed in ECs and is directly involved in vessel maturation and quiescence control via the ANG/endothelial receptor tyrosine kinase (TIE) system. Additionally, ANG2 inhibits TIE2 signaling as a competitive ligand to ANG1, thereby destabilizing mature vessels (63). In response to pericyte detachment, ECs loosen their adherens junctions (AJs), and the nascent vessel dilates (Figure 2). The EC-specific transmembrane protein vascular endothelial cadherin (VE-cadherin/CDH5) is the main constituent of AJs and, thereby, a key player in cell shape changes, proliferation and vascular stabilization (64–66). In the presence of VEGFR, NOTCH ligands and Delta-like 4 (DLL4), one of the ECs develops into a tip cell (56). Lateral inhibition originating from the tip cell determines adjacent EC development into stalk cells (67). Lateral inhibition acts through DLL4-dependent activation of NOTCH, which decreases VEGFR2 expression. Besides its key role in tip cell determination, VEGFR2 mediates enhanced vascular permeability, migration, proliferation and survival of ECs (68,69). Stalk cells proliferate, elongate and form the lumen of the sprouting vessel (54,70). Filopodia of the tip cells follow gradients of angiogenic guidance signals to direct vessel growth and detect adjacent vessels. This way, myeloid bridge cells can connect the growing vessel with pre-existing ones (56). VEGFA is one of the key players in angiogenic processes (54). While tip cell filopodia sprout in response to VEGFA guidance cues, stalk cells proliferate in response to VEGFA (71). After EC migration, pericytes are recruited to the vessel's stalk cells, where they mature and stabilize the new structure (56). The platelet-derived growth factor receptor β (PDGFRβ) and PDGF-B activate paracrine signaling, mediating VSMC and pericyte progenitor recruitment to the newly formed vessel (72,73). AJs of the ECs re-establish, and vascular maintenance proteins are produced to establish the new vessel as an integral part of the vasculature. CDH5 inhibits VEGFR2 signaling, thereby stabilizing the vasculature (74).

3.4 Zebrafish Cardiovascular Development and Disease

Within the past 40 years, the tropical freshwater fish *Danio rerio* (zebrafish) has emerged as a powerful model for human disease, developmental biology, and toxicology. Its easy genetic manipulation, rapid *ex utero* development, the optical transparency of larvae and high fecundity led to a relatively rapid establishment of this new animal model (Figure 3) (75). For the first time, Streisinger *et al.* demonstrated that forward genetics could be performed in zebrafish in 1981 (76). Since then, mutants and genetics screens have greatly contributed to understanding disease development and progression (77,78). Zebrafish are comparably easy to alter genetically, with a growing set of tools to introduce mutations, such as CRISPR/Cas9, N-ethyl-N-nitrosourea (ENU) mutagenesis and transcription activator–like effector nuclease (TALEN) (79,80). Besides genetic modification, morpholino oligomers (MOs) and reporter plasmids can be utilized to transiently explore gene functions *in vivo* (79,81). Almost the entire genome of zebrafish has been sequenced, and high conservation was observed (82). Comparisons have shown that 71.4% of human genes have at least one orthologue in zebrafish, and 69% of zebrafish genes have at least one human orthologue (83,84). Moreover, more than 80% of human drug targets have orthologues in zebrafish (83,85). Further, improved imaging technologies allow for high-resolution imaging of whole embryos as well as automated high-throughput imaging of hundreds of zebrafish within an hour *in vivo* (86–88). Increased data output caused by faster image acquisition is supported by the continuous advancement of automated tools, creating a manageable high-quantity and -quality platform (89). All these factors make zebrafish an ideal model for studying organogenesis, angiogenesis and tissue-specific gene and protein functions during embryonic development.

3.4.1 Zebrafish Heart Development

In the course of the last three decades, the zebrafish has emerged as a model for cardiovascular diseases due to genetic screens that led to the identification of multiple cardiovascular mutants (Figure 3) (82). In zebrafish, the heart is the first organ that forms and functions (82). The two-chambered zebrafish heart, comprised of atrium and ventricle, seems simple compared to the four-chambered mammalian heart. Nevertheless, early heart development, including cell types, structures and mechanisms of all chordate hearts, is highly conserved, making zebrafish a suitable model to study human cardiac disease (82,90,91). Moreover, the two-chambered zebrafish heart at 48 hpf (Figure 4) is comparable with a mouse heart at 12 days post fertilization (dpf) and a human heart at 35 dpf (92) (Figure 1).

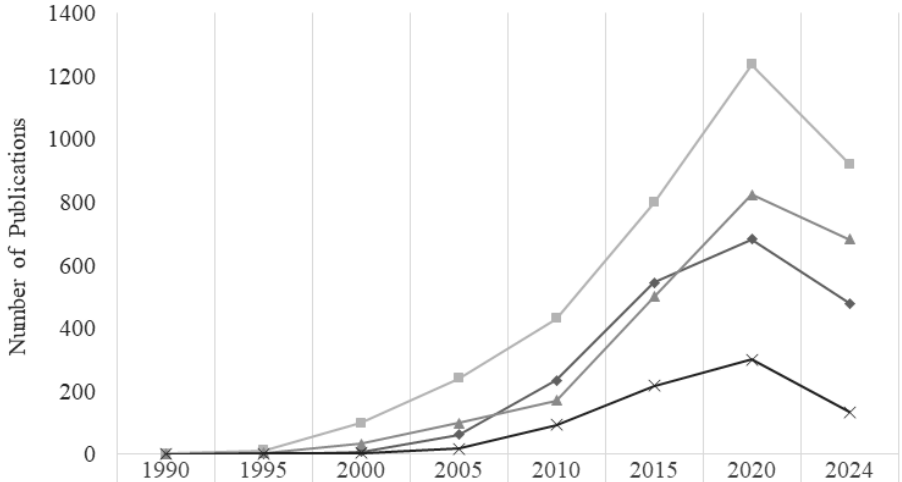

	1990	1995	2000	2005	2010	2015	2020	2024
Zebrafish Angiogenesis	0	0	8	63	234	545	682	480
Zebrafish Heart Development	1	11	99	241	431	800	1238	922
Zebrafish Cardiovascular Diseases	0	3	33	99	170	501	824	682
Zebrafish Drug Screen	0	1	4	18	94	218	300	134

Figure 3: Publication Overview of Zebrafish Models Between 1990 and 2024 (16/05/2024)
The publication history of different zebrafish models within 40 years. The x-axis displays the time from 1990 to 2024 in 5-year bins. The last time point only includes data from 2021 to 2024. The y-axis shows the number of publications in PubMed on a logarithmic scale, while the exact numbers are provided in the table below. MeSH terms used to gather the data are displayed in the bottom left legend. It is important to note that the MeSH term "Drug Screen" also yielded results for genetic screens in zebrafish that started sooner than the first chemical screens conducted in the early 2000s.

Zebrafish cardiac progenitor cells develop in the anterior bilateral stripes of the lateral plate mesoderm (LPM) as early as 5 hpf (82,93). Cardiac progenitors migrate medially from both sides of the LPM to build the intermediate cardiac crescent that forms the primitive heart tube (Figure 4 A-B) (93). At the 12-somite stage (14-15 hpf), cardiogenic differentiation is initiated by the expression of cardiac myosin in the future ventricle cells (82). Later, at the 13-14 somite stage (16 hpf), the first progenitors' differentiation into cardiomyocytes (CMs) can be detected via the early myocardial marker myosin light chain polypeptide 7 (*myl7*) (94,95). Expression of chamber-specific ventricle myosin heavy chain (*vmhc*) and atrial myosin heavy chain (*myh6*) at 19 hpf prefaces regionalization of the heart field into the atrium and ventricle (93,95). The bilateral heart field fuses at the midline to form a cardiac disc (82,93,95). At 21-23 hpf, the heart tube begins to beat. Rhythmic membrane depolarization of the pacemaker cells in the IFT causes changes in action potential leading to CM contraction (96). The still linear heart tube's contractions begin to synchronize at 24 hpf (Figure 4 C) and thereby start to support the rudimentary vascular system (dorsal aorta (DA) and cardinal vein (CV)) by circulating erythrocytes through the body (93). In

pacemaker cells, Wnt/β-catenin signaling via M2 cholinergic receptor signaling allows parasympathetic signals (96).

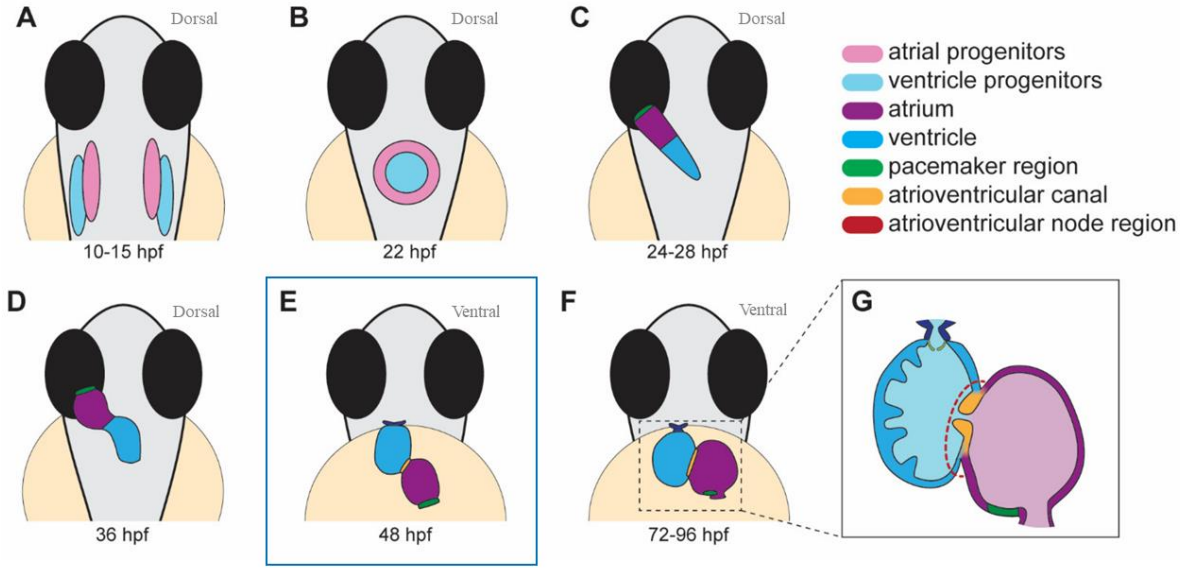

Figure 4: Zebrafish Heart Development from 10-96 hpf

Overview of different zebrafish heart development stages. **A**, Cardiac progenitors migrate to form the intermediate crescent **B**. **C**, The primitive heart tube is already divided into atrium and ventricle with a polarized pacemaker region. In this study, treatment with drugs started at 24 hours post fertilization (hpf). From **C** to **E**, the heart tube undergoes a leftward jog, and the *bulbus arteriosus* develops at the ventricle. Additionally, the atrioventricular canal (AVC) forms, which separates the atrium and ventricle. The blue box in **E** indicates the treatment stop and imaging time point. **F**, The heart chambers expand and align horizontally between 72 and 94 hpf. Additionally, the endocardium starts to trabeculate and endocardial leaflets form in the AVC. This figure was adapted with permission from Gauvrit *et al*. (97).

At 36 hpf, the previously linear heart tube begins to loop towards the left (Figure 4 D), under the control of the so-called Kupffer's vesicle, which determines asymmetry via lateral cues (98). This process forms the first asymmetric organ in zebrafish. Subsequently, at 48 hpf, the heart is fully looped, and the atrium and ventricle have formed, separated by the AVC (Figure 4 E) (94). The heart is now lined by the endocardium (93). Additionally, the cardiac myofilaments mature and organize in a chamber-specific manner. In the ventricle, myofilaments form cortical filaments, while in the atrium, they form transverse filaments (91). Subsequently, during the next three days, the epicardium forms (99); AVC, OFT and IFT develop; ventricular myocardium trabeculates (90), and the *bulbus arteriosus* (BA) differentiates into a pressure capacitator (Figure 4 F-G). The BA is a teleost-specific structure.

In zebrafish, the AVN develops circumferentially around the AVC. The AVN is a part of the CCS that can already be observed as early as 36 hpf (14,25). The mature PPN described in humans does

not exist in zebrafish, however, evolutionary studies suggest that the trabecular CMs are Purkinje cell precursors. In mammals, Purkinje cells originate from the trabecular CMs that serve as Purkinje fiber network precursors during embryogenesis (100,101).

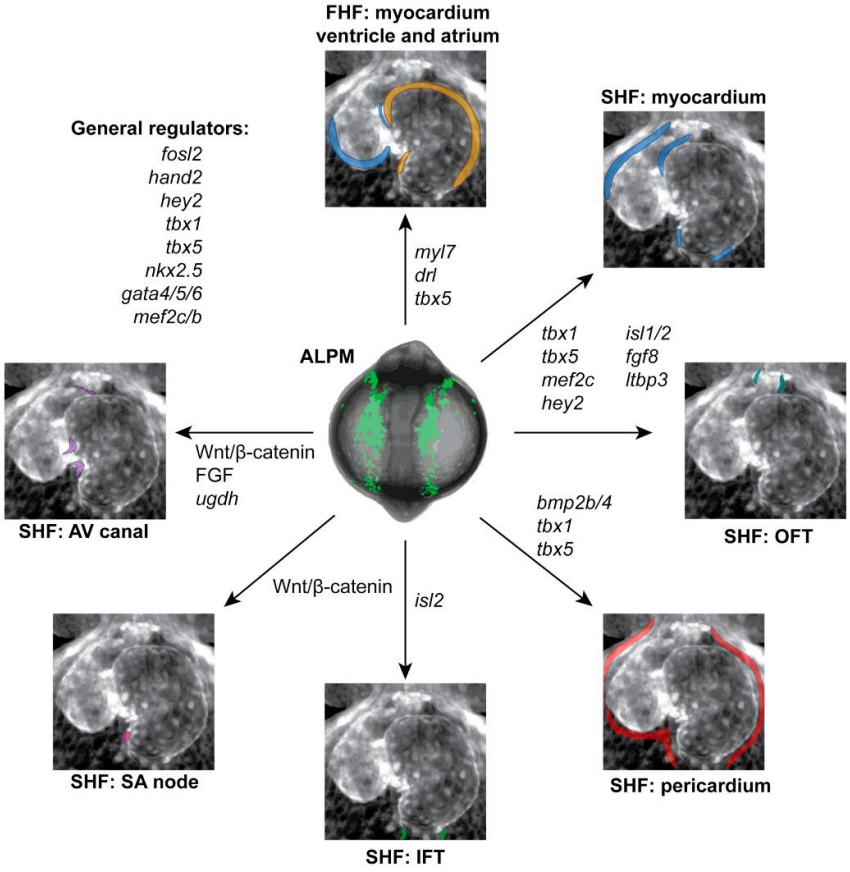

Figure 5: Genes Involved in Early Zebrafish Heart Development
Overview of the most prominent genes and pathways involved in early heart development of zebrafish 3 days post fertilization. Vertebrate cardiomyocytes derive from two different types of anterior lateral plate mesoderm (first heart field (FHF) and second heart field (SHF)). In zebrafish, the FHF forms the myocardium of the primary heart tube, thereby connecting the heart to the systemic circulatory system. The SHF adds to the myocardium of both poles of the heart tube, outflow tract and *bulbus arteriosus*. (AV canal) Atrioventricular canal; (IFT) inflow tract; (OFT) outflow track; (SA node) sinoatrial node. This figure was taken with permission from Kemmler *et al.* (93).

3.4.2 Zebrafish Angiogenesis

As previously described, angiogenesis is the process that forms new blood vessels from pre-existing ones (102). Excessive or reduced angiogenesis, termed angiopathy or pathologic angiogenesis, is associated with a wide variety of diseases, such as atherosclerosis, Crohn's disease and diabetes (58). Therefore, it´s undeniably important to find new therapeutic targets and therapeutics. Here, zebrafish emerged as a promising model. Early embryonic and larval stages are translucent until

about 21 dpf, allowing observation of vascular maturation and angiogenesis *in vivo* in real-time (54,103). Moreover, zebrafish have a complex vascular system with a conserved development and pathology compared to humans (104).

In zebrafish, vasculogenesis forms the primary aorta and vein up until 24 hpf (54). Migration of intersegmental vessels (ISVs) in the developing zebrafish embryo begins as early as 19 hpf (105). Starting at 24 hpf, blood cells circulate through the aorta and vein. At 28 hpf, ISVs form dorsal longitudinal anastomotic vessels (DLAV) dorsal to the neural tube (65,105). After only 48 h, zebrafish embryos have developed a rudimentary vasculature with established primary and secondary blood vessels. At this stage, trunk and tail ISVs have developed into mature vessels with a lumen that connects to major blood vessels to allow blood flow. New ISVs form at the tail as the fish continues to grow, and the lymphatic system starts to develop between 48 hpf and 72 hpf. Therefore, between 24 and 48 hpf effects of anti- and pro-angiogenic factors can be investigated.

3.5 Zebrafish as a Model for CVD

As previously described, sarcomeres assemble around 24 hpf, and synchronized contraction begins in the developing zebrafish heart. Zebrafish can continue to develop at this point, even without a circulatory system, as their oxygen uptake proceeds via passive diffusion (82,93,106). By 48 hpf, the myofilaments mature and organize chamber-specifically. A disruption in these processes can result in several known cardiomyopathies.

To visualize the effects of genetic modifications or drug treatments on cardiovascular morphology and function, several transgenic reporter lines have been developed. One of the most commonly used transgenic reporter lines for cardiovascular phenotypes is Tg(*myl7:eGFP*), previously known as Tg(*cmlc-2:eGFP*), which expresses enhanced green fluorescent protein (eGFP) in the CMs (107). Another common line is Tg(*fli1a:eGFP*)^{y7} which expresses eGFP in the ECs of the vasculature. A transgenic line used for cell-fate tracking is Tg*(nkx2.5:Kaede)*, which expresses the photoconvertible Kaede protein in Nkx2.5+ cells. A study revealed that Nkx2.5+ precursors develop into atrial and ventricular CMs and IFT pacemaker CMs (108).

As previously mentioned, zebrafish exhibit physiological differences from humans, however, most of their cardiac ion channels are more similar to humans than those of other animal models (109–111). A tool to assess physiological and pathophysiological mechanisms, such as the heartbeat, are fluorescent, genetically encoded Ca^{2+} indicators (GECIs). GECIs in transgenic lines, such as *Tg*(*cmlc2*:*gCaMP*)^{s878}, enables the visualization of the excitation-contraction coupling within the heart (25,110). Aside from transgenic reporter lines, various genetic models for human diseases

have been developed. CRISPR/Cas9-mediated mutagenesis produced several mutants with affected heart symmetry and complex CHD phenotypes (112,113). There is also a broad spectrum of mutant models for vascular phenotypes that induce reduced or excessive angiogenesis. Loss of *vegfaa* e.g. results in altered initiation of filopodia formation, thereby deficient ISV development (71,114,115). On the contrary, the downregulation of *flt1* in zebrafish caused excessive ISV branching and increased tip cell formation (71). Downregulation of *cdh5* in zebrafish induced a hypersprouting phenotype with vascular instability and increased permeability (64,116).

While numerous transgenic lines have been developed to model CVDs, CVDs are also inducible via drugs. One example is a study from 2017 that showed terfenadine to induce HF in a dose-dependent manner in zebrafish at 4 dpf (117). Another study demonstrated drug-induced bradycardia in zebrafish at 48 hpf (118). In 2020, a study demonstrated that impaired glucose homeostasis in *pdx1*$^{-/-}$ mutants induces hyperbranching and hypersprouting in the retina of larval and adult zebrafish (119). Further, the antiangiogenic action of thalidomide resulted in deformities of major blood vessels (120).

Taken together, many cardiovascular phenotypes in zebrafish are well enough understood to draw conclusions about pathways and molecular mechanisms. Therefore, the zebrafish constitutes a good model to investigate the effects of drugs on cardiovascular morphology and function.

3.6 High-Content Small Molecule Screen and Drug Repurposing

Chemical screens have been an important method for drug and target discovery for a long period of time. The search for ingredients with healing properties is as old as the practice of medicine. One pioneer of the active screening for compounds was Paul Ehrlich, who discovered salvarsan, a treatment for syphilis (121). Another was Alexander Fleming, who made the fortunate discovery of penicillin in 1928 (122). After the Second World War, pharmaceutical research included large-scale screening for antibiotics and later for other active compounds (123). Today, chemical screens are not only performed on a large scale in biomedical and pharmaceutical research but in academic research as well (124).

There are two general screening approaches: The phenotype-based screen, also called the traditional approach and the target-based screen, a modern approach. In the target-based approach, the target or molecular mechanism is usually identified in human genetic studies or biological research with strong evidence that the candidate gene or mechanism is disease-causing (92,125). Nevertheless, there are complex diseases that are difficult to target, and the identified targets may only play a small part in the overall disease mechanism. This is especially true for cardiovascular arrhythmias

(92). While target-based screens have the advantage that the target is known, phenotypical screens display the effect of the drug on the whole organism. Recent statistics showed that of all the drugs that made it through clinical trials and Food and Drug Administration (FDA)-approval, most came from phenotype-based screens. Besides displaying the effect of a chemical on the whole system, the phenotype-based screen can identify compounds that show a therapeutic effect via activity at multiple target sites (92).

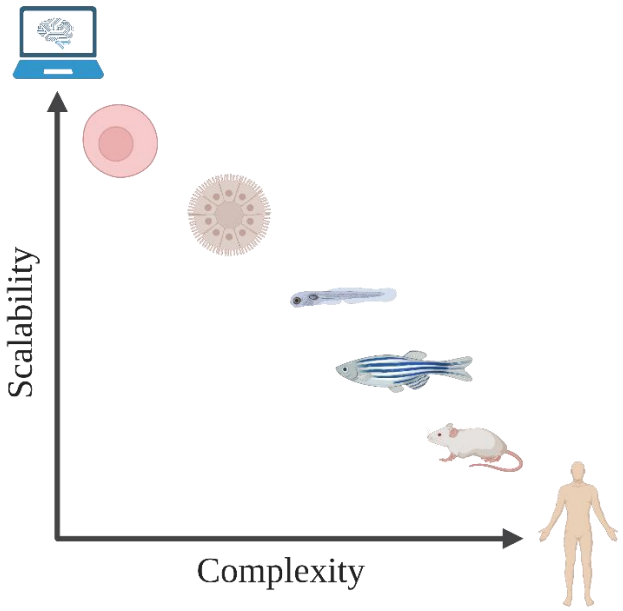

Figure 6: Advantages of Different Models for High-Content Screens
Two of the most important factors for choosing a model for high-content screenings are scalability and complexity. Besides *in silico* methods, cells have the highest scalability and enable large, often target-based screenings. On the other hand, rodents and other higher vertebrates have a high complexity similar to humans, but they cannot be used for large-scale screens. Here, zebrafish provide the best in-between. This image was created with BioRender.com.

Discovery of new active chemicals is a long process that can take years, is failure-prone and costly (126–128). Therefore, another approach, called *drug repurposing*, uses existing approved drugs in screenings unrelated to the original purpose of the drug (127). If an approved drug shows an effect in the treatment of another disease or causes side effects useful in other applications, the drug can be developed faster and more cost-effective, as it was already proven to be safe (129).

Most large-scale screens are performed in cells. However, while cells can be tested in large numbers, they lack the complexity a whole organism displays (Figure 6). An alternative model is organoids, cells grown in matrigels that form primitive organs. Organoids are a lot more complex than cells, but their scalability is lower than that of cells or *in silico* approaches. On the other side of the

spectrum humans and other mammals display a very high complexity but low scalability. This is one of the reasons why zebrafish have emerged as an alternative screening model. While zebrafish are not as scalable as cells, they have high complexity and can be screened on a much larger scale than other vertebrates, thereby providing the best in-between option (130).

3.6.1 High-Content Compound Screens in Zebrafish

Traditionally, mammalian models are used to study drugs, but they are expensive, require a lot of space and have a long generation time (131,132). The first high-content drug screen on embryo development in zebrafish was published in 2000 by Peterson *et al*. (133). Since then, zebrafish have become a widely used model for high-content drug screens with a high degree of accuracy. While several *in vivo* screens in zebrafish have been performed until today, their relevance to human medicine is often questioned. Nevertheless, there have been several successful screenings that not only confirmed findings in human patients but also identified new chemicals and new purposes for approved drugs, and their findings are transitioning to clinical trials (92,133). Zhao *et al*. reported that after lead optimization, hits identified in their zebrafish screenings were effective in rodents as well, indicating suitable pharmacokinetic properties for preclinical trials (92).

Zebrafish screens only require low drug doses, and zebrafish larvae are relatively resistant to higher concentrations of dimethylsulphoxide (DMSO), a common solvent for drugs (75). DMSO solubilizes compounds in water, thereby increasing biological availability and drastically increasing compound exposure of the organism without alterations to the compound or damage of biological membranes (134,135). The Organization for Economic Cooperation and Development (OECD) validation demonstrated low toxicity of LC10:30 g/L (0.3%) (136,137). Moreover, Kais *et al.* studied the autofluorescence of DMSO and its effects on the chorion's barrier function (134). They demonstrated that autofluorescence of DMSO is inconsequential for overall fluorescent measurements. Additionally, they showed that depending on the compound, at least 0.1% DMSO is needed to pass the chorion barrier.

Readymade drugs in drug libraries are usually dissolved in one solvent only, such as DMSO, regardless of their solubility (91). Another challenge is to predict the compound dose and exposure relationship. Additionally, there are no standard protocols for high-content screens in zebrafish, therefore, varying husbandry and experimental designs can lead to impaired reproducibility (138). Nevertheless, there are currently 8 compounds in clinical trials that have been discovered in zebrafish screens.

Here, a drug repurposing approach in a phenotype-based screening was conducted to identify new cardiovascular drug targets.

3.6.1.1 The RTKs inhibitor sunitinib malate (SuM)

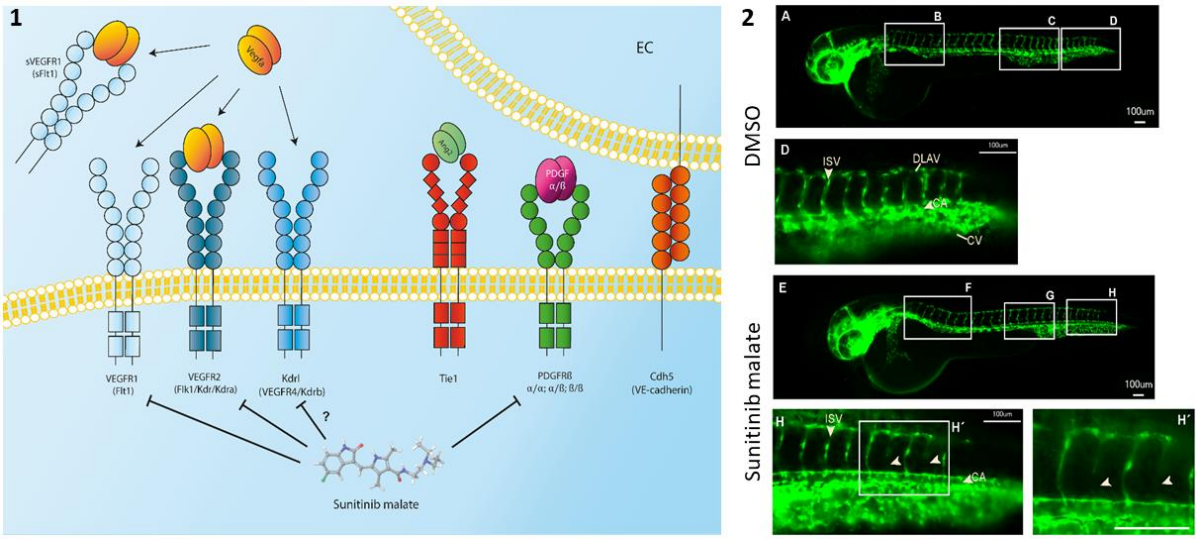

Figure 7: SuM Inhibits Angiogenesis in Zebrafish

1, Overview of ligands and receptors involved in angiogenesis and the receptor tyrosine kinase (RTK) inhibitor sunitinib malate (SuM). The receptors have an extracellular immunoglobulin domain and intracellular tyrosine kinase domains. SuM inhibits the phosphorylation of the RTKs on the intracellular side and thereby inhibits signal transduction. **2**, Images of Tg(*fli1a:eGFP*)^{y7} zebrafish were taken at 48 hpf after treatment with 5 µM SuM for 6 h. Treatment shows disrupted ISVs in **H** and **H'**. (Cdh5) vascular endothelial cadherin; (CV) caudal vein; (DLAV) dorsal longitudinal anastomotic vessel; (ISV) intersegmental vessels; (EC) endothelial cell; (Kdr) kinase insert domain receptor, (Kdrl) Kdr-like; (PDGF) platelet-derived growth factor; (PDGFR) PDGF receptor (VEGF) vascular endothelial growth factor; (VEGFR) VEGF receptor; (?) It´s uncertain whether SuM inhibits Kdrl, even if the origin of the receptor indicates it. Scale bars = 100 µm. This figure was adapted from the master thesis of Vedder (2018) (139).

As shown in Figure 7, the VEGFRs belong to the type III receptor tyrosine kinase (RTK) family and play an essential role in angiogenesis (140). In vertebrates, the VEGF signaling pathway is highly conserved. Sunitinib malate (SuM) is a known FDA-approved inhibitor of the RTKs of membrane-bound VEGFRs, preventing signal transduction on the intracellular side of the cell (141). SuM prevents phosphorylation of the RTKs of VEGFR1 and 2 as well as the platelet-derived growth factor receptor β. Additionally, SuM is indicated to target KDRL (VEGFR4) based on its origin. In patients, SuM is used to treat different metastasized tumors (142). In 2014 Kanada *et al.* showed that SuM completely inhibited the formation of new secondary blood vessels in zebrafish (142). Here, SuM was used as a positive control for the primary screen with Tg(*fli1a:nEGFP*)^{y7}.

3.6.1.2 Atorvastatin

The competitive 3-hydroxy-3-methylglutaryl-CoA (HMG-CoA) inhibitor atorvastatin (ATO) was the most common lipid-lowering agent in 2019 in Norway (143) prescribed to treat hyperlipidemia, hypercholesterolemia and CVDs (144,145). Inhibition of HMG-CoA reductase's conversion to mevalonate leads to decreased liver cholesterol production (146), thereby lowering blood lipid levels. However, ATO is classified as a D drug, thereby not recommended for consumption during pregnancy (146,147). In humans, ATO is absorbed 1-2 h after oral administration, but the poor performance of the drug can lead to the administration of higher doses with adverse effects (148–150). In zebrafish, ATO induces bradycardia, intercranial hemorrhaging, looping defects of the heart, and reduction of CM numbers in a dose-dependent manner (151,152). Another study also showed strong adverse effects of HMG-CoA inhibitors on pronephros development, indicating toxicity and teratogenicity of ATO (124). In this study, ATO was used as a positive control for cardiac phenotype screening with Tg(*myl7:eGPF*)$^{twu34/+}$.

3.6.2 Toxicity

3.6.2.1 Teratogenicity

Teratogenicity is one of the most common forms of toxicity-related adverse drug reactions (153,154). Teratogens are factors, such as drugs, infections, environmental exposures and genetics that cause developmental disorders, thereby drastically affecting a person's life. Despite different studies estimating 1-4% of congenital defects being caused by adverse drug effects, 55-90% of women receive at least one drug prescription per pregnancy (155–159). However, data on prenatal and postnatal teratogenicity and cardiotoxicity of specific drugs is often retrospective (160). Since 1993, regulations for drug approval have become stricter and require embryo-fetal developmental and reproductive toxicity (DART) studies that are performed in one rodent model and one non-rodent animal model (161). Most commonly, DART studies are performed in rats, rabbits and mice. These studies are low-throughput, labor-, cost-intensive and time-consuming and require a large number of animals, and thus alternative *in vitro* studies have been developed and validated by the European Centre for Validation of Alternative Methods (ECVAM) (75). Two examples of these alternative methods are the mammalian micro-mass test (MM) (162) and the whole embryo culture test (WEC) (163). Although more efficient, MM and WEC do not cover the whole organogenesis. Therefore, zebrafish screening assays, such as the fish embryo test (164,165), and additional guidelines have been developed and improved to evaluate teratogenic effects (75,166). Several studies have shown the translatability of mammalian toxicities to zebrafish embryonic and/or larval

toxicities (75,153,165,167,168). Phenotypes considered for teratogenicity scores differ throughout the literature and can add up to these 18 parameters: absence of the lateral fins, bent tail, body axis defects, body length, cardiovascular form and function, developmental delay, eye size, facial deformations; facial, pericardial and yolk edema; hatching ratio, motility, otic vesicle defects, otoliths defects, pigmentation, scoliosis, tissue necrosis, yolk size (75,167,169).

3.6.2.2 Cardiotoxicity

Cardiotoxicity is an important parameter in drug discovery and target identification to develop safe medications, but the term is not properly defined. In 1946 it was described as cardiac toxicity from local anesthetics, mercurial diuretics and digitalis (170,171). Later, in the 1970s, it also encompassed complications in cancer therapies (170–172). In 2020, the CARDIOTOX study was conducted to better understand the relationship between cardiotoxicity and cancer treatment (173). They defined cardiotoxicity as the new onset or progression of the damage of cardiac tissues and/or disruption of the electrophysiological properties of the heart, which was found to be present in 37.5% of the patients during follow-up (173–176). Often cardiotoxic effects, such as arrhythmias, are not detected in phase I clinical trials with mice, but only in phase II and III when administered to human patients (172). In the past two decades, zebrafish have been shown to be a useful model for studying cardiotoxic effects (153). In the zebrafish, cardiotoxic effects are assessed by blood circulation, heart size (HS), pericardial edema and edema size, as well as heart rate (HR) and fractional area changes (75). Dose-dependent bradycardia, in combination with increasing pericardial edema and increased HS, is considered a cardiotoxic effect.

4 Aims of this Work

According to the WHO, 27% of deaths are caused by CVDs (4). This highlights the importance of developing new treatments, identifying new targets and strengthening the knowledge of mechanisms underlying disease development. In recent years, zebrafish have emerged as an ideal model for *in vivo* high-content screens, due to their small size, rapid development, optical transparency and 86% orthology to known human drug targets (85). Therefore, this thesis aimed to perform a phenotype-based high-content screening for heartbeat and angiogenesis modulators via drug repurposing in zebrafish to identify translatable drug targets. Embryos of Tg(*fli1a:eGFP*)^{y7} that express eGFP in the nucleus of the vascular ECs, were used to study the effect of compounds on the cardiovascular system. Additionally, potential heartbeat hits were validated in Tg(*myl7:eGFP*)$^{twu34/+}$, a transgenic line tagging the myosin light chain 2 in the myocardial cells with eGFP.

The following milestones were set to achieve the defined aims:

I. Establishing a high-content screening protocol in zebrafish embryos.

II. Performing a primary high-content screening for vascular modulators using Tg(*fli1a:eGFP*)^{y7} zebrafish embryos.

III. Conducting a primary screening for heartbeat modulators using Tg(*fli1a:eGFP*)^{y7} zebrafish embryos.

IV. Filtering primary hits of the angiogenesis and heartbeat screening.

V. Optimizing compound concentrations of heartbeat hits for further testing.

VI. Validating effects of heartbeat hits in Tg(*myl7:eGFP*)$^{twu34/+}$.

VII. Assessing heart morphology using Tg(*myl7:eGFP*)$^{twu34/+}$ zebrafish embryos.

VIII. Identifying target clusters and their role in cardiac morphology and function.

IX. Modeling of a human and zebrafish target *in silico* to assess transferability between species.

5 Material and Methods

5.1 Ethics Statement

According to the European legislation this work does not involve work with animals. All experiments were conducted at early stages of zebrafish development before legal onset of animal life. Zebrafish embryos and larvae were obtained from closed stocks at the Fraunhofer Institute for Marine Biology (EMB), Lübeck. The facility is under supervision of the local animal welfare agency representative. All animal experiments were performed in accordance with the German animal welfare regulations (Tierschutzgesetz 111, Abs 1, Nr. 1, AZ35-9185.64/BH).

5.2 Zebrafish Husbandry

Adult zebrafish were kept under standard conditions at a 12 h:12 h light/dark cycle in system water at 28°C (177). Pairs were housed in 3.5 L tanks in a ZebTEC Active Blue Stand Alone and fed twice daily with Tetra Tetramin tropical fish food and artemia. Larvae housed in 500 ml plastic containers and fed paramecia and dry food until 12 dpf, when artemia were added to the feeding plan (Table 30). Then, larvae were transferred into a 1 l plastic container. At 21 dpf zebrafish larvae were transferred into the ZebTEC Active Blue Stand Alone.

System water was composed of 0.06 g NaCl and 0.06 g Instant Ocean Salt/L in filtered reverse osmosis water. Water pH was maintained at approx. 7.5 with a water conductivity beyond 30 µS. Egg water was composed of system water and 3 drops/L 0.05% methylene blue. The medium was used to rinse the fertilized eggs from a plastic sieve into a petri-dish with a washing bottle and to rear embryos. Methylene blue sterilizes the water to inhibit growth of mold in the petri-dish and it stains deceased embryos blue (177).

5.3 High-content Screening

5.3.1 Prestwick Chemical Library

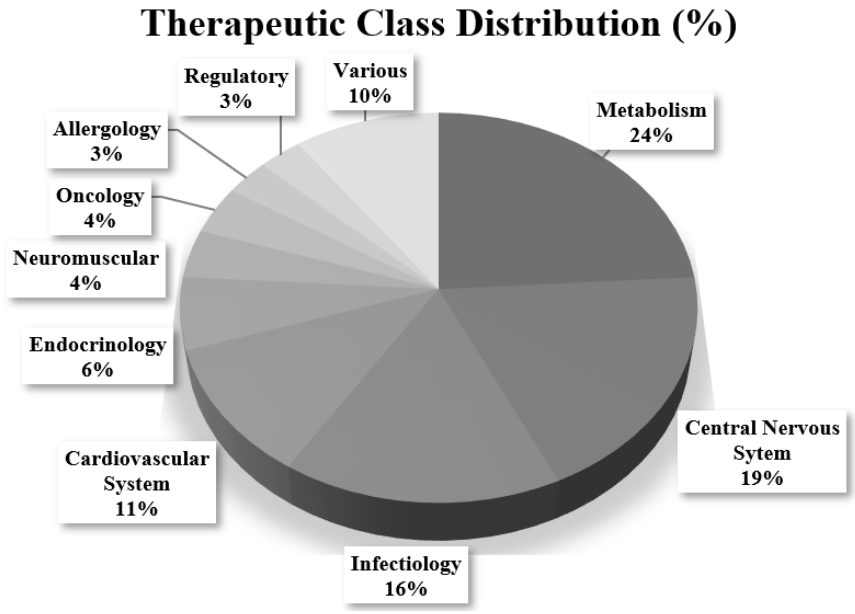

Figure 8: Prestwick Chemical Library Therapeutic Targets
Therapeutic class distribution of the Prestwick Chemical Library in percent. Drugs used for treatment of metabolic disorders, the central nervous system, cardiovascular system, and infections are overrepresented in the drug library.

The 1,280 small molecule library (Prestwick Chemical Library® V. 2019) was obtained from Prestwick Chemical. The compounds were ordered as a pre-dissolved 10 mM dilution in 100% DMSO in a 96-well plate format. Each 96-well plates' column 1 and 12 were empty, to leave room for controls. The library and its dilutions were stored at -20°C. In preparation for the drug screen all drug library plates were diluted 1:10 with water into black 96-well PCR plates in the same format as the original library. The dilution of the drug library was performed in semi-darkness to protect light sensitive compounds. All plates were sealed with a silicone lid that was tested for evaporation under handling conditions with repeated freezing beforehand. Additionally, every plate was wrapped in aluminum foil to protect light sensitive compounds as the silicone lids are transparent.

5.3.2 Zebrafish Lines

Tg(fli1a:eGFP)y7 zebrafish were obtained from the European Zebrafish Resource Center (EZRC), Karlsruhe, Germany. The transgenic line *Tg(fli1a:eGFP)* expresses eGFP in the nucleus of the EC of the vasculature driven by the *fli1a* promoter (178). *fli1a* is the earliest vascular EC marker in the developing zebrafish embryo. It can already be detected 12 hpf in the ventral mesoderm (179).

Table 4: Zebrafish Lines Used for the Establishment and Execution of the High-Content Screen for Cardiovascular Modulators.

Organism	*Genotype*	*Properties*	*Origin*
Danio rerio			
fli1a	*Tg(fli1a:eGFP)*^{y7}	Nuclear green fluorescence, ECs of the vasculature	European Zebrafish Resource Center

5.3.3 Mating, Egg Collection and Sorting

Adults from the Tg(f*li1a:eGFP*)^{y7} line were fed half an hour, before breeding tanks were set up with an acrylic mesh inlay, to prevent egg predation, and a divider in the middle. Breeding tanks were filled halfway with system water. Adult male and female of each pair or group were placed into the breeding tank separated by sex. On the next morning, when the lights turned on, the water of each breeding tank was exchanged with approx. the same amount of fresh system water to avoid a pheromone habituation effect and to stimulate the zebrafish with increased water temperatures and fresh oxygen supply. Dividers were removed immediately after water exchange. One hour after the dividers were removed, adults were removed from the breeding tank using the inlay and moved back into their original tank. Fertilized eggs left in the breeding tank were collected with a nylon sieve and transferred into a glass petri-dish of 10 cm diameter with Egg water. Unfertilized eggs were removed with a plastic Pastette from Alpha Laboratories Limited before the collected eggs were incubated in the KB 115 incubator at 28°C until 20 hpf.

5.3.4 Dechorionation

At 20 hpf zebrafish embryos were removed from the incubator, before deceased embryos were removed with a Pastette. Remaining embryos were transferred into a 6-well plate (Greiner Bio-One International GmbH, Cellstar) without mixing embryos from different parents. Embryos of different lineages were placed on separate 6-well plates to avoid cross-contamination. Using a 1000 µl VWR pipette, remaining egg water was removed from each well and replaced with 2 ml system water each. Then 45 µl 10 mg/ml pronase (Merck Chemicals GmbH) was added to each well with a 100 µl Eppendorf pipette to create a final dilution of 0.22 mg/ml pronase. Right after the pronase was added to the last well, the plates were moved gently in horizontal circular motions to evenly distribute the pronase and to coat the chorions of all embryos. A timer was set for 12 min, as experience showed that this time should not be exceeded. The plates were moved gently as

described every 2 min. Treatment was stopped as soon as the first embryo hatched. Embryos were immediately rinsed with fresh system water to reduce enzyme concentrations, as the embryos are very sensitive. The dechorionated embryos were washed 3-4 times, to remove the pronase. Subsequently, embryo development was assessed, and healthy clutches were transferred together into a 10 cm petri-dish containing system water. Embryos were gently mixed with a Pasteur pipette to avoid batch effects from single pairs. Healthy and properly developed embryos[1] (180), were transferred and evenly distributed into a U-bottom 96-1.2 ml-deepwell plate. The deepwell plate was sealed with a silicone lid and placed into an incubator (KB 115) at 28°C for 1.5 - 2 h until treatment preparation, to give the embryos time to recover from dechorionation and pipetting.

5.3.5 High-Content Screening Using the Prestwick Chemical Library

As a foundation for the assay, a protocol for high-content *in situ* hybridization from Poureetezadi *et al.* (2014)(181) was used and adapted for *in vivo* screening as described below.

The evening before treatment, 1:10 dilutions of the required drug library plates are placed in a fridge at 4°C to thaw overnight. The day of the drug treatment, a 1:100 dilution plate was prepared in a 96-well plate using 100 µl filter tips (Sigma Aldrich GmbH). Compounds were diluted to a final working concentration of 20 µM for all compounds. Angiogenesis was one of the focus points of the screening, therefore, 20 µM of the previously established RTKs inhibitor SuM was used as a positive control (139). All compounds, including SuM, were dissolved in DMSO. Therefore, a concentration of 0.2% (v/v) DMSO was used as a vehicle control.

Excess system water was removed from the 96-deepwell plate containing zebrafish embryos 24 hpf using a glass pipette (Assistent). With a 100 µl Eppendorf pipette and a flat tip (Gilson Incorporated) as much water as possible was removed. Subsequently, the 100 µl from the drug dilution plate were transferred using a 12-multi-channel pipette from VWR and added to the deepwell plate. The plate was sealed with a silicone lid and transferred to the incubator in a Styrofoam container. Then, the 96-well plate was placed into a tray and covered with a black tray to keep out the light[2], before being placed into the incubator. Embryos were kept in the incubator at 28°C until 48 hpf. Treatment was stopped by taking off the silicone lid and washing the embryos three times with system water using a glass capillary. Four 24-well plates were labelled according to a 96-well plate and each well was filled with 500 µl of 0.03% tricaine (Sigma Aldrich) using a 25 ml Ritip from Eppendorf.

[1] Embryonic development standards were based on the embryonic development atlas of Kimmel *et al*. from 1995.
[2] The Prestwick Drug Library contains light-sensitive compounds in more than half of the library plates.

Subsequently, treated embryos were transferred with one drop of system water using the glass pipette into the four 24-well plates containing tricaine.

5.3.6 Preparation of Agarose Orientation Plates and Positioning

One to two days before the treatment ended, orientation plates were prepared. The plates must not be older than two days, to avoid height differences of the agarose due to evaporation. The number of plates needed was dependent on the number of embryos that went into the experiment.

1.5 gr agarose (Biozyme) was dissolved in 100 ml 0.03% buffered tricaine by heating in a microwave twice and stirring it with a magnetic stirrer. Hot agarose was poured into a plastic pipetting tray that was reused for each experiment. After 2 min of cooling at room temperature (RT) 65 µl of 1.5% agarose were transferred using a VWR 12-channel pipette into each well of a flat-bottom 96-well plate (CELLSTAR). This step was performed quickly to avoid hardening of the agarose gel in the tips. Bubbles in the agarose were removed with a pipetting tip. The plate was left for cooling at RT for 2.5 – 3 min, bevor the 3D-printed orientation tool (182) was placed into the agarose-filled 96-well plate. To harden the agarose gel, the 96-well plate still containing the orientation tool, was placed into the cooling room at 4°C for at least 20 min. Subsequently, the orientation tool was removed gently from the plate. In case that the hardened agarose stuck to the tool, it was carefully removed and placed back into the well with a tweezer and a pipette tip. As soon as all orientation plates needed for the experiment were prepared, they were wrapped with a humid cotton towel and placed into a plastic zip bag to preserve moisture of the agarose gel. Plates were stored at 4°C for several days until they were needed for the experiment. On the day of the experiment orientation plates were warmed at RT for 2 h, before single embryos (48 hpf) were transferred into the orientation plate with 50 µl of 0.03% tricaine from the 24-well plates. It's important to note that one orientation plate copied the original plate with each well containing one embryo from the respective treatment. By keeping the 96-well plate format throughout the experiment, a mix-up and a batch effect were avoided.

Subsequent to the transfer of the embryos into orientation plates, they were positioned using self-developed tools. Several 1 ml pipette tips were stacked firmly to create a handle for the positioning tool. The tip was created by bending an injection needle and filing the tip to decrease danger to the embryos. Tools were used to carefully turn the embryos, so their heads were facing to the left and their yolks were facing up, as image acquisition flips the images vertically.

5.3.7 Image and Video Acquisition

The script-based widefield high-content screening microscope ACQUIFER Imaging Machine 3rd generation (ACQUIFER Imaging GmbH, Heidelberg, Germany) was used to acquire image stacks and videos of *fli1a* and *myl7* zebrafish. The Imaging Machine was equipped with a white light-emitting diode (LED) array for brightfield imaging and a LED fluorescence excitation light source (124,183). The stationary plate holder combined with moving optics ensured that the positioned embryos did not move due to vibration during image acquisition. Images were captured by a sCMOS (2048 × 2048 pixel) camera. The temperature-controlled incubation lid was used for long-term imaging only. Each regular image acquisition of a full 96-well plate took approx. 16 min.

Table 5: Imaging Machine Settings for 2x Image Acquisition

	Settings		*Settings*
Time Lapse	1	No. of slices	10
Interval [s]	0	Z Slice Height	15.0
Plate File Indication	96STANDART	Z Stack Center	19500-20300
Objective	2x	Autofocus control	Software Autofocus 1 and 2
470 nm	Intensity: 100% Integration: 100 ms	Autofocus 1	No. of Z Slices: 5 Z Slice Height: 150 µm Binning: 2x2 Objective: 2x Light: 470 nm Intensity: 10% Integr. Time 10 ms
BF	Intensity: 55% Integration: 20 ms	Autofocus 2	No. of Z Slices: 3 Z Slice Height: 50 µm Binning: 2x2 Objective: 2x Light: 470 nm Intensity: 10% Integr. Time 10 ms

Table 6: Imaging Machine Settings for 4x Image Acquisition

	Settings		*Settings*
Time Lapse	1	No. of slices	10
Interval [s]	0	Z Slice Height	15.0
Plate File Indication	96STANDART	Z Stack Center	19500-20300
Objective	4x	Autofocus control	Software Autofocus 1 and 2
470 nm	Intensity: 100% Integration: 100 ms	Autofocus 1	No. of Z Slices: 5 Z Slice Height: 150 µm Binning: 2x2 Objective: 2x Light: 470 nm Intensity: 10% Integr. Time 10 ms
BF	Intensity: 55% Integration: 20 ms	Autofocus 2	No. of Z Slices: 3 Z Slice Height: 50 µm Binning: 2x2 Objective: 2x Light: 470 nm Intensity: 10% Integr. Time 10 ms

Table 7: Imaging Machine Settings for Heartbeat Video Acquisition (fli1a)

	Settings		*Settings*
Time Lapse	1	No. of slices	72
Interval [s]	0	Z Slice Height	0
Plate File Indication	96STANDART	Z Stack Center	19500-20300
Objective	2x	Autofocus control	Software Autofocus 1 and 2
470 nm	Not selected	Autofocus 1	No. of Z Slices: 5 Z Slice Height: 150 µm

			Binning: 2x2 Objective: 2x Light: 470 nm Intensity: 10% Integr. Time 10 ms
BF	Intensity: 55% Integration: 20 ms	Autofocus 2	No. of Z Slices: 3 Z Slice Height: 50 µm Binning: 2x2 Objective: 2x Light: 470 nm Intensity: 10% Integr. Time 10 ms

5.3.8 Concentration Optimization

The high- content screening was designed for a concentration that had the highest survival rate and showed the lowest toxicity during the establishment period. As the standard concentration of 20 µM is naturally not the optimal concentration for each compound, filtered hits were tested in addition with 5, 10, 20, 40 and 80 µM in the *fli1a* zebrafish line following the same protocol as 5.3.5. Some compounds, that showed a noticeable effect at the lowest concentration were also tested for 1 µM. This step was also used to assess compounds for reproducibility.

Table 8: Zebrafish Lines Used for Concentration Optimization of Cardiovascular Hits.

Organism	*Genotype*	*Properties*	*Origin*
Danio rerio			
fli1a	*Tg(fli1a:eGFP)^{y7}*	Nuclear green fluorescence, ECs of the vasculature	European Zebrafish Resource Center

5.3.9 Heartbeat Data Handling and Analysis with *HeartBeat* v2.1

Image data was stored and processed on six WD Elements Portable 5 Tb external hard drives. Raw brightfield (BF) image stacks were pre-processed using a customized Perl script (Gierten *et al.* (2020)) that creates two subfolders for JPEG and TIFF images in addition to a procession Fiji macro

(Supplements Perl script 1) (88). The resulting Fiji macro pseudo-flat-field corrected and intensity normalized all acquired images by applying a Gauss-filter (sigma = 200) duplicate to TIFF images that were subsequently multiplied with 8000. Resulting images were saved with shortened filenames as 16-bit TIFFs and JPEGs. Further image processing required a folder structure corresponding to 96-well plate numbering, which was achieved with the Perl script created by S. Haider. (Supplements Perl script 2). In order to run the files in the *HeartBeat* software, all images required time-stamps according to yy.mm.dd_HH.MM.SS,FFF at given framerate (Table 7) and to be listed in subdirectories by well coordinates. This was achieved by using the previously published MATLAB (MATLAB 2019b) script (Supplement MATLAB script 1) (88).

The processed frames were then analyzed using the MATLAB based *HeartBeat* Software v.2.1 (88) that analyzes heartbeats by segmenting regions of interest (ROIs), feature extraction as well as classification and frequency analysis. The graphical user interface (GUI) allows to adjust given standard settings according to the users' needs. Here, a single fish per well in a 96-well format approach was used with 5 frames for segmentation, 2 px smoothing and a 99.8% threshold.

5.3.10 Vascular Data Handling and Analysis

As described above (5.3.9), image data were stored and processed on six WD Elements Portable 5 Tb external hard drives. Raw fluorescence (GFP) image stacks were processed using the ACQUIFER PlateViewer GUI. Images of each stack that were out of focus were excluded from max projections before stacks of the 96-well plate were saved as TIFF images.

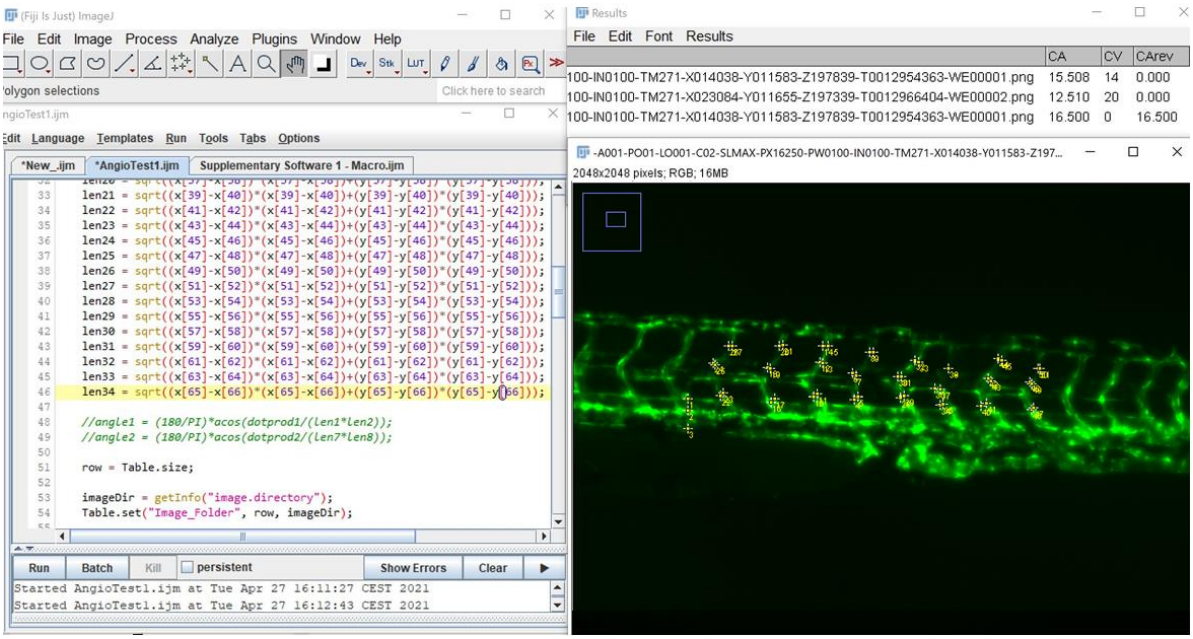

Figure 9: Vessel Measurement Macro

The vessel measurement Fiji macro, used to measure vessel diameters for the angiogenesis and vasculogenesis portion of this study, was adapted from Westhoff *et al*. (124). The 67 reference points have to be manually entered, before the script shown in 9.4.1.1 provides vessel diameters for intersegmental vessels, the dorsal aorta and the dorsal vein in a data sheet (184).

To quantify vessels in embryos at 2 dpf a Fiji macro (9.4.1.1) adapted from Westhoff *et al.* (124) was used to open the created GFP max projections one after another in Fiji and to assign set coordinates (Figure 9) to each image using the multi-point tool (184). A total of 67 point-selections need to be selected to calculate distances between coordinates according to Figure 9. Measurements are automatically saved into a Fiji table that was exported as .xtml when the vessels of all embryos of one plate were measured. Four ISVs left and four to the right of the urogenital pore (UGP) were measured at the top, middle and bottom to create a mean diameter for each vessel and a mean of the vessels, representative for one fish. Additionally, the DA and DV diameter were measured to the left of the UGP.

5.3.11 ToxScore

Pericardial edemas were manually assessed. Mild fluid accumulation, that did not extent the pericardial cavity was considered a mild phenotype. Edemas, that extended from the body were considered moderate. Severe edemas caused drastical extension of the pericardial cavity with fluid between heart and body that pushed the heart outwards. Developmental delays were defined by the

curvature of the head around the yolk[3], pigmentation and head morphology. Significant HR changes were also considered a sign of compound toxicity. Furthermore, zebrafish that were intact but had no detectable heartbeat were counted as fish with cardiac arrest. To assess overall cardiotoxicity and teratogenicity, a ToxScore was developed, that considers pericardial edemas, developmental delay, HR and cardiac arrest.

$$ToxScore = \frac{n\ pericardial\ edema}{n\ total} + \frac{n\ developmental\ delay}{n\ total} + (1 = HR \pm 1.64) + \frac{n\ cardiac\ arrest \times 2}{n\ total}$$

First, the proportions of pericardial edemas and developmental delays were calculated before assigning a score of 1 to each HR z-score exceeding the 90% CI threshold. Then, the proportions of zebrafish with cardiac arrest were doubled to assign more weight to this phenotype. If a compound was completely lethal with no measurable parameters, the concentration was assigned a ToxScore of 5.

5.3.12 Heartbeat Hit Validation

To validate significant hits and exclude line specific effects, a second transgenic line was tested with hit compounds. Hits that showed the same effect on HR in Tg(myl7:eGFP)$^{twu34/+}$ were considered valid.

Table 9: Zebrafish Lines Used for the Heartbeat Hit Validation.

Organism	*Genotype*	*Properties*	*Origin*
Danio rerio			
Myl7	Tg(*myl7:eGFP*)$^{twu34/+}$, formerly Tg(*cmlc:eGFP*)	Nuclear green fluorescence, tagging the myosin light chain 2 in the myocardial cells(107)	University of Potsdam

[3] Embryonic development standards for 48 hpf development were based on the embryonic development atlas of Kimmel *et al*. from 1995.

5.4 pyHeart4Fish

Treated Tg(*myl7:eGFP*)$^{twu34/+}$ zebrafish embryos were analyzed with the newly developed tool *pyHeart4Fish* (185) to gain deeper insights into the compounds' effect on cardiac morphology and function. The Python-based tool is operated via a GUI and is adaptable to every microscope type, via flexible selection of data input (TIF, PNG, AVI, MP4 and CZI files). However, quality of the output is dependent on resolution and speed of the camera used for imaging. Here, we used 20 s long videos with 9.5 frames per second (f/s) captured with the ACQUIFER Imaging Machine and 6 s with 6 f/s acquired with a ZEISS Fluorescence Binuclear Stereomicroscope. *pyHeart4Fish* detects the heart via fluorescence tags expressed in zebrafish embryos and crops the videos to the region of interest (ROI). Then, user-assisted chamber-selection determines the chamber-specific ROI together with segmentation via fluorescence thresholds using the AVC. HS and shape are determined as median of the first six frames.

Chamber-specific raw heartbeat curves are derived from the sum of pixel intensities and normalized chamber areas of each frame. To determine the chamber frequencies [beats per second (bps)] sine curve fitting or Fast Fourier Transformation (FFT) are applied using the respective SciPy modules "optimize.curve_fit" and "fft.rfft/ fft.rfftfreq" (185,186). A max of 30 iterations is used to perform the curve fitting with increased frequencies of the fitted sine function. Correlation coefficient between raw data and fitted function (NumPy) is used to select the best fit. For the first quarter of signals a fitted sine function and fitting score are determined. Then, the best-fitted sine function is used to account for unstable heartbeat signals (185). The first harmonic signal in the FFT is used as the chamber's heartbeat frequency. The video results are displayed as a GIF marking ROIs for atrium and ventricle throughout the analysis of the whole video and a PNG file containing the frequencies and sine function of each chamber (Figure 10). A data sheet provides all quantitative data derived from the analysis.

The additional BF module of *pyHeart4Fish* provides an automated quantification of the HR and offers an overview of the blood flow. Here, the area of the heart is automatically detected via area of highest pixel intensity changes. Values of pixel intensities per frame with the highest standard deviation (SD) across all frames were used to determine the HR. Curve fitting and FFT for the detected signals were performed as previously described. This feature of the tool was used to retrospectively analyze concentrations rows for a ToxScore assessment.

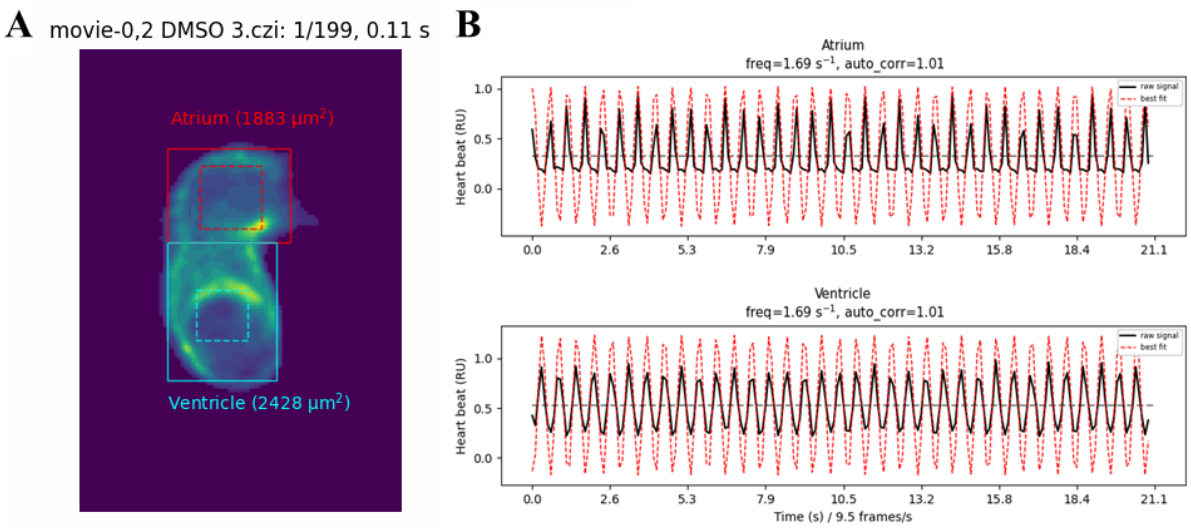

Figure 10: *pyHeart4Fish*

A-B, Representative analysis output of control treated Tg(*myl7:eGFP*)$^{twu34/+}$ embryos at 48 hpf. **A**, The boundary box and region of interest (ROI) are automatically selected for atrium and ventricle. LUT displays differences in fluorescence intensity from minimum (blue) to maximum (yellow). **B**, Heartbeat is detected via changes in size and intensity within the ROI. The atrium- and ventricle-frequency is measured independently, enabling detection of chamber-specific arrhythmias. Straight line = boundary box; dotted line = ROI; auto_corr = auto correlation; freq = frequency; fft_freq = Fast Fourier transformation frequency. The tool was developed together with Dr. Tobias Reinberger.

5.5 *In Situ* Hybridization (ISH)

In situ hybridization (ISH) is one of the most important methods for visualizing and analyzing gene expression in whole embryos. Additionally, ISH allows to determine the role of genes during embryonic development. Here, digoxigenin (DIG)-labeled anti-sense RNA probes bind to the complimentary messenger RNA (mRNA) produced *in vivo*. The DIG-label serves as a target for anti-DIG antibody stainings, eventually detected in the form of nitro blue tetrazolium (NBT) /5-bromo-4-chloro-3-indolyl phosphate (BCIP). The anti-DIG antibody is linked to an alkaline phosphatase (AP) that cleaves the substrate BCIP to an indoxyl intermediate. Under alkaline conditions this tautomerization results in dimerization of the intermediates leading to a leucoindigo that is oxidized by NBT to insoluble 5,5-dibromo-4,4,-dichloro indigo (BCI). Hydrogen ions released during dimerization of indoxyl intermediates cause reduction of NBT to insoluble NBT diformazan. Both reactions create a dark blue stain close to the bound antibody, providing a specific signal of gene expression (187). The *in-situ* hybridization protocol used in this study was adapted from Thisse and Thisse (2008) (188).

5.5.1 Polymerase Chain Reaction (PCR)

The polymerase chain reaction (PCR) was conducted to generate linearized DNA fragments from embryonic zebrafish complimentary DNA (cDNA). The reaction was performed with the 2x HotStart RedTaq PCR Mastermix following the protocol displayed in Table 10 with the PCR program of TAdvanced thermocycler from Biometra® shown in Table 11. Primers displayed in Table 12 were created using the described sequences provided by the National Center for Biotechnology Information (NCBI) and the web-based tool Primer3 + BLAST. The T7 promoter sequence was attached to each reverse primer.

Table 10: PCR for Linear Template Generation

Components	*Volume*
2x RedTaq PCR Mastermix	10 µl
MilliQ H_2O	7 µl
Primer (Forward + Reverse)	2 µl
cDNA	1 µl

Table 11: HotStart PCR Reaction Protocol

Application	*Temperature (°C)*	*Duration (min:sec)*	*Cycles*
Activation	95	05:00	1
Denaturation	95	00:15	35
Annealing	55	00:30	35
Elongation	72	00:40	35
Final elongation	72	07:00	1
Holding	16	∞	∞

Table 12: Whole Mount *In Situ* Hybridization (WISH) Primers Used for HotStart PCR

Name	*Reference Seq.*	*Sequence (5'-3')*	*Product size [bp]*	*Origin*
hrh1 WISH fw	NM_001042731.1	GATGGACTATGTGGCGAGCA	667	Integrated DNA Technologies, Inc
hrh1 WISH rv +T7	NM_001042731.1	TAATACGACTCACTATAGGG TTCCCCGTCATCGCTTTGAA		Integrated DNA Technologies, Inc
hrh1_2 WISH fw	NM_001042731.1	CAGAAGGGCGGCCATCATTA	498	Integrated DNA Technologies, Inc
hrh1_2 WISH rv +T7	NM_001042731.1	TAATACGACTCACTATAGGG CGTTGCAGAGCGGGTAAATG		Integrated DNA Technologies, Inc
hrh2a WISH fw	NM_001045338.2	TCCGCTACGATACCCAATGC	656	Integrated DNA Technologies, Inc
hrh2a WISH rv +T7	NM_001045338.2	TAATACGACTCACTATAGGG AATGGGCGTGTCCAGTCATT		Integrated DNA Technologies, Inc
hrh2a_2 WISH fw	NM_001045338.2	CCACTAAGGAGGCGGGGATA	508	Integrated DNA Technologies, Inc
hrh2a_2 WISH rv +T7	NM_001045338.2	TAATACGACTCACTATAGGG CGCAAAGTAGCGATCCAAGC		Integrated DNA Technologies, Inc
hrh2b WISH fw	NM_001109738.1	TGACCGCTACCTTGCCATTT	410	Integrated DNA Technologies, Inc
hrh2b WISH rv +T7	NM_001109738.1	TAATACGACTCACTATAGGG CGAGGGTCACTGTGGCTTTA		Integrated DNA Technologies, Inc
hrh2b_2 WISH fw	NM_001109738.1	GAATGAATGACCCTGGGCTGA	408	Integrated DNA Technologies, Inc
hrh2b_2 WISH rv +T7	NM_001109738.1	TAATACGACTCACTATAGGG AGAAAACACCCCCAAGAGGC		Integrated DNA Technologies, Inc
hrh3a WISH fw	NM_001025518.1	ACAGGGAAATGGATGCTGGG		Integrated DNA Technologies, Inc
hrh3a WISH rv +T7	NM_001025518.1	TAATACGACTCACTATAGGG ACACATCGCATCGAGAGACC		Integrated DNA Technologies, Inc

Name	*Reference Seq.*	*Sequence (5'-3')*	*Product size [bp]*	*Origin*
hrh3b (chr. 2) WISH fw		AGTCTAGCCAACCGTTTCCG		Integrated DNA Technologies, Inc
hrh3b (chr. 2) WISH rv +T7		TAATACGACTCACTATAGGG ACAAGGTCTGACAATGAACACA		Integrated DNA Technologies, Inc
hrh3c (chr. 22) WISH fw	XM_003200921.5	GGGAAACGCGCTGGTTATTC		Integrated DNA Technologies, Inc
hrh3c (chr. 22) WISH rv +T7	XM_003200921.5	TAATACGACTCACTATAGGG TGGCGAAACTTCTTCGTCGT		Integrated DNA Technologies, Inc
nr3c1 WISH fw	NM_001020711.3	CATATGCGGGGTCACCACTT	545	Integrated DNA Technologies, Inc
nr3c1 WISH rv +T7	NM_001020711.3	TAATACGACTCACTATAGGG GCTGGATTACCTTTCCGGCT		Integrated DNA Technologies, Inc

5.5.1.1 Gel-Electrophoresis

All gels generated in the process of generating probes during this study were 1% gels with 1x TBE containing Midori Green Advance DNA Stain from Nippon genetics Europe GmbH. Midori Green was used as an alternative for ethidium bromide to visualize DNA bands on the gel. All gels were run with a BlueMarine™ Horizontal Submarine Electrophoresis Unit at 120 V.

5.5.2 DNA Gel Extraction

The gel extraction was used to separate the linear DNA templates from additional bands. The bands were cut from the gel on a UV table using a scalpel, before they were transferred into individual 1.5 ml tubes. Gel slices were weighed and the protocol of the Monarch® DNA Gel Extraction Kit from New England Biolabs® Inc. was followed. The DNA purification followed the kits protocol with minor changes. Gel slices were incubated for at least 10 min to ensure complete dissolving of the gel. Instead of a second washing step, columns were spun dry in the Mikro 120 centrifuge from Hettich Zentrifugen at 13.000 rpm for 1 min. 8 µl MilliQ ultrapure water were added to the dry column, before incubation for at least 2 min at RT, before DNA was eluted. Eluate was added to the column again and eluded a second time, to increase DNA recovery. These concentrations were measured using the Nanodrop 2000.

5.5.3 *In Vitro* Transcription (IVT)

In this step RNA is synthesized *in vitro* using a linearized plasmid template containing a T7 promotor sequence. The T7-polymerase uses ribonucleoside triphosphates (NTPs) to synthesize the complimentary RNA that can be used for *in situ* hybridization. As the linear template DNA concentrations were comparably low, double the usual value for probe synthesis (188) was used as shown in Table 13. All components were thoroughly mixed by gentle up and down pipetting, before the samples were placed into a T3 Thermocycler from Biometra® at 37°C for 3-4 h.

Table 13: *In vitro* transcription

Components	*Volume*	*Final concentration*
5x Transcription buffer	2 µl	1x
DTT 0.1 M	1 µl	10 mM
Linear template DNA	5 µl	50-200 ng
RNAsein (40 U/µl)	0.5 µl	10 U
DIG-RNA labeling mix (UTP)	1 µl	
T7 RNA polymerase (20 U/µl)	0.5 µl	5 U

5.5.3.1 RNA Purification

Following the amplification of the RNA probes, 2 µl of RNase-free DNase I in addition to 8 µl of RNAse-free water was added to the probe mixture to digest any impurities from DNA fragments. Then, the mix was incubated for another 30 min at 37°C.

5.5.3.2 RNA Purification MiniPrep

The RNA was further purified and DNase treatment was stopped using the Zymo Research RNA Clean & Concentrator Kit. All steps followed the original protocol: “Total RNA Clean-up”. Before elution in the last step, columns were kept for 3 min at RT, so the remaining ethanol (EtOH) from the columns could evaporate. Finally, 10 µl previously sealed, RNase-free MilliQ water not contained in the Kit was added to the columns. After 2 min of incubation, columns were placed into a Mikro 120 from Hettich Zentrifugen centrifuge at 13.000 rpm for 1 min as described in the protocol. RNA concentrations were measured using the Nanodrop 2000. Here, 60 ng/µl were used as a threshold for a viable probe. The yield of this protocol varied greatly depending on the

expression of the original target and its amplification during the first PCR and later the *in vitro* transcription.

5.5.4 Methanol Dehydration Gradient

The methanol (MeOH) dehydration is used to prepare embryos for *in situ* hybridization. Fertilized eggs were incubated in egg water O/N, before water was exchanged for 0.003% N-Phenylthiourea (PTU) in egg water (PTU-EW) to prevent pigment formation 22-24 hpf. Water was exchanged daily with fresh PTU-EW to continuously inhibit pigment formation. Embryos were collected at the following developmental stages: 18 hpf, 1 dpf, 2 dpf, 3 dpf and 5 dpf. Collected embryos were dechorionated following protocol 5.3.4 or when older than 2 dpf, were manually dechorionated using forceps. The dechorionation is necessary to enable visualizations of a straight body axis. Then, embryos were washed in phosphate-buffered saline (PBS), before being transferred into 4% paraformaldehyde (PFA) in PBS. Samples were then stored at 4°C until dehydration. The dehydration was performed in a 12-well plate with Corning™ Costar™ Netwell™ inserts to move the samples through the dehydration sequence described in Table 14.

Table 14: Methanol Substitution Gradient

Methanol	*PBS*	*Duration*
25%	75%	10 min
50%	50%	10 min
75%	25%	10 min
100%		10 min

5.5.5 Rehydration (PBST)

In preparation for the staining, fixed and dehydrated embryos must be rehydrated in a MeOH/PBS + Tween (PBST) gradient at RT (Table 15). For less than 50 embryos 500 µl of each solution is used to treat the embryos in a 2 ml Eppendorf tube. For more than 50 embryos 1 ml was used in each step. During every step fish were rocked gently at the lowest speed on a CAT ST5 rocker to increase the area of exposure to the solutions for every fish.

Table 15: PBST Rehydration Gradient

Methanol	*PBST*	*Duration*
75%	25%	5 min
50%	50%	5 min
25%	75%	5 min
0%	100%	4x 5 min

5.5.6 Digestion

The digestion step with proteinase K in PBST is necessary to make embryos more permeable for the RNA *in situ* probe. If digestions were conducted too shortly, the probes are unable to penetrate the skin, while over-digestion would alter embryo morphology (188). Therefore, digestion time and proteinase K concentration was adapted according to developmental stages of the fish (180):

Table 16: Proteinase K Digestion Protocols

Developmental stage	*Incubation time*	*Proteinase K dilution*
9-18-somite	3 min	1:1000
24 hpf	5 - 10 min	1:1000
36-72 hpf	10 - 15 min	1:1000
>72 hpf	15 - 20 min	1:500
5 dpf	30 min	1:500

The reaction was stopped by washing with PBST two times for 5 min. Embryos should not be rocked at this point, as the digestion makes them fragile, and the egg yolk may be lost.

5.5.7 Refixation

The refixation stabilizes the embryos and fixes them again, so they stay preserved and intact. In this step, embryos were incubated in 1 ml 4% PFA at RT for 20 min, before being washed five times for 5 min while being rocked gently at the lowest speed on a CAT ST5 rocker.

5.5.8 Prehybridization

In this step the embryos were prepared for probe addition. The prehybridization buffer (Prehyb) contains formamide that disrupts double-stranded DNA and RNA bonds and saturates the embryos with the solution. The buffer was prepared according to the protocol described in Table 17. Acide citrique was used to bring the Prehyb to a final pH of 6, before water was added. The Eppendorf Thermomixer comfort 1.5 ml and the Prehyb were pre-heated to 70°C. Then, 500 µl of the Prehyb were added to the embryos, before they were incubated at 70°C for 2-5 h. At this point embryos can be stored at -20°C and be kept for up to 2 months.

Table 17: Prehybridization Buffer

Buffers and Solutions	*Volume*	*Final*
Formamide	25 ml	50% formamide
20x SSC	12.5 ml	5x SSC
Heparin 5 mg/ml	0.5 ml	50 µg/ml
tRNA 50 mg/ml	0.5 ml	500 µg/ml
Tween 20 20%	0.25 ml	0.1%
Acide citrique 1M	0.46 ml	-> pH 6
H_2O	To 100 ml	

5.5.9 Hybridization

After preparation of the embryos for the staining, the previously created DIG-labelled RNA (Probe) (protocol 5.5.3) was added to bind to the specific, complementary targets. The hybridization mix was prepared with 500 µl of Prehyb, 50µg/ml heparin and 500 µg/ml tRNA. The tRNA in the hybridization mix will block unspecific RNAs. Heparin acts as a stabilizing co-factor for the process. Then, 500 µl/probe of hybridization mix was preheated to 70°C. In case embryos were stored at -20°C, they were warmed to RT, before being heated to 70°C as well in order not to damage the samples. Embryos were divided into 1.5 ml tubes according to the respective probes. Here, different developmental stages that were divided before, were placed together in one tube/probe as they can be separated later in the images. Afterwards, Prehyb was removed with a Pasteur pipette and replaced with 500 µl hybridization mix. Then, a total of 200 ng of probe was added to the respective

tubes to start the hybridization process. Probe concentration may vary depending on the target and quality of the probes. Finally, samples were incubated at 70°C O/N. Probes can be used several times to stain embryos. In this case, instead of adding hybridization buffer and probe, the previously used mixture containing the probe was added to the samples after removal of the Prehyb.

5.5.10 Washes

Saline-sodium citrate (SSC) buffer was used during washing steps to ensure stringency. Washing solutions were preheated to 70°C and all following steps described in Table 18 were performed at 70°C as well. Probes removed from the samples in the first step were kept and stored at -20°C. Probes can be used several times for staining and may work best at second/third use as a lot of unspecific background was removed in the last staining.

Table 18: Stringency Washes

Washing solution		*Volume*	*Temperature*	*Incubation time*
SSC / PBST	*Prehyb*			
-	***100% Prehyb***	500 µl	70°C	20 min
50% SSC (2x)	***50% Prehyb***	500 µl	70°C	20 min
75% SSC (2x)	***25% Prehyb***	500 µl	70°C	20 min
100% SSC (2x)		1 ml	70°C	2x 20 min
100% SSC (0.2x)		1 ml	70°C	3 x 20 min
PBST		1 ml	70°C	5 min

5.5.11 Blocking

The blocking minimizes unspecific background staining. 10 mg/ml bovine serum albumin (BSA) in PBST was added to 1 ml of 5% sheep serum at RT for 2-5 h on a rocker at the lowest speed in the dark.

5.5.12 Antibody-Incubation

Anti-DIG-AP was diluted 1:5000 in blocking buffer, before 500 µl was added to the samples. Embryos were then incubated O/N at 4°C.

5.5.13 NTMT Washes

The Anti-DIG-Antibody that did not bind to the probes was thoroughly washed off of the embryos following the protocol shown in Table 19. The NTMT solution was created following the standard protocol (Table 20).

Table 19: Antibody Removal Washes

Washing solution	*Temperature*	*Incubation*
1 ml PBST	RT	2x 5 min
1 ml PBST	RT	6x 30 min
1 ml NTMT	RT	3x 5 min

Table 20: NTMT Solution

Buffers and Solutions	*Volume*	*Final*
100 mM Tris HCl pH 9.5	2 ml	Tris HCL pH 9.5 [1 M]
50 mM MgCl2	1 ml	MgCl2 [1 M]
100 mM NaCl	2 ml	NaCl [1 M]
0.1% Tween 20	200 µl	Tween 20, 20%
H2O	14.8 ml	

5.5.14 Staining

After this last washing step embryos were transferred into an aluminum foil covered 24-well plate, as the staining solution is light sensitive and light exposure should be reduced as much as possible. The supernatant was removed and replaced with ~1 ml staining solution to start the staining reaction. The staining solution was prepared with 1:500 NBT/BCIP in NTMT.

Once the staining was started, the duration of the staining was tracked with a stereo microscope and stained embryos were monitored in 10–15 min intervals for the first hour, then 30 min intervals for the next hour and finally every hour afterwards. The staining solution was light yellow and turned purple, when it was exposed to too much light as it precipitates. In this case the staining solution was replaced with fresh staining solution to prevent background staining.

At the end of the day, embryos were divided in two groups. One was stained O/N, the other was paused by washing the embryos twice for 5 min with NTMT. This step does not stop the staining completely.

5.5.15 Stop

In order to stop the staining process altogether, when the desired staining intensity was achieved, embryos were washed three times for 5 min with PBST, before being washed thrice with stop solution for 5 min each. The stop solution was prepared with 1 mM Ethylenediamine tetraacetic acid (EDTA) pH 5.5 in PBST. Finally, embryos can be stored in stop solution at 4°C in the dark for up to several months.

5.5.16 First Clearing

The first clearing step with MeOH dehydrates the embryos and clears some of the background in the stained embryos. Following the MeOH dehydration as described in Table 21, embryos were incubated at least O/N. In 100% MeOH they can also be stored at 4°C for several days.

Table 21: Second MeOH Dehydration Gradient

Methanol	*PBST*	*Duration*
25%	75%	5 min
50%	50%	5 min
75%	25%	5 min
100%		3 x 5 min

5.5.17 Second Clearing

Depending on the clearing method, the second clearing removes not only the staining background, but also pigments of the body and the yolk.

5.5.17.1 Glycerol Clearing

Glycerol is a mild optical clearing agent that clears the tissues it comes in contact with by leveling out the refractive index and decreasing light scattering. Thus, glycerol does not clear tissues completely, but it can create a contrast needed for imaging of certain tissues. Additionally, glycerol

enables easy mounting of the embryos, unrestricted image visualization and it keeps the embryos from drying up during imaging.

5.5.18 Image Acquisition of WISH

Whole mount *in situ* hybridization (WISH) stainings without fluorescence were captured using the Canon EOS 5D Mark III mounted on a Zeiss Axioscope. Images were captured in lateral, dorsal and ventral view. Embryos were mounted in 80% glycerol / 20% stop solution between a microscopic slide and a coverslip. Left and right between slide and coverslip 4–5 small coverslips were stacked using super glue to create a cavity in which the embryo can be positioned in virtually any orientation (189). To visualize the heart fish were clipped close to the yolk sack using a forceps and mounted upright to visualize in an anterior frontal view.

5.6 Organ Dissections

Organs from adult AB WT zebrafish were removed following the standard protocol from Gupta and Mullins (2010) (190). For the dissection of the hearts, zebrafish were opened using a Y cut. Head and organs were removed together and placed into PBS in a petri dish, before muscles, gills and the lower jaw were removed, and the esophagus was cut to remove the organs from the head. Then, the heart was carefully extracted to keep the atrium and BA intact and excess tissue was removed. Afterwards, the eyes and the brain were extracted and finally, the other organs were separated. Organs were either transferred to 4% PFA for cryosections or were frozen in liquid nitrogen for RNA extraction.

5.7 Frozen Section Procedure (Cryosections)

The frozen section procedure, also called cryosectioning, provides thin slices of any organ for microscopic analysis on a cellular level (191). As samples are frozen, prevention of ice crystals forming within the tissues should be avoided. Therefore, the hearts used for sectioning were fixed in 4% PFA for 48-72 h in a 2 ml tube. In the next step, zebrafish hearts were dehydrated in 10% sucrose in PBS for 24 h and then fixed in 30% sucrose in PBS for another 24 h. Finally, the sucrose was replaced with Tissue freezing medium from Leica and saturated O/N. Each of the fixation steps was extended if tissues were not saturated and did not sink to the bottom of the 2 ml tube. Hearts were positioned sagittally and frozen at -80°C for at least 20 min, before they were sectioned at -20°C using the Thermo Scientific™ CryoStar™ NX50 cryostat. A new blade was used for every day of sectioning. The frozen samples were transfered with enough Tissue freezing medium onto the mount, so the blade would not brake on the mount. Section thickness was set to approx. 4.5–

6 µm. After cutting, each tissue section was transferred to a RTed covered slide. The temperature difference allows for proper adhesion of the sample to the slide. All slides were left out to air-dry O/N to ensure proper adhesion, before they were transferred into a plastic container and frozen at -20°C until staining.

5.8 RNA Isolation from Larvae

To increase yield of RNA extraction, 20 larvae at 5 dpf were pooled in one tube and frozen in liquid nitrogen. Larvae were then lysed with 600 µl of the lysis buffer for 15 min. Accordingly, 600 µl 70% EtOH were added to the respective samples. Otherwise, RNA isolation followed the protocol of the IST Innuscreen GmbH innuPREP RNA Mini Kit 2.0. For centrifugation steps the Eppendorf AG Centrifuge 5415R was used. RNA was eluted with 30 µl RNase-free ddH_2O provided by the kit.

5.9 TRIzol RNA Isolation from Adult Organs

Deep frozen organ tissues were added to 2 ml tubes together with ceramic beads and 1 ml TRIzol® Reagent from ambion on ice. Tissues were then lysed in the Qiagen TissueLyser LT for 10 min at 50 s^{-1} oscillation. In the next step, 200 µl chloroform were added to the samples, before they were mixed using a vortex mixer and then centrifuged for 30 min at 13.000 rpm at 10°C to separate phases. The top phase was transferred into a RNase-free tube (usually 450 µl) and the rest discarded. The same volume of 70% EtOH was added to the clear phase and 700 µl of the mixture was transferred onto a RNeasy spin column of the Qiagen RNeasy® Plus Mini Kit and spun down. Flow-through was discarded and the leftover phase was added onto the same column before being centrifuged again. Then, 350 µl of RWI buffer was added to the column and spun. In the next step 10 µl DNAse diluted in ddH_2O was added to 70 µl buffer and then transferred onto the column. DNAse treatment was continued for 30 min, before it was stopped by adding 350 µl RWI buffer and spinning it down. Receiver tube with content was discarded and replaced with a new receiver tube. Then, 500 µl RPE buffer was added to the column, incubated for 5 min, before being spun down. This step was repeated twice. For final cleanup, 500 µl of 80% EtOH was added to the column and centrifuged. EtOH was discarded and the column was spun dry for 3 min at 13.000 rpm at 23°C. Finally, the column was transferred into a clean RNAse-free tube and eluted with RNase-free ddH_2O. Depending on the tissue, RNA was eluted with either 25 or 50 µl RNase-free ddH_2O. Every centrifugation step, if not otherwise indicated, was performed for 2 min at 10.000 rpm at 23°C.

5.10 Reverse Transcription

RNA was transcribed into cDNA for subsequent analysis. All samples belonging together were diluted to one concentration on ice. Then, RNA was incubated for 5 min at 68°C, before samples were placed on ice again to cool down. In the next step, 10 µl mastermix per sample were prepared (Table 22) and added to the RNA to a total volume of 20 µl. Samples were thoroughly homogenized and incubated for 60 min at 37°C, before the enzyme was denatured for 5 min at 95°C. Finally, samples were placed on ice, when directly used for RT-qPCR. Otherwise they were frozen at -20°C.

Table 22: Mastermix for 20 µl Reverse Transcription

Components	*Volume*
5x First strand buffer	4 µl
dNTPs (4 mM)	2 µl
DTT	1 µl
Hexanucleotide Random Primer Mix	1 µl
Reverse transcriptase MLV-RT	1 µl
RNAse inhibitor RiboLock	1 µl
Zebrafish RNA	10 µl

5.11 Primer-Testing and Gel Electrophoresis

The functional analysis of the RT-qPCR-primers was performed with a RT-PCR (Table 10) in a TAdvanced thermocycler from Biometra® using the Taq red mix program with minor adaptions (Table 11). Annealing was set to 60°C for 30 s and the elongation step was changed to 72°C for 20 s. Control cDNAs from zebrafish embryos 3 dpf were used to assess functionality of the primers. Working primer sequences designed with NCBI and the web-based tool Primer3 + BLAST, are displayed in Table 23. 1% agarose gels in 1x TAE containing 3 µl Midori Green/50 µl agarose gel were utilized to visualize DNA bands on the gel. 5 µl of the marker and 5 µl of each PCR-product were applied with loading buffer. Agarose gels were run with a BlueMarine™ Horizontal Submarine Electrophoresis Unit for 35 min at 120 V. Afterwards gels were visualized using a UV table.

Table 23: Oligonucleotides Used for RT-qPCR

Name	*Reference Seq.*	*Sequence (5'-3')*	*Product size [bp]*	*Origin*
nr3c1_F2	NM_001020711.3	CAAACGAGCAACTGAGGGGA	132	Eurofins Genomics
nr3c1_R2	NM_001020711.3	TTGCTCAGGCCATTGGGAAT		Eurofins Genomics
zf_18s_F1	(192)	TCGCTAGTTGGCATCGTTTATG	150	Eurofins Genomics
zf_18s_R1	(192)	CGGAGGTTCGAAGACGATCA		Eurofins Genomics

5.12 Quantitative Real-Time Polymerase Chain Reaction (RT-qPCR)

RT-qPCR followed the protocol displayed in Table 24. The 384-well plates were sealed with Crystal qPCR Foil from © 2014 Biolab*products* GmbH and centrifuged with the ROTANTA 460 R from Andreas Hettich GmbH & Co.KG to remove air bubbles and ensure that the RT-qPCR mix is at the bottom of the well. All RT-qPCRs were performed on the 7900HT Fast Real-Time PCR System (TaqMan) from Applied Biosystems™ - Thermofisher Scientific with a total volume of 8 µl per sample in 384-well plates (Sarstedt) following the reaction protocol displayed in Table 25. A melting curve analysis at the end of the RT-qPCR was used to assess the specificity of the amplification. Threshold cycles (CTs) were obtained from the data output file of the TaqMan. After calculating the arithmetic mean of the technical triplicates for the targeted gene and the housekeeping gene (HKG) (18s), the ΔCT was determined.

$$\Delta CT = avCT(target\ gene) - avCT(HKG)$$

The ΔΔCT was calculated by normalizing the expression levels of the target genes to that of the average HKG *18s*.

$$\Delta\Delta CT = av\Delta CT(sample\ target) - av\Delta CT(sample\ HKG)$$

Relative gene expression compared to the control group was obtained by subtracting the ΔΔCT values from the amplification efficiency (2 = 100%).

$$Relative\ gene\ expression = 2\text{^} - \Delta\Delta CT$$

Calculations followed Livak and Schmittgen (2001) (193).

Samples with an HKG CT over 24 were excluded, as they exceeded the normal range of values for the HKG in this institute, which suggests degraded or insufficient RNA. All experiments were performed in biological and technical triplicates. Values that differed more than 2 CTs from the other two values of a technical triplicate were removed due to pipetting errors. If only one value was left after the removal of pipetting errors, the whole sample was not considered for the calculations.

Table 24: RT-qPCR Mastermix Protocol

Buffer and Solutions	*Quantity*
cDNA	1.5µl
2x PowerUp™ SYBR® Green Master Mix	3,75 µl
Forward and reverse primer	1.125 µl
ddH_2O	1.125 µl

Table 25: RT-qPCR Reaction Protocol

Application	*Temperature (°C)*	*Duration (min)*	*Cycles*
UNG-Digestion	50	2	1
Inactivation	95	10	1
Denaturation	95	15	40
Annealing and Elongation	60	1	40
Holding temperature	16	∞	∞

5.13 Schrödinger Maestro

5.13.1 System Setup

Schrödinger Maestro 2022 version 3 (194) with an OPLS4 (195) force field was used to perform molecular docking approaches.

5.13.2 Protein X-Ray Structure Selection

To identify the most suitable crystallographic structures the US data center for the global Protein Data Bank (PDB) archive (196,197) was searched for the term “NR3C1” and filtered for *Homo sapiens* crystallographic structures in a non-DNA-bound conformation with co-crystallized steroidal agonists at a resolution lower than 3 Å. After filtering of the 44 crystallographic structures, seven X-ray structures remained. In turn, three of seven structures had the same co-crystallized ligand dexamethasone. 4UDC not only had the best resolution of 2.5 Å but also did not include any special co-activators and was thereby comparable to the other structures (198).

5.13.3 Protein Preparation

Imported PDB structures were preprocessed with the Schrödinger Protein Preparation Wizard (199). This tool ensures high quality structures by adding missing hydrogens, correcting metal ionization and removing co-crystallized water, as even high-resolution X-ray structures may be incomplete. Here, PDBs were preprocessed by assigning bond borders via Conserved Domain Database (CCD) (200), replacing hydrogens and creating zero-order bonds to metals, and disulfide bonds. Terminal oxygens were added to protein chains and selenomethionines were converted to methionines. Missing loops were filled/refined with Prime (201). Het states at a pH of 7.4 ± 2.0 were generated using Epik (202). H-bond assignments were performed utilizing PROPKA with sample water orientations. During minimization, heavy atoms were converged to an root-mean-square deviation score (RMSDs) of 0.3 Å with the OPLS4 (195) force field, while waters with a 5 Å distance from the ligands were deleted.

5.13.4 Ligand Preparation

Ligands were prepared using LigPrep (203) with an OPLS4 force field minimization and Epik at a pH of 7.4 ± 2.0. Furthermore, ligands were desalted, tautomers were generated and specified chiralities were retained.

5.13.5 Sequence Comparison, Template and Target Selection

Today’s X-Ray and NMR databanks for human proteins have become extensive; however, datasets for animal models such as zebrafish are still relatively small. One option to balance this deficit is to develop 3D computational models. Homology modeling operates on the assumption that sequence similarity can equate structural similarity. In this case, AlphaFold (204,205) was not able to provide a zebrafish Nr3c1 structure (19/09/2022). Therefore, the Schrödinger modeling software was utilized to develop a zebrafish Nr3c1 model.

There are two strategies to generate a sequence alignment for homology modeling: global and local. Local methods align similar partial sequences in the primary structures, while global methods align sequences along the full lengths of the primary structures. One advantage of the local methods is that the search for homologue proteins is limited to an area with similar partial sequences, such as protein domains. One example of a local method is the Smith-Waterman-Algorithm (206). FASTA and BLAST (207) are both methods that approximate the Smith-Waterman-Algorithm in simpler, heuristic ways for local alignments (208). Here, National Institutes of Health (NIH) standard protein BLAST®'s (207) remote Homology Search in the Schrödinger Suite was used to search for proteins with high structural similarity to the zebrafish protein based on the UniProt (209) FASTA (210) sequence Q1XHK0 (19/09/2022), encoding Nr3c1 (template). As a result, a large number of homologue proteins were identified, the top ten are listed in Supplementary Table 12. Both X-ray crystal structures of the ancestral glucocorticoid receptor 2 (AncGR2) in complex with dexamethasone (211), displayed an identity of 85.89% with 0 gaps and a significant E-value of $5.51E^{-154}$. Both structures, A and B, were identical in regard to their sequence. Therefore, the B-factor was determined in a 5 Å radius from the ligand in the binding pocket. The B-factor, also called the atomic displacement parameter, describes the attenuation of thermal motion scattering (212). While both structures demonstrated great similarities, A had a B-Factor of 31.39, while B had a B-Factor of 30.51. Therefore, the ANcGR2_B was selected for homology modeling with the ligand dexamethasone included to model the agonistic state with a steroidal agonist (Figure 43 A). The model was minimized with the OPLS4 force field minimization to minimize steric errors.

5.13.1 Homology Modeling and Evaluation

Schrödinger Prime was utilized to generate the homology model. Alignments between template and target were created based on their sequences and secondary structures. Prime Homology Modeling follows five basic steps. First, copying of backbone atom coordinates for aligned regions and conserved side chain coordinates. Second, optimization of side chains. Side chains that are not conserved are compared to the target and modelled accordingly. Then, non-conserved residues are energy optimized with the OPLS4 force field. Finally, loops that are not template-based are refined.

5.13.2 meta-Model Quality Assessment Program (MQAP) Top Score

The homology model developed in 5.13.1 was verified using the meta Model Quality Assessment Program (meta-MQAP) TopScore (213). The TopScore predicts the Local Distance Difference Test

(IDDT) error of the protein globally. Thus, low scores correspond to low estimated error and thereby with high quality (Figure 43 B, blue/cyan).

5.13.3 Ramachandran Plot

The Ramachandran plot, originally developed by Ramachandran *et al*. in 1963 (214), visualizes energetically allowed regions for backbone dihedral angles of amino acids (AAs) residues by plotting the ψ angle against the φ angle (215). It can also be utilized to visualize theoretical conformations of the ψ and φ angles for AA residues. Furthermore, it can be utilized for structure validation by presenting the empirical distribution of datapoints in one or several structure/s. The Ramachandran plot is asymmetric as it is based on the stereochemistry of the AA's backbone (216). Stable proteins have a hierarchical structure: Secondary structures interact with one another and form tertiary structures (215,216). A secondary structure is present when each van-der-Waals radius and dihedral angle remains (almost) the same throughout the segment (215). Here, validation of the homology model was performed with a Ramachandran Plot from the Ramachandran Plot Server (217). Glycine and proline residues were excluded from the analysis.

5.13.4 MultAlin Multiple Sequence Alignment

To identify areas within the protein that are not conserved, a multiple sequence alignment was performed with the MultAlin (218) multiple sequence viewer. For the comparison the FASTA sequence Q1XHK0 of the zebrafish Nr3c1 was aligned against the human NR3C1 3CLD PDB sequence (Supplementary Figure 7).

Further, to generate the correct in situ probes, the correct identity of duplicated and triplicated genes was verified using the MultAlin multiple sequence viewer with the sequences displayed in Table 37 (see Supplementary Figure 2, Supplementary Figure 3 and Supplementary Figure 4).

5.13.5 Receptor-Based Glide Grid Generation

The crystallographic structure of NR3C1 in complex with FCP (3CLD) (219) was utilized to identify the binding pocket. The receptor grid was generated via centroid of workspace ligand with a scaling factor of 1.0 and a partial charge cutoff of 0.25. A grid for Glide docking was established as a 12 Å cube prior to Glide ligand docking.

5.13.6 Flexible Glide XP Docking

Prepared ligands from LigPrep (5.13.4) were docked into the receptor Glide grid using extra precision (XP) docking with flexible ligand sampling. Ligands from the Prestwick Drug Library

(PDL) V. 2019 database were imported as a 2-dimensional (2D) SDF format and converted to 3D for docking studies.

In addition to Epik state penalties, torsion of amides with nonplanar conformation were penalized and van der Waals (vdW) radii were scaled to the factor of 0.8 with a partial charge cutoff of 0.15. Number of ligand poses were limited to 1. For post-docking minimization 10 poses per ligand were included with a rejection threshold of 0.5 kcal/mol for minimized poses. The Glide Score and Prime energy were used to score ligand poses, before the best pose for each ligand was superimposed against the prepared crystal structure of the protein-ligand-complex without changing the structure. RMSDs of each protein-ligand complex from XP Glide docking compared to the original co-crystallized protein-ligand complex were measured. For the analysis, carbon alpha (Cα) atoms were used.

5.13.7 Flexible XP Induced Fit Docking (IFD)

As described in 5.13.6, LigPrep prepared ligands (5.13.4) were docked into the receptor Glide grid with XP induced fit docking (IFD) (220,221). The box center and size were selected via position and size of the co-crystallized ligand. The docking was not restricted to the reference position. Ring conformations were sampled with an energy window of 2.5 kcal/mol and non-planar conformation of amide bonds in the ligand were penalized. Previously LigPrep prepared ligands were docked into the protein with vdW radii of 0.5 for protein and ligand respectively during Glide docking. The best 20 poses for each ligand were sampled to assess protein plasticity using Schrödinger Prime Refinement. Residues with at least one atom within 5 Å of the 20 ligand poses were refined with optimization of the backbone, side chains and ligand via minimization. Residues outside of the 5 Å range were fixed (222). In the next step, ligands were re-docked into the top 20 overall structures within 30.8 kcal/mol of the lowest energy structure. All dockings were performed using Glide XP (223). Ligand poses were scored using the Glide Score and Prime energy. Then, the best pose for each ligand was superimposed against the prepared crystal structure of the protein-ligand-complex, before RMSD of the ligands was calculated according to 5.13.6.

5.14 Statistical Analysis

5.14.1 Z-Score Normalization of Cardiovascular Screening Hits

Data acquired from the *HeartBeat* v.2.1 software, *pyHeart4Fish* and the angiogenesis Fiji macro were collected and processed using Microsoft Office Professional Plus 2019 Excel. As the dataset from the primary screen was relatively small, no outliers were removed. Each measurement was divided by the mean parameter of DMSO controls from the respective experiment. This step

minimizes variation and creates specific fold change values. An additional z-score normalization enables cross-compound comparison across the whole library. z-score normalized values were merged with data provided by Prestwick Chemicals containing detailed information of the compound's chemical properties. Due to the low number of fish per compound two thresholds of 95 and 90% Confidence Interval (CI) (±1.96 and ±1.64) were set to identify potential hits. After thresholding, compounds with n<3 and vessel measurements were filtered out, as they do not have enough representative values. Additionally, potential hits that presented known and published side-effects were removed. Heatmap visualizations were created using GraphPad Prism 9.5.0 and 9.5.1.

5.14.2 Correlation Analysis

5.14.2.1 Spearman Correlation Analysis

Spearman correlation analysis was performed using GraphPad Prism 9.5.0. Depending on the hypothesis, a one-tailed or two-tailed parametric test was applied with a 95% CI.

5.14.2.1.1 Ranked Spearman Correlation Analysis

XP IFD scores were ranked from lowest to highest IFD docking score for each protein model. Then, ranking positions for each protein-ligand interaction were assessed with a GraphPad Prism 9.5.0 correlation analysis. Ranked correlation analysis was performed with a parametric two-tailed Spearman r test.

5.15 Material

Most used resources are listed here. Specific resources for certain methods are listed in extra tables.

5.15.1 Buffers, Solutions and Reagents

Table 26: Buffers, Reagents and Solutions

Material	*Composition/ Concentration*	*Application*	*Manufacturer*
100bp marker	Diluted 1:10 in ddH_2O	Gelelectrophoresis	New England Biolabs
BioWhittaker® PBS without calcium or magnesium	Ref. No.: 17-516Q LOT: 0001023468	Used for dissections	Lonza
70% Ethanol	Ref. No.: K928.4 70% Ethanol 99.8% denaturated 30% ddH_2O	Used to sterilize the equipment	Carl Roth GmbH & Co. KG

Liquid Nitrogen	N/A	Used to freeze organs for RNA extraction	N/A
Bovine Serum Albumin (BSA)	Diluted in PBST 10 mg/ml working solution Ref. No.: A3294-50G LOT: SLCH8449	Used in blocking solution for *in situ* hybridization.	Sigma Aldrich
di-sodium hydrogen phosphate (≥98%)	Ref. No.: T876.1 LOT: 381311149	Used for PBS	Carl Roth® GmbH
Digoxigenin (DIG)-RNA-AP	Ref. No.: 11093274910	Labeling mix for probes created by IVT	Roche Diagnostics GmbH
Digoxigenin (DIG) RNA Labeling Mix	10x concentrated stock solution Ref.: 11277073910 LOT: 57127420	DIG-11-UTP; Labeling mix for probes created by IVT	Roche Diagnostics GmbH
DTT (pH 8.3)	0.1 M working solution Ref.: P117A LOT: 226775003	Used for IVT and RT-qPCR	Promega™ Corporation
EDTA	1 mM pH 5.5 working solution	*In situ* hybridization Stop solution.	Carl Roth® GmbH
Ethanol (EtOH)	70% EOH diluted in ddH_2O	RNA Isolation	J.T.Baker®
Ethanol (EtOH)	Ref. No.: K928.4 70% Ethanol 99.8% denaturated 30% ddH_2O	Used to sterilize the equipment for fish dissection	Carl Roth GmbH & Co. KG
Ethyl 3-aminobenzoate methanesulfonate salt (Tricaine/MS222)	Dissolved in H_2O Stock solution: 0,3% Working solution: 0.003%	Anesthesia of embryos for imaging.	Sigma
Formamide (99%)	Ref. No.: 34724	Ingredient of loading dye and prehybridization buffer	Fluka™
Glycerol	100% stock solution 80% working solution Art. No.: 3783.1	Clearing and fixation of stained embryos.	Carl Roth® GmbH
Heparin	50 µg/ml stock solution	*In situ* hybridization	Roche Diagnostics GmbH - Sigma Aldrich
Hybridization buffer	500 µl Prehyb, Heparin, tRNA	*In situ* hybridization	N/A
Liquid nitrogen	N/A	Used to freeze organs for RNA extraction	N/A
Methanol (MeOH) (≥99%)	100% stock solution Working solution: 75%, 50% and 25% Ref. No.: 4627.6; 8388.6 LOT: 032318578	Rehydration and dehydration of embryos.	Carl Roth GmbH & Co. KG

Magnesium chloride hexahydrate ($MgCl_2$)	1 M stock solution 50 mM working solution	*In situ* hybridization	Carl Roth GmbH & Co. KG
Magnesium chloride hexahydrate ($MgCl_2$)	1 M stock solution 50 mM working solution Ref. No.: 208337-100G LOT: MKBR7462V	*In situ* hybridization	Sigma Aldrich Co.
Midori Green Advance DNA Stain	Ref. No.: MG04	Visualizes DNA bands in gels after gel electrophoresis.	Nippon genetics Europe GmbH
MilliQ sterile H_2O	N/A	Used as solvent for buffers and solutions.	Produced with MilliQ from Merck
Nitroblue tetrazoliumchloride (NBT) / 5-bromo-4-chloro-3-indolyl-phosphate p-toluidin (BCIP)	Diluted in NTMT 1:50 working solution Ref. No.: 11681451001	*In situ* hybridization	Roche Diagnostics GmbH - Sigma Aldrich
Normal Sheep Serum (sterile)	Diluted in PBST 100% stock solution 5% working solution Ref. No.: ab7489 LOT: GR3219231-3	Blocking of unspecific binding sites.	Abcam plc.
NTMT	2 ml 1 M TRIS-HCl pH 9.5, 1 ml 1 M $MgCl_2$, 2 ml NaCl 1 M, 20 µl Tween 20; 14.8 ml H_2O	*In situ* hybridization	N/A
Paraformaldehyde (PFA)	Diluted in PBS 4% stock solution Ref. No.: 11762.01000 LOT: 32607-11	Fixation of embryos.	Morphisto GmbH
Phosphate-buffered saline (PBS) Dulbecco	Without Ca^{2+} and Mg^{2+} Ref. No.: L182-50 LOT: 0512G	*In situ* hybridization; dissection	Merck Biochrom GmbH
Phosphate-buffered saline with Tween (PBST)	100% stock solution with 0.1% Tween	Rehydration and dehydration of embryos; washing.	N/A
Prehybridization buffer (Prehyb)	N/A	Saturation of embryos with formamide	N/A
Proteinase K	Diluted in PBST 10 µg/ml stock solution 1:1000 working solution Ref. No.: EO0491	Embryo digestion	Thermo Fisher Scientific Inc.
Color (Red) Taq PCR Mastermix	Ref. No.: EURX E2525 LOT: 060722; 140617	Used for HotStart PCR to generate linearized template DNA.	Roboklon GmbH

RNAse inhibitor	40 U/µl stock solution 10 U/µl working solution	IVT	Thermo Fisher Scientific Inc.
Potassium chloride	Ref. No.: 60130-250G LOT: SZBG0530V	PBS	Fluka™ - Sigma Aldrich Co.
Potassium dihydrogen phosphate	Ref. No.: 4873.0250 LOT: 032 A511673	*In situ* hybridization	Merck
RiboLock RNAse inhibitor	40 U/µl stock solution 10 U/µl working solution Ref. No.: EO0382	Reverse transcription	Fermentas - Thermo Fisher Scientific
Sodium chloride (NaCl)	1 M stock solution 100 mM working solution Ref. No.: 9265.2	*In situ* hybridization	Carl Roth® GmbH
Sodium chloride (NaCl) CELLPURE® (≥99.5%)	1 M stock solution 100 mM working solution Ref. No.: HN00.2 LOT: 052318751	High-content screen	Carl Roth® GmbH
T7 RNA polymerase	20 U/µl stock solution 5 U/µl working solution Ref. No.: EP0112	Synthetization of the linear RNA fragments	Thermo Fisher Scientific Inc.
Transcription buffer	5x working solution	IVT	Thermo Fisher Scientific Inc.
TRIS hydrochloride	1 M stock solution 100 mM working solution Ref. No.: 9090.3	*In situ* hybridization	Carl Roth® GmbH
tRNA	500 µg/ml stock solution Ref. No.: 10109517001 LOT: 59998920	Blocking of unspecific RNA during in situ hybridization	Roche Diagnostics GmbH - Sigma Aldrich
Tween® 20 Ph. Eur.	Art. Nr.: 9127.2	*In situ* hybridization	Carl Roth GmbH & Co. KG
BioWhittaker® PBS without calcium or magnesium	Ref. No.: 17-516Q LOT: 0001023468	Used for dissolve sucrose for cryosections	Lonza
Sucrose (99 +%)	Ref. No.: S-0389 LOT: 81K0262 Working solutions: 10% in PBS; 30% in PBS	Used to dehydrate organs for cryosections	Sigma-Aldrich Co.
Paraformaldehyde (PFA), 4% in PBS pH 7.4	Ref. No.: 11762.01000 LOT: 32607-11	Primary fixation of tissues.	MORPHISTO GmbH
Tissue freezing medium	Ref. No.: 14020108926 LOT: 03822696	Embedding organs for cryosections	Leica Biosystems Richmond, Inc.

TRIzol Reagent	Ref. No.: 15596018 LOT: 20653601; 20130101	Whole organ tissue lysis	Ambion life technologies
UltraPure™ Distilled Water	Ref. No.: 10977-035 LOT: 20653601; 2436574	Used for dilutions and stains	Invitrogen - Thermo Fisher Scientific, Inc.
Ethanol (EtOH), 99.8% denaturated	Ref. No.: K928.4	Used for re- and dehydration of sections	Carl Roth GmbH & Co. KG
Cytoseal™ XYL	Ref. No.: 8312-4 LOT: 370177	Sealing tissue samples to microscopic slides	Thermo Fisher Scientific, Inc.
PowerUp™ SYBR™ Green Master Mix	Ref. No.: A25742 LOT: 01296403	RT-qPCR	Applied Biosystems - Thermo Fisher Scientific Baltics UAB
DTT *0.1 M; pH 8.3*	Ref. No.: Y00147 LOT: 2445411	Reverse transcription	Invitrogen - Thermo Fisher Scientific, Inc.
5x First strand buffer	Ref. No.: Y02321 LOT: 2357788	Reverse transcription	Invitrogen - Thermo Fisher Scientific, Inc.
Nucleoside triphosphate (dNTP) 100mM, 4mM each	Ref. No.: U151A LOT:	Reverse transcription	Promega
Roth Hexanucleotid Random-Primer	Ref. No.: HP28 LOT: 231310607 Dissolved in 500 µl ddH_2O	Reverse transcription	Carl Roth GmbH & Co. KG
Reverse Transcriptase MLV-RT	Ref. No.: 28025-021 LOT: 2374834	Reverse transcription	Invitrogen – Thermo Fisher Scientific, Inc.
RiboLock	Ref. No.: LOT: 01202937	Reverse transcription	Fermentas - Thermo Fisher Scientific, Inc.
Dimethyl sulfoxide (DMSO)	Working solution: 0.02% in system water	Solvent for drug library; negative control	Sigma-Aldrich
Pronase	10 mg/ml stock solution 0.22,g/ml working concentration; Dissolved in H2O	Dechorionation	Merck Chemicals GmbH
Prestwick Chemical Library	Dissolved in DMSO 10 mM stock solution 20 µM working solution Ref. No.: PCL 10-100-G	High-content screen	Prestwick Chemicals
Sunitinib malate (SuM)	Dissolved in DMSO 10 mM stock solution 20 µM working solution	Positive control for angiogenesis phenotypes	Sigma-Aldrich

Sodium saline solution (NaCl)	20 µM working concentration	Used as a control for hydrochlorides in the high-content screening	Berlin-Chemie AG
LE Agarose	Working concentrations: 1% dissolved in 1x TBE, 1.5% dissolved in 0.003% Tricaine	Gel-electrophoresis; Orientation molds	Biozym
Dextran blue	Working solution: 1%	Ingredient of loading dye	Sigma-Aldrich
UltraPure™ DNase/RNase-free water	Ref. No.: 10977-35 LOT: 2436574	RT-qPCR, *in situ* hybridization	Gibco - Thermo Fisher Scientific
Loading Buffer (standard buffer)	99% formamide; 1% dextran blue; 80µl/ml 5x nucleic acid loading buffer	Gel-electrophoresis	N/A
1x and 10x TBE-Buffer	1x: 100mM Tris Base; 83 mM Boric acid (Sigma-Aldrich); 1mM EDTA (Carl Roth GmbH & Co. KG)	Gel-electrophoresis	N/A
5x Nucleic acid loading buffer	Ref. No.: MG04	Gel-electrophoresis	Bio-Rad
Stop solution	PBST, 1mM EDTA pH 5.5	*In situ* hybridization	N/A
≥99.5% Chloroform	Ref. No.: C2432-500ML LOT: SHBD9951V	TRIZOL RNA isolation	Sigma-Aldrich

(N/A) Not applicable

Table 27: Buffers and Solutions Used for Larval Rearing and the High-Content Screening

Material	*Composition/ Concentration*	*Application*	*Manufacturer*
Methylthioninium chloride (Methylene blue)	3 drops/L	Inhibits growth of mold in the water; stains deceased embryos blue	Sigma Aldrich
Sodium chloride (NaCl)	Working solution: 0.06 g/L	Mineralizing water	Carl Roth GmbH & Co. KG
Sea Qua Salt	Working solution: 0.06 g/L	Mineralizing water	Instant Ocean®

Filtered reverse osmosis water (VE-water)	Filtered reverse osmosis water	Preparation of system water for adult fish and larvae	N/A
System water	0.06 g NaCl and 0.06 g Sea Qua Salt/L filtered reverse osmosis water	Zebrafish nursing	N/A
Egg water	3 drops methylene blue/L system water	Embryo and young larvae nursing	N/A

5.15.2 Kits

Table 28: Kits Utilized in This Study

Material	*Composition/ Concentration*	*Application*	*Manufacturer*
Kits			
Monarch® DNA Gel Extraction Kit	Ref. No.: T1020L LOT: 10054639	Extraction of DNA from agarose gel to clean up PCR samples.	New England BioLabs® Inc.
DIG RNA Labeling Kit	Ref. No.: 11175025910	DIG labeling during IVT.	Roche - Thermofisher Scientific
innuPREP RNA Mini Kit 2.0	Ref. No.: 845-KS-2040250 LOT: 017-22	RNA extraction from larvae.	IST Innuscreen GmbH
RNA Clean & Concentrator™-5 - RNA Miniprep	Ref. No.: R1015 LOT: 208038	RNA probe extraction after IVT for *in-situ* hybridization. Protocol II: Total RNA Clean-up.	Zymo Research
RNA Clean & Concentrator™-5 – DNase I included	Ref. No.: R1013 LOT: 212513	RNA probe extraction after IVT for *in-situ* hybridization. Protocol II: Total RNA Clean-up.	Zymo Research
RNeasy® Plus Mini Kit (250)	Ref. No.: 74136 LOT: 172030936	RNA extraction from adult zebrafish organs.	Qiagen GmbH

RNase-Free DNase Set	Ref. No.: 79254 LOT: 172018563	RNA extraction from adult zebrafish organs.	Qiagen GmbH
Direct-zol RNA Miniprep	Ref. No.: R2052; R2050	RNA probe extraction for in-situ hybridization. Protocol II: Total RNA Clean-up.	Zymo Research

5.15.3 Consumables

Table 29: Consumables Used for This Study

Material	*Composition/ Concentrations*	*Application*	*Manufacturer*
Consumables			
10 ml serological pipette	Ref No.: 86.1254.001 LOT: Y12; 2175E	Pipetting of large volumes.	Sarstedt Aktiengesellschaft & Co. KG
10 ml serological pipette	Ref No.: 86.1254.001 LOT: 2175E	Pipetting of large volumes.	Sarstedt Aktiengesellschaft & Co. KG
50 ml serological pipette	Ref No.: 86.1685.001 LOT: 2150K	Pipetting of large volumes.	Sarstedt Aktiengesellschaft & Co. KG
15 ml Falcon tubes, sterile	Ref. No.: 62.554.502 LOT: 2041921; 0041722	WISH	Greiner Bio-One GmbH
24-well plate	Ref. No.: 142475 LOT: 171865	Used for anesthesia of embryos	Thermofisher Scientific
384 PCR Plate	Ref. No.: 72.1984.202 LOT: F23474	RT-qPCR	Sarstedt Aktiengesellschaft & Co.
5 ml serological pipette	Ref. No.: 89.1253.001 LOT: 2051E; 1300E	Pipetting of large volumes	Sarstedt Aktiengesellschaft & Co.

Material	*Composition/ Concentrations*	*Application*	*Manufacturer*
50 ml Falcon tubes, sterile	Ref. No.: 62.547.254 LOT: 2041199	Disposal of unwanted body parts	Sarstedt Aktiengesellschaft & Co. KG
50 ml Falcon tubes, sterile	Ref. No.: 227261 LOT: E21013M5	WISH	Greiner Bio-One GmbH
6-well plate	Ref. No.: 657160	Used to keep embryos from different pairs separated during dechorionation	Greiner Bio-One International GmbH, Cellstar
Aluminum foil, 18 my	Ref. No.: 2049633	Used to cover a Styrofoam lid to create a surface for dissections; Provides coverage for tubes and plates containing light-sensitive reagents.	IGEFA Handelsgesellschaft mbH & Co. KG
BD Microlance™ 3, sterile	Ref. No.: 302200 LOT: 111007	Used to pin zebrafish.	Becton, Dickinson & Co. Ltd.
Biosphere® plus sterile Filter tip 100µl	Ref. No.: 70.3050.255 LOT: 1052821, 2053121; 2051421; 2052721	Pipetting of sensitive reagents	Sarstedt Aktiengesellschaft & Co. KG
Biosphere® plus sterile Filter tip 1000µl	Ref. No.: 70.3030.255 LOT: 1055021, 2051421; 2053121; 2051921	Pipetting of sensitive reagents	Sarstedt Aktiengesellschaft & Co. KG
Biosphere® plus sterile Filter tip 20µl	Ref. No.: 70.3020.255 LOT: 2050521; 2051421; 2053122	Pipetting of sensitive reagents	Sarstedt Aktiengesellschaft & Co. KG
CELLSTAR® 96 Well Cell Culture Plate, sterile, F-bottom, with lid	N/A Ref. No.: 655180 LOT: E21Ø83M7	Used to keep embryos from different pairs separated during dechorionation	Greiner Bio-One International GmbH, Cellstar

Material	*Composition/ Concentrations*	*Application*	*Manufacturer*
Cover glasses 18 x 18 mm	N/A	Used to create a cavity for the whole-mounting of WISH embryos	Carl Roth® GmbH
Cover glasses 22 x 22 mm	N/A	Used to create a cavity for the whole-mounting of WISH embryos	Menzel-Gläser
Coverslips	N/A	Used as a lid to cover the mounted embryos	Carl Roth® GmbH
CRYSTAL qPCR-Folie, optical clear	Ref. No.: LOT: 13-SP-0605L	RT-qPCR	Biolabproducts GmbH
Dispenser tips Ritips® Bioclean®, 25 ml, 500-2500 µl	Ref. No.: 702380 LOT: 576894	Distribution of tricaine into well-plates	Eppendorf AG
PIPETMAN EXPERT Tips E200ST Gel Loading Flat Tips (200 µl)	Ref. No.: F1733381	Removal of excess water; orientation of embryos	Gilson Incorporated
Glass Pasteur pipette	ISO 7712, 230cm total length; No. 40567002	Removal of excess water	Assistent
Glass Petri-dish, 100/20 mm Ø/h	Ref. No.: LOT:	Dissection of adult zebrafish; Collection and rearing of zebrafish embryos	Avantor / VWR
Labsolute® PE 3 mlPasteur pipette	N/A	Removal of deceased embryos, debris and unfertilized eggs	Th. Geyer GmbH
Menzel-Gläser SuperFrost® Microscope Slides	Ref. No.: AGAA000081##32E LOT:0589	Used to check the gating.	Thermo Fisher Scientific, Inc.
Microcentrifuge tube, 5 ml, clear	Ref. No.: 525-0660 LOT: 210417-274	WISH	VWR® International bvba

Material	*Composition/ Concentrations*	*Application*	*Manufacturer*
Micro tube 1.5 ml SafeSeal	Ref No.: 72.706 LOT: 1085021	Used for cryo-conservation in liquid nitrogen	Sarstedt Aktiengesellschaft & Co.
Micro tube 2.0 ml SafeSeal	Ref No.: 72.695.400 LOT: 0084721	Used for tissue fixation	Sarstedt Aktiengesellschaft & Co.
PCR SingleCap 8er-SoftStrips, 200 µl, colorful	Ref. No.: 710988 LOT: 21441	Used to contain the IVT mix and run the IVT	Biozym Scientific GmbH
Pipette tip 1000 µl, blue	Ref. No.: 70.3050.110	Pipetting of large volumina	Sarstedt Aktiengesellschaft & Co.
Pipette tip 200 µl, yellow	Ref. No.: 70.3030.020 LOT: 2051621	Pipetting of large volumina	Sarstedt Aktiengesellschaft & Co.
Plastic Petri-dish, 100/20 mm Ø/h	Ref. No.: 664102 LOT: E22013HJ	Used to wrap in aluminum foil to keep tubes containing light-sensitive samples safe; WISH	Greiner Bio-One GmbH
Polystyrol transparent containers, 500 ml	N/A	Larval rearing	abcMeine Verpackung.de e.K.
Safe-Lock Tubes 1.5 ml	Ref No.: 0030 120.086; 0030 121.589 LOT: K197810M; K197382M	WISH; Trizol RNA isolation	Eppendorf AG
Safe-Lock Tubes 2 ml	Ref No.: 0030 120.094 LOT: G175660P	WISH	Eppendorf AG
SafeSeal tube 5 ml	Ref.: 72.701 LOT: 21P1040900	WISH	Sarstedt Aktiengesellschaft & Co.

Material	*Composition/ Concentrations*	*Application*	*Manufacturer*
SafeSeal SurPhob pipette reload tips, 20 µl	Ref. No.: VT0143 LOT: 21437	Tips used to pipette non-critical steps.	Biozym Scientific GmbH
SafeSeal SurPhob pipette tips, 10 µl, extra long	Ref. No.: VT0200U	Filter tips were used to pipette critical steps that required additional sterility.	Biozym Scientific GmbH
SafeSeal SurPhob pipette tips, 1000 µl, sterile	Ref. No.: VT0260	Filter tips used to pipette critical steps that required additional sterility	Biozym Scientific GmbH
SafeSeal SurPhob pipette tips, 20 µl, sterile	Ref. No.: VT0220	Filter tips used to pipette critical steps that required additional sterility	Biozym Scientific GmbH
Scalpel	N/A	Cut out bands from gel; Organ dissections	
Sterile cell culture plate 12-well plate	Sterile, non-pyrogenic, non-cytotoxic, DNAse/RNAse/DNA-free ISO:	Used in the staining process of the *in-situ* hybridization.	SPL Life Sciences Co., Ltd.
Sterile cell culture plate 24-well plate	Sterile, non-pyrogenic, non-cytotoxic, DNAse/RNAse/DNA-free ISO: 13485	Used in the staining process of the *in-situ* hybridization.	SPL Life Sciences Co., Ltd.
SuperFrost Microscope Slides (75 x 25 mm)	Ref. No.: 42409110	Covered slides used to collect cryo-slides	Glaswarenfabrik Karl Hecht GmbH & Co. KG
Superfrost™ Microscope Slides	Ref. No.: AG00008032 E01MNZ10 ISO: 8037/1 LOT: 0481	Used for imaging of WISH embryos.	Gerhard Menzel GmbH

Material	*Composition/ Concentrations*	*Application*	*Manufacturer*
TipOne 10 µl graduated reload tips	Ref. No.: S1111-3700 LOT: K130388K	Tips used to pipette non-critical steps.	Starlab
TipOne 1000 µl blue graduated reload tips	Ref. No.: S1111-6701 LOT: K131527Q	Tips used to pipette non-critical steps.	Starlab
UHU Superglue	N/A	Gluing together small coverslips for WISH.	UHU GmbH & Co.
α Pastette® 3 ml graduated plastic Pasteur pipette	Ref No.: LW4111 LOT: 20480300; 15350448	Used for PBST and Stop solution washing steps; removal of unfertilized eggs and debris; Used to empty petri-dish after each dissection	Alpha Laboratories Limited
α Pastette® 3 ml graduated plastic Pasteur pipette	Ref. No.: LW4111 LOT: 20480300	Used for PBST and Stop solution washing steps.	Alpha Laboratories Limited
Ceramic Beads 1.4 mm	Ref No.: 13113-325 LOT: CB16F16	Tissue Lysis.	MO BIO Laboratories, Inc.
Ceramic Beads 2.8 mm	Ref No.: 13114-325 LOT: CB16F21	Tissue Lysis.	MO BIO Laboratories, Inc.

Table 30: Dry and Live Food Used to Feed Larvae, Juveniles and Adults

Food	*Application*	*Company*
Sera Micron	Dry food, larvae nursing	Ser GmbH
TetraMin X1 Flakes (Tetra)	Dry food, feeding juvenile and adult fish	Tetra GmbH
Frozen artemia cysts	Live food, larvae, juvenile and adult fish nursing	Sanders, USA
Paramecia	Live food, larvae nursing	

5.15.4 Equipment

Material	*Application*	*Manufacturer*
Equipment		
Orientation tool	Used to mold agarose in a 96-well plate into slits that were used to orientate embryos for imaging.	Produced with a 3D-Printer
Multipette®	Pipetting of a large number of equal volumes.	Eppendorf AG
VWR® EHP Pipettor 12-channel, 1-10 µl	Pipetting dilutions of the Prestwick drug library and other small volumina	VWR® International
VWR® EHP Pipettor 12-channel, 20-200 µl	Pipetting agarose gel into 96-well plates to generate orientation plates for embryonic imaging 2 dpf	VWR® International
VWR® Single-channel pipettes,1000 µl	Dechorionation	VWR® International
Eppendorf Research® plus single-channel pipette, 0.5-10 µl	Pipetting of small volumes.	Eppendorf AG
Eppendorf Research® plus single-channel pipette, 10-100 µl	Pipetting of small volumes.	Eppendorf AG
Eppendorf Research® plus single-channel pipette, 20-200 µl	Pipetting of small volumes.	Eppendorf AG
Eppendorf Research® plus	Pipetting of small volumes.	Eppendorf AG

single-channel pipette, 100-1000 µl		
Feather forceps	Dissection of zebrafish organs	N/I
Forceps	Dissection of zebrafish organs	N/I
Brushes	Used to remove unusable samples from the cutting blade.	N/A

(N/A) No information; (N/I) No information

Table 31: Equipment Used for Zebrafish Husbandry

Material	*Composition/ Concentration*	*Application*	*Manufacturer*
Equipment			
Acrylic breeding tank with acrylic mesh and divider (1 l)	Ref. No.: ZB10BTIE; ZB10BTI; ZB10BTD; ZB10BTL	Mating of adult zebrafish; prevention of egg predation	TECNIPLAST Deutschland GmbH
Nylon sieve	N/A	Egg collection	Fackelmann GmbH
Fass Oval water tank 100 l	N/A	System water storage	GRAF GmbH
Probau bucket, 20 l	N/A	Greywater transfer	Bauhaus GmbH
ZebTec Active-Blue Standalone	N/A	Zebrafish housing.	TECNIPLAST Deutschland GmbH

5.15.5 Devices

Table 32: Overview of Devices Used in This Study

Material	*Composition/Notes*	*Application*	*Manufacturer*
Devices			

Thermo Scientific™ CryoStar™ NX50	Ref. No.: 957170-NX50	Thermo Fisher Scientific, Inc.
Incubator	Egg/Embryo incubation	
KB 115 incubator	Larval rearing at 28°C	Binder GmbH
Leica M80 Binocular	Used for positioning of embryos in the orientation plates	Leica Microsystems
Euromex HOLLAND Stereo Microscope	Control of cryo slices S. Plan 4x, 0.4, ∞/1.20 S. Plan 10x, 0.25, ∞/1.20 S. Plan 20x, 0.4, ∞/1.20	Euromex HOLLAND
ACQUIFER Imaging Machine	Image acquisition	AQUIFER
Zeiss Stemi305 Binocular	Dissection of organs	Carl Zeiss AG
All-in-One Fluorescence Microscope BZ-X800	Recording of heartbeat videos; imaging of slides; imaging of acridine orange stained larvae	Keyence Corporation
Qiagen TissueLyser LT	Lysis of zebrafish organs.	Qiagen N. V.
Centrifuge 5415 R	RNA isolation	Hassa Laborbedarf
Water bath	Thawing of pre-prepared tricaine	Hassa Laborbedarf
7900HT Fast Real-Time PCR System (TaqMan)	RT-qPCR	Applied BiosystemsTM - Thermofisher Scientific
Thermomixer comfort 1.5 ml	Heating buffers and solutions	Eppendorf
CAT ST5 Rocker	Used to gently rock samples for optimal exposure to buffers and solutions	M. Zipperer GmbH
Mikro 120 centrifuge	Used to spin down buffers and solution through columns.	Hettich Zentrifugen
T3 Thermocycler	Used for long-term heating steps during the IVT(5.5.3)	Biometra
T Advanced	Thermocycler used for PCR (5.5.1)	Biometra
NanoDrop 2000 Spectrophotometer	Measurement of DNA and RNA content	Thermo Fisher Scientific Inc.

Milli-Q	Purification and sterilization of VE water		Merck
Canon EOS 5D Mark III	Image capture of WISH embryos		Canon
Zeiss Axioscope Trinocular microscope	Objectives: 5x/0.12 na Achroplan; 10x/0.25 na Achroplan Ph1; 20x/0.45 na Achroplan Ph2; 40x/0.65 na Achroplan Ph2	Image acquisition for WISH imaging.	Zeiss
LM-Scope digital SLR widefield adapter	Adapter used to mount the Canon D on the direct image C-Mount Port.		MICRO TECH LAB
LM Direct Image C-Mount port 1x	Ref. No.: TUST37C 37 mm internal diameter 1x magnification	C-mount connection for c-mount cameras or video cameras.	MICRO TECH LAB
BlueMarine™ 100 Horizontal Submarine Electrophoresis Unit	Separation on nucleic acids in agarose gel		Serva Elektrophoresis
BlueMarine™ 200 Horizontal Submarine Electrophoresis Unit	Separation on nucleic acids in agarose gel		Serva Elektrophoresis
UV-Table	Visualization of nucleic acid bands on agarose gel.		
ROTANTA 460 R	RT-qPCR		Andreas Hettich GmbH & Co.KG

5.15.6 Software and Databases

Table 33: Software and Databases Utilized in This Study

Software	*Application*	*Company*
Adobe Acrobat Reader DC	Reading and commenting publications used in this thesis.	Adobe LLC
PlateViewer 1.5, 1.7.0 & 1.7.5	GUI for viewing acquired images from the ACQUIFER Imaging Machine in a 96-well plate format; optimization of Z-Stacks and creation of maximum projections for angiogenesis analysis	ACQUIFER
Microsoft Office Professional Plus 2019	Excel used for data management, analysis and primary visualization; Word to write the current thesis; PowerPoint to generate figures.	Microsoft

Excel, Word, PowerPoint		
GraphPad Prism 9.2.0 - 9.5.0-	Data analysis and graph creation for this thesis.	GraphPad
Adobe Illustrator	Creation of figures.	Adobe LLC
ImageJ2 1.51W/ Fiji	Vessel measurements; image preparation for later analysis; white balance of *in situ* images; Image processing for video and gif preparation.	National Institutes of Health
MATLAB-based GUI HeartBeat v.2.1	Detailed heartbeat analysis and creation of Excel files containing analysis output.	Gierten et al. 2020 (88)
MATLAB v2019b	Creating timestamps at given framerates	The MathWorks, Inc.
BZ-X800 Viewer	Recording of heartbeat videos; imaging of slides; imaging of acridine orange stained larvae	Keyence Corporation
Zotero v.6.0.12 – 6.0.20	Literature and citation manager.	Corporation for Digital Scholarship
NanoDrop 1000 v.3.8.1	Readout and visualization for measurements of DNA and RNA content.	Thermo Fisher Scientific Inc.
NanoDrop 2000	Firmware version 1.1.03: 1.1.03:1.04.11ND0:100004 — Readout and visualization for measurements of DNA and RNA content.	Thermo Fisher Scientific Inc.
EOS 5D Mark III Utility Software	Capture of WISH images with white balance.	Canon

Table 34: Datasets Applied in This Study.

Datasets	Application	Company

Digital Prestwick Drug Library (PDL)	v. 2019	Docking of hits into common target protein.	Prestwick Chemical Libraries®

5.15.7 Zebrafish Lines

Table 35: Zebrafish Lines Used in This Study

Organism	*Genotype*	*Properties*	*Origin*
Danio rerio			
fli1a	*Tg(fli1a:eGFP)*^{y7}	Nuclear green fluorescence, ECs of the vasculature	European Zebrafish Resource Center
myl7	Tg(*myl7:eGFP*)$^{twu34/+}$, formerly Tg(*cmlc:eGFP*)	Nuclear green fluorescence, tagging the myosin light chain 2 in the myocardial cells(107)	University of Potsdam
AB WT	Wildtype		European Zebrafish Resource Center

6 Results

6.1 High-Content Screen for Cardiovascular Modulators

6.1.1 Establishment of a High-Content Screening Assay

Based on Poureetezadi *et al.*´s high-content *in situ* hybridization protocol, published zebrafish screens, and the previously established angiogenesis assay, a zebrafish high-content screening assay for cardiovascular active compounds was developed (124,139,181). Following the optimization of imaging parameters, including the generation of orientation plates (182) and adaption of tricaine concentrations to adjust for prolonged anesthesia, imaging time-point and treatment duration were defined. Additionally, the pooling approach was determined.

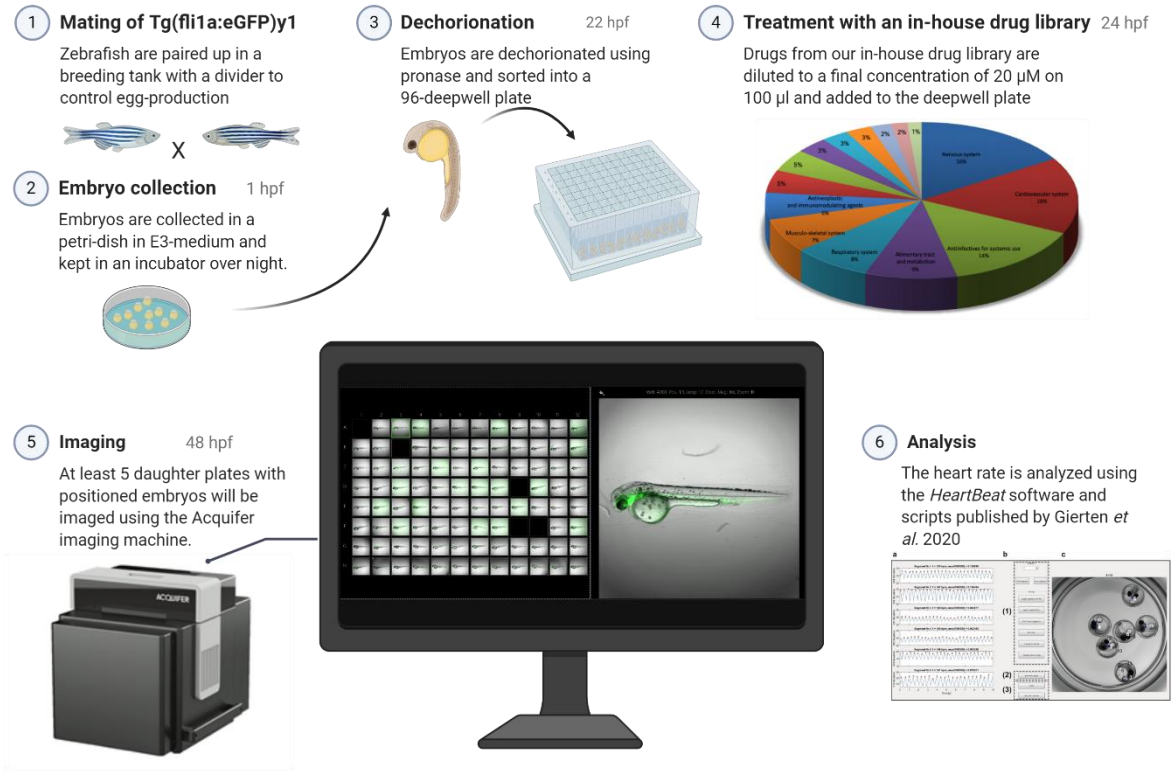

Figure 11: High-Content Screening Workflow
After pairing the fish on day one, on the second day the divider was removed and fish were mated for 1 h before egg collection. Afterwards, fertilized eggs were incubated overnight and the next day dechorionated 3 h before treatment start. Dechorionated embryos were transferred into a 96-deepwell plate. For the treatment excess water was removed and replaced with 20 µM of each compound. Finally, after 24 h of treatment in the dark, embryos were washed and placed into orientation plates that were imaged using the Aquifer Imaging Machine. Finally, the data was analyzed using the *HeartBeat* software (88). This image was created using BioRender.com.

There are several pooling strategies: one-compound one-well, which is the most prominent approach; adaptive pooling, where information from the first stage is used to design the next; non-adaptive pooling, where compounds are screened several times in one stage; and orthogonal pooling, a self-deconvoluting matrix strategy, where each compound is tested twice, each time with a different set of compounds (224). The one-compound one-well strategy can reduce specificity and sensitivity (224), nevertheless, this approach has a simple experimental design that is less prone to errors in execution and analysis. Therefore, this approach was used to develop the screening protocol.

To increase the fecundity of the fish, zebrafish husbandry was optimized by increasing feedings from twice to three times per day (225). Furthermore, the use of breeding tanks that keep the sexes separated during the night enabled timed, parallel production of fertilized eggs from several mated pairs. This method drastically increases comparability between individual animals and different experiments, which is especially important for large-scale screens (Figure 11 1).

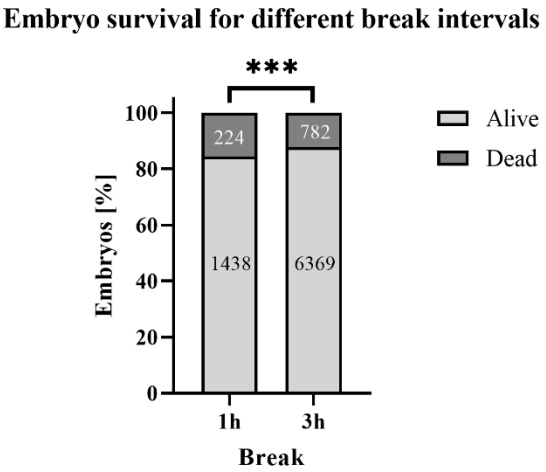

Figure 12: Longer Break Intervals Increased Embryo Survival
Overview of embryo survival for different break intervals between dechorionation and treatment start. Increasing the break between dechorionation and treatment positively impacted larval survival with a significance of p = 0.0003 (one-tailed Fishers exact test).
(ns) P > 0.05; (*) P ≤ 0.05; (**) P ≤ 0.01; (***) P ≤ 0.001; (****) P ≤ 0.0001

After incubation of the embryos over night, they were enzymatically dechorionated with 0.22 mg/ml pronase to enable parallel dechorionation of hundreds of embryos (Figure 11 3). *Post-hoc* analysis showed that increasing the time between dechorionation and treatment of the embryos from 1 h to 3 h significantly increased survival after 24 h of treatment by 3% (Figure 12). Data was

analyzed using a one-tailed Fishers exact test for the comparison of two different groups with adjustment of different sample sizes.

For the screening, the in-house Prestwick Chemical Library® was utilized (Figure 11 4). The library encompasses 1,280 compounds, mostly consisting of ~98% approved drugs (FDA, European Medicines Agency (EMA) and others). All compounds were diluted in 100% DMSO, a commonly used dipolar aprotic solvent that quickly crosses the dermal barrier in high doses (135). DMSO was considered the limiting factor in this study, as DMSO alters genome-wide DNA methylation profiles and gene expression (226,227). Treatment of zebrafish embryos with 1% DMSO for 24 h was shown to affect DNA methylation significantly (227). Based on published screens and under consideration of the effects mentioned above of DMSO at higher concentrations, the high-content screening was performed at a standard concentration of 20 µM in 0.2% DMSO for each compound (124).

The screening was designed to generate a large dataset encompassing the cardiovascular system while at the same time to adhere to the 3R principle[4] of reduce, refine, replace (228,229). Therefore, the transgenic line Tg*(fli1a:eGFP)*^{y7}, which expresses enhanced green fluorescence protein (eGFP) in the nucleus of vascular ECs driven by the *fli1a* promoter, was used to visualize the vasculature (178). In addition to lateral brightfield overview and fluorescence images, videos of the heartbeat and blood flow were captured with a widefield screening microscope (Figure 11 5).

Data analysis was performed according to the filtering step of the screening. In the primary screening for vascular modulators, data was analyzed using the Fiji macro 9.4.1.1 to measure ISV, DA and DV diameters. Heart videos of the primary heartbeat screen were analyzed using the *HeartBeat* software (88). Hits identified with these approaches were then filtered for previously published effects, incl. information from safety data sheets, unknown targets and low n. Remaining hits were used to treat additional fish in the secondary screening step. Finally, hits were validated using a second transgenic line to avoid line-specific effects. For the analysis of HR hits, a new tool, *pyHeart4Fish*, was developed that provides deeper insights into chamber-specific cardiac morphology and function.

[4] In 1959, William Russell and Rex Burch introduced the 3R principle of reduce, refine, replace in their book "The Principles of Humane Experimental Technique." as a framework to guide ethical considerations in animal experimentation.

6.1.2 Proof of Concept

6.1.2.1 Phenotypic Reproducibility

To show not only the validity of this screening approach but also how it is applicable to humans, three exemplary compounds from the library with previously published effects were selected as proof of concept (Figure 13). Measurements throughout this study were z-score normalized to adjust for different population sizes and variation between different experiments, if not otherwise indicated. This approach makes the data comparable and offers standardized thresholds of ± 1.64 for a 90% CI and ± 1.96 for a 95% CI. ATO, enilconazole and auranofin displayed previously described morphological and functional as well as toxic effects on humans and zebrafish.

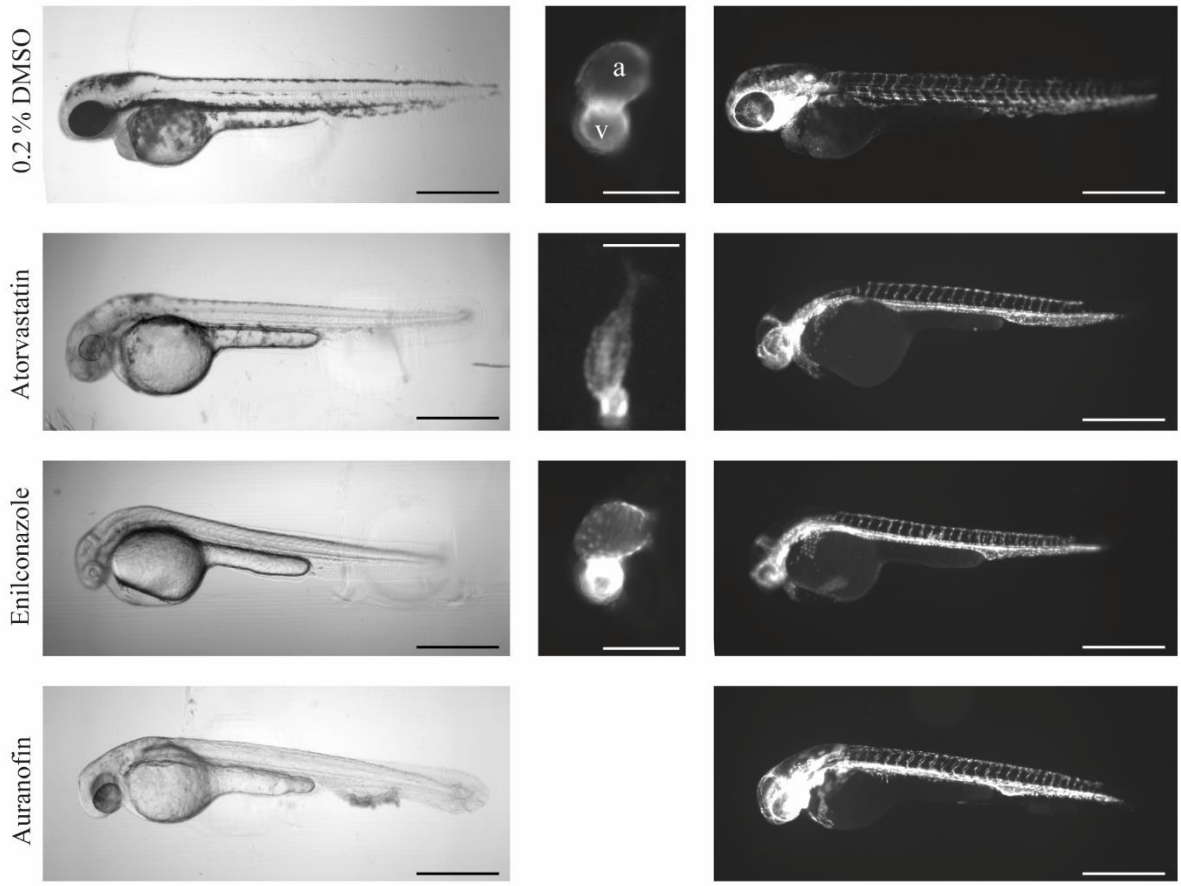

Figure 13: Reproducible Effects of Known Active Compounds
Overview of selected proof of concept compound-treated zebrafish embryos 2 days post fertilization. Atorvastatin treatment resulted in developmental delays, including delayed pigmentation, and changed heart morphology. Enilconazole and auranofin-treated fish showed clear signs of teratogenicity. Due to high lethality rates at standard concentration, auranofin was not tested in a secondary transgenic line. 0.2% DMSO served as a vehicle control. The scale bar of brightfield and fluorescence images indicates 500 µm. The scale bar of heart images represents 150 µm. Brightfield and heart image of enilconazole were taken with permission from Vedder *et al.* (2023) (185).
(a) atrium; (v) ventricle; (fli1a:eGFP) Tg(*fli1a:eGFP*)^{y7}; (*myl7:eGFP*) Tg(*myl7:eGFP*)$^{twu34/+}$

The competitive HMG-CoA inhibitor ATO (146) induced mild bradycardia in the primary screen (-0.758; n = 5), altered heart morphology, and developmental delay (Figure 13). Analysis of heartbeat videos with *pyHeart4Fish* of Tg(*myl7:eGFP*)$^{twu34/+}$ zebrafish presented a chamber-specific phenotype with a stronger decrease of the HR in the atrium (-2.90; n = 11) than in the ventricle (-1.57). Therefore, this compound was selected not only as a proof of concept but also as an internal positive control for validation of HR hits, later analyzed with *pyHeart4Fish*.

Enilconazole, an imidazole derivate, also known as imazilil, is an effective fungicide used in crop production. In the primary screen of this study, enilconazole significantly reduced HR in Tg(*fli1a:eGFP*)*y7* zebrafish embryos at 2 dpf (-3.405, 95% CI, n = 5). Treatment of Tg(*myl7:eGFP*)$^{twu34/+}$ confirmed these findings with both atrium and ventricle showing significant bradycardia (atrium: -3.479, 95% CI; ventricle: -2.846, 95% CI; n = 5). While not significantly affected, relative contractility of the atrium was increased to a z-score of 1.493 (95% CI). HS was not affected, and no arrhythmias or conduction defects were detected. However, enilconazole caused developmental delays and inhibited pigmentation in 100% of treated fish in both transgenic lines, indicating teratogenicity (Figure 13).

Auranofin is a well-known thioredoxin reductase (TrxR) inhibitor (230) which is FDA-approved for the treatment of rheumatoid arthritis (231,232). Here, auranofin did not only demonstrate severe teratogenic effects, such as developmental delay, reduced pigmentation and cardiac arrest but also induced a dose-dependent caudal fin phenotype of dysmorphia and apoptosis (Figure 13). Additionally, the ISV diameter was significantly reduced (-2.576; 95% CI; n = 11). Due to high lethality rates of auranofin at 20 µM, the compound was not tested in Tg(*myl7:eGFP*)$^{twu34/+}$.

6.1.2.2 Transferability of the Results

To assess the relevance of the zebrafish HR screen for human phenotypes, the sensitivity (true positives) and 1-specificity (false positives) were plotted against each other on a Receiver Operating Characteristics (ROC) curve. The absolute z-score normalized values were ranked by effect size before a literature and database search was performed by systematically choosing the terms compound name and “heart rate”. Human phenotype information was gathered using the Open Targets platform, the Mayo Clinic Drugs and Supplements Database, and if no information was forthcoming, the first five pages of publications on NCBI PubMed were sorted by relevance (233,234).

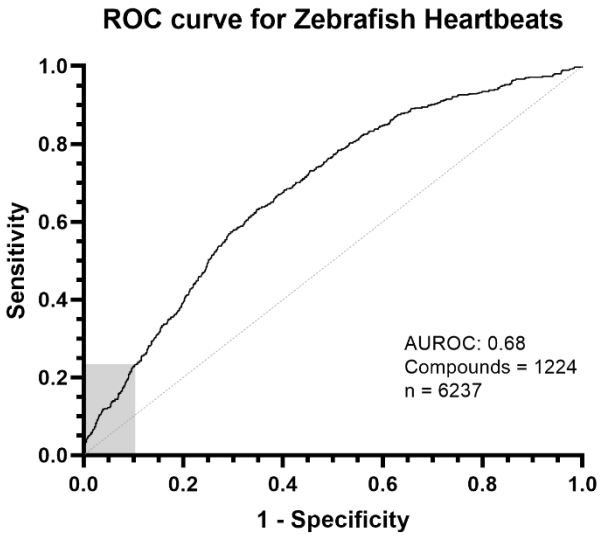

Figure 14: ROC Curve of HR Analysis Based on Human Phenotypes
The Receiver Operating Characteristics (ROC) curve was generated by ranking absolute Z-normalized values of heartbeat data. True positives and true negatives were identified based on the Open Targets Platform (233) (Last accessed 04/04/2022), Mayo Clinic Drugs and Supplements Database (Last accessed 04/04/2022) and scientific literature, identified with the search terms compound name + "heart rate". Ø n = 5, N = 6237. Gray line = baseline, AUROC: 0.68; black line = ROC curve; (AUROC) Area under ROC curve; gray box = 90% CI of Z-normalized values used as cutoff.

While the PDL contains 1,280 compounds, lethal and mostly lethal compounds at a standard concentration of 20 µM with an $n \leq 3$ were removed, leaving 1,224 compounds that were used to generate the ROC curve (Figure 14). The ROC curve shows an Area Under the ROC curve (AUROC) value of 0.68 (95% CI 0.66-0.7). This value is used to measure the performance of a test, a study or, in this case, a drug screen. Therefore, in almost 70% of all events, the drug screen correctly assigned a higher probability for cardiac events in zebrafish when the effect was known in humans. Moreover, the ROC curve can be used to determine cut-offs for high sensitivity and specificity when assessing a testing procedure. As a retrospective analysis was performed, the threshold was set by z-score normalization significance thresholds for a 90% CI (±1.64), marked by the gray box in Figure 14.

6.2 Primary Screening for Vascular Modulators

The first part of the high-content screening focused on vascular active compounds altering angiogenesis. Diameters of three points in each ISV, and eight ISVs per fish were measured above the UGP and analyzed to assess the compounds effect on the vascular system (see 5.3.10). Additionally, the diameter of the DA and DV were measured to get a general overview of the vasculature. As both vessels are primary blood vessels derived from the process of vasculogenesis,

their data is grouped together. All 1,280 compounds were tested in the primary screen. Here, the effects of 320 compounds on the vasculature were analyzed (Figure 15). Of the 1,280 compounds 45 were lethal to a point, where no data could be obtained. Of the 320 analyzed compounds, 23 affected ISVs diameter and 44 affected DA and DV diameter. Between the datasets was an overlap of 10 compounds affecting the whole vasculature. The identified 57 primary hits were then filtered for aquatic toxicity, FDA black box warning and unknown targets. Further, compounds with published effects concurrent with data from this study were removed. If the described effect was opposite to our findings, the compound was selected for further testing. Additionally, compounds with an $n \leq 3$ were removed. Small n were caused by predominantly lethal compounds at 20 µM and a lack of image quality. Application of these filters resulted in a total of 11 primary hit compounds with one compound overlapping both groups (Figure 15, Figure 16).

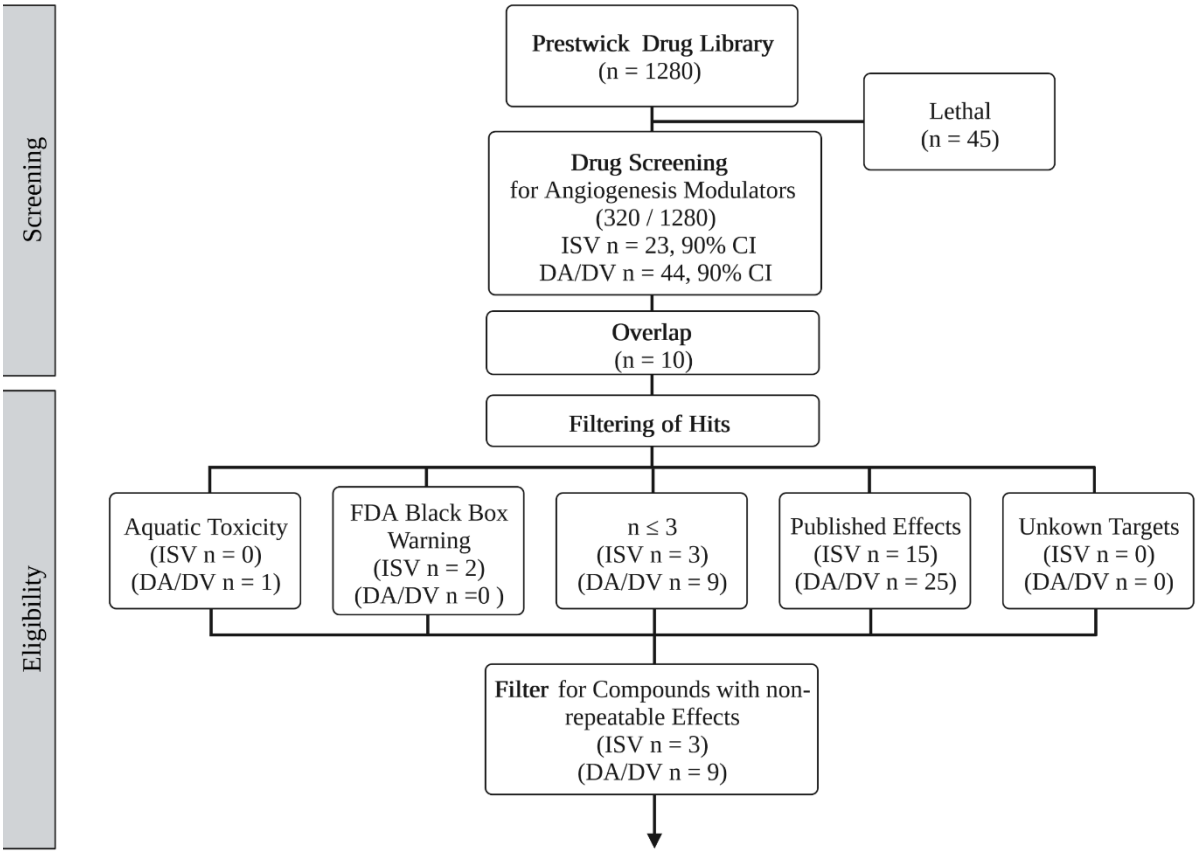

Figure 15: High-Content Screening Workflow for Vascular Modulators
Identification process of targets affecting the vascular system. A total of 1,280 compounds of the Prestwick Chemical Library® were tested. The vessel sizes of larvae treated with 320 different compounds were measured to identify compounds altering vasculogenesis and angiogenesis. After application of several filters, 11 compounds were identified for further testing. (CI) confidence interval; (DA) dorsal aorta; (DV) dorsal vein; (ISV) intersegmental vessel; (n) number of animals. This figure was created using BioRender.com.

As all compounds were dissolved in DSMO, 0.2% DMSO was used as a vehicle control. In our hands, DMSO caused mild pericardial edema in 50% of treated embryos (Figure 16 C), which was considered in comparison with other compounds. Overall morphology and development were not affected (Figure 17). The positive control SuM induced a similar number of pericardial edemas as DMSO. However, across seven experiments SuM significantly impaired angiogenesis (-7.572, 95% CI; n = 103). This z-score was used as a reference for complete angiogenesis inhibition. In concurrence with current literature, SuM did not significantly affect established vessels (DA: -0.198; DV: -0.703). While morphology of the treated fish was normal, a developmental delay was observed (Figure 17).

The glucocorticoid receptor 1 (NR3C1) agonist **desonide** significantly reduced ISV diameter (-2.156, 95% CI; n = 6), but did not affect DA and DV significantly (DA: -1.091; DV: 0.029). Overall, desonide did not induce teratogenic effects and caused only mild edemas (Figure 17). **Flunisolide** is another NR3C1 agonist. While flunisolide did not affect angiogenesis (-0.968, n = 4), it significantly increased DV diameter (2.202, 95% CI) and increased DA diameter (0.897). Flunisolide caused mild to moderate edemas in zebrafish at 2 dpf (Figure 16 C), but did not affect morphology (Figure 17).

Oxibendazole (OXB), an anthelminthic drug, significantly affected angiogenesis (-2.410, 95% CI; n = 3) and vasculogenesis (DA: -2.669; DV: -1.002) in zebrafish at 2 hpf, while inducing cardiac arrest. While OXB only induced pericardial edema in 33.33% of tested fish (Figure 16 C), it caused necrosis in 66.66% of treated embryos and led to developmental delay in the same number of fish. Additionally, OXB-treated embryos were smaller than the controls (Figure 17).

Azlocillin sodium salt (AZS) is a penicillin-binding protein inhibitor. In zebrafish AZS significantly reduced ISV diameter (-1.745, 90% CI; n = 4) without affecting vasculogenesis (DA: -0.144; DV: 0.252). AZS caused more moderate pericardial edemas than the DMSO control. However, this increase in severity was not significant (two-tailed Fishers' exact test p = 0.169) (Figure 16 C). Overall morphology of AZS-treated zebrafish embryos did not differ from the controls (Figure 17). Another bacterial penicillin-binding protein inhibitor **cefpiramide** did not affect ISV and DV diameter (ISV: -0.276; DV: 0.458; n = 3). Nevertheless, DA diameter was significantly increased (1.837, 90% CI). The morphology of treated embryos was inconspicuous (Figure 16 C).

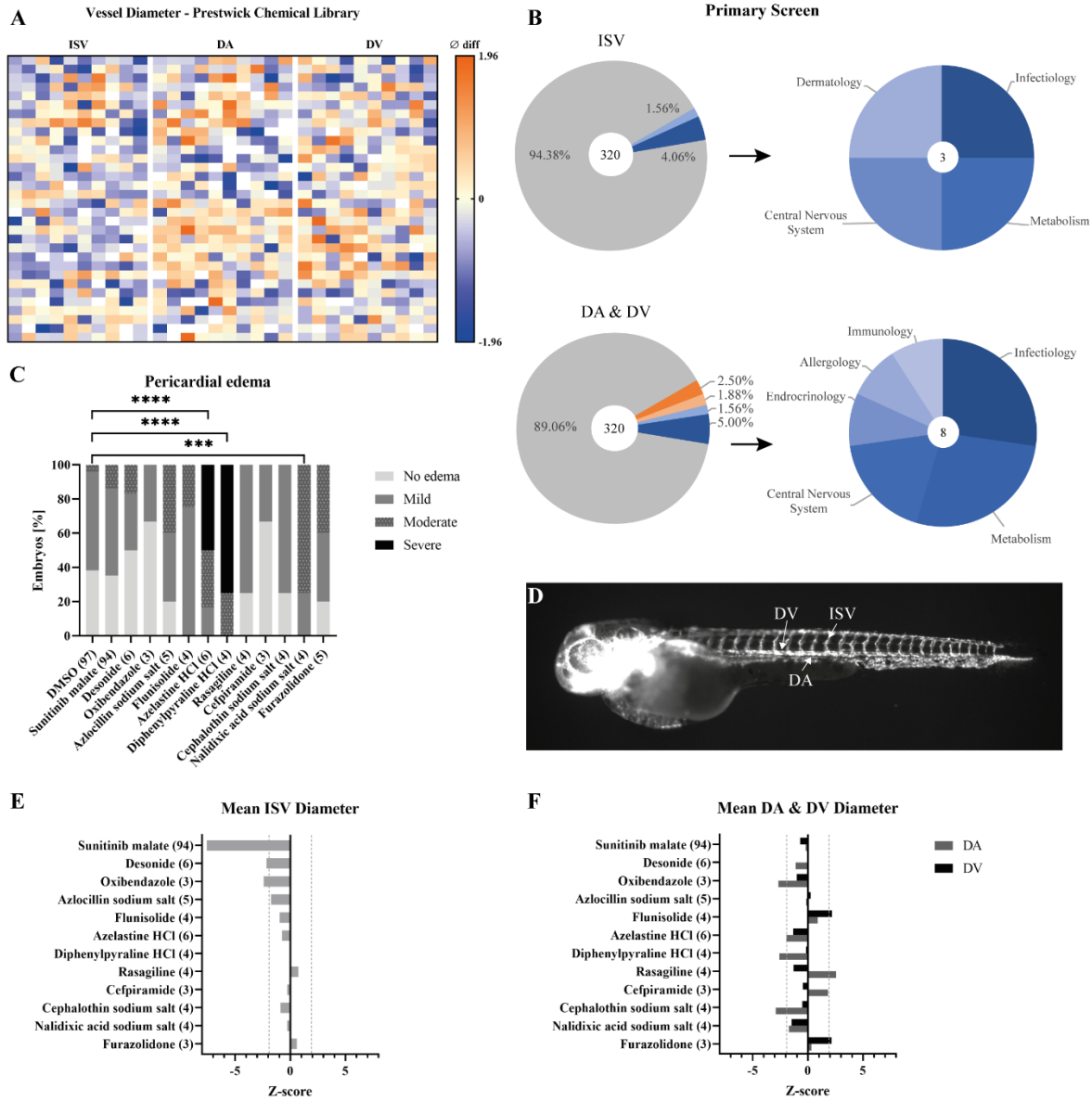

Figure 16: Z-Score Normalized Vessel Sizes for PDL-Treated Embryos

A, Heatmap of z-normlized vessel diameters of zebrafish larvae at 2 days post fertilization (dpf) treated for 24 h with 320 drugs from the Prestwick Drug Library. **B**, Top left and bottom left pie-charts display the evaluated compounds. Gray indicates no significance. Dark orange represents significant increases of vessel diameter (z-score: 1.96; 95% CI), while bright orange shows significance for a CI of 90% (z-score: 1.64). Bright blue represents a z-score of -1.64 (90 CI) and dark blue displays a z-score of -1.96 (95% CI). Pie-charts on the right show composition of the therapeutical classes identified as primary hits after application of filters described in Figure 15 (n displayed in the center). Some compounds belong to multiple classes, when they have been repurposed previously. **A**-**B**, All measurements were z-score normalized against their respective DMSO controls to adjust for multiple comparisons and varying sample sizes. N = 2,150. **C**, Overview of pericardial edema caused by treatment with the 12 primary hit compounds. The number of zebrafish embryos analyzed for this data is displayed in brackets after treatment condition. **D**, Overview of vessel development at 2 dpf in vehicle control-treated Tg(*fli1a:eGFP*)^{y7} zebrafish larvae. **E**-**F**, Z-score normalized vessel diameters. The n is presented in a bracket behind the indicated treatment. Dotted lines indicate a 95% CI of a ±1.96 z-score threshold.

(ISV) intersegmental vessel; (DA) dorsal aorta; (DV) dorsal vein; white = wells with deceased embryos; orange = Embryos with increased vessel size; blue = Embryos with decreased vessel size; (ns) $P > 0.05$; (*) $P \leq 0.05$; (**) $P \leq 0.01$; (***) $P \leq 0.001$; (****) $P \leq 0.0001$

Cephalothin sodium salt (CPS) is a broad-spectrum antibiotic that is active against gram-positive and gram-negative bacteria. In zebrafish, CPS significantly reduced DA diameter (-2.913, 95% CI; n = 4), ISVs and DV were not affected (ISV: -0.091; DV: -0.510). While CPS did not induce more severe pericardial edemas than the controls (Figure 16 C), 50% of the embryos showed a developmental delay.

The bacterial DNA polymerase inhibitor **nalidixic acid sodium salt (NAS)** did not affect ISV diameter (-0.278; n = 4), but DA and DV diameters were decreased (DA: -1.718, 90% CI; DV: -1.469; n = 4). A two-tailed Fisher's exact test showed that treatment with NAS caused significantly more moderate pericardial edemas than the DMSO controls (Figure 16 C; p = 0.0008). Moreover, 50% of the embryos displayed a developmental delay and 25% showed signs of apoptosis. However, morphology did not differ from the controls (Figure 17).

Azelastine hydrochloride (HCl) (AAH) belongs to the group of histaminergic H1 receptor (HRH1) antagonists. Treatment with AAH resulted in reduced ISV diameter (-0.752; n = 6), significantly reduced DA diameter (-1.948, 95% CI) and reduced DV diameter (-1.341). Additionally, comparison with DMSO controls via two-tailed Fisher's exact test showed significantly more severe edema caused by AAH (p = 0.0001) (Figure 16 C). Overall, AAH-treated embryos were smaller than the controls (Figure 17). **Diphenylpyraline HCl (DPH)** is another HRH1 antagonist that significantly reduced the DA diameter (-2.581, 95% CI; n = 4). However, it did not affect ISV diameter (0.046) and DV diameter (-0.159). Like AAH, DPH induced significantly more severe pericardial edema in treated zebrafish (two-tailed Fisher's exact test p = 0.0001) (Figure 16 C) and reduced body length (Figure 17).

The monoamine oxidase (MAO) B inhibitor **rasagiline** did not affect angiogenesis (0.735; n = 3). However, it significantly increased DA diameter (2.564, 95% CI) and decreased DV diameter (1.294) (Supplementary Table 4). Gross morphology of all embryos was inconspicuous (Figure 16 C). Another MAO inhibitor and antibacterial agent is **furazolidone**. This compound did not alter ISV and DA diameter (ISV: 0.599; DA: 0.321; n = 3), but it significantly increased the DV diameter (2.147, 95% CI). Treatment with furazolidone did not cause more pericardial edemas than the DMSO controls (Figure 16 C).

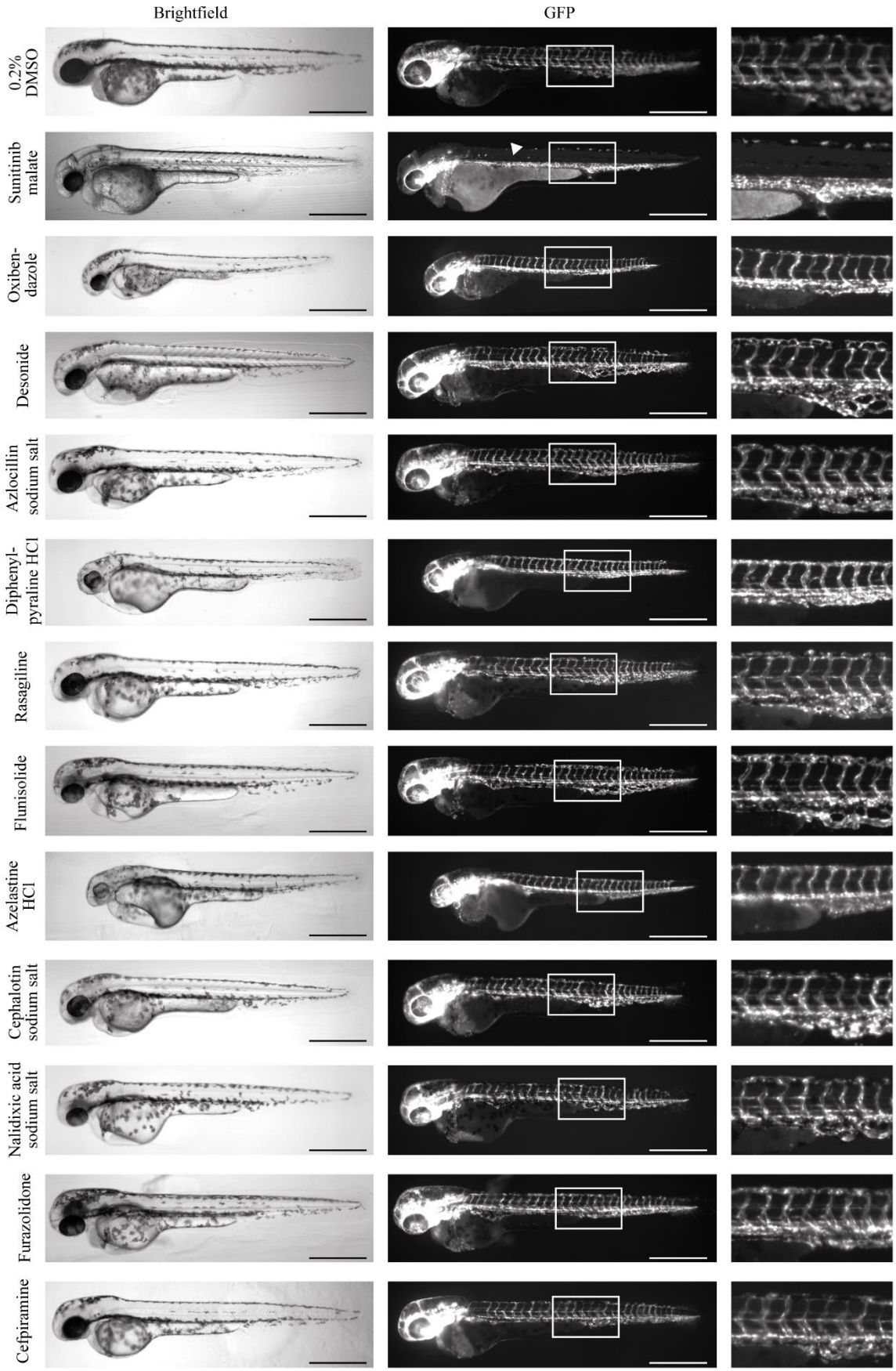
Brightfield
GFP
0.2% DMSO
Sunitinib malate
Oxiben-dazole
Desonide
Azlocillin sodium salt
Diphenyl-pyraline HCl
Rasagiline
Flumisolide
Azelastine HCl
Cephalotin sodium salt
Nalidixic acid sodium salt
Furazolidone
Cefpiramine

Figure 17: Phenotype of Zebrafish 2 dpf Treated with Compounds Active in the Vascular System
Overview of gross morphology and vasculature for primary hit compound treatments. Tg(*fli1a:eGFP*)^{y7}) were treated for 24 h with respective test compounds until 48 hours post fertilization before imaging. DMSO was used as a vehicle control and sunitinib malate (SuM) as a positive control. SuM inhibits angiogenesis of newly establishing vessels leading to missing intersegmental vessels as indicated by the white arrow. Images displayed on the right are computationally magnified images of the selected area in the middle panel. (HCl) Hydrochloride.

6.3 Heartbeat Modulator Screening

The second part of the high-content screening focused on cardiac active compounds altering HR. This phenotype was selected under the assumption that morphological and/or functional alterations during development will present a HR phenotype.

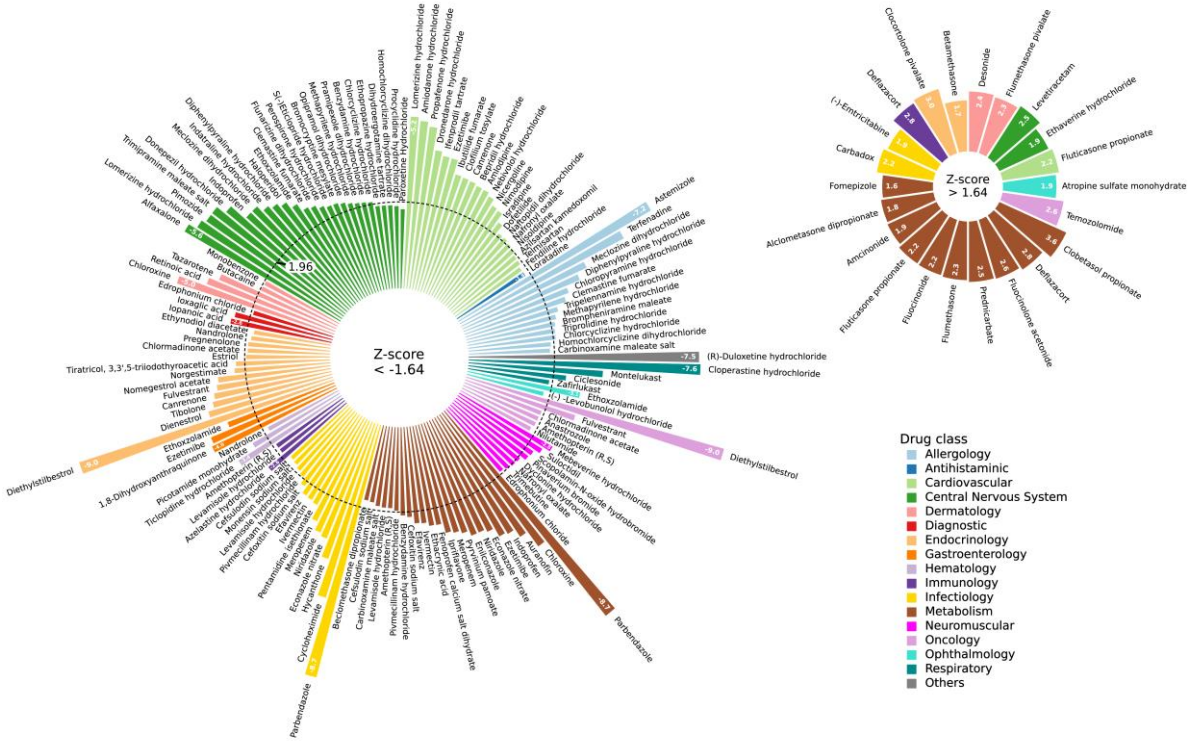

Figure 18: Unfiltered Z-Score Normalized Heartbeat Data from the PDL
Heartbeat analysis of zebrafish larvae 2 dpf treated for 24 h with drugs from the Prestwick Drug Library. All treatments were z-score normalized against their respective DMSO controls to adjust for multiple comparisons and varying sample sizes. A 90% CI was used to identify potential hit compounds, while reducing the false negative rate. Here, 134 compounds with significantly decreased (left plot) or increased (right plot) heart rate were grouped by drug class and sorted by z-score. Compounds with more than one drug class were represented twice. Dotted circle in the left plot represents a 95% CI cutoff; n = 9,173. This graph was plotted by Tobias Reinberger.

HR of treated zebrafish in the primary screen was analyzed using the *HeartBeat* software (88) and z-score normalized (Figure 18). As this screening was performed using heterozygote *fli1a:eGFP*

embryos and the standard concentration could be lethal depending on the compound, a mean n of 6 zebrafish were treated. After the treatment with all 1,280 compounds, 45 compounds proved to be lethal at a standard concentration of 20 µM after repeated testing. 134 compounds significantly increased or decreased the HR with a 90% CI (Supplementary Table 5, Figure 18).

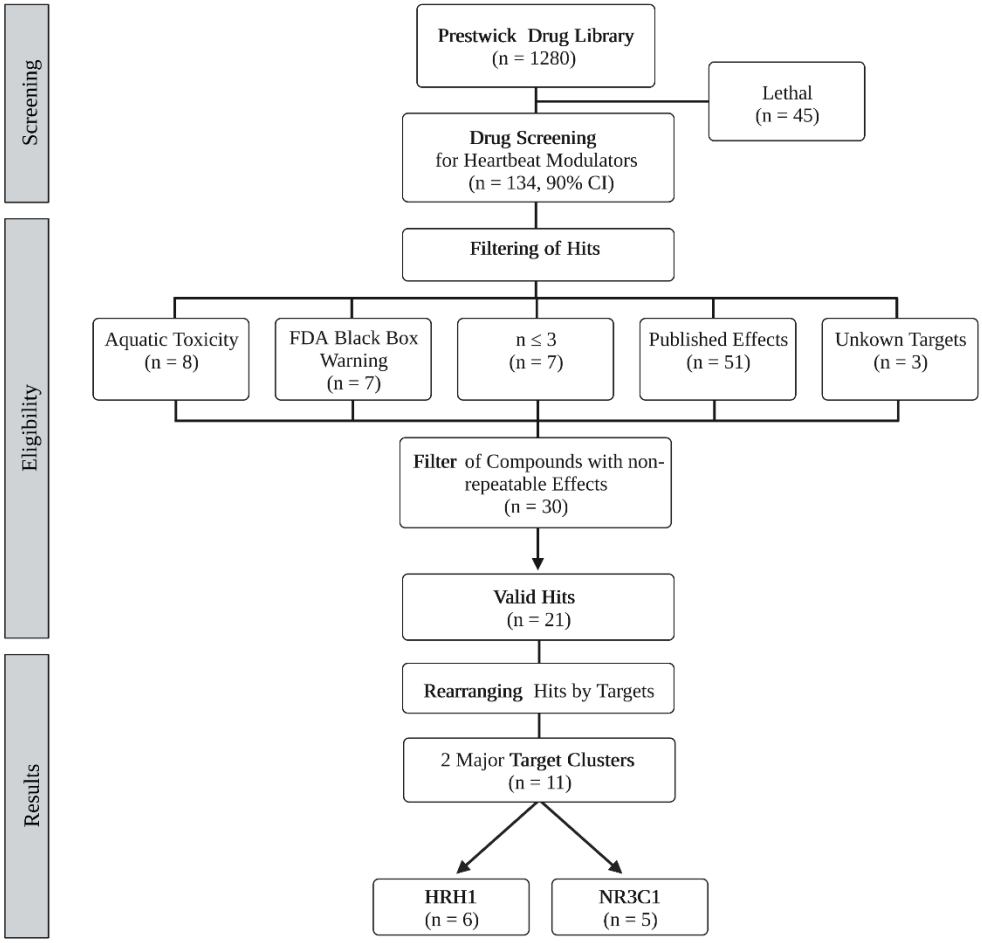

Figure 19: Heartbeat Screening Workflow

Identification process of cardioactive compounds and their respective targets in zebrafish. The Prestwick Drug Library containing 1,280 compounds was screened for heartbeat modulators in zebrafish. After application of several filters, this phenotypical screen identified HRH1 and NR3C1 as two major target clusters impacting the cardiac system. This figure was created using BioRender.com.

Primary hit compounds were then filtered and all compounds with known aquatic toxicity, FDA black box warning, unknown targets, $n \leq 3$ and with published effects were removed. Following the primary screening 58 compounds were tested again at different concentrations to ensure repeatability as the number of the primary screen was relatively low.

Toxic side effects such as developmental delay, pericardial edema, cardiac arrest and HR were weighted against the effect size (Figure 20) to optimize concentration for testing in

Tg(*myl7:eGFP*)$^{twu34/+}$. The 30 resulting compounds were then tested in Tg(*myl7:eGFP*)$^{twu34/+}$ to visualize atrium and ventricle, assess gross morphology, and to differentiate contractility between heart chambers. In addition, testing of the compounds in a second transgenic line was used to remove compounds with line-specific effects. Serial images of 6 images/s were recorded *in vivo* for 6 s for each embryo using the Aquifer Imaging Machine. The analysis was performed with the newly developed heart analysis tool *pyHeart4Fish* (185). This way, nine additional compounds were removed and the other 21 compounds that showed repeatable, significant results were considered valid hits. These hits were rearranged by targets, revealing two major target clusters, NR3C1 and the HRH1. Five compounds targeted Nr3c1, while six compounds targeted Hrh1. Out of the remaining 10 compounds, there is some overlap in their targets, but for the most part, their mode of action (MoA) and targets are different from one another.

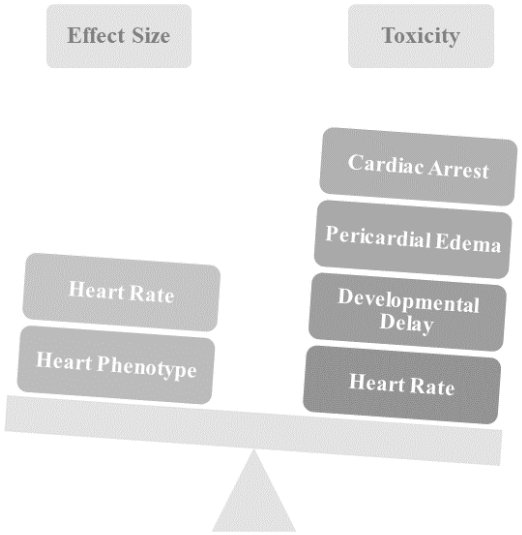

Figure 20: Phenotype-Based Concentration Optimization

Factors that were weighted against each other, when determining the optimal concentration for each compound. As displayed here, besides cardiac edema and bending of the body, HR is one of the factors considered for teratogenicity. Therefore, to be able to assess the HR as a phenotype rather than a toxic effect, effect size and toxicity must be balanced.

6.3.1 pyHeart4Fish – Quantitative Heart Chamber Phenotyping

The primary heartbeat screening and the concentration optimization steps were analyzed using the *HeartBeat* software. This tool can analyze heart frequency and arrhythmias. However, inspection of captured videos implicated that a more detailed analysis was required to analyze the heartbeat data chamber-specifically. Therefore, we developed a novel Python-based tool with Fiji (184)

integration to quantify heart function and morphology of atrium and ventricle independently, termed *pyHeart4Fish*. This tool is adaptable to various data types (Figure 21) and thereby independent of any microscope and imaging system. Analysis with *pyHeart4Fish* can yield the following quantitative output: arrhythmia, conduction defects, contractility, ejection fraction (EF), HR and HS. The quality of the output is dependent on resolution and speed of the camera used for imaging. To adjust for these differences, the tool provides two different frequency calculations: a fitted sine function more suitable for higher frame rates (≥9 frames per second (f/s)) and a FFT, also suitable for lower frame rates (6 f/s). However, for precise arrhythmia detection higher frame rates and manual confirmations are required.

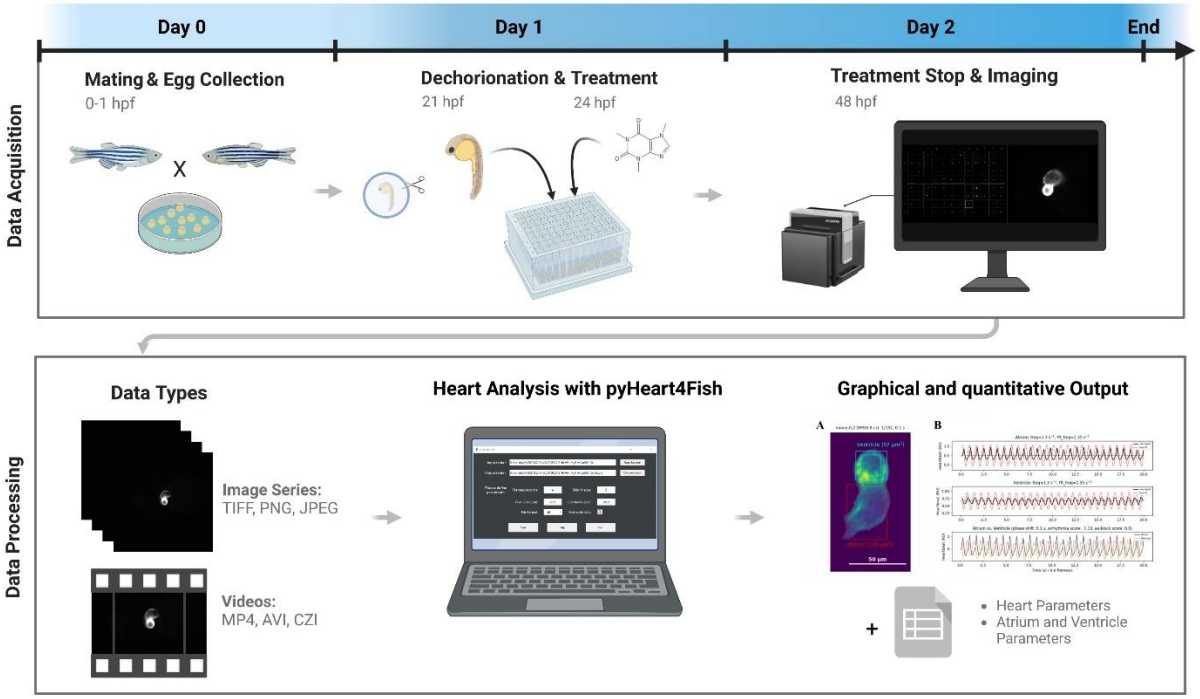

Figure 21: *pyHeart4Fish*

Eggs were collected from pairwise mating, one hour after dividers were removed. After incubation over night embryos were enzymatically dechorionated at 21 hours post fertilization (hpf) and transferred into 96-deep well plates. Treatment with the Prestwick Drug Library was started at 24 hpf and stopped at 48 hpf. At this stage Tg(*myl7:eGFP*)$^{twu34/+}$ zebrafish were mounted in orientation plates, before being imaged. In the next step, output data files were quantified using *pyHeart4Fish*. **A-B**, Representative visual analysis output of treated Tg(*myl7:eGFP*)$^{twu34/+}$ embryos at 48 hpf. Figure was taken with permission from Vedder *et al*. (185).

6.4 Identification of Target-Clusters and Their Role in Cardiac Morphology and Function

Identifying target clusters is crucial in understanding the complex interplay of molecular mechanisms underlying cardiac pathophysiology. Therefore, we utilized a second transgenic line (Tg(*myl7:eGFP*)$^{twu34/+}$) with a fluorescently labelled heart in the third part of the screening to reduce line specific effects and gain deeper insights into the pathophysiological mechanisms of the identified hit compounds.

In this part of the study, DMSO continued to serve as a vehicle control, while the embryotoxic compound ATO served as a positive control for functional and morphological phenotypes for all treatments. Moreover, as one third of all 21 potential hit compounds (Supplementary Table 5) were hydrochlorides (HCl), a sodium chloride (NaCl) control was applied as a salt control. Treatment with NaCl reduced HR, however not significantly, and did not affect heart development and function. Further, NaCl did not affect conduction between the atrium and ventricle ($p = 0.745$) and overall morphology.

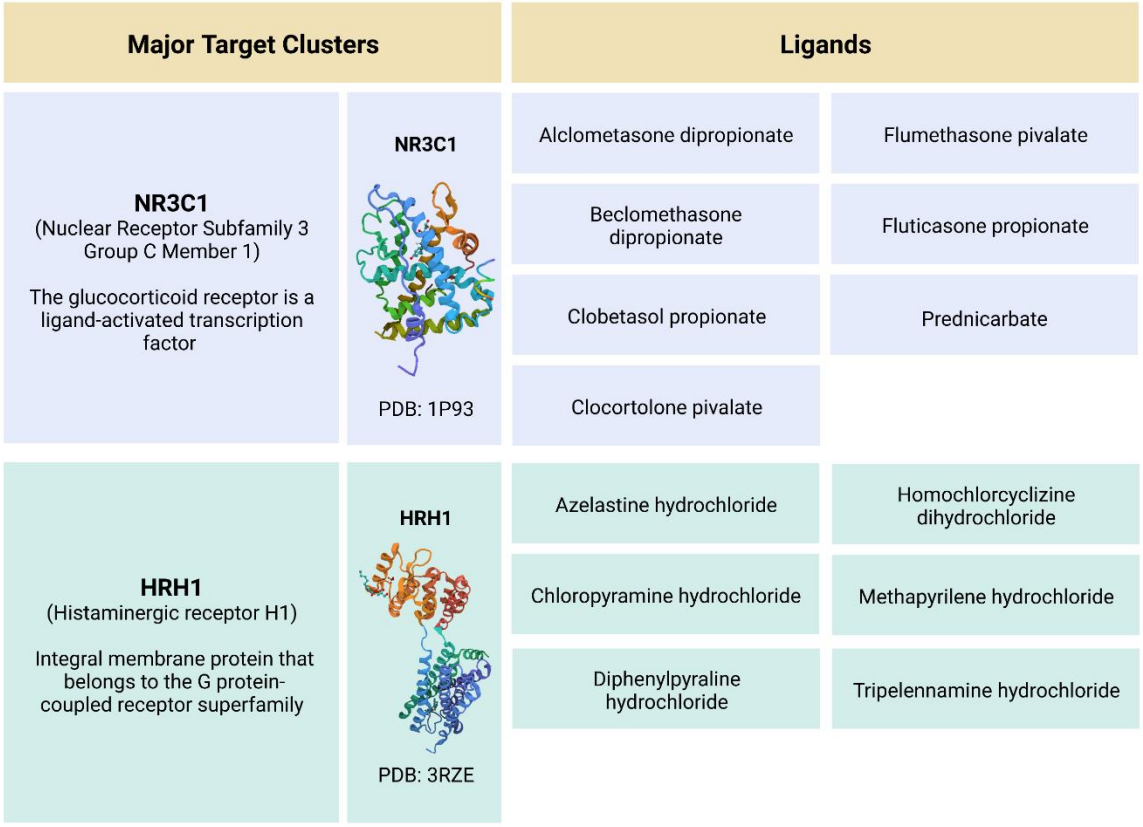

Figure 22: Overview of Major Compound Target Clusters
NR3C1 and HRH1 are the two biggest target clusters identified in the cardiovascular high-content screening. Both targets have orthologues in zebrafish (Nr3c1 and Hrh1). Seven agonists targeting the glucocorticoid receptor NR3C1 led to increased HR in zebrafish embryos 2 days post fertilization. Six HRH1 antagonists significantly reduced HR in zebrafish embryos.

All data except arrhythmias, AVB scores and the ToxScore were z-score normalized against their respective DMSO controls as described in 5.14.1. Differences in arrhythmia and AVB scores between compound and control treated zebrafish were analyzed with a two-sided Fisher's exact test to adjust for small sample sizes.

Sorting valid hits, revealed two major target clusters: NR3C1 and HRH1 (Figure 19, Figure 22). All compounds targeting NR3C1 were agonists increasing zebrafish HR in the primary and secondary screen. In contrast, all compounds targeting HRH1 acted in an antagonistic MoA and decreased HR in treated zebrafish. Therefore, we proceeded to analyze these compounds and their targets as well as their roles in heart development and function.

6.4.1 The Effect of Various Heart Rate Hits on Cardiac Phenotypes

Although this study focuses on targets, it's equally crucial to investigate the toxic effects of various compounds. Prenatal and postnatal exposure to chemicals and pharmaceuticals may adversely affect development. It is estimated that 1-4% of congenital anomalies are caused by adverse drug effects (155–157). About 55-90% of pregnant women take at least one prescribed drug during gestation (158,159), even though, information on teratogenicity and cardiotoxicity is limited and often retrospective (160).

This part of the study focuses on the morphology and function of zebrafish treated with the 10 hits not included in major target clusters listed in the Supplementary Table 6. HR optimized treatment concentrations were determined by weighting effect sizes and toxic side effects such as edemas, body dysmorphia and lethality. Then, Tg(*myl7:eGFP*)$^{twu34/+}$ were treated with optimized concentrations to assess overall cardiac phenotypes using *pyHeart4Fish*.

The antiparasitic 80s ribosome inhibitor **Cycloheximide (CHX)** was shown to induce apoptosis in rat CMs (235). In zebrafish, CHX displayed dose-dependent toxic effects, including cardiac arrest, developmental delay and yolk necrosis (see Figure 23 C and Supplementary Figure 1 B). During the primary screen at a treatment concentration of 20 µM CHX significantly decreased HR (-5.679, 95% CI, n = 4). At 10 µM CHX only displayed mild edema with significant bradycardia in atrium and ventricle (atrium: -4.214; ventricle: -4.077, 95% CI; n = 6) and a smaller heart (-0.757) (Figure 24 A-B). The areas of max dilation and contraction of the atrium were significantly reduced (dilation: -4.061; contraction: -2.284, 95% CI). On the other hand, only the area of max dilation of the ventricle showed a significant decrease of -5.138 (Figure 24 C-D). Despite these changes, the EF and relative contractility in both chambers were not significantly impacted (as shown in Figure 24 E-F).

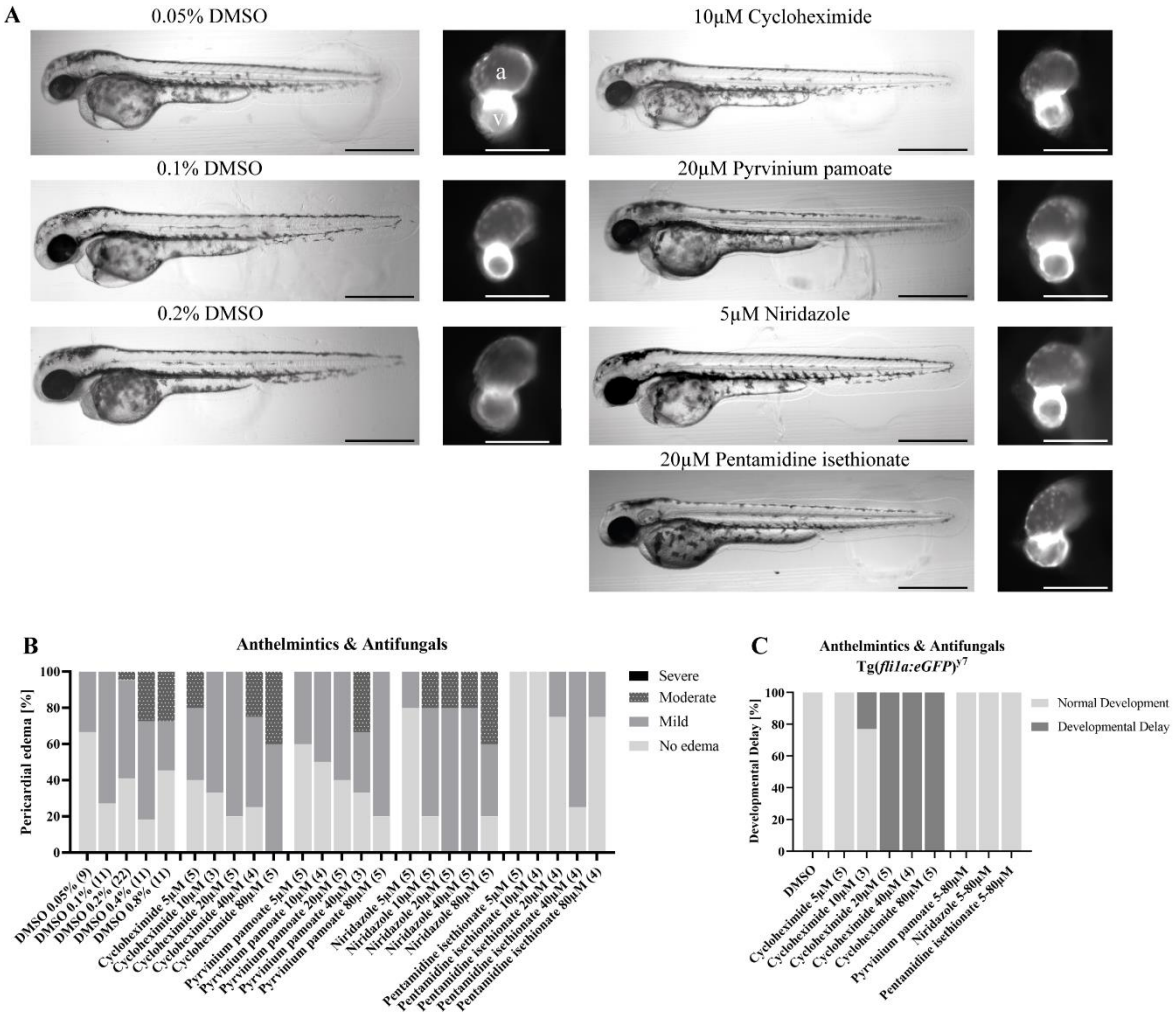

Figure 23: Anthelminthics and Antifungals

Overview of treatment effects of different anthelminthics and antifungals. **A**, Morphology of treated embryos did not show differences compared to the controls. **B**, Dose-dependent overview of pericardial edema in Tg(*fli1a:eGFP*)^{y7}. None of the compounds caused more severe pericardial edema compared to the controls. **C**, Developmental delays were not induced by pyrvinium pamoate, niridazole and pentamidine isethionate. In contrast, CHX induced dose-dependent developmental delay.

The FDA has approved **pyrvinium pamoate (PP)** is an antifungal and anthelmintic agent (236). Recent studies have explored its potential as an anti-cancer treatment, demonstrating its effectiveness through various pathways including WNT signaling, NADH-fumarate mitochondrial inhibition, tumor stemness, unfolded protein response, and hedgehog signaling (237). The data from this study showed a decrease in HR during the primary screening (-3.196, n = 5) and in the validation step, with a z-score of -8.538 in both heart chambers (n = 5)), when being treated with 20 µM PP (Figure 24 B). However, the treatment did not affect relative contractility, conduction, or HS. Furthermore, the gross morphology of the body and heart remained unaffected by the PP treatment (Figure 23 A).

In primary screening, the drug **niridazole (NZ)**, which has antiparasitic, anthelmintic, and antiprotozoal properties, reduced HR at a treatment concentration of 20 µM (-3.405, 95%, n = 4). Moreover, it induced a significant decrease in HR at every tested concentration. Pericardial edemas were mainly mild in every concentration, as shown in (Figure 23 B). When administered at a concentration of 5 µM, NZ caused mild edema in 20% of Tg(*fli1a:eGFP*)^{y7} zebrafish, while the other 80% remained unaffected (Figure 23 B). No developmental delays were observed at any concentration (Figure 23 C). No other signs of toxicity were detected, therefore 5 µM were used for hit validation. Although not statistically significant, NZ also reduced HR in Tg(*myl7:eGFP*)$^{twu34/+}$ at a concentration of 5 µM (atrium: -1.35; ventricle: -1.20; n = 4), as shown in (Figure 24 B). However, relative, and absolute contractility of the ventricle remained unaffected, while max dilation (-1.17) and max contraction (-2.08) were decreased (Figure 24 C-D). Atrial relative contractility was increased (1.59) (Figure 24 F), and HS was significantly reduced with a z-score of -4.11 (Figure 24 A).

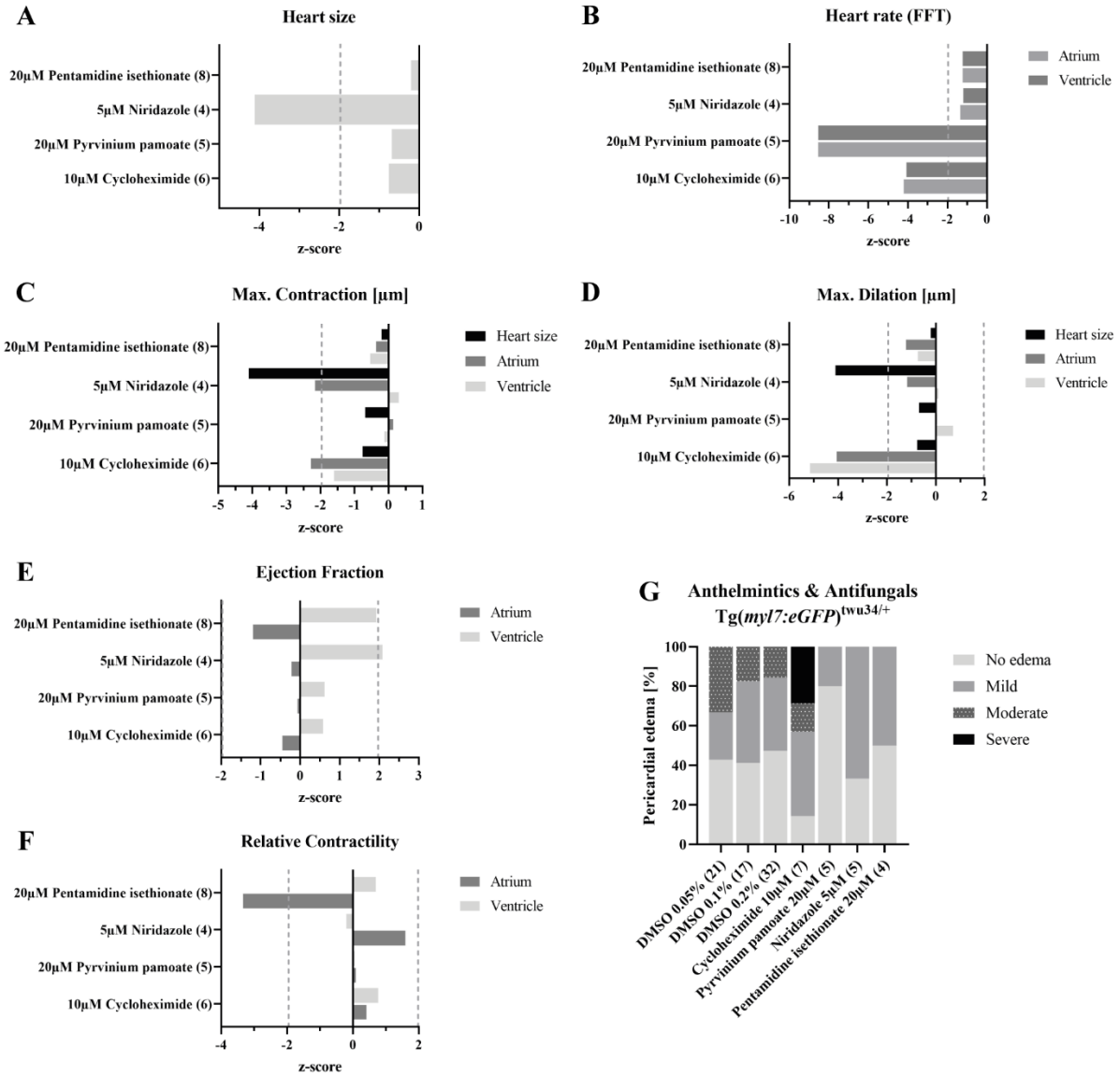

Figure 24: *pyHeart4Fish* Analysis of Anthelminthics and Antifungals

Overview of quantitative data obtained from analysis with pyHeart4Fish. **A**, 5 µM niridazole (NZ) displayed significantly smaller hearts. **B**, Heart rate was reduced after treatment with all compounds. **C**, Maximal contraction was significantly decreased in the atrium of NZ- and pyrvinium pamoate (PP)-treated embryos. **D**, Maximum dilation of both heart chambers in cycloheximide (CHX)- treated embryos was significantly decreased. **E**, Ejection fraction of ventricles of NZ-treated embryos was significantly increased. **F**, Pentamidine isethionate significantly reduced relative contractility of the atrium. **G**, In Tg(*myl7:eGFP*)$^{twu34/+}$, CHX induced stronger pericardial edemas with a p = 0.0761 (two-tailed Fisher's exact test). **A-F** Data was z-score normalized against respective DMSO controls. Dotted lines indicate 95% CI significance thresholds. (ns) $P > 0.05$; (*) $P \leq 0.05$; (**) $P \leq 0.01$; (***) $P \leq 0.001$; (****) $P \leq 0.0001$

Pentamidine isethionate (PEN) is an antiprotozoal drug that interacts with the minor groove of AT-rich DNA regions of the pathogen genome. In the primary screen PEN significantly decreased HR (-2.518, 95%, n = 5). However, further testing did not show a dose-dependent effect on HR or teratogenic effects (Figure 23 B-C). In Tg(*myl7:eGFP*)$^{twu34/+}$ zebrafish embryos 2 dpf, PEN reduced

HR to a z-score of -1.237 (n = 8) with a 20 µM compound concentration (Figure 24 B). Approximated HS did not differ from the controls and no conduction defects were detected (Figure 24 A). However, there was a significant decrease in relative atrium contractility (-3.86) (Figure 24 F) due to the smaller max dilation (-1.22) while max contraction was unaffected (Figure 24 C-D). Visual comparison of the heartbeat videos confirmed the atriums contractility reduction.

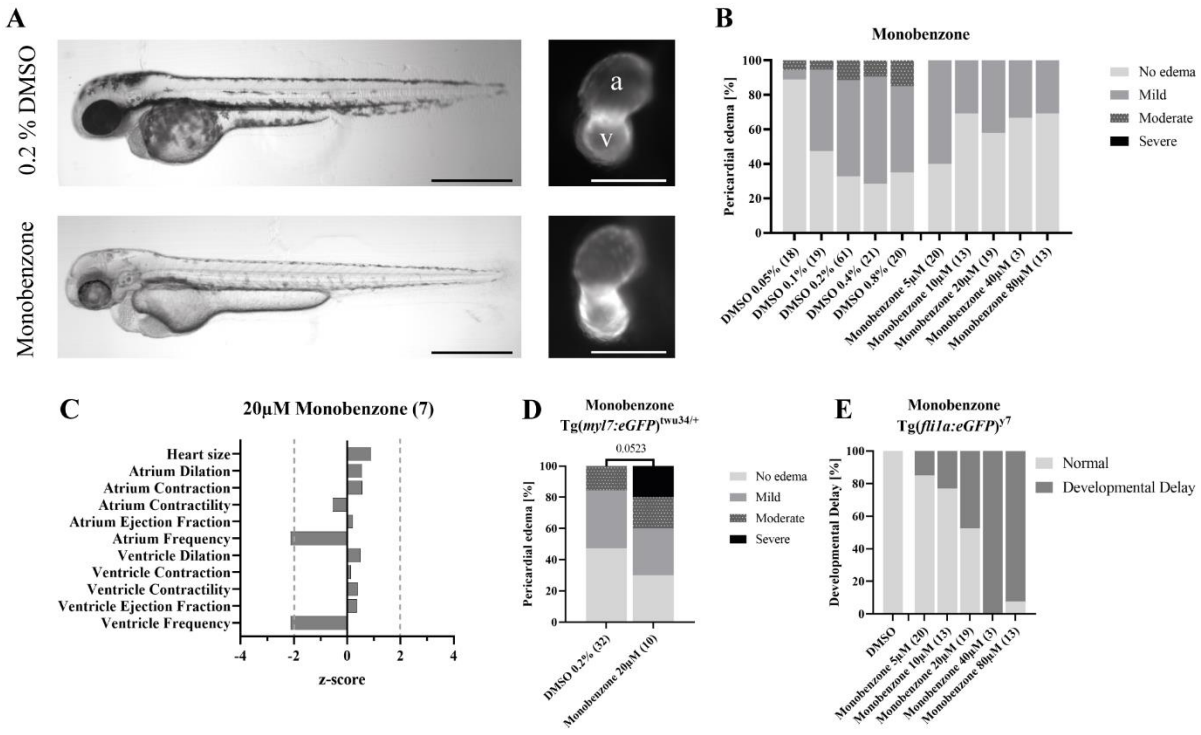

Figure 25: Monobenzone (MBEH)

Monobenzone (MBEH) treatment demonstrated significant results in all screening steps. **A**, MBEH-treatment in zebrafish 2 days post fertilization causes vitiligo. **B**, Dose-dependent overview of pericardial edema in Tg(*fli1a:eGFP*)^{y7}. **C**, While MBEH significantly reduced the heart rate in zebrafish embryos, no other cardiac phenotypes were induced. Dotted lines indicate 95% CI significance thresholds. **D**, MBEH induces more severe pericardial edema in Tg(*myl7:eGFP*)$^{twu34/+}$, than DMSO. Data was analyzed with a two-tailed fishers' exact test. **E**, Developmental delays detected in treated embryos. No delays were detected in DMSO-treated fish at any concentration, while MBEH caused dose-dependent developmental delays. (ns) $P > 0.05$; (*) $P \leq 0.05$; (**) $P \leq 0.01$; (***) $P \leq 0.001$; (****) $P \leq 0.0001$

In humans, the use of **monobenzone (MBEH)** has been associated with contact vitiligo (238). Not only does MBEH cause depigmentation in zebrafish as shown in Figure 25 A, but also caused decreased HR at 20 µM in Tg(*fli1a:eGFP*)^{y7} (-1.908; n = 3) and Tg(*myl7:eGFP*)$^{twu34/+}$ (atrium: -2.595; ventricle: -2.119; n = 7). Although MBEH induced dose-dependent developmental delay, it did not induce dose-dependent pericardial edemas (Figure 25 D). Nonetheless, treatment of Tg(*myl7:eGFP*)$^{twu34/+}$ with MBEH presented more severe pericardial edemas than the treatment of Tg(*fli1a:eGFP*)^{y7}. Analysis of HS and contractility did not reveal any differences. Furthermore,

MBEH induced dose-dependent developmental delay, while not inducing dose-dependent pericardial edemas.

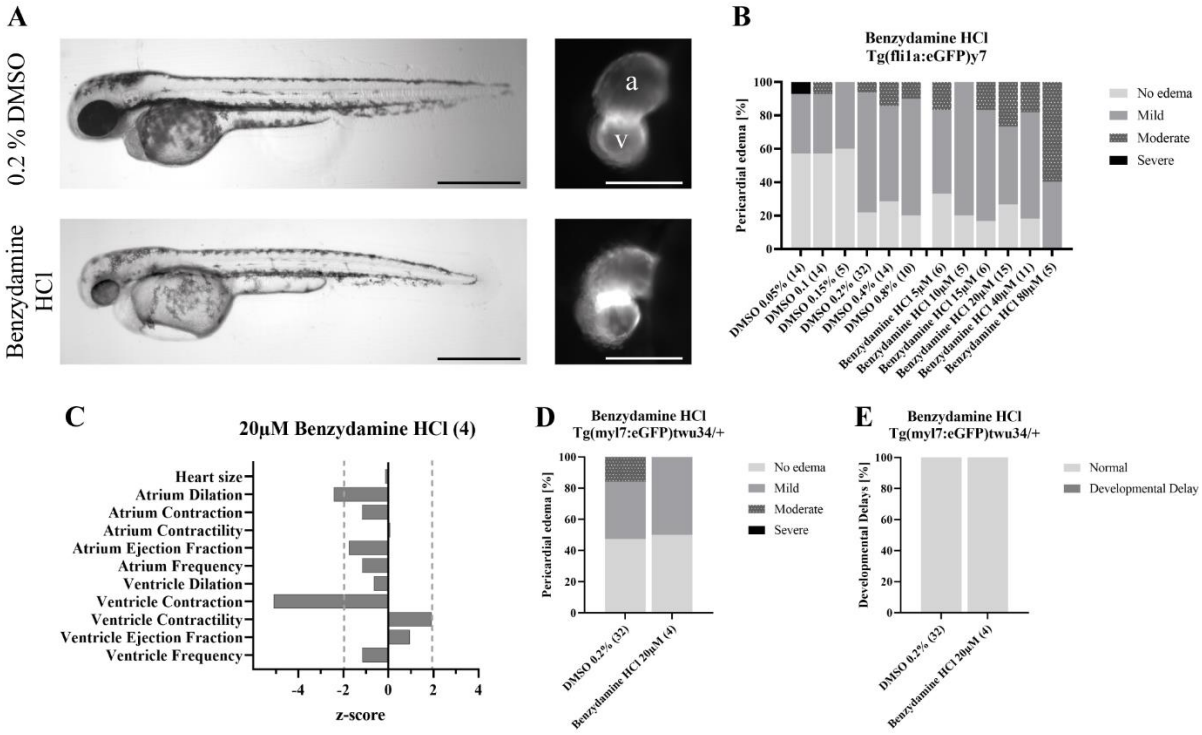

Figure 26: Benzydamine Hydrochloride (BZY)

Effects of benzydamine hydrochloride (BZY) treatment for all screening steps. **A**, Morphology of BZY-treated zebrafish 2 days post fertilization. **B**, Overview of pericardial edema in Tg(*fli1a:eGFP*)^{y7} for different concentrations. **C**, Dotted lines indicate 95% CI significance thresholds. Maximum atrium dilation and maximum ventricle contraction are significantly reduced. **D**, Pericardial edema in BYZ-treated Tg(*myl7:eGFP*)$^{twu34/+}$. **E**, Developmental delays detected in treated embryos.

The EMA approved local non-steroidal anti-inflammatory drug (NSAID) **Benzydamine HCl (BZY)** has antiseptic, analgesic and anesthetic properties in humans (239,240). BZY mitigates the liberation of arachidonic acid from phospholipids, thus inhibiting phospholipase A_2. It also weakly inhibits prostaglandin endoperoxide H synthase 1 and 2 by decreasing prostaglandin production (241–243). In Tg(*fli1a:eGFP*)^{y7} zebrafish embryos at 48 hpf, 20 µM BZY caused significant bradycardia (-2.10, 95% CI, n = 11). Similarly, in Tg(*myl7:eGFP*)$^{twu34/+}$, 20 µM of the compound reduced HR in atrium and ventricle, although not significantly (-1.16, n = 4) (Figure 26 C). Moreover, the max area of dilation of the atrium was significantly decreased (-2.90, 95% CI), leading to a decrease in the atrial EF (aEF) (-1.75, 90% CI). The ventricles area of max dilation was normal, while the max contraction was significantly higher (-5.07, 95% CI). Although the overall HR was slower, approximated HS and conduction were not affected (Fisher's exact p = 0.121). However, in 50% of treated zebrafish embryos BZY caused mild pericardial edema (Figure 26 D).

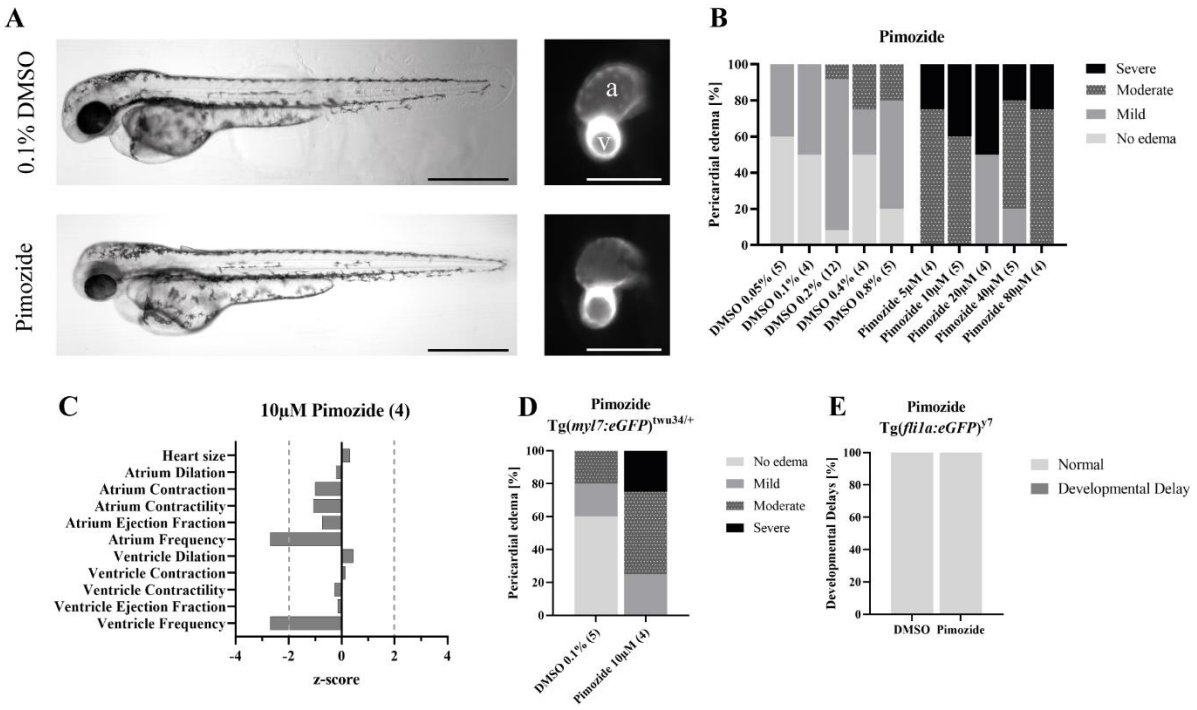

Figure 27: Pimozide (PI)

Effects of pimozide (PI)-treatment on zebrafish embryos 2 days post fertilization. **A**, Morphological overview of PI-treated zebrafish. **B**, PI induces pericardial edema in Tg(*fli1a:eGFP*)^{y7} at different concentrations. **C**, While heart rate is significantly reduced in PI-treated embryos, no other phenotypes were detected. Dotted lines indicate 95% CI significance thresholds. **D**, PI induces more severe pericardial edema than the DMSO controls in Tg(*myl7:eGFP*)$^{twu34/+}$ zebrafish embryos. **E**, No developmental delays were observed in PI-treated embryos.

The serotoninergic 5-HT2a-receptor and dopamine receptor antagonist **pimozide (PI)** is a potent neuroleptic drug (244). In the primary screening PI induced significant bradycardia (-5.092, 95% CI, n = 4). Further, PI induced significant bradycardia for concentrations between 10 and 80 µM. All tested PI concentrations induced moderate to severe pericardial edema (Figure 27 B). A concentration of 10 µM displayed the strongest effect on HR (-7.488, 95% CI, n = 4), and was therefore selected for the validation step. At this concentration, PI caused significant bradycardia in both heart chambers in Tg(*myl7:eGFP*)$^{twu34/+}$ (-2.69, 95% CI, n = 4), but did not affect relative and absolute contractility, EF, or HS. No arrhythmias or conduction defects were detected. PI induced more severe pericardial edema in both zebrafish lines, but did not delay their development (Figure 27).

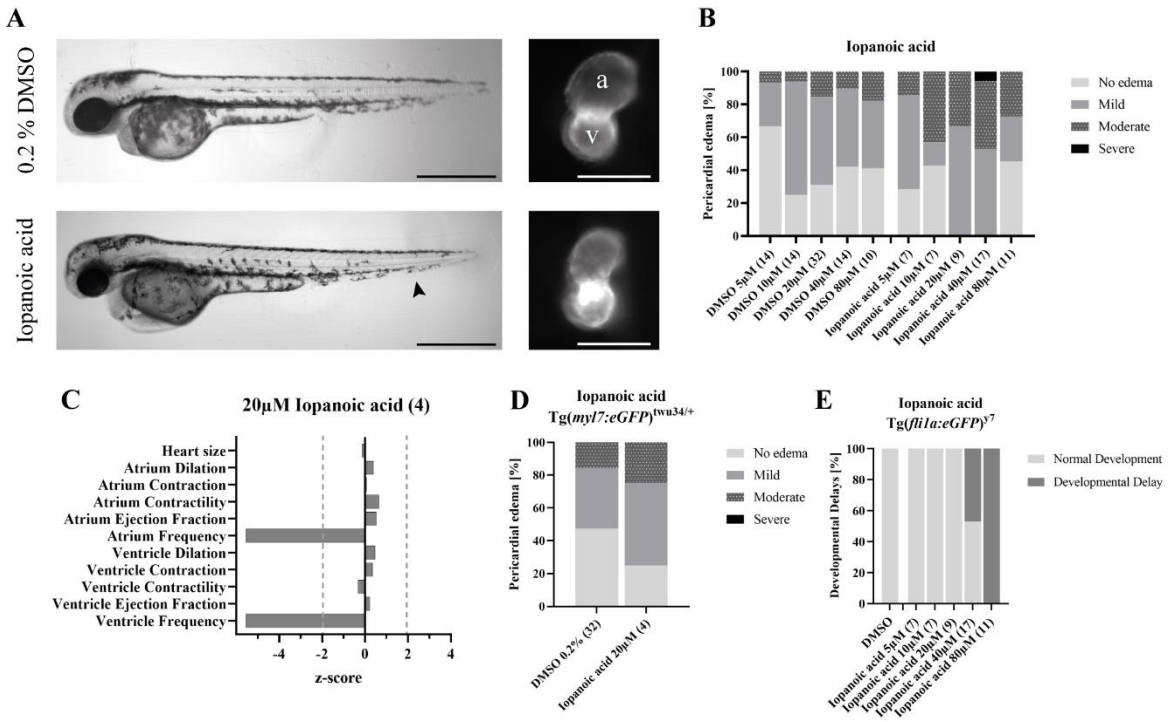

Figure 28: Iopanoic Acid (IOP)

Iopanoic acids (IOP) effect on zebrafish 2 days post fertilization. **A**, Morphological overview of IOP-treated zebrafish shows, that the contrastant accumulates in the yolk. **B**, IOP induces more moderate pericardial edemas in Tg(*fli1a:eGFP*)^{y7} at different concentrations. **C**, IOP significantly reduced heart rate, while not affecting functionality. Dotted lines indicate 95% CI significance thresholds. **D**, IOP induces pericardial edema similar to the DMSO controls in Tg(*myl7:eGFP*)$^{twu34/+}$ zebrafish embryos. **E**, Dose-dependent developmental delays were detected in IOP-treated embryos.

The contrastant **Iopanoic acid (IOP)** is an inhibitor of the thyroxine to 3,5,3'-triiodothyronine (T4-T3) conversion. In the primary screen, a 20 µM dose of IOP led to a decrease in -2.647 (95% CI, n = 4). Additionally, the application of IOP resulted in a dose-dependent delay in development (Figure 28 E). When tested in Tg(*myl7:eGFP*)$^{twu34/+}$ zebrafish, a concentration of 20 µM caused an even greater effect, with a z-score of -5.534 in both the atrium and ventricle (n = 4). However, the contractility of the heart chambers, EF, and overall HS were not affected, and no conduction defects or arrhythmias were detected. Nonetheless, IOP caused developmental delays and edema in both zebrafish lines. Moreover, caudal fin deformities with apoptosis at these sites were observed as indicated with an arrow in Figure 28.

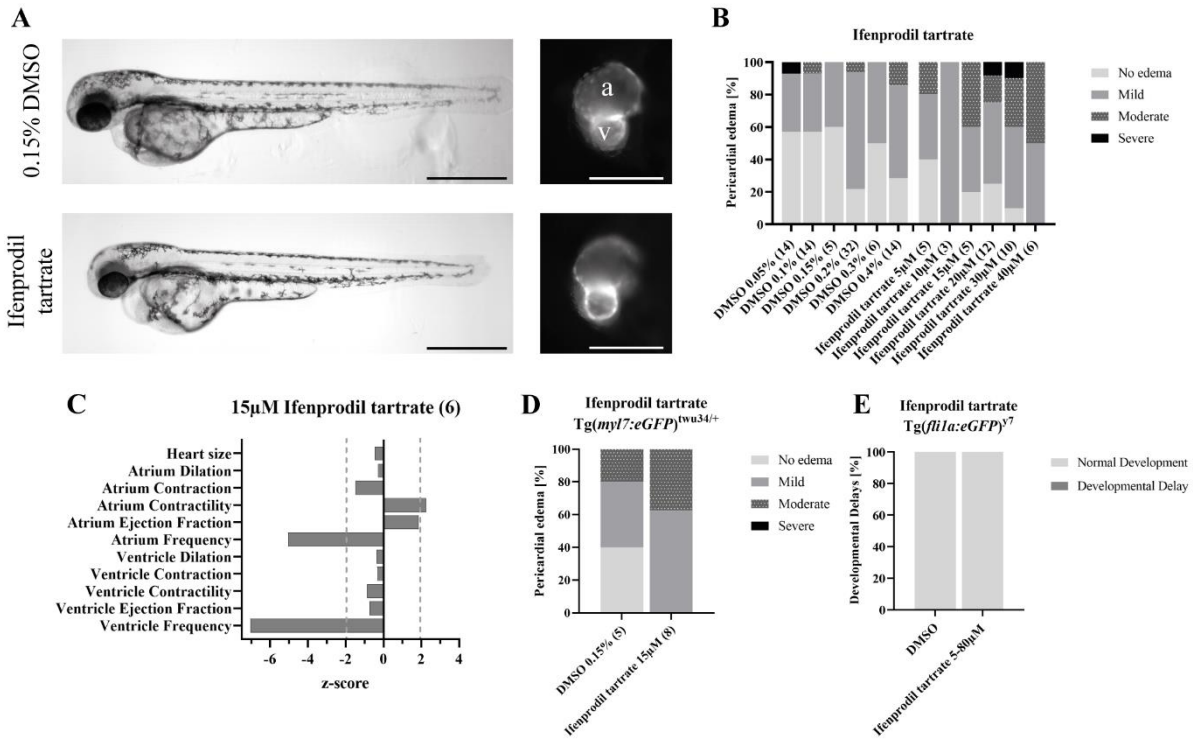

Figure 29: Ifenprodil Tartrate (IPT)

Overview of the effects of ifenprodil tartrate (IPT) treatment on zebrafish 2 days post fertilization. **A**, Morphology of treated fish was not altered, aside from caudal fin deformities indicated by the arrow. **B**, IPT-treatment induced more moderate and severe pericardial edemas in Tg(*fli1a:eGFP*)^{y7} at different concentrations and was lethal at 80 µM. **C**, IPT significantly reduced heart rate and significantly increased atrium contractility and atrium ejection fraction. Dotted lines indicate 95% CI significance thresholds. **D**, IPT induces larger pericardial edemas than the DMSO controls in Tg(*myl7:eGFP*)$^{twu34/+}$ zebrafish embryos. **E**, No dose-dependent developmental delays were detected after IPT treatment.

In the primary screening, the use of **ifenprodil tartrate (IPT)** as a vasodilator showed a significant decrease in HR (-3.885, 95% CI, n = 4). However, IPT caused dose-dependent pericardial edema and was lethal at a dose of 80 µM (Figure 29 B). Doses ranging from 5-10 µM did not significantly reduce HR, but doses higher than 15 µM induced significant bradycardia. Therefore, a 15 µM dose was used to treat Tg(*myl7:eGFP*)$^{twu34/+}$ zebrafish, which also resulted in significant bradycardia in both the atrium (-5.04, 95% CI, n = 6) and ventricle (-7.05, 95% CI) (Figure 29 C). IPT reduced the area of atrial max contraction (-1.48) but increased contractility (1.96) and aEF (1.86). However, the functionality of the ventricle was not affected, and the gross morphology and HS remained unchanged after IPT treatment.

6.4.2 The Histaminergic Receptor H1 (Hrh1)

It is well known, that the biological processes of allergy, inflammation, vasodilation, and neurotransmission involve histamine (H) and its receptors (245–247). Mammals have four types of G-protein-coupled receptors (GPCR): HRH1-HRH4 (248), while zebrafish have six histaminergic

receptors: Hrh1, Hrh2a-b, Hrh3a-c (249). However, HRH4 has no known orthologue in zebrafish (249). Moreover, the recent discovery of a triplication of *hrh3* in zebrafish led to previous publications on *hrh3* to be focused on *hrh3a* (chromosome 7). *hrh3b* is located on chromosome 2, while *hrh3c* is located on chromosome 22 (249). Their broad involvement in biological processes and their pleiotropic effects (250) make GPCRs difficult targets to study. Their active and inactive conformations exist in a delicate equilibrium (251), so tipping the scale to one side can be beneficial for one process, while it may have a negative impact on another.

Since the 1940s, it has been known that Hs play an important role in cardiac function and that the cardiac response to Hs is species dependent (252). Nevertheless, the role of H and its receptors in cardiac function are not well understood to this day.

6.4.2.1 HRH1 Antagonists Identified as Valid Hits

This study identified six hit compounds that target HRH1 with the same MoA and HR phenotype. Therefore, the library was then filtered for all HRH1 antagonists resulting in 41 identified antagonists. Of these, 12 significantly decreased HR with a 95% CI, and three more with a 90% CI. These 15 HRH1 antagonists are listed in Supplementary Table 7. This study focuses on the six valid hits and the target itself.

During the primary screening, **AAH** significantly reduced HR with a z-score of -2.60 (95% CI; n = 5) at 20 µM compound concentration. AAH significantly induced bradycardia at all tested concentrations while it induced cardiac arrest in at least 66.67% of the embryos at concentrations ≥40 µM. Further, AAH showed dose-dependent toxicity according to the calculated ToxScore (Figure 30 D). Treatment of Tg(*myl7:eGFP*)$^{twu34/+}$ with 10 µM AAH resulted in significant bradycardia (Atrium: -5.29, 95% CI; Ventricle: -4.54, 95% CI; n = 11). Maximum atrium and ventricle dilation (Atrium: -1.41, 95% CI; Ventricle: -3.83) and contraction (Atrium: -1.34, 95% CI; Ventricle: -2.46) were significantly decreased (Figure 31 C-D). Uniform reduction in atrium dilation and contraction did not alter aEF significantly (Figure 31 E). However, reduction in max ventricle dilation and contraction led to significantly decreased ventricular EF (vEF) (-4.25) and relative contractility (-2.46). Furthermore, AAH treatment reduced HS with a z-score of -1.84 in treated embryos (Figure 31 A). In addition, a two-tailed Fisher's exact test showed that AAH induced significantly more severe pericardial edemas than the DMSO controls (p = 0.009; Figure 31 G).

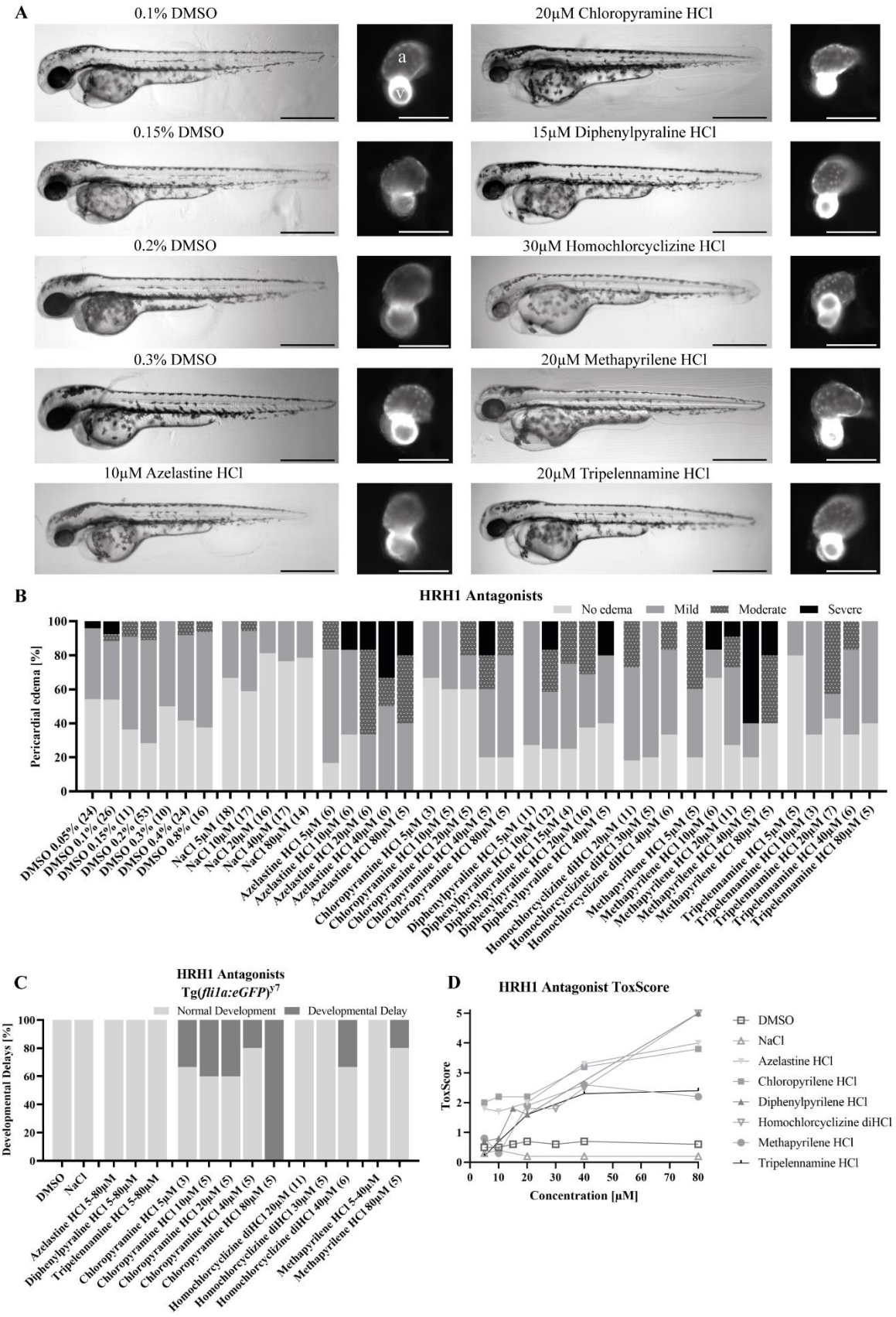

Figure 30: Effect Overview of HRH1 Antagonists

Effects of different HRH1 antagonists on zebrafish 2 days post fertilization. **A**, Morphological overview of treated embryos. **B**, Overview of dose-dependent pericardial edemas in treated Tg(*fli1a:eGFP*)^{y7}.

Azelastine HCl and methapyrilene HCl induced dose-dependent pericardial edema. **C**, Dose-dependent developmental delay was observed in chloropyramine HCl-treated embryos. Most compounds did not induce developmental delays. **D**, ToxScore of tested compounds showed dose-dependent toxicities.

The HRH1 antagonist **chloropyramine HCl (CHCl)** was identified as a hit with a significant z-score of -2.97 (95%, n = 5) in zebrafish embryos 2 dpf. Testing of different concentrations showed dose-dependent induction of pericardial edema, cardiac arrest and overall toxicity (Figure 30 D). CHCl doses higher than 10 µM also induced significant bradycardia. At a standard concentration of 20 µM the effect size and ToxScore were well balanced, therefore, Tg(*myl7:eGFP*)$^{twu34/+}$ were treated with the standard concentration. The validation step showed a z-score of -3.19 for the atrium and -4.45 for the ventricle (95% CI, n = 5), without significantly affecting HS, EF, and relative contractility (Figure 31 C-F).

In the primary screen treatment with **DPH** induced significant bradycardia (-3.55, 95% CI; n = 3). Concentration rows showed that all DPH doses higher than 10 µM induced significant bradycardia. Treatment with 80 µM DPH was lethal (Figure 30 B), and DPH induced dose-dependent severity of pericardial edemas and toxicity (Figure 30 D). Therefore, 15 µM was used to treat Tg(*myl7:eGFP*)$^{twu34/+}$, to balance effect size and toxicity. At 15 µM DPH significantly reduced HR in both heart chambers (Atrium: -3.43, 95% CI; Ventricle: -4.74, 95% CI; n = 5) (Figure 31 B), without affecting EF, dilation, contraction, and HS (Figure 31 A & C-F). However, it induced more severe edemas, which were not significant according to a two-tailed Fisher's exact test (p = 0.167).

Treatment of Tg(*fli1a:eGFP*)^{y7} with **homochlorcyclizine diHCl (HOD)** in the primary screen resulted in significant reduction of the HR (-1.77, 90% CI; n = 10), and all concentrations higher than 10 µM induced significant bradycardia. A concentration of 80 µM HOD was lethal to embryos 2 dpf and therefore assigned a ToxScore of 5 (Figure 30 D). At 30 µM HOD did not induce edemas and had a ToxScore of 1.8, while significantly reducing HR. Thus, 30 µM HOD were used to treat Tg(*myl7:eGFP*)$^{twu34/}$ zebrafish embryos. In both heart chambers, 30 µM of HOD significantly reduced HR (Atrium: -4.21, 95% CI; Ventricle: -3.71, 95% CI; n = 9), max atrium dilation, and contraction (Dilation: -3.07; Contraction: -3.18), while max ventricle dilation was significantly increased (2.43), and max contraction was not affected (-0.19). This concurs with significant increase in vEF (4.39), without significantly affecting aEF and HS (Figure 31 B & E).

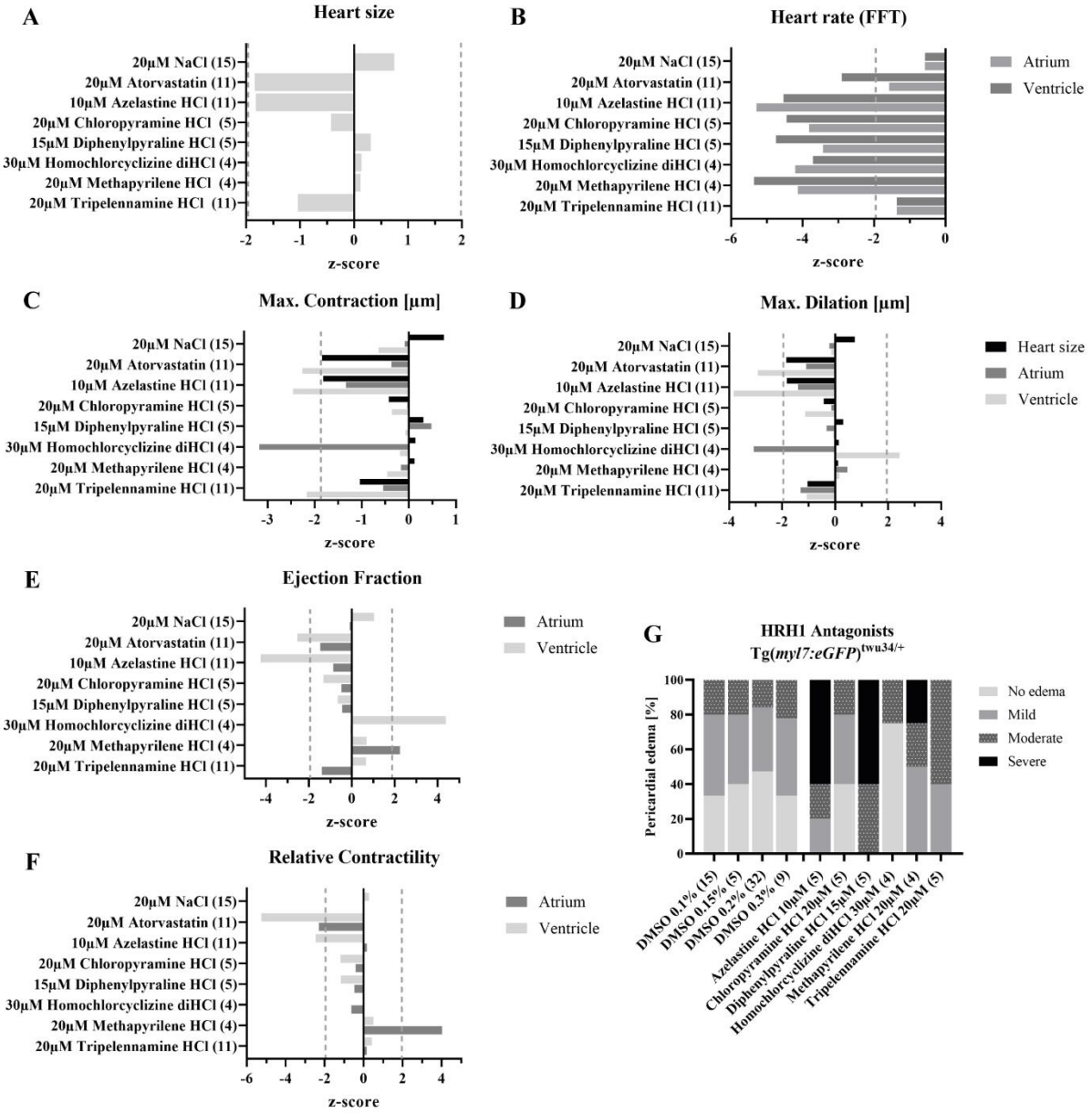

Figure 31: *pyHeart4Fish* Analysis of HRH1 Antagonists

Overview of quantitative data for HRH1 antagonists obtained from analysis with pyHeart4Fish. **A** None of the compounds showed significant changes in heart size, however, azelastine HCl (AAH) induced smaller hearts. **B**, Heart rate was reduced after treatment with all HRH1 antagonists. **C**, Maximal contraction was significantly decreased after treatment with three different compounds. **D**, Changes in maximum dilation were not target specific. **E**, Ejection fraction was significantly affected for AAH, homochlorcyclizine diHCl and methapyrilene HCl (MP)-treated zebrafish embryos. **F**, MP significantly increased atrial relative contractility. **G**, In Tg(*myl7:eGFP*)$^{twu34/+}$, AAH and diphenylpyraline HCl induced stronger pericardial edemas. **A**-**F**, Data was z-normalized against respective DMSO controls. Dotted lines indicate 95% CI significance thresholds. (HCl) Hydrochloride; (NaCl) sodium chloride.

In the primary screen, **methapyrilene HCl (MP)** was found to significantly reduce HR compared to other HRH1 antagonists (-2.21, 95% CI, n = 6). Concentrations higher than 10 µM induced bradycardia, while higher concentrations between 40 and 80 µM caused toxic side effects (Figure

30 D). In the validation step, a concentration of 20 µM MP was tested in Tg(*myl7:eGFP*)$^{twu34/+}$ and was found to reduce HR chamber-specifically (Atrium: -4.13, 95% CI; Ventricle: -5.36, 95% CI; n = 4). Additionally, the ariums relative contractility was significantly increased in MP-treated embryos (4.03; 95% CI; n = 4), while the ventricle was not significantly affected (0.50). HS, dilation and contraction were not significantly affected, however the aEF increased with a z-score of 2.25 (95% CI), while vEF was not affected (0.68; 95% CI). The compound did not cause significant conduction defects (Fisher's exact test p = 0.121).

Another HRH1 antagonist, **tripelennamine HCl (TRP)** was also found to significantly reduce HR in the primary screen (-2.36 95% CI, n = 5). However, testing different concentrations showed cardiac arrest in 50% of treated embryos at 40 and 80 µM (Figure 30 D). At a concentration of 20 µM, TRP significantly reduced HR, without signs of cardiac arrest and a comparably low ToxScore (Figure 30 D). Therefore, this concentration was used to treat Tg(*myl7:eGFP*)$^{twu34/+}$. In the validation step, treatment with TRP caused reduced HR the atrium with a z-score of -1.37 and ventricle of -3.00 (95% CI, n = 11). HS, while smaller, was not significantly affected (-1.04). Half of all TRP-treated embryos displayed an AVB (Fisher's exact test p = 0.022).

In summary, HRH1 antagonists induced bradycardia and cardiac arrest at higher concentrations. Most HRH1 hit compounds were lethal at 80 µM.

6.4.2.2 Expression of Histaminergic Receptors in Zebrafish

Extensive research on GPCRs as drug targets has greatly expanded our understanding of the expression patterns and intracellular signals of HRHs in mammals (253). Although *HRHs* are expressed almost ubiquitously, their expression levels vary between different types of *HRHs*. While the role of HRHs in neurology and behavior in zebrafish has been extensively studied, their expression patterns in different organs during development remain poorly established (Table 36). To address this gap, *in situ* probes were designed to assess the overall expression of all six *hrhs* in zebrafish embryo and larval stages.

Table 36: HRH Expression and Signaling in Mammals and Zebrafish

Receptor	Model	Expression*	Literature
HRH1 / hrh1	Murine	Gastrointestinal tract, heart, hemolymphoid system, hepatobiliary system, nervous system, reproductive tissues, sensory system, skeletal muscle, vascular permeability, and vasoconstriction	(254,255)
	Zebrafish	7 dpf: Brain (telencephalon) Adult: Brain, gills, intestine, liver, spleen	(248,256)
HRH2 / hrh2a-b	Murine	Gastrointestinal tract, heart, nervous system, reproductive tissues, vasoconstriction	(254,255)
	Zebrafish	Adult: Brain, gills, heart, spleen	(248)
HRH3 / hrh3a-c	Murine	Nervous system	(254)
	Zebrafish	Adult: Brain (cerebellum (*hrh3c*), diencephalon, *griseum centrale*, habenular (*hrh3a-c*), hypothalamus (*hrh3a*), inferior lobe, optic tectum (*hrh3a*), parvocellular preoptic region (*hrh3a*), posterior tuberal nucleus, telencephalon (*hrh3a*), thalamus (*hrh3a*), torus lateralis, tuberculum), heart, gut (*hrh3c*), spleen	(248,249,257,258)
HRH4	Murine	Brain	(254)

*If not otherwise indicated, information was published under the collective gene name instead of a specific subset of genes. MARRVEL last accessed 05/24/2023 (254).

To identify the correct sequences due to duplicates and triplicates of some *hrh*s in zebrafish, multiple sequence alignment was performed using ClustalW 2.1 (last accessed 07/03/2022) (259) and MultAlin (last accessed 07/03/2022) (218), see Table 37, Supplementary Figure 2, Supplementary Figure 3 and Supplementary Figure 4. Sequences aligned up to 52% between human and zebrafish. Further, to ensure that the sequences we identified as Hrh3b and Hrh3c were not identical to the more commonly known Hrh3, both sequences were compared. A 49-57% alignment between zebrafish Hrh confirmed that all selected sequences encoded different proteins. From here on out, Hrh3 will be referred to as Hrh3a.

Table 37: Multiple Sequence Alignment of the Histaminergic Receptors

Zebrafish protein	***Transcript ID / RefSeq***	***Human protein***	***Transcript ID / RefSeq***	***Sequence alignment [%]***
Hrh1	NM_001042731	HRH1	NP_001091682.1	39.6
Hrh2a	NP_001038803.2	HRH2	NP_001380389.1	45.3
Hrh2b	NP_001103208.1	HRH2	NP_001380389.1	45.4
Hrh3a	NP_001020689.1	HRH3	NP_009163.2	51.9
Hrh3b	ENSDARG00000045137	HRH3	NP_009163.2	51.5
Hrh3c	ENSDART00000164061.2	HRH3	NP_009163.2	50.8
Hrh3b	ENSDARG00000045137	Hrh3a (zf)	NP_001020689.1	51.5
Hrh3b	ENSDARG00000045137	Hrh3c (zf)	ENSDART00000164061.2	57.3
Hrh3c	ENSDART00000164061.2	Hrh3a (zf)	NP_001020689.1	48.6

Primers were designed to generate all six probes. Four of the six probes were successfully generated and were able to specifically label areas of gene expression: *hrh1*, *hrh2a*, *hrh2b* and *hrh3b*. While the expression patterns of all *hrhs* were highly similar in larvae 3 and 5 dpf, the different receptors also showed tissue specific expression (Figure 32). All *hrhs* are expressed in the eyes, gills, medulla oblongata, olfactory epithelium, optic tectum, tegmentum and posterior tuberculum. Prolonged exposure to the stain revealed expression of *hrh1* in the heart as early as 3 dpf (Figure 32 E'-E''). Further, *hrh1* was strongly expressed in the dorsal telencephalon at 2-5 dpf (Figure 32 E'''). While *hrh2a* did not show expression patterns deviating from the other *hrhs*, *hrh2b* was expressed in the pancreas as early as 3 dpf (Figure 32 G-G'). Moreover, extended staining revealed expression of *hrh2b* in neuromast cells. *hrh3b* was also shown to be strongly expressed in the dorsal telencephalon 3-5 dpf and further in the liver at 3 dpf.

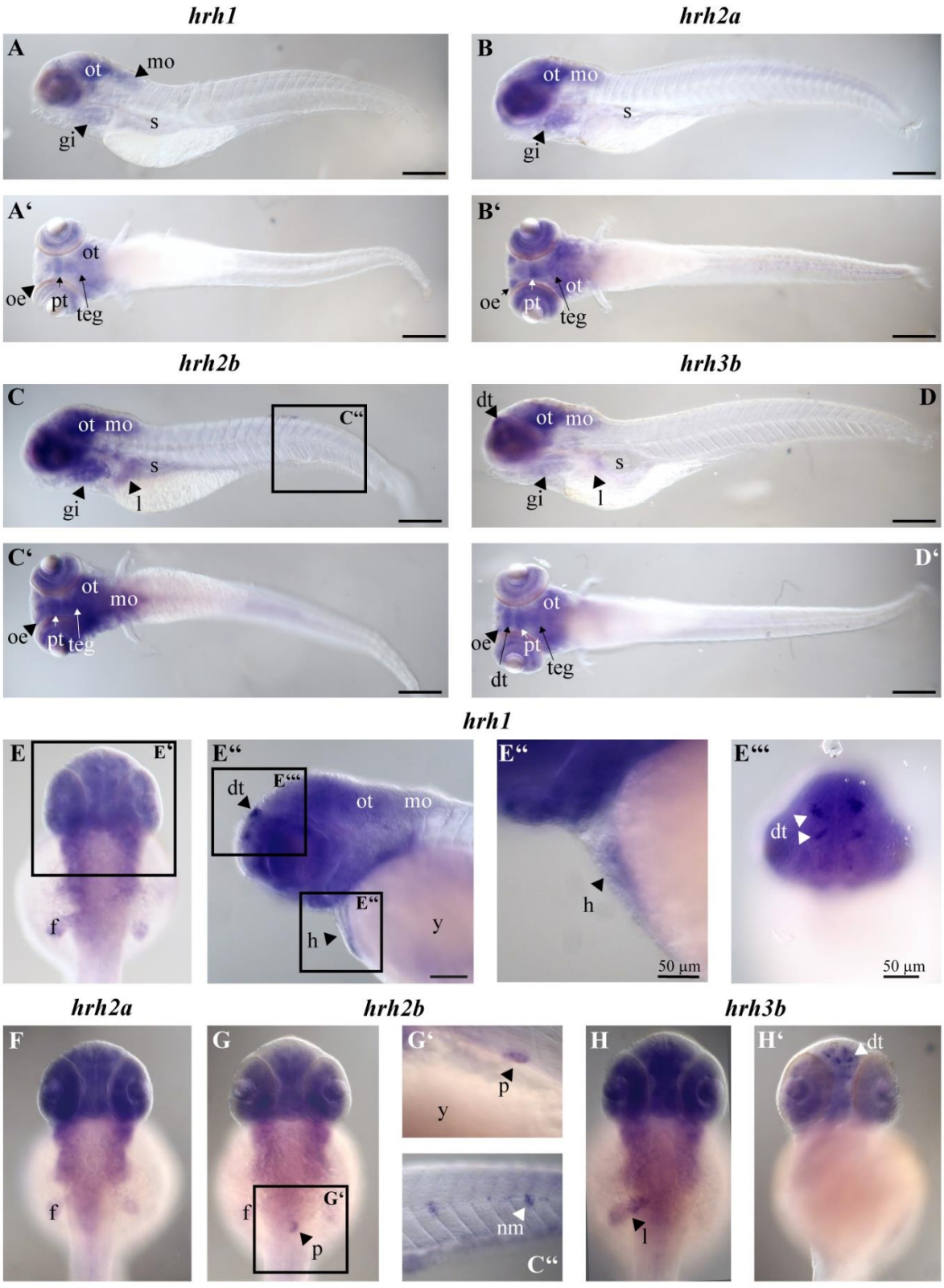

Figure 32: Whole-Mount *in situ* Hybridization of Zebrafish Histaminergic Receptors

A-A' & E-E''', *hrh1* is expressed in the dorsal telencephalon/pallium and heart. **B-B' & F**, *hrh2a* is primarily expressed in the brain, eyes, fin buds and gills. **C-C'' & G-G'**, besides specific expression patterns in the brain, liver and gills, *hrh2b* shows distinct expression in the pancreas at 3 days post fertilization (dpf) (**G-G'**). **D-D' & H-H'**, in addition to strong expression in the telencephalon and eyes,

hrh3b is expressed in the larval liver at 3 dpf. (dt) telencephalon/pallium, (e) eyes, (f) fin buds, (gi) gills, (h) heart, (l) liver, (mo) medulla oblongata, (nm) neuromast cells, (oe) olfactory endothelium, (ot) optic tectum, (s) swim bladder, (teg) tegmentum, (p) pancreas, (pt) posterior tuberculum, (y) yolk; **A-D, A'-D' & E''** scale bar = 100 µm. Images were improved with Fiji using the white-balance script described in 9.4.1.2.

Figure 33 shows that the cornea, lens, ciliary marginal zone, retinal outer nuclear layer (ONL), and retinal pigmented epithelium (RPE) do not express any of the tested *hrhs*. All tested *hrhs* are expressed in the retinal inner nuclear layer (INL). Moreover, *hrh2a*, *hrh2b* and *hrh3b* are expressed in the retinal ganglion cell layer (GCL) and retinal inner plexiform layer (IPL).

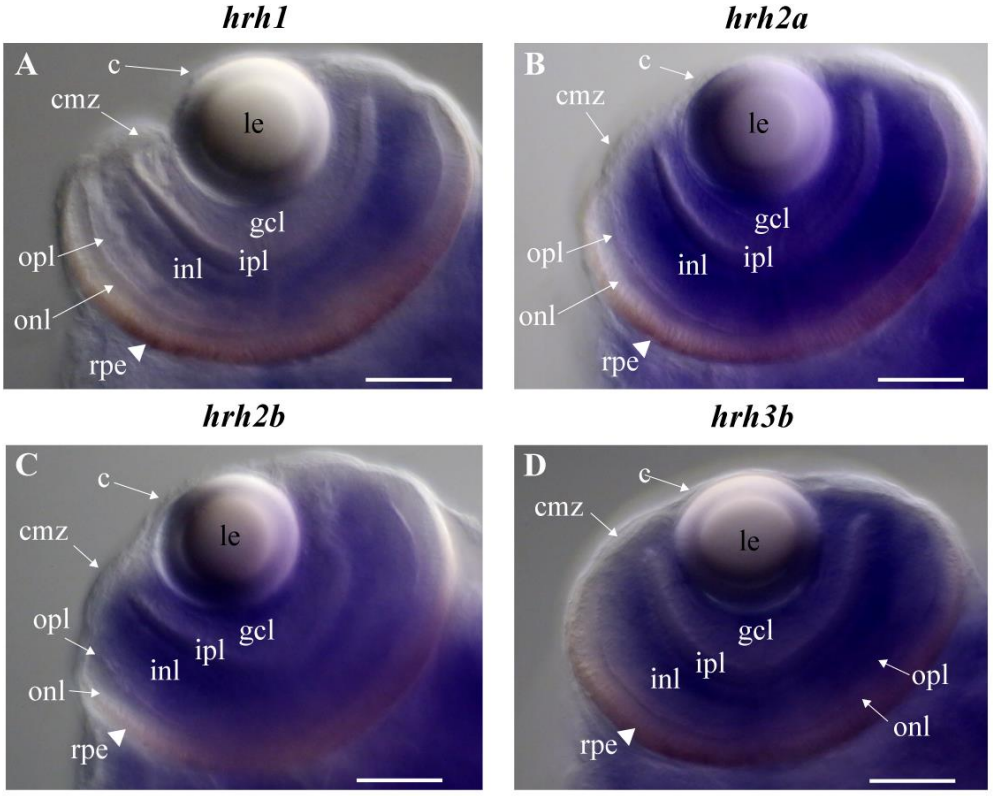

Figure 33: Expression Patterns of *hrh* in the Larval Retina

While all histaminergic receptors (*hrh*) are expressed in the eye at 5 day post fertilization, their expression patterns differ. (c) cornea, (cmz) ciliary marginal zone, (gcl) retinal ganglion cell layer, (inl) retinal inner nuclear layer, (ipl) retinal inner plexiform layer, (le) lens, (onl) outer nuclear layer, (opl) outer plexiform layer, (rpe) retinal pigmented epithelium. **A-D** scale bar = 50 µm. Images were improved with Fiji using the white-balance macro described in 9.4.1.2.

6.4.3 The Glucocorticoid Receptor NR3C1

Glucocorticoids (GCs) are steroid hormones mainly produced in the adrenal cortex, regulating metabolism, inflammation and stress response among others (260,261). In humans and teleost fish, cortisol is the most abundant GC, while corticosterone is predominant in rodents (262). GCs bind

to either the α or β isoform of the GC receptor (GR), a ligand-activated transcription factor encoded by *NR3C1*(263). NR3C1 consists of a N-terminal transactivation domain (NTD), a central DNA binding domain (DBD), a hinge region and a C-terminal ligand binding domain (LBD) (Figure 34 A) (198).

GRα is mostly located in the cytoplasm in a complex with heat shock proteins and immunophilin FK506-binding protein 51 (FKBP51) in absence of ligands (264,265). When activated by GC, the GRα dissociates from the repressor complex and enters the nucleus with the help of chaperone proteins (263,265,266). Once in the nucleus, the monomeric or dimeric NR3C1 can modulate gene expression by binding directly to DNA, tethering to DNA-bound transcription factors, or interacting directly with DNA and adjacent transcription factors (267). GRα can also translocate into mitochondria to regulate mitochondrial transcription (Figure 34) (268). GRβ, on the other hand, is believed to inhibit GRα's transactivational abilities and does not bind to traditional GC agonists, but has been reported to bind to antagonists (269,270). Interestingly, GRβ is not conserved across species: Rodents do not express GRβ, due to the absence of the alternative splice-site (271), but zebrafish have been shown to express both isoforms (269). However, GRβ does not play a functional role in transcriptional regulation in zebrafish (272). Overall, the lack of conservation of GRβ across species suggests that it does not play a significant regulatory role (271,272).

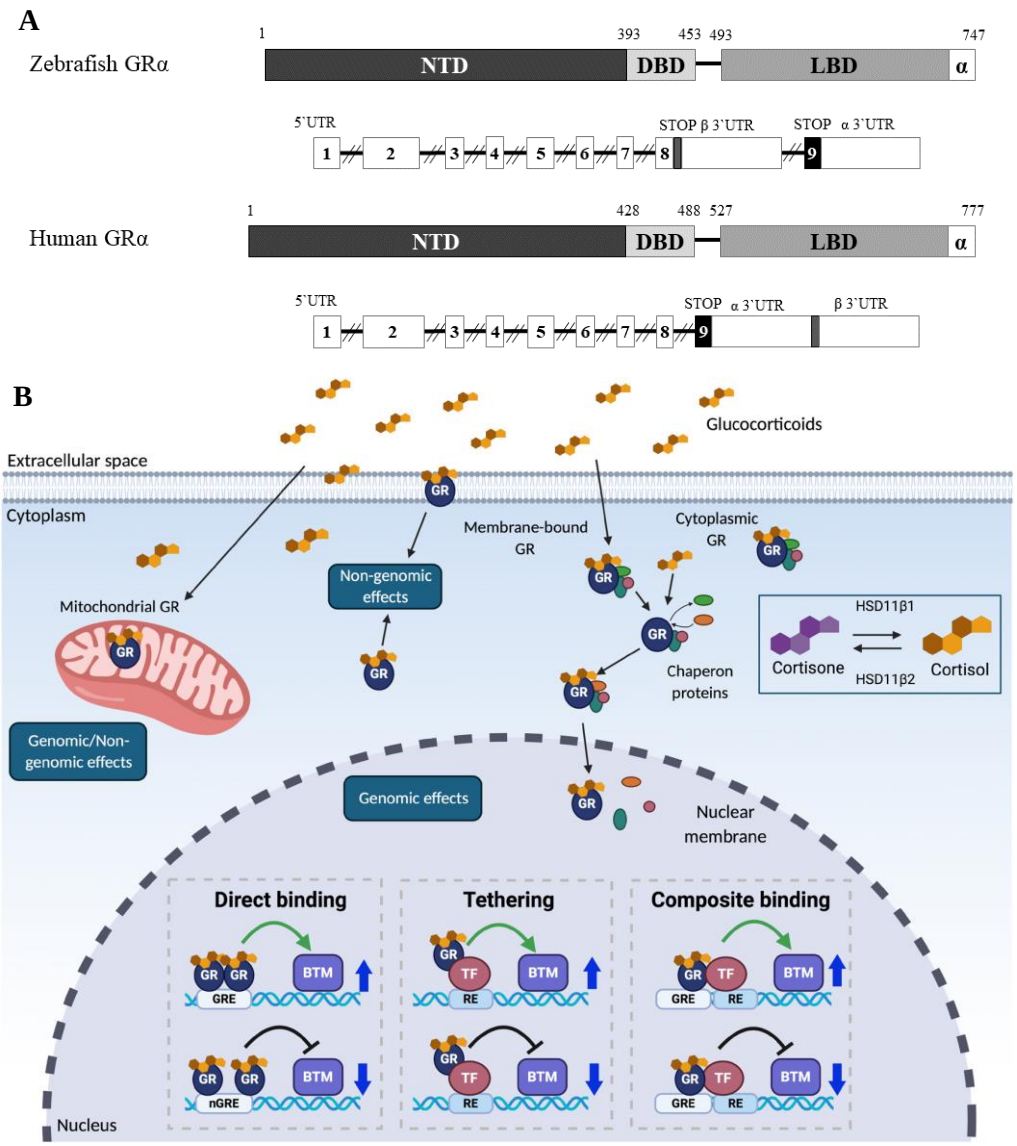

Figure 34: NR3C1 and its Signaling Pathways

A, Human and zebrafish GRα display high similarity between α-isoforms. Percentages represent the amino acid fraction similar between human and zebrafish per domain. The α-isoforms demonstrate an overall similarity of 59.3%. Both human and zebrafish NR3C1 consist of 9 exons, the first of them non-coding. The human β-isoform is located on exon 9, whereas the zebrafish isoform is located on exon 8. **B**, GCs cross the ECM barrier and are proposed to bind to cytoplasmic GRs to trigger rapid, non-genomic responses. Inactive GRs form a complex with heat shock proteins and immunophilin FKBP51. Once activated, GRs migrate to the nucleus, where they act as transcription factors.
(**DBD**) DNA-binding domain; (**LBD**) ligand-binding domain; (**NTD**) N-terminal domain. This figure was adapted with permission from Dinarello *et al.* (2020) (265).

In the past decade it has been discovered that GCs and GRs are not only expressed in the brain but also in other parts of the body such as the cardiovascular system, intestines, lymphoid organs, and skin (261). Particularly in the cardiovascular system, an imbalance in GCs can increase the risk of CVDs like bradycardia, AVB, and impaired cardiac function. For instance, Addison's disease,

which is caused by low cortisol and aldosterone production, can lead to hyperpigmentation, low blood pressure, and muscle weakness (273). In contrast, patients with hypercortisolism, also known as Cushing's syndrome, can develop hypertension and metabolic syndrome, both risk factors for CVDs (274,275). In 2003, a study with patients of Anglo-Celtic descent found a 4-fold elevation of the *NR3C1* variant p.N363S associated with CAD (276). High cortisol levels can also be caused by therapies that involve non-selective glucocorticoid receptor (GR) /mineralcorticoid receptor (MR) agonists or selective GR agonists for anti-inflammatory purposes (277).

6.4.3.1 The Role of NR3C1 Agonists: Impacts on the Heart and Conduction

After applying multiple filters and conducting further testing, Figure 19 displays the identification of four hit compounds that effectively targeted NR3C1 using an agonistic MoA. Following this, 134 significant compounds from the primary screen were filtered for NR3C1 agonists, resulting in the discovery of 13 compounds that had a comparable effect on HR. Out of these 13 compounds, 10 significantly increased HR with a 95% CI, while the remaining three did so with a 90% CI. Additionally, pregnenolone (P5), a GC-precursor, was included in this section as it also induced an elevated HR. The first part of this chapter will focus on the four identified NR3C1 agonists, the previously published NR3C1 agonist Clobetasol propionate (CLO) (278) and the GC-precursor P5.

6.4.3.1.1 NR3C1 Agonists and Their Influence on Cardiac Function

It has been previously observed that the NR3C1 agonist **CLO** can cause tachycardia in zebrafish in a dose-dependent manner (278). In our primary screening, CLO was also found to induce tachycardia (3.64; 95% CI; n = 5), making it a suitable positive control. Although increasing doses of CLO resulted in moderate edemas, the difference was not significant compared to the DMSO controls (Figure 35 B). There were no detectable pericardial edemas, and the ToxScore remained below 2 at every concentration (Figure 35 D). Moreover, CLO significantly increased HR at every tested dose. A concentration of 10 µM CLO was selected for further testing, as no moderate edemas were detected at this concentration. In Tg(*fli1a:eGFP*)^{y7} CLO also induced tachycardia in both heart chambers (atrium: 1.945; ventricle 2.225; 95% CI; n = 11) and increased the area of max dilation (atrium: 2.79; ventricle: 1.28) and contraction (atrium: 2.57; ventricle: 1.19) in atrium and ventricle. This was reflected in a mild increase in HS (1.39). However, EF was not significantly affected. Aside from a darker pigmentation, the treated fish and their heart morphology did not differ from the DMSO controls.

Beclomethasone dipropionate (BEC) induced significant tachycardia in the primary screen with a 95% CI (2.43; n = 3). When tested with various BEC concentrations, fish exhibited tachycardia

and there was a dose-dependent severity of pericardial edemas. At 80 µM concentration, BEC had the greatest impact with a z-score of 4.16 (n = 4). At this concentration, embryos also displayed the highest ToxScore of 3.3 with a significant increase in severe pericardial edemas (Fisher's exact test p = 0.0005) and developmental delays (Figure 35 B-D). The hit validation step utilized a 10 µM concentration, which exhibited a moderate ToxScore and adequate effect size. In Tg(*myl7:eGFP*)$^{twu34/+}$ BEC also resulted in tachycardia, but did not affect any other measured heart parameter or overall morphology. Nevertheless, BEC led to moderate and severe edema.

In the primary screen, **clocortolone pivalate (CCP)** caused a significant increase in HR in treated Tg(*fli1a:eGFP*)^{y7} (3.05). Edemas caused by CCP became more severe at varying concentrations, but remained within the DMSO control level. Some zebrafish with developmental delays were identified, but these delays were not significant nor dose-dependent. The highest ToxScore of 1.8 was observed in the 80 µM CCP treatment (Figure 35 D). Since the standard concentration did not show any signs of acute toxicity and was able to reproduce tachycardia, it was selected for further testing. In the validation step, 20 µM CCP induced significant tachycardia in both heart chambers without causing arrhythmias (atrium and ventricle: 4.11; 95% CI; n = 5. The max area of atrial contraction was significantly increased (2.12) without effect on dilation (0.83). Consequently, the relative contractility of the atrium was reduced (-1.30). The max contraction of the ventricle was reduced to a z-score of 1.3, while dilation did not differ from that of the controls. CCP treatment did not affect HS or overall morphology (Figure 35 A).

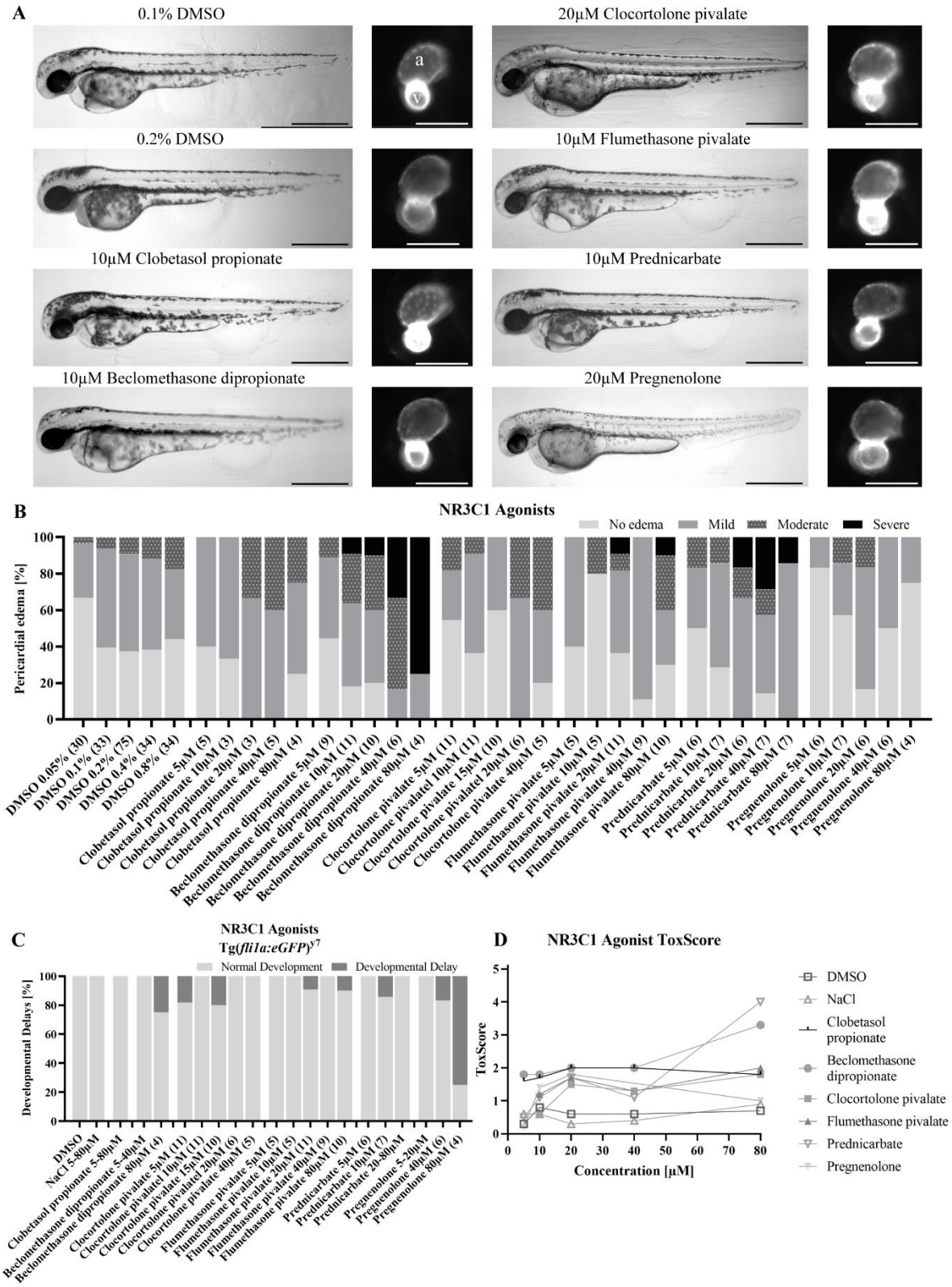

Figure 35: Phenotype Overview of NR3C1 Agonist-Treated Zebrafish

Overview of NR3C1 agonist-induced phenotypes. **A**, Body, and heart phenotypes of treated embryos. **B**, Dose-response overview for pericardial edemas in treated Tg(*fli1a:eGFP*)^{y7}. Data from prednicarbate-treated embryos indicates dose-dependent severity of pericardial edemas. Dose-dependent pericardial edemas of sodium chloride control treated embryos was excluded in this figure for space purposes. They can be found in Figure 30. **C**, Of all six compounds, dose-dependent developmental delay was only

observed in pregnenolone-treated embryos. Most compounds did not induce developmental delays. **D**, Except for prednicarbate, the ToxScore of tested compounds showed only mild dose-dependent toxicities.

During the primary screening, **flumethasone pivalate (FMP)** caused a significant increase in HR (2.29). Further testing with varying concentrations of FMP revealed a mild dose-dependent increase in ToxScore, with little to no developmental delays and pericardial edema, comparable to the controls (Figure 35 B-D). Each concentration tested resulted in significant tachycardia, with the strongest effect observed at 10 µM. Therefore, this concentration was used for subsequent testing. At 10 µM, FMP caused a significant increase in HR in Tg(*myl7:eGFP*)$^{twu34/+}$ at 2 dpf (atrium: 4; ventricle: 3.75; 95% CI; n = 5). Further, the max ventricle contraction was significantly larger (2.05), while max dilation was not altered (-0.24), resulting in a significantly reduced vEF (-2.68) and relative contractility (-3.34). The atrium was not significantly affected, and the overall morphology and HS remained unchanged (Figure 35 A).

The NR3C1 agonist **Prednicarbate (PRC)** caused a significant increase in HR in zebrafish embryos 2 dpf (2.48; 95% CI, n = 5) with a dose-dependent increase in pericardial edema severity. While developmental delays were detected on rare occasions, there was no indication of a dose-dependence. The highest ToxScore was detected with a concentration of 80 µM PRC (ToxScore: 4.0), leading to a cardiac arrest in all embryos, though the embryos remained intact (Figure 35 D). Further, PRC presented a dose-dependent effect on HR. Lower concentrations of PRC resulted in increased tachycardia. Hence, a concentration of 10 µM was utilized for the hit validation. In Tg(*myl7:eGFP*)$^{twu34/+}$ PRC also caused significant tachycardia in both heart chambers (atrium: 3.56; ventricle: 3.75; 95% CI; n = 5), but no changes were observed in the overall morphology of the body and heart.

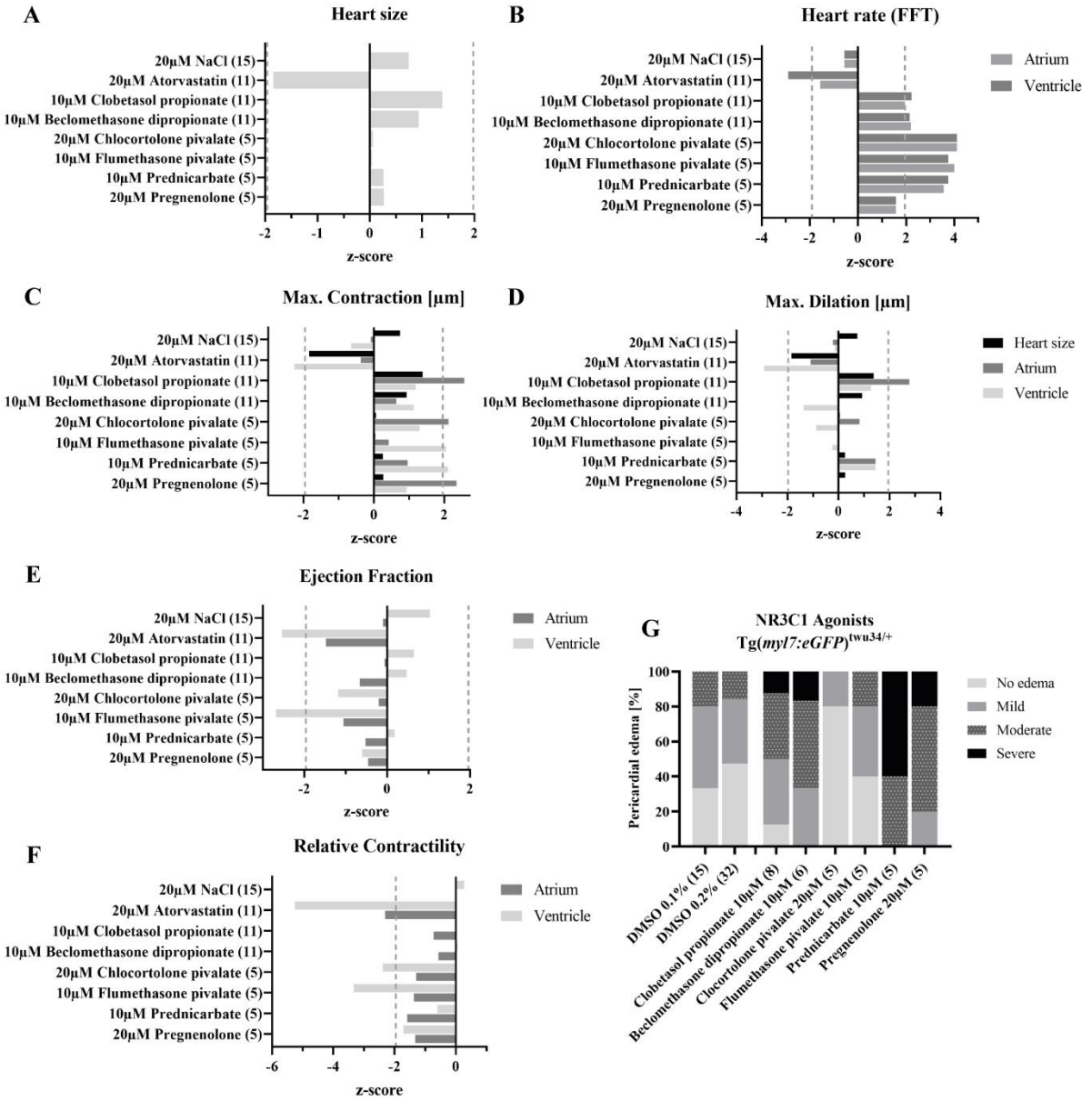

Figure 36: Analysis of NR3C1 Agonists and Pathway Related Compounds

pyHeart4Fish analysis for NR3C1 agonist-treated zebrafish embryos 2 days post fertilization. **A**, No significant changes in heart size were observed, even though clobetasol propionate (CLO) and beclomethasone dipropionate (BEC) show a mild reduction of heart size. **B**, All NR3C1 agonist and the prehormone pregnenolone (P5) induced tachycardia. **C** Maximal contraction of atrium and ventricle was affected in all treatments. **D**, The maximum area of dilation was only significantly affected in BEC-treated embryos. **E**, Ejection fraction of the atrium was significantly reduced in flumethasone pivalate-treated zebrafish embryos. **F**, Almost all tested compounds showed a tendency towards reduced contractility compared to the controls. **G**, In Tg(*myl7:eGFP*)$^{twu34/+}$, CLP, BEC, prednicarbate and P5 induced more severe pericardial edemas. **A-F**, Data was z-normalized against respective DMSO controls. Dotted lines indicate 95% CI significance thresholds. (HCl) Hydrochloride; (NaCl) sodium chloride.

P5, an adrenal corticosteroid precursor for mineralocorticoids, GCs, and others, initially reduced HR in the primary screen (-1.86 ;90% CI; n = 6) but increased it in repeated testing at different concentrations. In Tg(*myl7:eGFP*)$^{twu34/+}$ the compound caused mild tachycardia in atrium and

ventricle equally (1.58, n = 5), but decreased relative contractility (atrium: -1.33; ventricle: -1.71). No changes were observed in the overall morphology and HS (0.27), but P5-treated embryos were smaller, with bent tails, developmental delays, moderate to severe pericardial and yolk edemas, and reduced skin pigmentation.

6.4.3.1.2 Conduction Defects Detected in NR3C1 Agonist-Treated Zebrafish

Some of the tested compounds induced conduction defects in single fish, while no defects were detected in the controls. Therefore, the second part of this chapter focusses on conduction defects between atrium and ventricle detected in NR3C1 agonist treated Tg(*myl7:eGFP*)$^{twu34/+}$ zebrafish embryos 2 dpf. Only eight of the 15 agonists were tested due to limited time, with five of them displaying single occurrences of conduction defects at tested concentrations: BEC, CLO, fluticasone propionate (FCP), FMP, and PRC. These five compounds, together with the controls ATO and DMSO were tested again. The data was analyzed with pyHeart4Fish to obtain chamber-specific frequencies, with varying numbers of tested animals per concentration due to optimized concentrations included in every experiment.

As previously described, a healthy zebrafish heart generates electrical impulses from the SAN that spread across the atrium. These impulses slow down at the AVC before moving rapidly across the fast CCS of the ventricle. Figure 37 A shows an overlay of frequencies that demonstrates how the atrium contracts before the ventricle does in a regular rhythm, indicating a normal heartbeat. The frequency derived from both, a fitted sine function and a Fast Fourier transformation (FFT) showing the same values for both heart chambers, leading to an av-block score of 0.

Figure 37 B displays an example of a detected AVB. Although the atrial contractions follow a regular sine function, the ventricular contractions are more irregular, and not every contraction from the atrium gets conducted to the ventricle, resulting in reduced ventricular frequency. Further, the av-block score exceeds the threshold of 0.5 with a score of 1.38.

The complete AVB, also called third-degree AVB, displays no conduction between the atrium and ventricle. In Figure 37 C, the tool detected changes in fluorescence intensity in the ventricle, but it's clear that an identical signal was detected in both the atrium and ventricle. Here, the movement of the atrium was detected in the ROI selected for the ventricle, as the ventricle did not contract. This fact was confirmed by visual inspection of the respective output gif given by *pyHeart4Fish*. Although the av-block score was 0, the arrhythmia score far exceeded the threshold of 0.7.

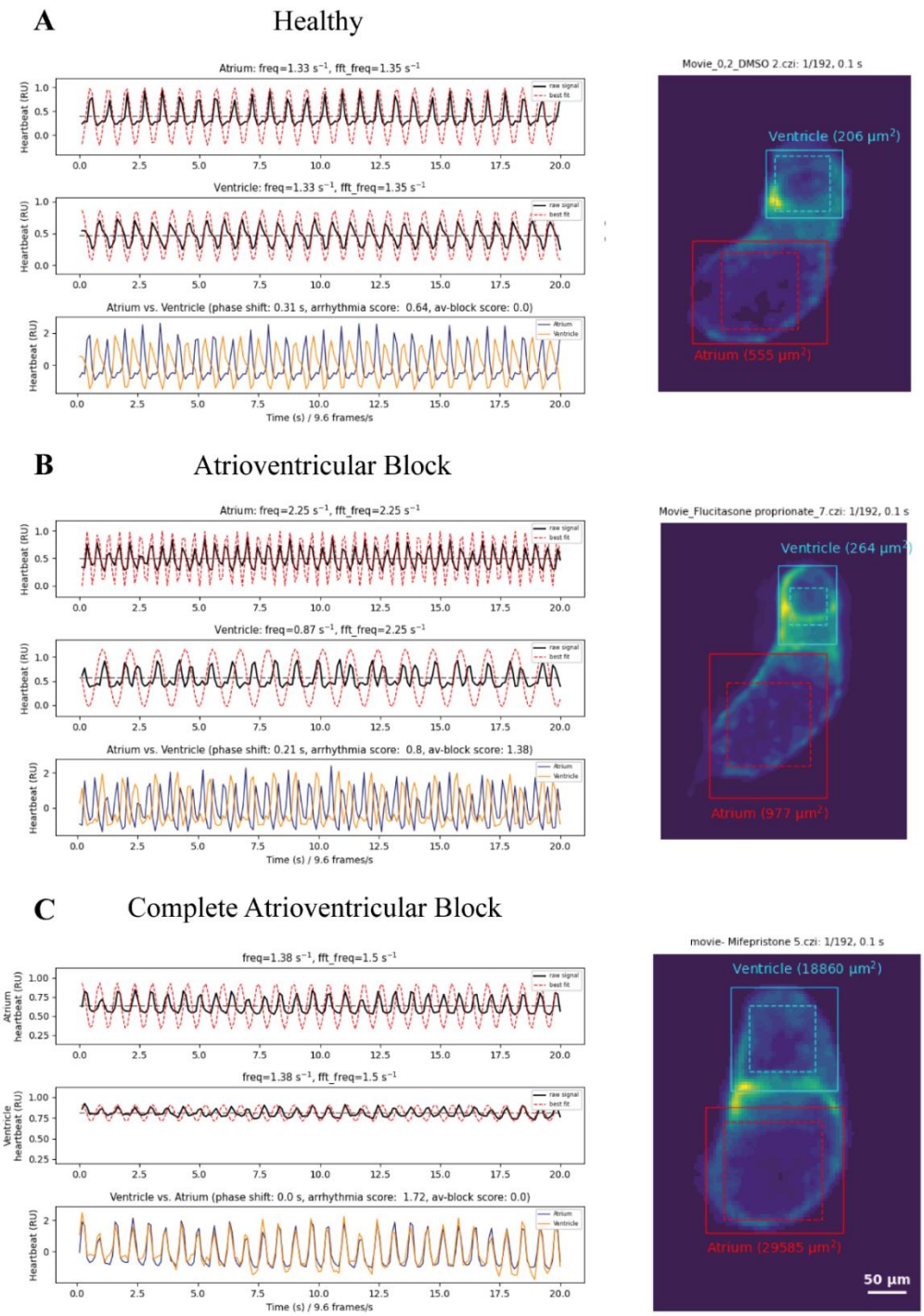

Figure 37: Atrioventricular Blocks (AVBs) Detected with *pyHeart4Fish*

Overview of atrioventricular blocks (AVBs) detectable with the chamber-specific analysis tool *pyHeart4Fish*. **A**, DMSO control-treated zebrafish display a regular heartbeat with atrial peaks being followed by ventricular peaks. **B**, Second degree AVB, where not every contraction is conducted to the ventricle. **C**, While the ventricle still displays a frequency, the overlay clearly shows, that the tool detected the same frequency from the atrium, because there is no contraction in the ventricle.

The first frequency describes the atrial frequency detected in the red region of interest (ROI) in the heart overview picture. The second frequency describes the ventricles heartbeat detected in the blue ROI in the heart overview. In the third row, an overlay of both frequencies is displayed. The heart overview on the right is displayed with a LUT that displays differences in fluorescence intensity from min (blue) to max

(yellow). Straight line = boundary box; dotted line = ROI; auto_corr = auto correlation; freq = frequency; fft_freq = Fast Fourier transformation frequency.

Figure 38 shows that AVBs were detected in zebrafish embryos2 dpf after 24 h-treatment with every tested NR3C1 agonist. CLO, CCP, and FMP were treated with their respective optimal concentration (Figure 38 A). At 10 µM CLO and FMP did not induce a significant amount of AVBs according to a two-sided Fisher's exact test. However, at 20 µM, CCB showed a tendency to have more AVBs compared to the controls. BEC, FCP, and PRC were tested at various concentrations to check for dose-dependency and reproducibility of the phenotype. Data from BEC and PRC suggest a dose-dependent increase in AVBs, but further experiments are required for collect equal numbers of each concentration. On the other hand, FCP induced a significant amount of AVBs at almost every concentration but was not dose-dependent. The ToxScore of FCP showed greater toxicity at lower doses with developmental delays and increased moderate pericardial edemas (Supplementary Figure 5 B-E). Despite this, the highest ToxScore detected was 1.9, and zebrafish morphology did not differ from DMSO controls.

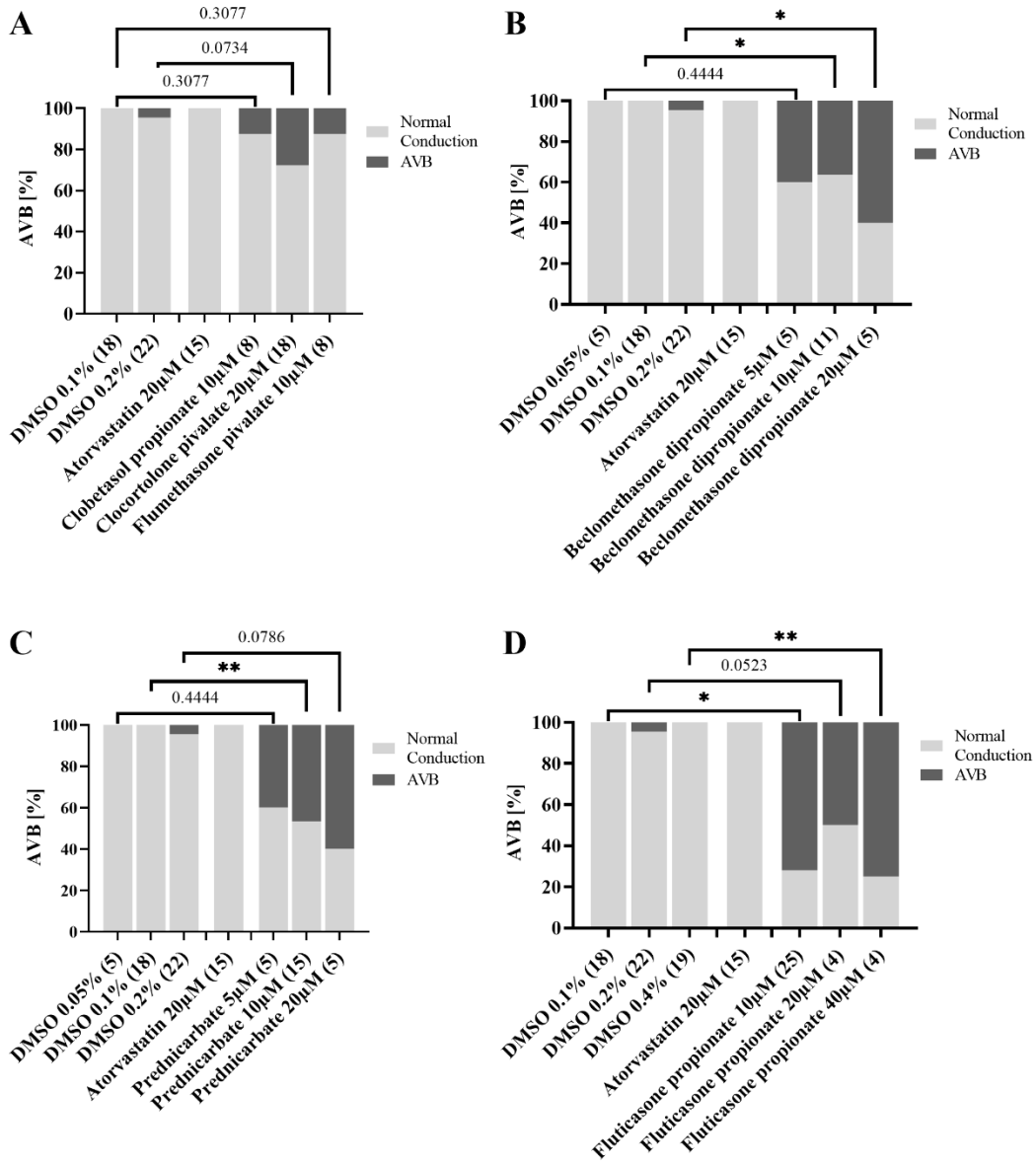

Figure 38: Atrioventricular Block (AVB) Detection Following NR3C1 Agonist Treatment

Overview of atrioventricular blocks (AVBs) induced by different NR3C1 agonists. **A**, Overview of various NR3C1 agonist, that were only tested at one concentration. **B**, Beclomethasone dipropionate significantly induced dose-dependent AVB. **C**, Overview of prednicarbate-induced dose-dependent AVB. **D**, AVBs induced by fluticasone propionate treatment. Statistics were performed with a two-sided Fishers' exact test. (ns) $P > 0.05$; (*) $P \leq 0.05$; (**) $P \leq 0.01$; (***) $P \leq 0.001$; (****) $P \leq 0.0001$

To summarize, treating zebrafish embryos with NR3C1 agonists led to tachycardia, increased area of max contraction in both heart chambers and tendencies to reduced EF and relative contractility in the atrium and ventricle, in addition to a tendentially reduced HS.

6.4.3.2 *nr3c1* Expression in Zebrafish

After identifying Nr3c1 as a significant target cluster and the analysis of heartbeats showing that the proteins upregulation results in AVB, an expression analysis was performed. To visualize the expression patterns of *nr3c1* in zebrafish embryos, we used WISH, as shown in (Figure 39).

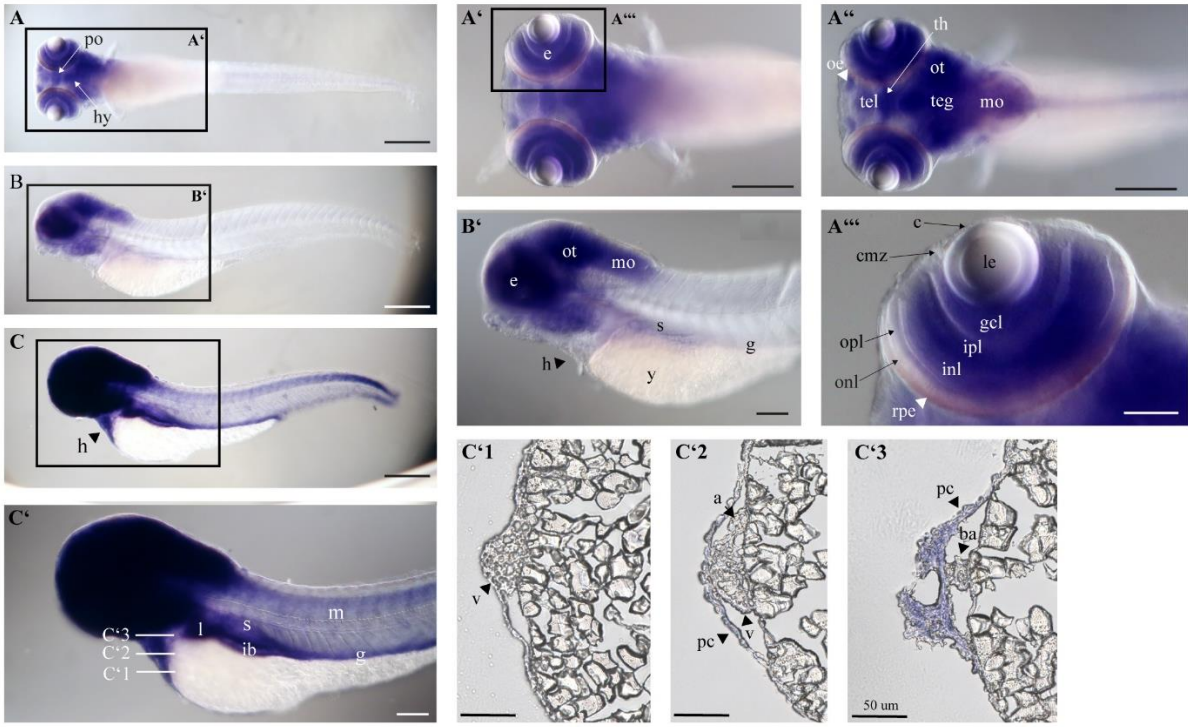

Figure 39: *nr3c1* Expression in Zebrafish 5 dpf

A-C, *In situ* stained zebrafish embryos at 5 dpf displaying *nr3c1* expression. **A''**, Dorsal view displays expression in the eyes, brain and notochord. **A'''**, 20x magnification of the retina. **C-C'**, Longer staining revealed expression of *nr3c1* in the heart, intestinal bulb, liver and myotomes. **C1-C3**, Cryo-slices of overstained *nr3c1* whole-mount *in situs* 5 dpf. Their depth is indicated with lines in displayed in **C'**. *nr3c1* is expressed in the tissue of the pericardial cavity, *bulbus arteriosus* (**C'3**), atrium and upper area of the ventricle (**C'2**). **A, A'** & **A''**, ventral view. **C-C'** & **C1-C3**, 24 h *in situ* hybridization staining. (a) atrium, (ba) bulbus arteriosus, (c) cornea, (cmz) ciliary marginal zone, (e) eye, (g) gut, (gcl) retinal ganglion cell layer, (h) heart, (hy) hypothalamus, (ib) intestinal bulb,(inl) retinal inner nuclear layer, (ipl) retinal inner plexiform layer, (l) liver, (le) lens, (m) myotomes, (mo) medulla oblongata, (ob) olfactory endothelium, (onl) outer nuclear layer, (opl) outer plexiform layer, (ot) optic tectum, (s) swim bladder, (tel) telencephalon, (teg) tegmentum, (th) thalamus, (pc) pericardial cavity, (po) preoptic area, (rpe) retinal pigmented epithelium, (v) ventricle, (y) yolk; **A-C**, **A'-C' & A''** scale bar = 100 µm; **A''' & C1-C3** scale bar = 50 µm. Images were improved with Fiji using the white-balance script described in 9.4.1.2.

The expression of *nr3c1* was detected in various organs such as the eyes, heart, intestine, liver, and swim bladder. In addition, lower expression was observed in the myotomes, which became visible after an extended staining process. A close-up of the eye 5 dpf (Figure 39 A''') revealed that *nr3c1* is present in the retina's IPL, INL, and outer plexiform layer (OPL), but not in the cornea, lens,

ciliary marginal zone, retinal GCL, ONL, and pigmented epithelium. Moreover, *nr3c1* was expressed in most areas of the brain, with stronger expression in the medulla oblongata, olfactory endothelium, hypothalamus, optic tectum, tegmentum, telencephalon, and thalamus (Figure 39 A & A'').

In Figure 39 B' a transparent staining of the heart was observed, prompting an increased exposure time to 24 h (Figure 39 C). However, even with the increased exposure, the expression of *nr3c1* in the heart could not be proven beyond reasonable doubt. Some hearts of embryos at 5 dpf displayed an entrapment rather than a stain of the tissue (data not shown). For this reason, WISH-stained embryos were sectioned horizontally through the frontal plane (Figure 39 C1-C3) and imaged, revealing expression in the atrium and BA, as well as in the wall of the pericardial cavity, but no expression was detected in the lower ventricle of the embryos.

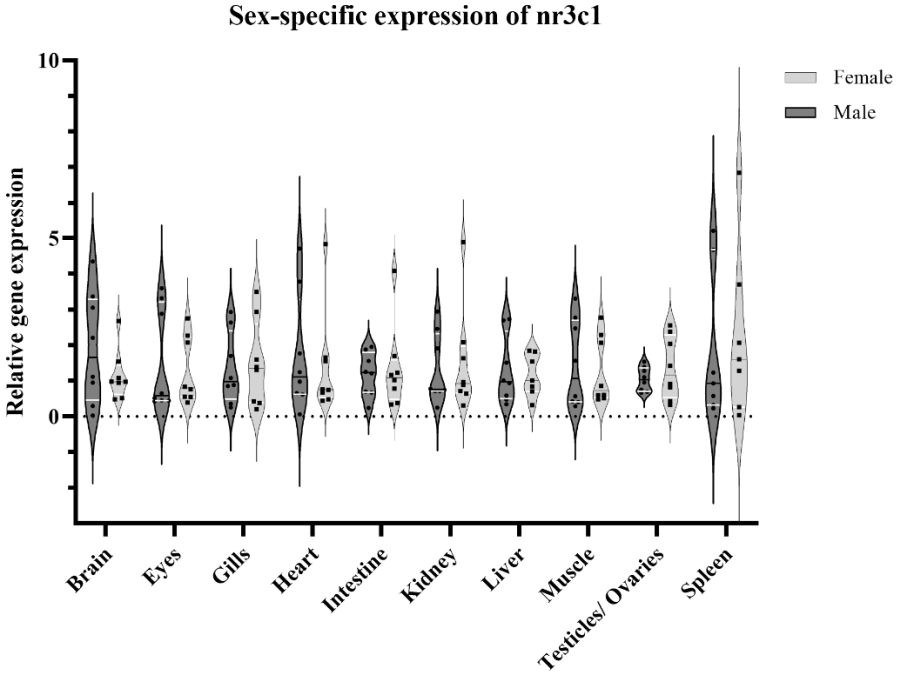

Figure 40: Sex-Specific Expression of *nr3c1*
Violin plot displays baseline sex- and organ-specific gene expression of *nr3c1* in adult AB WT zebrafish. Data was normalized against the housekeeping gene 18s ribosomal RNA. Black lines within the violin plot represent the median, while white lines represent the quartiles. mean±SD, n = 8.

After conducting baseline expression analysis in adult zebrafish, an almost ubiquitous *nr3c1* expression was detected in different tissues of both male and female fish. RT-qPCR CT values were normalized against the HKG 18s ribosomal RNA (18s), which was determined to be one of the most stable HKGs across tissues according to McCurley and Callard (2008) (192). In the male brain, the data was highly varied with a mean of 2.27±1.16, while in females, the expression was more

consistent with a mean of 1.06±0.17. The expression of *nr3c1* in the eyes of males (1.01±0.08, SD) and females (1.04±0.13, SD) was almost equal. Females showed an expression of *nr3c1* in the gills with a mean of 1.29±0.37, while males had a mean of 1.15±0.27. The male heart exhibited greater heterogeneity with a mean of 1.42±0.4, SD, while the female heart data was more consistent with a mean of 1.03±0.11. For the intestine, the fish were not fed for one day before they were sacrificed and the distribution of gut expression data in male (1.27±0.35, SD) and female (1.15±0.28, SD) zebrafish were found similar to other tissues. Moreover, mean relative expression of *nr3c1* in male and female kidneys, livers, muscle tissues and reproductive systems was similar between sexes. Muscle tissues in male zebrafish presented the second-largest SD of all male samples (1.21±0.44, SD). Female muscle tissues showed a relative gene expression of 1.02 with an SD of 0.11. In this dataset, the ovaries showed the second-largest SD. The largest SD was observed in female spleen tissues (2.73±1.34, SD). Male spleen tissues displayed a relative *nr3c1* expression of 1.13±0.24 SD. However, none of the data presented significances in a multiple unpaired t-test.

6.4.3.3 Potential Phenotype-Causing Targets Regulated by NR3C1

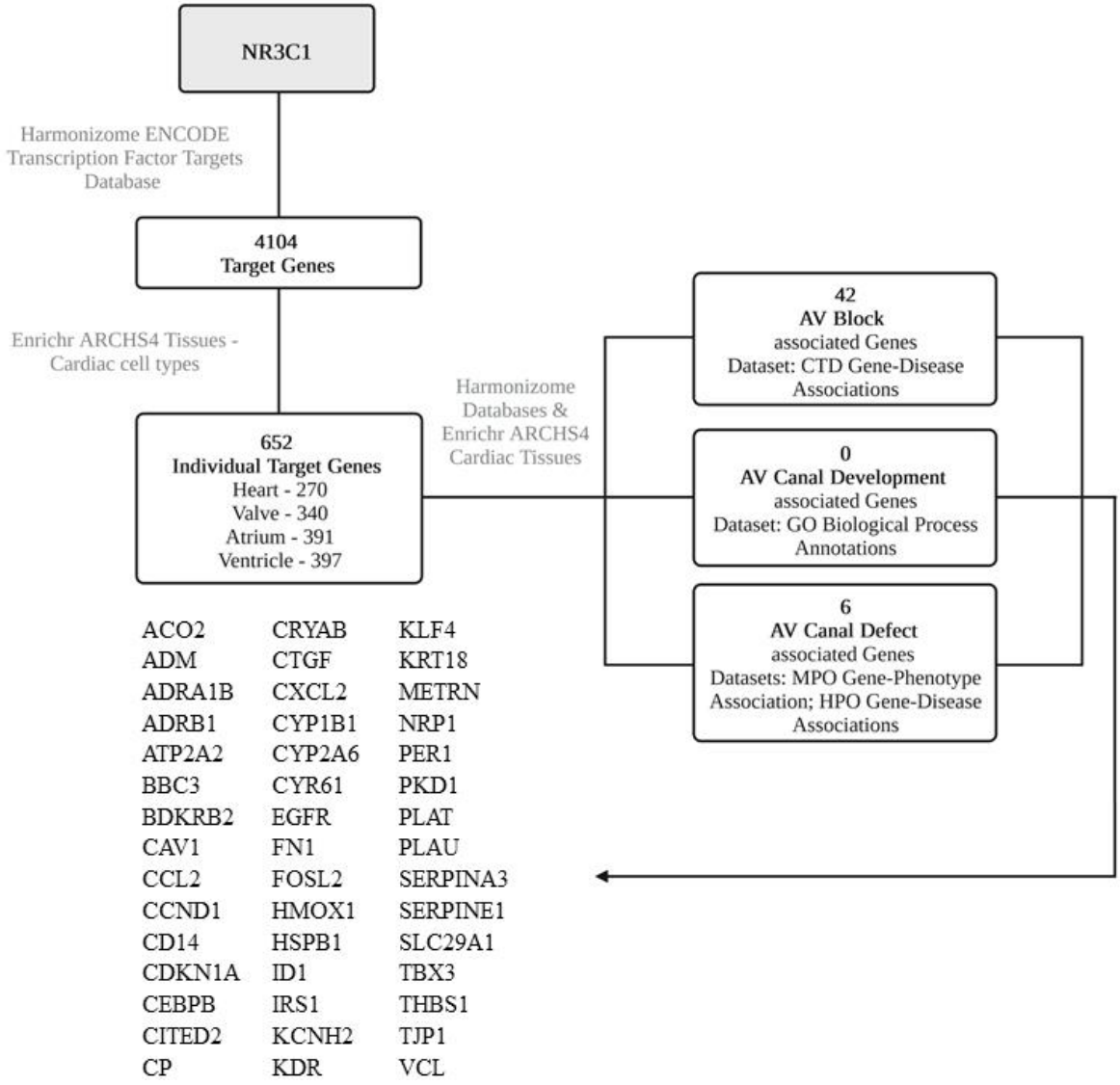

Figure 41: NR3C1 Harmonizome and Enrichr Gene Target Identification

Potential targets of the transcription factor NR3C1 were identified using Harmonizome and Enrichr. NR3C1 targets 4104 genes, 652 of them are expressed in the heart and 45 of them are known to be disease causing in humans and mammals. This image was created using BioRender.

Entering NR3C1 into Harmonizome (279) using the Encyclopedia of DNA Elements (ENCODE) Transcription Factor Targets Database provided 4104 target genes in the whole body. To narrow down the search, Enrichr (280) was utilized to filter for genes expressed in the heart using the All RNA-seq and CHIP-seq Sample Search Space (ARCHS4) Tissues Databank. As this databank contains datasets from various studies, heart tissues such as the heart, valve, atrium, and ventricle had to be selected individually. From the resulting NR3C1 regulated genes in these four datasets,

duplicates were removed and a new set of 652 individual target genes was generated. Harmonizome was then used to search for phenotypes related to development and disease, leading to the identification of 48 disease-related genes regulated by NR3C1. Combined, these datasets provide a total of 45 individual disease related genes that could be responsible for the phenotypes in zebrafish caused by NR3C1 agonists. The data mining platform Model organism Aggregated Resources for Rare Variant ExpLoration V1.2 (MARRVEL^2) (281), predicted orthologues from the Drosophila RNAi Screening Center Integrative Ortholog Prediction Tool (DIOPT) (282) and the DIOPT score were used to determine the likelihood of zebrafish target genes to be orthologous to human genes. One example is the BCL2-binding component 3 (BBC3), which was predicted by two out of 15 tools to have at least one orthologue in zebrafish. However, due to medium confidence and low evidence, it will be considered uncertain as a disease-causing gene (Supplementary Table 8). To validate potential phenotype-causing targets, one compound with low confidence was removed. MARRVEL2 (last accessed 02/21/2023) was then used to search for the gene name and associated cardiac phenotypes. The cardiac phenotypes of mammalian models such as mice were listed in Supplementary Table 9. Genes that yielded no search results were removed. Gene-searches that provided data only for non-mammalian animal models were listed in Supplementary Table 10. Further, phenotypes associated with the listed genes, that concur with findings from this study, were highlighted with bold text.

6.4.4 *In silico* Protein Modeling of Human and Zebrafish NR3C1/Nr3c1 (hGR1 & zfGR1)

The steroid receptor family includes the GC receptor NR3C1, the mineralocorticoid receptor (MR), androgen receptor and progesterone receptor. These receptors bind to cholesterol derivates (198). NR3C1 is comprised of four domains: the NTD (AA 1-427), the central DBD (AA 428-488), the C-terminal LBD (AA 528-777) and the hinge region (AA 489-527) separating DBD and LBD (Figure 34) (283). The NTD contains the ligand-independent constitutive transcriptional activation function 1 (AF1) and is crucial for transcription initiation (283,284). Moreover, this domain is the most variable domain in nuclear receptors across different species (284). The DBD contains two highly conserved zinc finger motifs and is required for DNA binding and NR3C1 dimerization. The hinge region between DBD and LBD enables structural flexibility between NR3C1 dimers and palindromic GC response elements (GREs) (283). Embedded into the LBD is the ligand-dependent transcriptional AF2 domain (285). Furthermore, the LBD forms a three-layered α-helical fold that forms the ligand binding pocket enclosing natural ligands and compounds. The steroid receptor family plays a critical role in essential processes, such as development and stress response (286).

Therefore, steroid receptors are prominent drug targets. However, many of these compounds cause target-related side effects, limiting their use for patients. Thus, existing drugs need to be studied more comprehensively *in vivo, in vitro* and *in silico*. The latter can improve the knowledge of protein-ligand interactions and can thereby be used to assess transferability of findings in animal models for human patients.

As previously described, human and zebrafish NR3C1 share a high similarity; therefore, *in silico* protein-ligand interaction analysis was determined suitable to assess protein-ligand docking likelihood (Figure 34) (287).

6.4.4.1 Proof of Concept and Method Establishment

To identify the most reliable protein model to test hit compounds from the previously described drug screening, different NR3C1 structures with co-crystallized ligands were tested (Figure 42).

The five NR3C1 protein crystal structures in agonistic conformation and their co-crystallized steroidal agonists were selected from 44 different crystallographic structures using the search term "NR3C1" on the US data center for the global Protein Data Bank (PDB) archive (196,197), filtered for *Homo sapiens* crystallographic structures and non-DNA-bound structures with a resolution lower than 3 Å. A proof of concept for ligand docking was performed using the steroidal agonists budesonide, desisobutyrylciclesonide, dexamethasone, FCP and mometasone furoate (Supplementary Table 11). Each ligand was docked into each NR3C1 protein structure and compared to the co-crystallized structure of the respective ligand.

The selected X-ray crystal structures had a resolution between 1.8 Å and 2.84 Å. Docking with flexible Glide XP docking showed, that 3CLD (219) was the most reliable NR3C1 structure with a mean RMSDs of 0.77 Å (Figure 42 A). Visual inspection of the results showed that all compounds were docked in the correct conformation, and single RMSDs for the test ligands did not vary greatly. Dexamethasone, originally co-crystalized with the 4UCD crystal structure (198), showed the best docking results to the 3CLD protein (0.51 Å) (Figure 42). While 4UDD (198) had the highest resolution of 1.8 Å, all compounds but desisobutyrylciclesonide (198) were incorrectly docked into the binding pocket via flexible Glide XP docking. Therefore, a second docking program XP IFD was tested for improved docking results. Here, 3CLD also yielded the best mean RMSD of 0.81 Å (Figure 42 B). Momethasone fumarate (288) together with dexamethasone (198) presented the best RMSDs for docking with 3CLD. 4P6W (288) showed the highest mean RMSD of all IFD docking scores (1.21 Å) (Figure 42 B). Furthermore, XP IFD with 4P6W showed the greatest variation in performance for the test ligands. Among the test ligands, dexamethasone displayed the lowest

RMSD (0.85 Å), while the 5NFP co-crystallized ligand budesonide (289) showed the highest RMSD (1.78 Å).

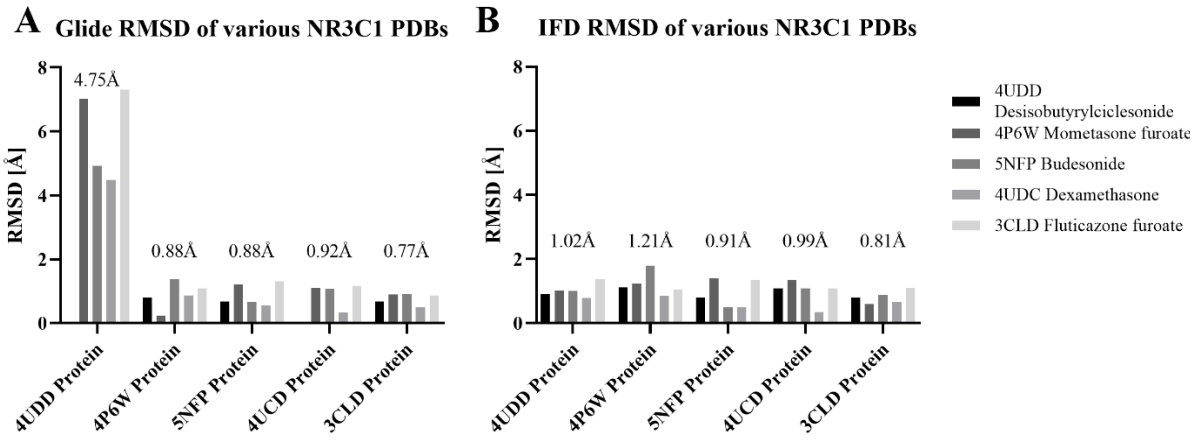

Figure 42: Selection of NR3C1 Structures and Docking Method

RMSD of all protein-ligand complex combinations were compared to the original co-crystallized structures after Glide XP docking (**A**) or IFD XP (**B**), respectively, to identify the most suitable protein structure to test hit compounds. Here, the 3CLD protein performed best in both docking approaches.

(IFD) Induced Fit Docking; (PDB) Protein Data Bank; (RMSD) Root-mean-square deviation; (XP) extra precision

Glide XP docking was able to provide reliable docking results; however, not all ligands were docked in the correct conformation, and not all ligands were docked into the binding pocket (missing bars in Figure 42 A). In contrast, the XP IFD approach was able to dock all ligands correctly into the respective binding pockets. Therefore, XP IFD was selected as a docking method to test the NR3C1 agonists identified in the zebrafish drug screening (Figure 42 B).

The 3CLD protein structure showed the lowest mean RMSDs for both docking approaches, demonstrating a high precision. Therefore, the 3CLD protein was used for docking studies with the PDL hit ligands. The 3CLD protein structure will be referred to as human GC receptor 1 (hGR1).

6.4.4.2 3D Structure Modeling

There are three existing methods for protein structure prediction: *de novo*, threading and comparative modeling. Here, comparative modeling was utilized. This method assumes that evolutionary similar sequences have similar 3D structures. It models the target protein based on structurally similar template proteins.

Schrödinger homology modeling was used to generate a zebrafish protein based on the UniProt FASTA sequence Q1XHK0, encoding Nr3c1 (209), as AlphaFold (204,205) was not able to provide

a zebrafish Nr3c1 structure (19/09/2022). The search result yielded several homologous proteins, the first ten are listed in Supplementary Table 12. Here, the AncGR2 in complex with dexamethasone (3GN8_B) (211) showed a high homology with no gaps and a significant E-value. Therefore, 3GN8_B was selected for homology modeling with the ligand included to model the agonistic state with a steroidal agonist (Figure 43 A). From here on out, this homology model will be referred to as zfGR1. Most of the models' full residue conformation was copied from the template. Due to the high homology, most residues were identical to the template (Figure 43 A, dark blue ribbon). For some residues, only the backbone conformation was copied from the template, as a sidechain mutation was found at this position (Figure 43 A, cyan ribbon). No residue positions had to be predicted.

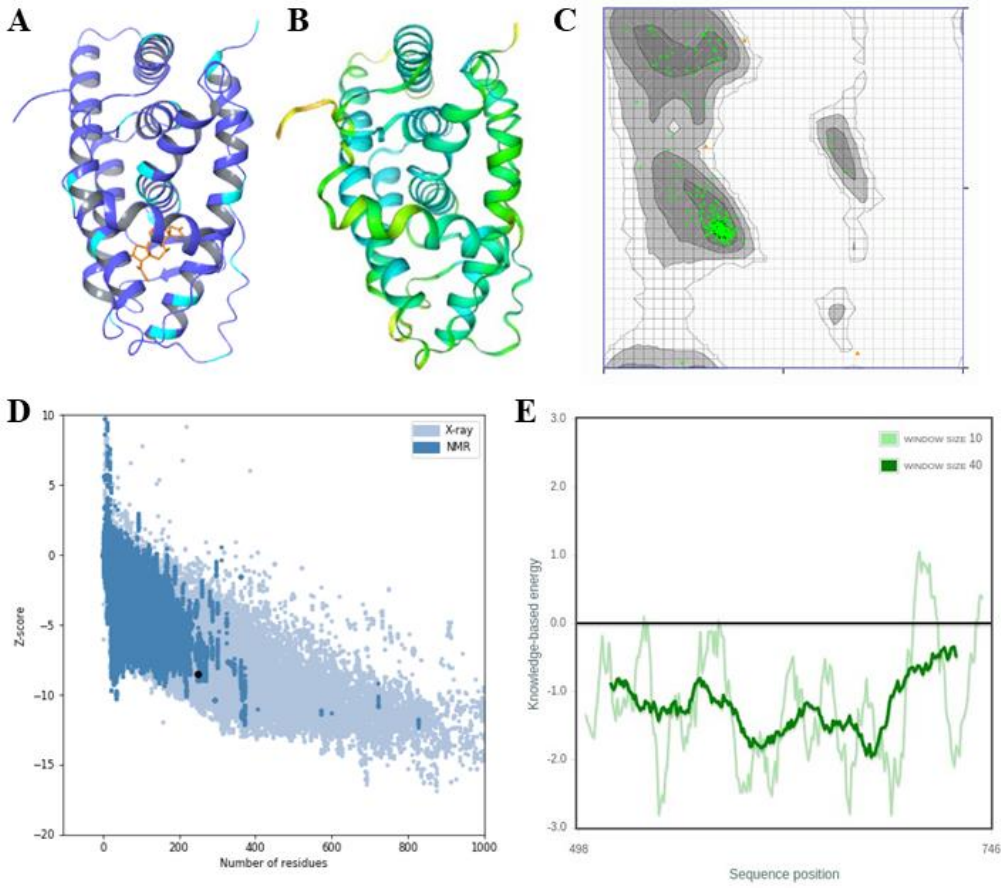

Figure 43: Quality Assessment of the zfGR1 Homology Model

A, zfGR1 Homology model based on the 3GN8 AncGR2 crystal structure with co-crystallized dexamethasone. Blue indicates that the full residue conformation was copied from the template; Cyan indicates that the residue backbone conformation was reproduced from the template to model the mutations accordingly. **B**, TopScore residue 3D assessment of zfGr1. Blue regions correspond to high-quality, and red regions to low-quality areas.; **C**, Ramachandran Plot of zfGr1 (217) demonstrates highly preferred

observations of 98.67% indicated by green crosses. Brown triangles represent preferred observations, here a total of 1.33%. Grey to black hues indicate highly preferred conformations with Delta > = -2, while white with a grey grid indicates questionable conformations with Delta < -4. **D** & **E**, ProSA-web protein structure analysis (290) confirmed the quality of zfGR1. **D**, The z-score of -8.56 is within the range of X-ray (bright blue) and NMR (dark blue) structures of native proteins of similar size. **E**, Local model quality shows a stable protein without erroneous parts within zfGR1.

The homology model was validated with a Ramachandran Plot from the Ramachandran Plot Server (217) (Figure 43 C). 98.67% of the AA demonstrated highly preferred conformations, and 1.33% showed preferred conformations. No questionable conformations were observed. Additionally, zfGR1 was validated using ProSA-web (290) for protein structure analysis Figure 43 D-E). The z-score of -8.56 is within the range of scores of native proteins' NMR and X-ray structures of similar size. Furthermore, this analysis showed that the models' quality is high, without erroneous parts within zfGR1 as the knowledge-based energy has a score lower than 0. Finally, the 3D structure of zfGR1 was verified with the meta Model Quality Assessment Program (meta-MQAP) TopScore (213). Thus, low scores correspond to low estimated error and thereby to high quality (Figure 43 B, blue/cyan). zfGR1 scored a TopScore of 0.3566 and a TopScoreSingle of 0.391, confirming previous analysis results for a good quality model.

6.4.4.3 IFD of NR3C1 Agonists into Selected Models

The previously established method of XP IFD was applied to hGR1 and zfGR1 in combination with the previously identified significant agonists for NR3C1 (Table 38). The steroid-ligand binding mechanism includes hydrophobic interactions and h-bonds in the LBT region. The XP IFD docking scores for ligands docked into zfGR1 ranged between -17.03 and -12.54, while the ligands XP IFD docking scores in hGR1 ranged from -16.63 to -13.87 (Table 38). Furthermore, all hydrophobic interactions are listed in Table 38. XP IFD was able to dock all ligands correctly into the binding pocket of zfGR1 and hGR1. The docking score of IFD can be utilized to prioritize compounds based on their likelihood of binding for each model.

Ranking correlation of the 12 Nr3c1 agonists with hGR1 and zfGR1 was performed by ranking IF docking scores from the lowest to the highest score for both receptors individually and correlating the data with a non-parametric Spearman r correlation (Figure 43). This correlation demonstrated a Spearman r correlation coefficient of 0.678, implying a moderate correlation between ranks with a significance of $p = 0.019$. In detail, this analysis revealed that flumethasone ranks in the first quartile for both models. In humans, flumethasone, FMP and fluocinolone acetonide (FCA) rank in the first quartile, while in zebrafish, amcinonide, ciclesonide and flumethasone rank in the first quartile. In

the first tierce, amcinonide, flumethasone and FMP show a ranking correlation between hGR1 and zfGR1. However, there is one outlier: FCA. It was third-ranked for docking in hGR but only ranked fifth for zfGR1 docking (Figure 43).

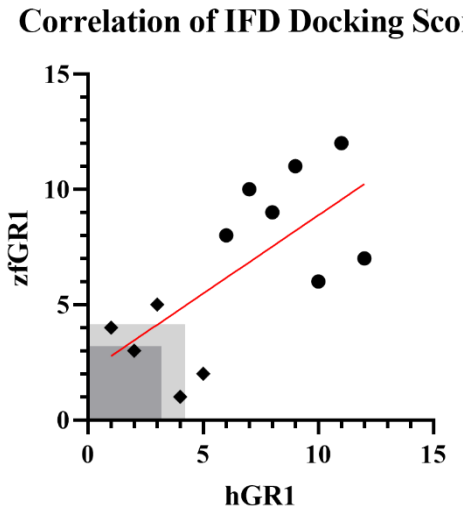

Figure 44: Ranking Correlation of IF Docking for hGR1 and zfGR1
Ranked IFD docking scores of hGR1 and zGR1 were correlated to identify the best candidates for further studies. Five compounds were identified within the first tierce of the data (diamond shape): Amcinonide, ciclesonide, flumethasone, flumethasone pivalate and fluocinolone acetonide. Data correlates with p = 0.019 and Spearman r = 0.678. Dark gray box = first quartile; light gray box = first tierce; diamond shape = data of first tierce; red line = Spearman r correlation

While docking results between hGR1 and zfGR1 significantly correlate, there are still differences between both models. Therefore, IFD docking poses of both models were aligned for the five highest ranked compounds and ribbons were color coded to visualize conserved (gray ribbons in Figure 45) and not conserved areas (colored ribbons in Figure 45) within the proteins. Different colors of the ligands serve merely for better visual differentiation. Observation of the different ligands within the models shows that AAs within the binding pocket are highly conserved. Mutations within other areas of the protein did not result in conformational changes that may affect the binding pocket and thereby, the binding affinity.

Table 38: Hit Compound Docking Overview

Compound	*IF (XP) Docking (hGR1)*	*IFD Score*	*Interaction sites (XP) (H-bonds)*	*Hydrophobic interaction sites (XP)*	*IF (XP) Docking (zfGR1)*	*IFD Score*	*Interaction sites (XP) (H-bonds)*	*Hydrophobic interaction sites (XP)*	*Structure*
Amcinonide	-15.852	-579.35	Asn^{564}, Gln^{570}, Arg^{611}, Tyr^{735}, Thr^{739}, Phe^{749}	Ile^{559}, Met^{560}, Leu^{563}, Leu^{566}, Val^{571}, Trp^{600}, Met^{601}, Met^{604}, Ala^{605}, Leu^{608}, Met^{639}, Cys^{643}, Met^{646}, Leu^{732}, Tyr^{735}, Cys^{736}, Phe^{740}, Met^{745}, Ile^{747}, Phe^{749}, Leu^{753}	-17.300	-454.40	Leu^{532}, Asn^{533}, Gln^{539}, Cys^{705}, Thr^{708}, Phe^{718}	Leu^{528}, Met^{529}, Leu^{532}, Leu^{535}, Val^{540}, Trp^{569}, Leu^{570}, Met^{573}, Leu^{577}, Phe^{592}, Met^{608}, Cys^{612}, Met^{615}, Val^{698}, Leu^{701}, Leu^{702}, Phe^{704}, Cys^{705}, Val^{716}, Phe^{718}, Leu^{722}, Ile^{726}	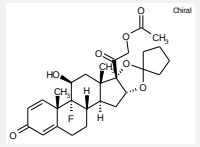
Ciclesonide	-15.656	-585.24	Asn^{564}, Gln^{570}, Tyr^{735}	Trp^{557}, Ile^{559}, Met^{560}, Leu^{563}, Leu^{566}, Val^{571}, Trp^{600}, Met^{601}, Met^{604}, Ala^{605}, Leu^{608}, Ile^{629}, Met^{639}, Tyr^{640}, Cys^{643}, Met^{646}, Leu^{732}, Leu^{733}, Tyr^{735}, Cys^{736}, Phe^{740}, Met^{745}, Ile^{747}, Phe^{749}, Leu^{753}	-16.106	-452.19	Asn^{533}, Gln^{539}, Cys^{705}	Leu^{528}, Met^{529}, Leu^{532}, Leu^{535}, Val^{540}, Trp^{569}, Leu^{570}, Met^{573}, Leu^{577}, Leu^{590}, Phe^{592}, Ile^{598}, Met^{608}, Cys^{612}, Met^{615}, Leu^{701}, Leu^{702}, Phe^{704}, Cys^{705}, Phe^{709}, Val^{716}, Phe^{718}, Leu^{722}, Ile^{726}	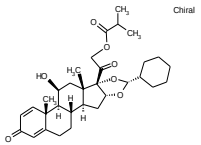
Flumethasone pivalate	-16.626	-587.58	Asn^{564}, Gln^{570}, Arg^{611}, Gln^{642}	Trp^{557}, Met^{560}, Leu^{563}, Leu^{566}, Trp^{600}, Met^{601}, Met^{604}, Ala^{605}, Ala^{607}, Leu^{608}, Phe^{623}, Met^{646}, Leu^{732}, Leu^{733}, Tyr^{735}, Cys^{736}, Met^{745}, Ile^{747}, Phe^{749}, Leu^{753}	-15.665	-452.60	Asn^{533}, Gln^{539}, Gln^{611}, Phe^{704}	Leu^{528}, Met^{529}, Leu^{532}, Leu^{535}, Val^{540}, Trp^{569}, Leu^{570}, Met^{573}, Leu^{577}, Phe^{592}, Tyr^{607}, Met^{608}, Cys^{612}, Met^{615}, Val^{698}, Leu^{701}, Leu^{702}, Phe^{704}, Cys^{705}, Val^{716}, Phe^{718}, Leu^{722}, Ile^{726}	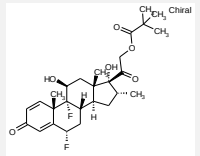

Flumethasone	-16.393	-579.60	Asn^{564}, Gln^{570}, Arg^{611}, Thr^{739}	Met^{560}, Leu^{563}, Leu^{566}, Val^{571}, Trp^{600}, Met^{601}, Met^{604}, Ala^{605}, Leu^{608}, Phe^{623}, Met^{639}, Cys^{643}, Met^{646}, Leu^{732}, Leu^{733}, Tyr^{735}, Cys^{736}, Ile^{747}, Phe^{749}, Leu^{753}, Ile^{757}	-15.658	-446.95	Asn^{533}, Arg^{580}, Gln^{611}, Thr^{708}, Phe^{704}	Met^{529}, Leu^{532}, Leu^{535}, Val^{540}, Trp^{569}, Leu^{570}, Met^{573}, Leu^{577}, Phe^{592}, Met^{608}, Met^{615}, Leu^{701}, Leu^{702}, Phe^{704}, Cys^{705}, Val^{716}, Phe^{718}, Leu^{722}	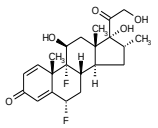
Fluocinolone acetonide	-16.293	-577.90	Asn^{564}, Gln^{570}, Arg^{611}, Tyr^{735}	Ile^{559}, Met^{560}, Leu^{563}, Leu^{566}, Trp^{600}, Met^{601}, Met^{604}, Ala^{605}, Leu^{608}, Phe^{623}, Met^{639}, Cys^{643}, Met^{646}, Leu^{732}, Tyr^{735}, Cys^{736}, Ile^{747}, Phe^{749}, Leu^{753}	-14.913	-448.8	Asn^{533}, Arg^{580}, Thr^{708}, Phe^{718}	Met^{529}, Leu^{532}, Leu^{535}, Val^{540}, Trp^{569}, Leu^{570}, Met^{573}, Leu^{577}, Phe^{592}, Met^{608}, Met^{615}, Leu^{701}, Leu^{702}, Phe^{704}, Cys^{705}, Phe^{706}, Phe^{709}, Val^{716}, Phe^{718}, Leu^{722}, Ile^{726}	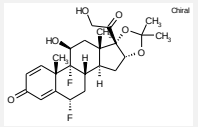
Desonide	-14.622	-580.17	Asn^{564}, Gln^{570}, Arg^{611}	Met^{560}, Leu^{563}, Leu^{566}, Trp^{600}, Met^{601}, Met^{604}, Ala^{605}, Leu^{608}, Phe^{623}, Met^{639}, Cys^{643}, Leu^{732}, Tyr^{735}, Cys^{736}, Phe^{740}, Ile^{747}, Phe^{749}, Leu^{753}	-14.177	-445.99	Asn^{533}, Gln^{539}, Thr^{708}, Phe^{704}	Met^{529}, Leu^{532}, Leu^{535}, Val^{540}, Trp^{569}, Leu^{570}, Met^{573}, Leu^{577}, Phe^{592}, Met^{608}, Cys^{612}, Met^{615}, Val^{698}, Leu^{701}, Leu^{702}, Phe^{704}, Cys^{705}, Phe^{709}, Val^{716}, Phe^{718}, Leu^{722}, Ile^{726}	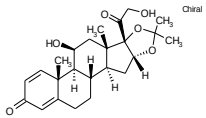
Betamethasone	-13.870	-576.61	Asn^{564}, Gln^{570}, Thr^{739}	Met^{560}, Leu^{563}, Leu^{566}, Val^{571}, Trp^{600}, Met^{601}, Met^{604}, Ala^{605}, Leu^{608}, Phe^{623}, Met^{646}, Leu^{732}, Leu^{733}, Tyr^{735}, Cys^{736}, Ile^{747}, Phe^{749}, Leu^{753}	-14.177	-445.99	Asn^{533}, Arg^{580}, Gln^{611}, Thr^{708}	Met^{529}, Leu^{532}, Leu^{535}, Val^{540}, Trp^{569}, Leu^{570}, Met^{573}, Leu^{577}, Phe^{592}, Met^{608}, Met^{615}, Leu^{701}, Leu^{702}, Phe^{704}, Cys^{705}, Val^{716}, Phe^{718}, Leu^{722}	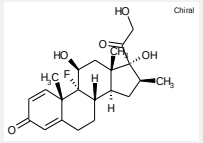

Prednicarbate	-15.530	-582.49	Asn^{564}, Gln^{570}, Arg^{611}	Trp^{557}, Ile^{559}, Met^{560}, Leu^{563}, Leu^{566}, Trp^{600}, Met^{601}, Met^{604}, Ala^{605}, Ala^{607}, Leu^{608}, Met^{639}, Cys^{643}, Met^{646}, Leu^{732}, Leu^{733}, Tyr^{735}, Cys^{736}	-14.148	-452.47	Asn^{533}, Gln^{539}, Arg^{580}, Cys^{705}	Leu^{528}, Met^{529}, Leu^{532}, Leu^{535}, Val^{540}, Trp^{569}, Leu^{570}, Met^{573}, Leu^{577}, Leu^{590}, Phe^{592}, Leu^{596}, Ile^{598}, Met^{608}, Cys^{612}, Met^{615}, Val^{698}, Leu^{701}, Leu^{702}, Phe^{704}, Cys^{705}, Val^{716}, Phe^{718}, Leu^{722}, Ile^{726}	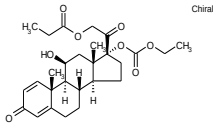
Fluticasone propionate	-14.788	-580.67	Asn^{564}, Gln^{570}	Ile^{559}, Met^{560}, Leu^{563}, Leu^{566}, Val^{571}, Trp^{600}, Met^{601}, Met^{604}, Ala^{605}, Leu^{608}, Met^{639}, Cys^{643}, Met^{646}, Leu^{732}, Leu^{733}, Tyr^{735}, Cys^{736}, Leu^{753}	-14.067	-449.81	Asn^{533}, Arg^{580}	Leu^{528}, Met^{529}, Leu^{532}, Leu^{535}, Val^{540}, Trp^{569}, Leu^{570}, Met^{573}, Leu^{577}, Phe^{592}, Ile^{598}, Tyr^{607}, Met^{608}, Cys^{612}, Met^{615}, Leu^{701}, Leu^{702}, Phe^{704}, Cys^{705}, Tyr^{707}, Leu^{714}, Val^{716}, Phe^{718}, Leu^{722}	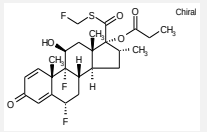
Clocortolone pivalate	-15.024	-582.52	Asn^{564}, Gln^{570}, Tyr^{735}	Ile^{559}, Met^{560}, Leu^{563}, Leu^{566}, Val^{571}, Trp^{600}, Met^{601}, Met^{604}, Ala^{605}, Leu^{608}, Phe^{623}, Ile^{629}, Met^{639}, Cys^{643}, Met^{646}, Leu^{732}, Leu^{733}, Tyr^{735}, Cys^{736}, Ile^{747}, Phe^{749}, Leu^{753}	-13.878	-455.54	Asn^{533}, Arg^{580}	Leu^{528}, Met^{529}, Leu^{532}, Leu^{535}, Val^{540}, Trp^{569}, Leu^{570}, Met^{573}, Leu^{577}, Leu^{590}, Phe^{592}, Ile^{598}, Tyr^{607}, Met^{608}, Cys^{612}, Met^{615}, Leu^{701}, Leu^{702}, Phe^{704}, Cys^{705}, Val^{716}, Phe^{718}, Leu^{722}, Ile^{726}	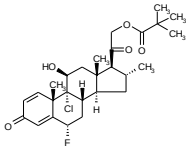
Alclometasone dipropionate	-14.750	-583.21	Asn^{564}, Gln^{570}, Arg^{611}	Ile^{559}, Met^{560}, Leu^{563}, Leu^{566}, Val^{571}, Trp^{600}, Met^{601}, Met^{604}, Ala^{605}, Ala^{607}, Leu^{608}, Ile^{629}, Met^{639}, Cys^{643}, Met^{646}, Leu^{732}, Leu^{733}, Tyr^{735}, Cys^{736}, Phe^{740}, Met^{745}, Ile^{747}, Phe^{749}	-13.404	-451.73	Asn^{533}, Arg^{580}	Met^{529}, Leu^{532}, Leu^{535}, Val^{540}, Trp^{569}, Leu^{570}, Met^{573}, Leu^{577}, Phe^{592}, Ile^{598}, Tyr^{607}, Met^{608}, Cys^{612}, Met^{615}, Val^{698}, Leu^{701}, Leu^{702}, Phe^{704}, Cys^{705}, Tyr^{707}, Leu^{714}, Val^{716}, Phe^{718}, Leu^{722}, Ile^{726}	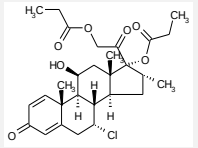

Deflazacort	-14.181	-580.22	Asn^{564}, Tyr^{735}	Arg^{611},	Trp^{557}, Leu^{566}, Met^{604}, Met^{639}, Leu^{733},	Ile^{559}, Val^{571}, Ala^{605}, Cys^{643}, Tyr^{735},	Met^{560}, Trp^{600}, Leu^{608}, Met^{646}, Cys^{736},	Leu^{563}, Met^{601}, Phe^{623}, Leu^{732}, Leu^{753}	-12.537	-454.32	Asn^{533}, Phe^{704}	Arg^{580},	Leu^{528}, Val^{540}, Leu^{577}, Cys^{612}, Leu^{702}, Phe^{718},	Met^{529}, Trp^{569}, Phe^{592}, Met^{615}, Phe^{704}, Leu^{722},	Leu^{532}, Leu^{570}, Tyr^{607}, Val^{698}, Cys^{705}, Ile^{726}	Leu^{535}, Met^{573}, Met^{608}, Leu^{701}, Val^{716},	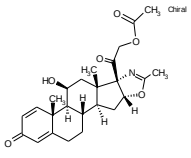

(IF) Induced fit; (IFD) induced fit docking; (XP) extra precision

Within zfGR1´s binding pocket, **amcinonide** forms 6 h-bonds. Amcinonide`s 11-hydroxyl group binds to the Leu^{532} keto group. Asn^{533} $N_{\delta 2}$-amino group binds to the keto group of the ligand's acetate. The 3-keto group forms an h-bond with the Gln^{539}´s $N_{\varepsilon 2}$-amino group. The thiol group of Cys^{705} forms an h-bond with the ligands 20-keto group. The $O_{\gamma 1}$ of Thr^{708} forms two h-bonds, one with the oxygen of the ligand's acetates group and one with the 20-keto group. Additionally, the ligand's acetates groups oxygen forms an aromatic bond to the C_{ζ}-carbon of Phe^{718}. In the hGR1, amcinonide only forms four h-bonds. Two h-bonds form between the 3-keto group of the ligand to Arg^{611} $N_{\eta 2}$- respectively Gln^{570} $N_{\varepsilon 2}$-amino group. Another h-bonds forms between the Asn^{564} $O_{\delta 1}$-keto group and the 11-hydroxyl group of the ligand. The last h-bond forms between the γ1-hydroxyl group of Thr^{739} and the keto group of the ligand's acetate. Additionally, amcinonide forms two more aromatic bonds with hGR1. Similar to zfGR1, one aromatic bond forms between the keto group of the ligand's acetate and the $C_{\varepsilon 2}$-carbon of Phe^{749}. The second aromatic bond connects the ligands 20-keto group with the $C_{\delta 2}$-carbon of Tyr^{735}. Both ligands display high IF docking scores; however, the zfGR1 amcinonide IF docking score is the highest of all Nr3c1 agonists due to its large number of h-bonds and hydrophobic interactions.

The zfGR1 Gln^{539} (respectively Gln^{570} in hGR1) $N_{\varepsilon 2}$-amino group forms an h-bond with **ciclesonide**`s 3-keto group. The ligands 11-hydroxyl group binds to the Asn^{533} (respectively Asn^{564} in hGR1) $O_{\delta 1}$-keto group. In zfGR1, the keto-group of the isobutyric acid residue of the ligand forms an h-bond with the thiol group of Cys^{705}; in hGR1, Asn^{564} forms an additional h-bond via the $N_{\delta 2}$-amino group with the same keto group.

In the zfGR1, the Asn^{533} $O_{\gamma 1}$-keto group binds to the 11-hydroxyl group of **FMP**. The Gln^{539} $N_{\varepsilon 2}$-amino group forms an h-bond with the 3-keto group, and the Gln^{611} $N_{\varepsilon 2}$-amino group interacts with the ligands 17-hydroxyl group. hGR1 forms an h-bond to FMP via the Asn^{564} $O_{\delta 1}$-keto group and ligands 11-hydroxyl group.

Flumethasone forms six h-bonds with zfGR1. The proteins Asn^{533} $O_{\delta 1}$-keto group binds to the ligands 11-hydroxyl group and 21-hydroxyl group. Thr^{708}'s $O_{\gamma 1}$-keto group binds to the ligands 20-keto group and 21-hydroxyl group. The 20-keto group also forms an aromatic bond with the Phe^{704} $C_{\delta 2}$-carbon group. Furthermore, Arg^{580} $N_{\eta 2}$-amino group binds to the ligands 3-keto group. In hGR1, flumethasone forms 5 h-bonds without any aromatic bonds. Similar to zfGR1, the Asn^{564} $O_{\delta 1}$-keto group binds to the 11-hydroxyl group, while the $N_{\delta 2}$-amino group binds to the ligands 20-keto group. The Thr^{739} $O_{\gamma 1}$-keto group forms an h-bond with the 21-hydroxyl group of flumethasone. Finally, the 3-keto group forms two h-bonds, one to the Arg^{611} $N_{\eta 2}$-amino group and the other to the Gln^{570} $N_{\varepsilon 2}$-amino group.

The zfGR1 forms h-bonds between the $N_{\gamma 2}$-amino group of the Asn^{533} with the 21-hydroxyl group of the ligand **FCA**; the $O_{\gamma 1}$-keto group of Asn^{533} with the ligands 11-hydroxyl group; $O_{\gamma 1}$-hydroxyl group of Thr^{708} with the ligands 21-hydroxyl group; and the amino group of Arg^{580} with the ligands 3-keto group. Furthermore, the 20-keto group of FCA builds 2 aromatic bonds with Phe^{718}, one with its $C_{\varepsilon 2}$-carbon and another with its C_{ζ}-carbon. The hGR1 Asn^{564} $O_{\delta 1}$-keto group forms two h-bonds, one with the 11- and one with the 21-hydroxyl group. The ligands 3-keto group binds to the $N_{\eta 2}$-amino group of Arg^{611} and the $N_{\varepsilon 2}$-amino group of Gln^{570}. Moreover, the ligand bonds to the zfGR1 Tyr^{735} $C_{\delta 2}$-carbon via an aromatic bond.

Docking of **desonide** into the zfGR1 homology model revealed four h-bonds and one aromatic bond. The zfGR1 Asn^{564} forms two h-bonds, one with its $O_{\delta 1}$-keto group to the ligands 11-hydroxyl group and the second one with its $N_{\eta 2}$-amino group with the ligands 21-hydroxyl group. Additionally. The Thr^{708} $O_{\gamma 1}$-keto group forms an h-bond with desonides 20-keto group. Finally, an aromatic bond forms between the zfGR1 Phe^{704} $C_{\delta 2}$-carbon and the ligands 17-keto group. In hGR1, desonide also forms four h-bonds and no aromatic bonds. hGR1s Asn^{533} $O_{\delta 1}$-keto group binds to desonides 11-hydroxyl group and 21-hydroxyl group. The ligands 3-keto group forms two h-bonds, one with the $N_{\varepsilon 2}$-amino group of Gln570 and the $N_{\eta 2}$-amino group of Arg^{611}.

Betamethasone forms five h-bonds with the zfGR1. The Arg^{580} $N_{\eta 2}$-amino group binds to the 3-keto group of the ligand. The $O_{\delta 1}$-keto group of Asn^{533} binds to the 11-hydroxyl group. Gln^{611}´s $O_{\varepsilon 1}$-keto group binds to the 17-hydroxyl group of betamethasone. The $O_{\gamma 1}$-hydroxyl group of Thr^{708} interacts with the 20-keto group and the 21-hydroxyl group of the ligand to form h-bonds. In the hGR1, betamethasone forms four h-bonds within the binding pocket. The Asn^{533} $O_{\delta 1}$-keto group binds to the ligands 11-hydroxyl group, while its $N_{\delta 2}$-amino group binds to its 21-hydroxyl group. This hydroxyl group also binds to the $O_{\gamma 1}$-hydroxyl group of Thr^{708}, similar to the zebrafish model. The Gln^{570} $N_{\varepsilon 2}$-amino group forms another h-bond to the 3-keto group of betamethasone.

PRC forms four h-bonds in zfGR1 and hGR1: the ligands 3-keto group interacts with the Arg^{580} $N_{\eta 1}$- (zfGR1) respectively Arg^{611} $N_{\eta 2}$- (hGR1) amino group and the Gln^{539} (hGR1 Gln^{570}) $N_{\varepsilon 2}$-amino group. In zfGR1, Asn^{533} binds to the keto group of the methyl propionate of the ligand. The thiol group of Cys^{705} binds to the 20-keto group of PRC. In hGR1 Asn^{564} forms two h-bonds: one with the $O_{\delta 1}$-keto group to the 11-hydroxyl group of the ligand and one with the $N_{\delta 2}$-amino group and the ligands methyl propionates keto group. IF docking scores for both protein-ligand interactions are ranked in the middle of all IF docking scores.

Alclometasone dipropionate, **deflazacort**, **FCP** and **CCP** form h-bonds with their 3-keto group and the zfGR1´s Arg^{580} $N_{\gamma 2}$-amino group as well as with its 11-hydroxyl group and the proteins

Asn^{533} $O_{\gamma 1}$-keto group. The only difference is that CCP forms h-bonds to two amino groups of Arg^{580} ($N_{\eta 1}$ and $N_{\eta 2}$) in zfGR1. In hGR1, CCP forms the same respective h-bonds, with the difference of Asn^{564} binding with its $O_{\delta 1}$-keto group. While CCP does not form aromatic bonds in zfGR1, in hGR1, it forms an aromatic bond between the ligands pivalate keto group and the Tyr^{735} $C_{\varepsilon 2}$-carbon. Alclometasone dipropionate and FCP form the same 11-hydroxyl group connection with the Asn^{564} $O_{\delta 1}$-keto group of hGR1. Both ligands also connect to the Gln^{570} $N_{\varepsilon 2}$-amino group via their 3-keto group. In the hGR1, Arg^{611} forms two h-bonds to the 3-keto group of the ligand via $N_{\eta 1}$ and $N_{\eta 2}$. Alclometasone dipropionate and FCP form no aromatic bonds in zfGR1. In hGR1, Arg^{611} $N_{\eta 2}$ forms an h-bond with deflazacort 3-keto group. The Asn^{564} forms two h-bonds: One via its $O_{\delta 1}$-keto group with the 11-hydroxyl group and the second with its $N_{\delta 2}$-amino group to the ligand's acetate keto group. Additionally, the zfGR1 Phe^{704} $C_{\varepsilon 2}$-carbon forms two aromatic bonds with the deflazacort acetate residues keto groups. In hGR1, deflazacort forms an aromatic bond with its 20-keto group and the hGr1 Tyr^{735} $C_{\delta 2}$-carbon.

Taken together, the 3-keto group and the 11-hydroxyl group of the ligands interact with the binding pocket of zfGR1. The AAs primarily involved in ligand binding are Asn^{533} and Arg^{580} (resp. Asn^{564} and Arg^{611}). Additionally, in hGR1 Gln^{570} is another essential AA in protein-ligand binding. Further, the following AAs are involved in hydrophic interactions in each hGR1 ligand binding: Met^{560}, Leu^{563}, Leu^{566}, Met^{601}, Met^{604}, Ala^{605}, Leu^{608}, Met^{646}, Leu^{732}, Tyr^{735}, Cys^{736} and Leu^{753}. In zGR1 there are 19 AAs involved in hydrophic interactions of each ligand binding: Met^{529}, Leu^{532}, Leu^{535}, Val^{540}, Trp^{569}, Leu^{570}, Met^{573}, Leu^{577}, Phe^{592}, Met^{608}, Met^{615}, Leu^{701}, Leu^{702}, Phe^{704}, Cys^{705}, Val^{716}, Phe^{718}, Leu^{722} and Ile^{726}.

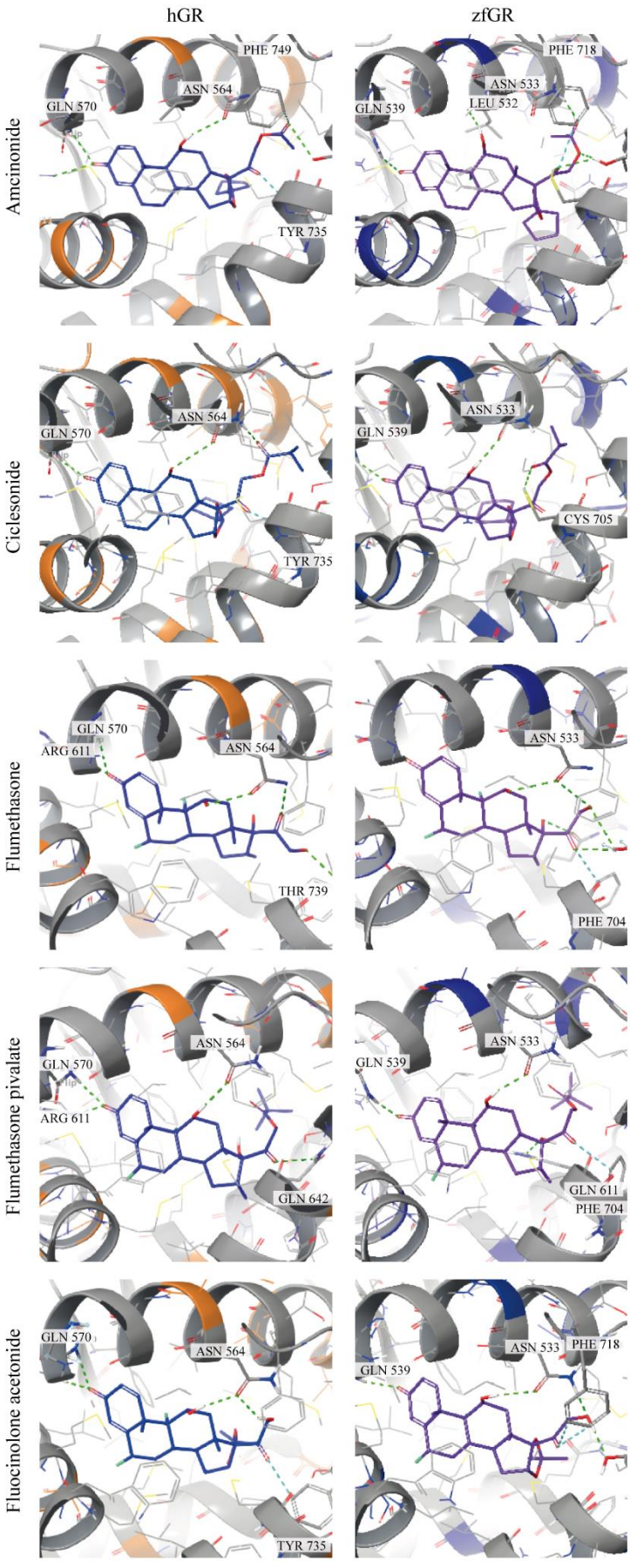

Figure 45: Compounds with Highest Ranked IF Docking Score Correlation

Ranked correlation of IF docking scores for zfGR and hGR revealed 5 compounds within the first tierce. Multiple alignment with the MultAlin (218) multiple sequence viewer of the 3CLD FASTA sequence of hGR with Q1XHK0 FASTA sequence of zfGR (Supplementary Figure 7) was used to determine conserved areas of the protein (gray ribbons). Not conserved areas labeled in color, show a highly conserved binding pocket within both protein structures. The protein structure is displayed as cartoon, while the ligand is displayed as stick. Hydrogens were hidden for clarity.
Orange ribbons = not conserved AAs of hGR1; blue ribbons = not conserved AAs of zfGR1; green dotted lines = intermolecular h-bonds; blue dotted lines = intermolecular aromatic h-bonds; (AA) amino acid

7 Discussion

CVDs continue to be one of the leading causes of death worldwide. Therefore, it is crucial to discover new therapeutic targets and treatments. Drug repurposing is becoming increasingly important to expedite the discovery of new drugs and make the process more cost-effective. However, one aspect of exposure to chemicals and pharmaceuticals in general during prenatal and postnatal periods is a possible negative impact on embryonic development. Therefore, assessment of toxicity in an embryonic animal model can provide valuable information regarding drug safety. Here, drug screenings were conducted that identified 11 compounds which alter the vasculature and 31 substances that alter heartbeat. This revealed Hrh1 and Nr3c1 as major target clusters.

7.1 Optimizing the Experimental Design for Zebrafish Drug Screening using the 3R Principle

To conduct this study, the PDL was chosen to screen for cardiovascular active compounds due to its high hit probability. A phenotype-based approach was utilized to identify novel drug targets and cardiovascular active compounds. This approach has been shown to yield reliable results as it observes the effect of a small molecule on a whole organism in a disease-relevant setting (92). Moreover, drugs that act through multiple targets, causing the desired phenotype, can be identified. However, the biggest challenge of phenotype-based drug screens is identifying targets. In this case, the PDL consists mainly of FDA-approved compounds with known targets and well-described side effects. This primary data was later used to identify targets and pathways potentially responsible for the observed phenotype.

Various pooling strategies, such as one-compound one-well, adaptive pooling, non-adaptive pooling, and orthogonal pooling, are available for screenings (224). However, the one-compound one-well strategy was chosen for ease of handling and analysis. Although this approach may produce false positive and false negative results, n = 6 was used to perform a quick screening and a CI of 90% instead of 95% was used to reduce false negatives when identifying hits.

In this study, zebrafish were selected as a model organism due to their small size, high scalability, complexity, evolutionary conserved physiology to humans, and well-established suitability for cardiovascular disease research. Zebrafish heart and vascular development is highly conserved, making them an ideal model for studying cardiovascular development and function in high-content screenings (29,93,291). The electrophysiological properties of human CMs are even more similar to zebrafish than to rodents (292). Moreover, zebrafish continue to develop without a functional

circulatory system (82), so even severe phenotypes can be observed *in vivo*. The application of compounds at different developmental stages can provide more information about the role of pathways in development and disease progression (130). Moreover, the effect of eight drug candidates identified in individual zebrafish screenings has been reproduced in follow-up studies (92,293–295). These points make zebrafish an ideal model for studying cardiac development and function in high-content screenings (93,296).

As part of the treatment itself, the compound uptake into the larval body must be considered. The first and most substantial barrier of a zebrafish embryo is the chorion. Depending on the compound, at least 0.1% DMSO is required to pass this barrier (134). Therefore, ideally, this barrier must be removed via chemical or manual dechorionation, which was part of the experimental design in this study. The second natural barrier is the larval skin that cannot be penetrated by all compounds. However, DMSO can solubilize compounds in water, increasing their bioavailability and allowing them to cross biological barriers without damage (75,134,135).

Next, the compound or in this case, drug library selection must be regarded critically. While commercially available smart libraries are well established for drug repurposing, their use creates a bias towards clinically active drugs. Therefore, often NSAIDs emerge as hits from zebrafish screens (130). This bias reduces the chance of new drug discoveries from various chemicals. In this study, an overrepresentation of therapeutic classes that dominate the PDL, such as central nervous system, cardiovascular system, metabolism and infectiology was mirrored in the distribution of unfiltered hit compounds as shown in Figure 18. However, about 45.5% of the hits represent the 30% of minor drug classes (Figure 8) and do not contain NSAIDs. Nevertheless, this screening aimed to identify targets rather than discover or re-purposing drugs. Therefore, the PDL was a suitable library to perform this screening.

Despite their advantages, zebrafish also have limitations that must be scrutinized. For example, their metabolism may be similar to mammals, but it differs in lipoprotein profile and low density lipid (LDL) makeup, and it lacks vitamin C synthesis (89,103,297). Another point to consider is the whole-genome duplication in teleosts that led to 20-30% of human genes having at least two zebrafish orthologues (298). The duplication often resulted in new or divided functionalities of the isoforms. This complicates the modeling of complex diseases such as AVB and other arrhythmias. Within cardiac cells, metabolism and pathways are highly conserved from zebrafish to humans; however, zebrafish only possess two heart chambers with a BA in contrast to a mammalian four-chambered heart. Moreover, current literature shows that zebrafish have no sophisticated AVN and

fast CS. Nonetheless, the AVC acts similarly to the AVN in slowing conduction (299). These limitations must be carefully considered for the study design and data interpretation.

In conclusion, this research employed a phenotype-based method that utilized the PDL to search for compounds with cardiovascular effects and to identify potential drug targets. Zebrafish were selected as a model organism due to their small size, scalability, and relevance to cardiovascular research. Their highly conserved vascular features and manner of heart development, as well as electrophysiological properties, make them ideal models for high-content screenings. This study's experimental design addressed the compound's penetrance into the larval body by removing the chorion barrier and using DMSO as a shuttle vector. Despite the limitations to consider, such as differences in metabolism and gene duplication in zebrafish, our research successfully identified targets linked to the observed phenotypes.

7.2 Drug Screening Proof of Concept

The screenings effectiveness and translatability to human patients was assessed to confirm the value of this research. The selected proof of concept compounds not only mirrored known side effects of human patients but also reproduced known side effects in zebrafish. For example, the competitive HMG-CoA inhibitor ATO (146) was previously shown to affect heart morphology and function dose-dependently (151). In line with the current literature, ATO induced mild bradycardia in the primary screen, altered heart morphology and induced developmental delay in this study (Figure 13). These findings were confirmed in a Tg(*myl7:eGFP*)$^{twu34/+}$ line, where ATO induced bradycardia chamber-specifically. However, observation of heartbeat videos did not indicate conduction defects. This can be explained by the developmental delay and deformities of the heart that prohibited proper chamber selection by *pyHeart4Fish*. As *pyHeart4Fish* detects chambers not only via user input but also via fluorescence intensity thresholds of the AVC, improper AVC development limits the quantification of heart parameters.

Enilconazole is a chemical that is frequently found in bodies of water and can have harmful effects on aquatic life over an extended period of time (300), thus, it was used as a toxic proof of concept compound. In 2022, Huan *et al.* published enilconazole-induced bradycardia (300). While the present study did not confirm data on edema, enilconazole did delay development in all treated embryos and significantly reduced HR. In addition, we found developmental delays and reduced pigmentation that were not reported previously.

Auranofin has been repurposed in the past 10 years for therapy of angiogenic diseases, cancer, HIV/AIDS and other conditions (301–303). While clinical trials were proceeding

(ClinicalTrials.gov Identifier: NCT01419691), several studies demonstrated prenatal teratogenicity (304). In zebrafish, auranofin resulted in severe pericardial edema, cerebral hemorrhaging, jaw malformations, and impaired reproductivity (305,306). Furthermore, a study from 2017 found a significant decrease in HR in 10 µM auranofin-treated zebrafish at 72 hpf (307). In the present study, teratogenic effects were observed, including cardiac arrest, developmental delay, reduced pigmentation, and ISV diameter. Moreover, this study is the first to report a dose-dependent auranofin-induced caudal fin dysmorphia and apoptosis (Figure 13)

Although the AUROC value of the ROC curve may not show a significant performance, it is important to note that the number of values displayed on the graph greatly exceeds the number of samples used for test specificity and sensitivity analysis. Furthermore, the study compared the results of an embryonic zebrafish screen to the known effects of compounds applied to adult humans. Therefore, a performance rate of almost 70% is sufficient to demonstrate the relevance of using zebrafish embryos for drug screenings aimed at human patients with cardiac phenotypes. While typically, true negative, false negative, true positive, and false positive rates would be counted to calculate further analytic values, this information's value would be questionable since these analytics do not apply to cross-organism comparisons. The ROC curve is only used here to visualize the relevance of the zebrafish model to human patients for cardiac phenotypes as a retrospective analysis. The three example compounds and the ROC curve demonstrate not only how well-suited zebrafish are as a model for cardiovascular phenotypic drug screening but also how the study design used here is sensitive enough to reproduce known effects and teratogenicity, as well as detect novel phenotypes.

This study successfully proved that zebrafish can be used as a suitable model for cardiovascular drug screening. The read-outs of the compound’s effects were sensitive enough to replicate known effects and teratogenicity, while also detecting new phenotypes. The results were validated through the mirrored side effects in human patients and the dose-dependent impacts on cardiac parameters in zebrafish. Examples such as the competitive HMG-CoA inhibitor ATO and enilconazole demonstrated dose-dependent effects on heart morphology, developmental delay, and reduced HR. Auranofin, repurposed for various conditions, showed teratogenic effects and dose-dependent impacts on cardiac parameters. A performance rate of almost 70% was achieved in using zebrafish embryos for cardiac phenotype screenings compared to human data, highlighting the model's relevance to human patients. Overall, the study demonstrates the sensitivity of the design in reproducing and detecting relevant phenotypes, but also identified novel vascular modulators.

7.3 Identification of Vascular Modulators Using Zebrafish as a Screening Platform

The formation of plaques within vessel, called atherosclerosis is a major risk factor for CVDs. The growth of new micro vessels, called neovascularization, within the plaque can impact its stability. There are several studies demonstrating growing plaque instability with increased neovascularization (89,308). Angiogenesis is the predominant form of neovascularization, that follows highly similar molecular mechanisms (309). Therefore, identifying an angiogenesis modulator that does not affect established vessels could be tested in atherosclerosis models for drug repurposing. However, due to time constraints, the search for vascular modulators only reached the primary screening stage. Therefore, these findings should be interpreted with caution, considering the small sample size. Additionally, these compounds have not undergone repeated testing, so a false positive cannot be ruled out at this stage. Discussions on this topic should be considered preliminary.

Desonide is a low-potency corticosteroid that is applied topically to treat inflammatory dermatoses (310). According to a recent study, endothelial NR3C1 deficiency leads to the activation of Wnt/β-catenin signaling, promoting angiogenesis (311). In our study, desonide significantly reduced ISV diameter without affecting established vessels. **Flunisolide**, another NR3C1 agonist, was found to increase DV diameter; however, there is currently no information in the current literature available on its effects on angiogenesis, vasculogenesis, or embryotoxicity. Further research is required to determine the EC50 and investigate the effects of flunisolide on the cardiovascular system by treating a second transgenic line such as Tg(*kdlr:mCherry*) with the compound.

OXB belongs to the group of benzimidazole (BZ) carbamates, that inhibits polymerization of tubulin, thereby, disrupting microtubules in parasite cells (312). Tubulin is a key factor in cell division, motility and proliferation, intracellular transport of organelles and more (313). In humans, BZ carbamates cause mild cytotoxicity in healthy cells, but they can also increase toxicity in cancer cells that proliferate rapidly (314). Therefore, it is plausible that OXB-induced cardiac arrest, reduced vessel diameter, and teratogenicity are a result of the compound inducing embryotoxicity.

AZS, a broad-spectrum beta-lactam antibiotic, was found to significantly reduce ISV diameter without causing any noticeable changes to the zebrafish's appearance at 2 dpf (Figure 17). **Cefpiramide**, another penicillin-binding protein inhibitor, is commonly used to treat biliary infections like acute cholangitis (315). In our study, it was found to increase DA diameter without affecting overall morphology. **CPS**, a first-generation cephem antibiotic, is classified as a class B

drug and has not been associated with any congenital defects or teratogenicity (316). However, in our zebrafish study, it was found to reduce DA diameter and cause developmental delays in half of the embryos. Therefore, this effect could be secondary due to the observed developmental delay. No information on the effects of AZS, CPS and cefpiramides on angiogenesis and vasculogenesis were forthcoming, so further investigations on our observations is required. This includes a normalization of the vessel diameter against the standard length[5] of each fish.

NAS specifically blocks bacterial RNA and thereby, bacterial protein synthesis (318). A study from 2022, tested metal-bound NASs cytotoxic properties as an anti-cancer drug (318). However, there is currently no information available in the literature about the effects of NAS on angiogenesis. In this study, NAS decreased DA and DV diameters without affecting the mean ISV diameter. However, NAS caused significantly more moderate pericardial edemas than the DMSO controls, developmental delays and showed indications for apoptosis. Together, these findings indicate embryo toxicity of NAS. Further studies need to be conducted with an EC50 determination to assess NAS toxicity.

The impact of the MAO B inhibitors, **rasagiline** and **furazolidone**, on the diameter of a major blood vessel was observed. Rasagiline increased DA diameter while furazolidone increased DV diameter. Although some of the common side effects of these inhibitors suggest toxicity, the small sample size of the compounds makes it more likely that this finding is a false positive. To confirm the results, the treatment should be repeated, and the compounds should be tested at varying concentrations. The current literature does not provide any information on toxicity or effects on angiogenesis for both compounds.

In summary, this research delved into the potential vascular modulators of the PDL. The results showed that desonide and AZS significantly reduced ISV diameter, while CPS reduced and rasagiline increased the DA diameter. Furazolidone and flunisolide increased DV diameter, but NAS decreased both DA and DV diameter. Further screening is needed to confirm these findings and understand the specific mechanisms through which these compounds impact vessel development and angiogenesis.

[5] Standard length describes the distance of the snout to the posterior tip of the notochord in young larva as described by Parichy *et al*. in 2009 (317).

7.4 High-Content Drug Screening for Heart Rate Modulators in Zebrafish

The focus of the screening was on the development of the zebrafish heart, specifically using an angiogenesis screening. The heart tube forms at 24 hpf, undergoes a leftward jog, and is structured into atrium and ventricle. During treatment start the heart tube contractions start to synchronize (82,93,98) and blood starts to circulate at 48 hpf (130). Thus, the compounds' effects can only be assessed on looping, AVC formation, pacemaker cells, blood circulation, and heart maturation. To better understand the phenotypes, treatment with valid hit compounds could be initiated earlier in development. The first CMs differentiate and express myl7 at the 14-somite stage, which may be a suitable time to begin treatment depending on the hypothesis. A short-term treatment should also be conducted to determine whether the phenotypes are functional or morphological.

The HR was used as a readout for the assay, assuming that it correlates with heart form and function (29). However, mild heart phenotypes may not be detected in this approach, as they may not necessarily cause an altered HR.

Further, while the complete HRH1 target cluster still has to be completely analyzed, all antagonists reduced HR. While anti-histaminics are known to increase tiredness and sleepiness in human patients, an impact on HR has not been observed before. However, it is essential to consider that the imaged fish were anesthetized with tricaine, and a combined effect of both compounds cannot be ruled out.

7.4.1 Miscellaneous Hits

While this study primarily examines the major target clusters that were identified, it is important to also consider the potential toxicity and teratogenicity of individual compounds and smaller clusters. This is particularly relevant in the context of prenatal and postnatal treatments.

Our analysis of embryos treated with **CHX** revealed a decrease in HS, affecting all chambers. In 2013, Yang *et al.* reported that CHX decreased ventricular volume in DMSO treated zebrafish embryos (319). The present study demonstrates the same effect of a significant reduction of ventricle size. However, Yang *et al.* did not report any data on atrial volume changes after treatment. Therefore, our findings add to the current knowledge of CHX effects on embryonic development. Li *et al.* found that CHX induced apoptosis in rat CMs (235), suggesting potential cardiotoxic effects. Further investigations using TUNEL stain and cLSM imaging could reveal more functional details about CHX's impact on embryonic development.

The antifungal agent **PP** has been found to enhance cardiac contractility in a mouse myocardial infarction model without causing cardiac rupture (320). In our study, PP caused significant

bradycardia but did not affect cardiac morphology and function. Although PP has been extensively studied in various models and affects multiple pathways, we believe we are the first to report significant bradycardia in zebrafish following exposure to PP (185).

While the mechanism of action for **NZ** is not well understood, it displays dose-dependent toxic effects, has been shown to act as a mutagen and was therefore sidelined after development of safer drugs (321–324). However, NZ also shows high efficacy at low concentrations which is why it was further investigated for topical applications (325,326). In 1969, Hatt *et al.* reported cardiotoxic effects of NZ, such as arrhythmia and tachycardia in patients, yet they were not able to replicate these effects in Wistar adult rats (327). In this study, NZ caused bradycardia in every tested concentration and displayed smaller hearts as well as an atrial contractility phenotype, while the ventricle was not affected. However, atrial frequency did not differ from the ventricle frequency, thus no conduction defects were shown. Furthermore, no other toxic effects aside from bradycardia and mild edema were detected after NZ treatment. However, severity of the pericardial edemas was not increased compared to the controls.

Treatment with **PEN** is associated with acquired long QT syndrome, tachycardia and sudden cardiac arrest (118,147,328,329). Side-effects arise due to off-target blockage of the potassium I_{Kr}/hERG current (185,328,329). Our study found that exposure to PEN led to mild bradycardia and reduced atrial contractility, affecting heart function. However, PEN did not seem to have any toxic effects on gross developmental morphology.

In 1939, a study by Oliver *et al*. found that rubber gloves from different manufacturers caused reversible depigmentation in dark-skinned workers (330). This condition, known as contact vitiligo, is caused by the selective destruction of melanocytes, which makes the skin vulnerable to premature aging and cancer (331). The drug-induced vitiligo can spread beyond contact areas due to immunity against melanocytes (332). When **MBEH** interacts with tyrosinase, it becomes a reactive quinone that can bind to thiol-groups of tyrosinase and other hapten formations (333). According to Boisson *et al*., converting phenolic/catecholic derivatives like MBEH can trigger oxidative stress (331). In this screening, MBEH caused depigmentation and bradycardia in zebrafish embryos, but did not affect their morphology and function. While bradycardia could indicate cardiotoxicity, there were no other signs of toxicity, making this the first study to report MBEH-induced bradycardia.

BZY is an NSAID and commonly prescribed to treat both acute and chronic pain during pregnancy. A study from 2012 showed that 22.6% of women reported using NSAIDs in the first trimester of pregnancy (157). In preterm neonates, NSAIDs have been administered to close patent *ductus arteriosus* (124). In 2015, Krzeszowski *et al.* reported three cases of premature constriction of the

fetal ductus arteriosus after self-medication of the mothers during pregnancy with BZY (243). This condition is associated with an increased risk of neonatal pulmonary hypertension, which can lead to a ventricle enlargement. The ventricle then has to pump harder to move blood through blocked pulmonary arteries (334–336). This impairment is unique to zebrafish, as they have a different circulatory system than humans. Instead of the *ductus arteriosus*, the unique aortic and pharyngeal arch artery together with ventricle driven blood circulation facilitate blood flow in zebrafish (337–339). Thus, an impaired pharyngeal arch artery could cause increased pressure, thereby also impacting the ventricle. In our study, exposure of zebrafish embryos to BZY impaired atrial dilation and decreased atrial EF, while increasing relative ventricle contractility. Other zebrafish drug screens indicate that NSAIDs can cause severe renal malformations, which suggests that BZY has embryotoxic effects (124). Though studies imply that NSAIDs have developmental toxicity, the overall risk depends on the treatment concentration, duration, and gestational stage. Therefore, BZY is classified as a B2 risk compound (147,157,340,341).

In humans, **PI**, commonly used to treat Tourette's syndrome, is contraindicated for patients with prior heart problems for QT prolongation and arrhythmias such as *torsade de pointes* (342,343). However, our study found that treated zebrafish embryos experienced regular bradycardia in both heart chambers, rather than the expected tachyarrhythmia associated with *torsade de pointes* (344). This suggests that PI may have cardiotoxic effects even at low doses, as evidenced by moderate to severe pericardial edemas and bradycardia (as shown in Figure 27).

Studies on the deiodinase inhibitor **IOP** indicate that it has no impact on cardiac β-adrenoceptor density or HR, as demonstrated by Stäubli and Studer (1986) and Perret et al. (1992) (345,346). In fact, a study in 2007 found that IOP had cardioprotective properties during regional anesthesia (347). However, overdose of IOP in guinea pigs leads to accumulation in the heart, causing bradycardia (348). Therefore, the significant bradycardia, coupled with edema and a dose-dependent rise in the ToxScore in zebrafish embryos in our study, suggest that IOP may induce embryotoxicity at 2 dpf.

IPT is not only an antagonist for ADRA1 but also showed antagonistic actions for the N-methyl-D-aspartate (NMDA) glutamate receptors NMDA2B and NMDA1G as well as protein-activated inward rectifier potassium channel (GIRK) 1, GIRK2 and GIRK4 (349–351). In a study from 1975, IPT dose-dependently lowered blood pressure, increased blood flow via vasodilation, induced tachycardia and augmented the contractile force of the myocardium in dogs (352). Here, IPT resulted in bradycardia and significantly increased atrial contractility, thereby increasing aEF. As previous research has indicated that IPT also causes vasodilation, it would be advantageous to

measure vessel diameters in IPT-treated zebrafish embryos to better evaluate its comparability to larger mammalian models.

To summarize the HR screening process, various data on heart morphology, blood circulation, and HR were gathered. The selection of compounds was based on significant differences in HR observed during the screening. However, mild heart phenotypes may not be detectable through monitoring HR alone. It is crucial to analyze individual compounds and smaller clusters to assess potential toxicity and teratogenicity. Specific compounds such as CHX, PP, NZ, PEN, MBEH, BZY, PI, IOP, and IPT showed distinct effects on heart morphology, function, and cardiac contractility. Further, the HRH1 target cluster antagonists consistently lowered HR, while NR3C1 target cluster agonists consistently increased HR. This suggests a correlation between HRH1 antagonists and bradycardia, and NR3C1 and tachycardia.

7.4.2 The Histaminergic Receptor Hrh1

In this study, as a result of the drug screening, the effects of Hrh1 antagonists on heart phenotypes, angiogenesis and vasculogenesis in zebrafish at 2 dpf, as well as the expression patterns of different histaminergic receptors were examined. The aim was to better understand their implications in cardiovascular development and function.

Research dating back to 1986 showed that stimulation of HRH1 in atria of male guinea pigs increased intracellular cAMP-independent Ca^{+}-channel conductance (353). More recently, a study on zebrafish embryos found that inhibition of Hrh1 by pyrilamine significantly decreased survival rates caused by severe pericardial edema and looping defects, with the HRs of the embryos decreasing significantly (245). However, it's important to note that these results were obtained using unusually high compound concentrations, which may have induced the phenotypes indicating teratogenicity.

A total of 41 HRH1 antagonists were identified in the PDL, but only 15 of them reduced HR. While all compounds shared the MoA, they do not necessarily share the same optimal concentration. Therefore, the concentration-bias created in the first screening step could have contributed to 26 false-negatives in this case. Nevertheless, 15 compounds with the same MoA and the same phenotype are more than sufficient to consider this target cluster relevant.

The anti-allergen **AAH** primarily targets HRH1, but studies have found that it also affects other mediators of allergic symptomatology, such as interleukin 6, tryptase, H and TNFα (354). In a phase IV clinical trial of dymista, a new drug applied for allergies and sinusitis, caused bradycardia in 0.36% of the patients, primarily in males over 60 (NCT04652245). Dymista combines the HRH1

antagonist AAH with the NR3C1 agonist FCP. In our own screening, we found that AAH induced significant changes in HR and significantly reduced vessel diameters of primary and secondary vessels. Detailed analysis with *pyHeart4Fish* showed decreased heart contractility and HS, and dose-dependent toxicity including more severe pericardial edema and cardiac arrest in concentrations ≥40 µM (Figure 31 G). Indeed, a cancer study in 2022 in HeLa cells showed that AAH increased reactive oxygen species (ROS), caused DNA damage and induced apoptosis, thereby displaying clear signs of toxicity (355). While still preliminary, to the best of our knowledge, this is the first study to indicate AAH-induced reduced vessel diameter in zebrafish.

In addition to inducing significant bradycardia, we found the antihistaminic **DPH** to reduce the vessel diameter of primary vessels, cause more severe edemas, and reduce overall body length (Figure 17). There is limited information available on the effects of DPH on HR and various vascular processes, including angiogenesis, vasculogenesis, and vasoconstriction. However, DPH is classified as a US FDA pregnancy category B2 drug, indicating that while animal studies have not demonstrated a risk to the fetus, there have not been sufficient trials in pregnant women (147). None of the antihistaminics have been deemed safe for use during pregnancy thus far (356).

Further, this study revealed that **CHCl** not only induced bradycardia but also led to dose-dependent pericardial edema, cardiac arrest, and overall toxicity. At 20 µM, the HR of the atrium was higher than that of the ventricle, which may indicate a delay or partial block in conduction between both heart chambers. About 18.2% of the treated embryos showed a Mobitz type II AVB (185). While impaired HRH1 has been linked to AVBs in various animals, including frogs, guinea pigs, rabbits, dogs, and humans, there have been no previous reports on CHCl-induced AVBs (356,357).

The HRH1 and serotonin antagonist **HOD**, was shown to not only work as an anaphylactic, but also resulted in coronary dilation and had anti-fibrillatory properties (358). While we do not have results for the angiogenesis screen at present, HOD was observed to decrease HR and induce dose-dependent toxicity, increased dilation of both heart chambers, and thus increased vEF. Moreover, the chamber-specific HR indicates a conduction defect between the atrium and ventricle, requiring further investigation. Although the effects of HOD on coronary dilatation were shown more than 60 years ago, to our knowledge, there have been no reports of the influence of HOD on HR or dilation to this day.

Our study has found that **MP** significantly reduces HR, even without any previous indications. Moreover, our analysis has shown an arrhythmia or conduction defect between the atrium and ventricle, as indicated by the chamber-specific HR analysis. In fact, 75% of the treated fish have had arrhythmias induced by MP, according to the arrhythmia scores calculated with *pyHeart4Fish*.

To verify our findings, the testing with 20 µM MP must be repeated to increase the sample size, and longer videos must be captured to further investigate the observed arrhythmia. Additionally, the mean HS of tested fish was increased with a z-score of 1.1. The increased HS together with the significant increase in atrium relative contractility, could explain the significant increase in aEF and mild increase in vEF. Although MP's structure is based on **TRP**, it has been shown to be less toxic compared to TRP (359). Similar to all the other HRH1 antagonists, TRP significantly reduced HR, but induced cardiac arrest in concentrations ≥40 µM (Figure 30 D), and caused AVBs in 50% of the treated embryos, confirming reports of its toxicity.

In summary, the most common phenotype observed in treatments with all HRH1 antagonists was bradycardia, even at lower concentrations, which concurs with Human Phenotype Ontology data from Harmonizome 3.0 (last accessed 07/06/2023), where a disease association between HRH1 and bradycardia was found (279,360). However, among the most common adverse reactions listed are hypotension and tachycardia, which contradicts our findings (361). In zebrafish, concentrations above 10 µM, especially 40 µM and 80 µM, led to cardiac arrest and higher ToxScores (Supplementary Figure 1). Nevertheless, the current consensus is that HRH1 antagonists do not cause CHDs in humans, even though studies with antihistaminics in pregnant women show conflicting results (362,363). In zebrafish embryos, HRH1 antagonists induced bradycardia at lower concentrations with fewer toxic side effects, indicating a direct effect of the antagonists binding to Hrh1. Furthermore, several HRH1 antagonists, such as CHCl, MP, and TRP, indicate a role in AVB and arrhythmia development. Therefore, we performed whole mount *in situ* hybridization for several *hrh* genes, including *hrh1*, *hrh2a-b* and *hrh3b*.

Probes of the *hrh*s showed highly similar expression patterns at 3 and 5 dpf. Prolonged exposure to the stain shows, expression of *hrh1* in the heart at 3 dpf. As *hrh1* was the only *hrh* to be expressed this early in the heart (Figure 32 E'-E''), protein modeling and protein-ligand-binding assays should be employed to assess the selectiveness of the HRH1 antagonists in zebrafish embryos. Further, *hrh1* was strongly expressed in the dorsal telencephalon as previously shown by different studies (Figure 32 E''') (248,256).

A study from 2009, showed that HRH1 was expressed in the IPL and INL in the mammalian retina. Further, HRH2 was expressed in Müller cells, the primary glial cells of the mammalian retina in the INL (364). While the findings of our study did not contradict the findings in mammalian models, further investigation of the expression patterns in of hrhs in the zebrafish retina is required (Figure 33).

While HRH2 has been shown to be expressed in the heart of adult male guinea pigs, where it mediates electrophysiological changes in the ventricular myocardium after stimulation with H, we found no evidence to suggest a role for either *hrh2a* or *hrh2b* in zebrafish heart development (353). Additionally, *hrh2a* expression did not indicate a specialized role in early development, while hrh2b was specifically expressed in the pancreas at 3 dpf (Figure 32 G-G'). Although there is no data on HRH2 involvement in pancreas development, The Human Protein Atlas (365) showed low-level expression of HRH2 in the human pancreas.

HRH3 is predominantly expressed in the brain and has become a popular drug target for psychological disorders (366–368). In zebrafish, inactivation of *hrh3* resulted in reduced aggression and increased anxiety (257). Recently, Panula *et al.* postulated that two not annotated genes may be part of a triplication of *hrh3*, proposing the existence of *hrh3a*, *hrh3b* and *hrh3c*. Indeed, sequence comparison between the proposed genes on chromosome 2, 7 and 22 suggested the same triplicate in our study. We found a strong expression of *hrh3b* in the dorsal telencephalon, but further research is needed to determine the expression of *hrh3a-c* in organs of the whole embryo at different stages. So far, only the expression patterns of all three genes have been mapped in the zebrafish brain (249). Further, no expression of *hrh3b* could be detected in the zebrafish heart and there is no association of HRH3 with CVDs in humans. For the sake of full disclosure, it should be mentioned that a study in rats showed an association of HRH3 with hypertension (369).

Research on HRHs in various organisms has revealed that the function of H and its receptors may change from early development to adulthood (255). Therefore, it is crucial to study the impact of HRH1 up and downregulation (both genetic and drug-induced) in adult zebrafish. However, this study's findings indicate that *hrh1* is implicated in early heart development in zebrafish, and HRH1 antagonists can cause bradycardia with moderate to severe embryotoxicity. HRH1 antagonists, including AAH, DPH, CHCl, HOD, and MP, exhibited dose-dependent toxicity and induced bradycardia in zebrafish embryos, with some compounds also affecting vessel diameter, cardiac arrest, and arrhythmias. Although HRH1 antagonists have not been linked to congenital heart defects in humans, their impact on early heart development and potential risks during pregnancy should be carefully considered.

7.4.3 Impact of NR3C1 Agonists on Heart Function and Cardiovascular Development in Zebrafish

After identifying NR3C1 as a target cluster in our screening, we examined its expression patterns during early development and adult stages and investigated the possibility of NR3C1 antagonists binding in zebrafish. By understanding the translatability of our findings to humans, we can lay the

groundwork for future research on *nr3c1* in cardiovascular diseases using zebrafish as an overexpression model. Gaining insight into the mechanisms by which *nr3c1* affects cardiovascular development and function can provide valuable information on the pathogenesis of cardiovascular diseases and guide the development of new therapeutic interventions that target NR3C1 signaling pathways.

Our research has found that the NR3C1 positive control **CLO** caused tachycardia in zebrafish, which was previously reported in another study (278). In our study, CLO was removed in the primary screening in the filtering process due to its known effect. Overall, CLO displayed low ToxScores and increased contraction and dilation, without affecting the heart phenotype. However, in 2017 Willi *et al*. reported increased toxicity in CLO-treated fish, including edemas and reduced spontaneous muscle contractions. However, the study did not show the actual morphology of the treated fish (278). In our study, we detected a mild increase in the severity of edemas, almost at the level of the DMSO control.

BEC is commonly used as anti-inflammatory, anti-pruritic and anti-allergy drug and administered via nasal sprays and inhalers. While there are some indications, for BEC-induced tachycardia in high cumulative doses and as an uncommon adverse reaction in humans, there is no clear association for this phenotype (370). However, in our zebrafish study, BEC not only induced tachycardia but also showed dose-dependent teratogenicity and single occurrences of conduction defects. BEC has a 92.59% H360 GHS hazard, indicating the risk of damage to fertility and the unborn child.

In this study, we found that the topical corticosteroid **CCP** caused significant tachycardia, low ToxScores at different concentrations, and reduced heart contractility. CCP has not been reported to induce CVDs and is commonly known to have a low acute toxicity (371). Therefore, it can be assumed that the observed effect results from the treatment rather than toxic side effects.

Similarly, **FMP** induced significant tachycardia, low ToxScores at different concentrations comparable to the DMSO controls, and reduced vEF. Additionally, conduction defects were detected in treated zebrafish larvae. For FMP, there were no previously reported cardiovascular adverse effects and no indications that the phenotypes may be caused by toxic side effects.

In our study, we did not detect any increased toxicity for tested **PRC** concentrations. However, there are indications of PRC embryo toxicity in the literature. According to the FDA drug safety report of DERMATOP® (PRC emollient cream), subcutaneous injections of high doses of PRC in

rodents during gestation showed teratogenic effects. Furthermore, conduction defects were detected with 10 µM-treatment.

Our research also found that the prehormone **P5** induced dose-dependent tachycardia and decreased contractility but did not induce conduction defects. P5-treated fish showed clear signs of teratogenicity, including smaller sizes, bent tails, developmental delays, edema, and pigmentation delays. Association of teratogenicity with prenatal exposure to hormones is well known (348,372). Further, a study in zebrafish showed, that P5 promotes cell migration during epiboly[6] (372). However, there are no studies aside from ours of P5 treatment in zebrafish embryos 24-48 hpf (185).

As previously discussed, two more NR3C1 agonists have been discovered during the vascular screening. **Desonide** is already known to increase HR when consumed at high dosage (373). In our zebrafish screening, desonide also increased HR, but was removed after application of the described filters in Figure 19. Meanwhile, **flunisolide** also belongs to the group of NR3C1 agonists, but it did not significantly affect HR at 20 µM and was therefore also removed in the filtering process. This outcome did not contradict the previous findings of the target cluster, but it does indicate that flunisolide treatment should be carried out at optimized concentrations.

The BEC and PRC data alone would suggest that tachycardia is caused by toxicity. However, significant tachycardia was induced even at lower doses by all NR3C1 antagonists and GC prehormone P5. This points to a specific phenotype caused by increased NR3C1 activity, rather than the cardiotoxic effects of individual compounds. As a result, we moved on to test expression in early developmental and adult stages in zebrafish. As previously demonstrated, the primary AA sequence and expression patterns of *nr3c1* are highly conserved across vertebrates (Supplementary Figure 7) (374). Thus, *in situ* hybridization was used to gain more information about expression patterns in early developmental stages. Expression of *nr3c1* in the brain, eyes, intestine, liver, myotomes, and swim bladder are shown in Figure 39.

nr3c1 was detected in various parts of the brain, including the olfactory endothelium, telencephalon, diencephalon (hypothalamus and thalamus), mesencephalon (optic tectum and tegmentum), and rhombencephalon (medulla oblongata) (as shown in Figure 39 A & A''). Recent research has confirmed the presence of GRα immunoreactivity in the same areas of the adult zebrafish brain (375). Additionally, the Human Protein Atlas indicates that NR3C1 is expressed in the

[6] Embryonic development standards were based on the embryonic development atlas of Kimmel *et al*. from 1995. The epiboly stage is reached 5-9 hpf. Epiboly describes the process of embryonic cells spreading from one animal pole to the opposite pole to enclose the yolk.

telencephalon, diencephalon, mesencephalon, and rhombencephalon, which aligns with the zebrafish findings (see Figure 46) (196,197).

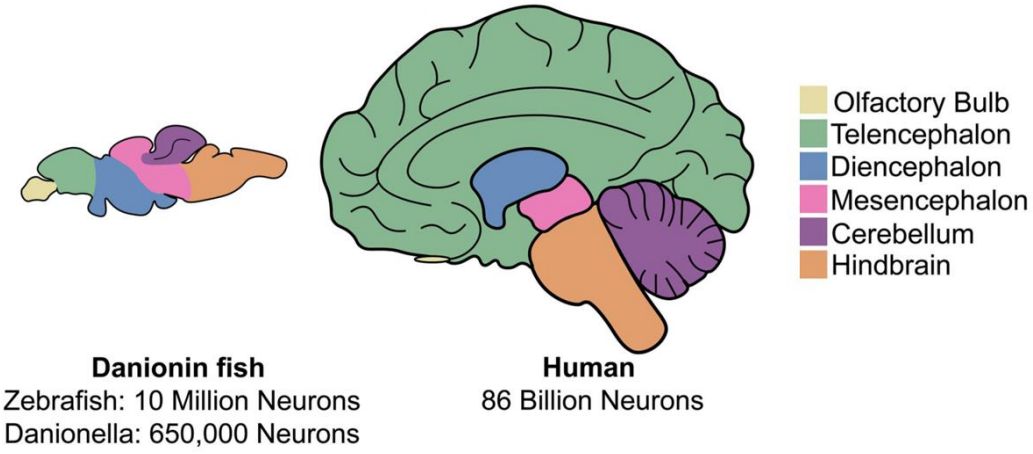

Figure 46: Brain Structure Overview
Comparative overview of the mammalian and zebrafish brain structures. Although the brains of both are anatomically similar, region sizes and organization vary. This figure was adapted with permission from Haynes *et al.* (376).

Further, data shows the presence of *nr3c1* in the retinal IPL, INL, and OPL. The INL consists among others of amacrine cells, horizontal cells, interplexiform neurons and Müller glia. Interplexiform neurons receive input from the IPL and project it to the OPL. Interplexiform neurons receive input from the IPL and send it to the OPL, forming synaptic connections that process signals from photoreceptors (377). The IPL consists of second order and third order neurons. Gallina *et al.* (2014) found that *nr3c1* was expressed in Müller glia and is directly involved in their maturation (374). These findings concur with the data we obtained from zebrafish. Our observations also suggest mild dysmorphia of the heart in NR3C1 agonist treated zebrafish embryos (data not shown), and expression in the heart at 3-5 dpf indicates involvement of *nr3c1* in heart development.

In 2019, a study showed sexually dimorphic changes in cardiac gene expression and pathogenesis in GR KO mice (378), indicating the need for sex-specific baseline expression of *nr3c1* in adult zebrafish. The RT-qPCR on adult AB WT fish showed almost ubiquitous expression throughout different tissues between male and female zebrafish (Figure 40). Although expression of nr3c1 is ubiquitous throughout the body, GR's demonstrate selective functions in different tissues and cell types (379). Our data from zebrafish also shows a greater heterogeneity in certain sexes in different tissues, such as the brains and hearts of males and the spleen of females.

7.4.3.1 Increased Nr3c1 Activity Leads to Conduction Defects in Zebrafish

This study revealed that some compounds tested on fish caused conduction defects, while no defects were observed in the control group. Consequently, the latter part of this chapter concentrates on conduction defects found between the atrium and ventricle in Tg(*myl7:eGFP*)$^{twu34/+}$ zebrafish embryos treated with NR3C1 agonists at 2 dpf. Due to time constraints, only eight of the 15 agonists were tested, and five of them exhibited single occurrences of conduction defects at the tested concentrations: BEC, CLO, FCP, FMP, and PRC. These five compounds, along with the control groups ATO and DMSO, were retested. pyHeart4Fish was employed to analyze the data and determine chamber-specific frequencies, with varying numbers of animals tested per concentration due to optimized concentrations being included in each experiment.

First signs of conduction defects were detected during the hit validation process. Following up on this discovery with additional experiments, clearly showed a significant amount of AVBs induced by NR3C1 agonists. The optimal concentrations used for the screen for AVBs was derived from the concentration step in Tg(*fli1a:eGFP*)^{y7}. However, these tests should be repeated in Tg(*myl7:eGFP*)$^{twu34/+}$ with focus on AVB for effect size. This way, optimal concentrations could possibly yield better results, than e. g. shown in CLO, CCP and FMP (Figure 38). Further, in combination with the gathered data on pericardial edemas, a correlation analysis between edemas and AVBs could be performed, although calculated ToxScores suggest, that it is unlikely, that the AVBs were induced by toxicity. Additionally, it would be beneficial to extend concentration tests for lower and higher doses for all 15 compounds and the GC prehormone P5 and increase the number for tested doses. In 2007, Sainte-Marie *et al*. already demonstrated that upregulation of NR3C1 in mice leads to AVBs (380). *GR*$^{-/-}$ mutants in mice are not viable, which is a major limitation of this model. Due to defects in lung maturation they die perinatally within a few hours (381). Therefore, different groups generated inducible *GR*$^{-/-}$ mice that produced contradictory results, probably due to different genetic backgrounds and pleiotropic effects of GR (379,382). In contrast, *gr*$^{-/-}$ mutants in zebrafish derived from heterozygote and homozygote carriers are viable and fertile. However, due to impaired stress response, they are more likely to die after mating (260). Facchinello *et al*. (2017) reported that *gr*$^{-/-}$ displayed general morphological alteration of the adult heart and intestine and a reduced trabecular network in the ventricle at 45 dpf. Additionally, they reported a significant decrease in HR at 5 dpf compared to the control (260). Involvement of Nr3c1 in AVB in zebrafish has been shown before by Peal *et al*. in 2010 (383). They induced type 2 AVB via *breakdance (bre)*$^{-/-}$ zebrafish mutants and performed a phenotype rescue screening. The *bre*$^{-/-}$ leads to perturbed cardiac repolarization, thereby causing a 2:1 AVB (92,383). They found that the

Nr3c1 agonist flurandrenolide shortens ventricular action potentials, thereby suppressing the AVB (383). In the screening we performed, flurandrenolide increased HR to 1.44, thereby not meeting the cut-off of 90% CI. In this case 20 µM of the compound was not a sufficient dose to cause the effect. The complex mechanisms that involve AVB and QT prolongation are not yet fully understood, but it is clear that Nr3c1 levels play a major role in this disease phenotype. Moreover, other studies in zebrafish are rather focused on *nr3c1* associations with neurological disorders and are therefore focused on downregulation and knockout (KO) of this gene rather than its overexpression. Further, to our knowledge this is the first report of AVBs caused by NR3C1 agonists. In contrast to the human phenotype, in this study tachycardia instead of bradycardia was observed together with the AVB. Other phenotypes such as AF and AFib were considered, however, regular heartbeats were observed, that did not indicate a flutter or fibrillation. Further, all Mobitz types (I-III) could be observed in the affected zebrafish. Aside from additional testing with the remaining compounds, overexpression experiments with and without agonists should be conducted to further investigate this phenotype. Generally, the topic of AVB is still widely debated, with more questions than answers, particularly in relation to interventions (384). In 1996, a family with multiple cases of AVB and early death was studied. Upon histological examination of the patients' hearts, an abundance of TdT-mediated dUTP-biotin nick end labeling (TUNEL) positive cells were found in the AVN, internodal and interatrial pathways, and the sinus node. This led to the conclusion that AVB may result in cardiac apoptosis (385). It was also discovered that prolonged exposure to maternal anti-Ro/SSA antibodies could cause Ca^{2+} channel internalization, which could disrupt cytoplasmic Ca^{2+} metabolisms and lead to apoptosis and cell death (7,386). However, there is no existing hypothesis that can explain the complete pathogenesis of AVBs.

When considering treatments for human patients, using Nr3c1 agonists to rescue an AVB may have potential risks. Although it may help, it could also contribute to the problem. If patients were to undergo a treatment with Nr3c1 agonists like flurandrenolide, they would need to be closely monitored and maintain discipline. Indeed, a recent population-based cohort study from the UK showed dose-dependent risk for CVD in patients treated with prednisolone (387). This study is only one of several showing dose-dependent effects of GC treatments. The study also emphasized that even low dose treatment for an extended period of time could result in an increased risk for CVD, even though this approach was previously deemed safe (387,388). Furthermore, drugs that cause QT prolongation are often withdrawn or restricted from the market, and the FDA recommends testing new compounds for their effects on QT duration (92,389).

To summarize, NR3C1 was identified as a target cluster during screening, leading to further investigations into its expression patterns and potential implications in zebrafish. Testing of NR3C1 antagonists resulted in induced tachycardia, while other compounds such as BEC and PRC also showed conduction defects in zebrafish, indicating a potential role of NR3C1 in heart function. This study also suggests a mild dysmorphia of the heart in NR3C1 agonist-treated zebrafish embryos, which requires further quantification. These effects were found to be specific to NR3C1 activity and not due to toxic side effects. Further analysis revealed expression of *nr3c1* in various tissues, including the brain, eyes, intestine, liver, myotomes, and swim bladder. The expression patterns of *nr3c1* in the eyes and brain of early developmental stages and adult zebrafish were consistent with those observed in other vertebrates, suggesting evolutionary conservation. Studying the mechanisms by which NR3C1 influences cardiovascular development and function can provide valuable insights into the pathogenesis of cardiovascular diseases and guide the development of new therapeutic interventions targeting NR3C1 signaling pathways.

7.4.3.2 NR3C1 Protein Modeling and Docking

Through our testing of Glide XP docking and XP IFD, we found that XP IFD accurately docked all test ligands from co-crystallized structures into the respective binding pockets. We found that the 3CLD protein structure had the lowest mean RMSDs for both docking approaches, indicating high precision. As a result, we used the XP IFD approach to test NR3C1 agonists with the 3CLD protein structure as hGR1. To model the target protein, we utilized comparative modeling based on an evolutionary similar template protein. Precise models can be generated with an RMSD of approximately 1 Å compared to the original crystallographic protein structure if the homology of a protein is at least 50% (390).

As previously described, the zebrafish protein model zfGR1 was designed based on the AncGR2 using Schrödinger homology modeling (Figure 43) (211). The model showed not only a high homology to the hGR1, without any questionable conformations and erroneous parts. The model was of good quality, as demonstrated by the low meta-MQAP TopScore (213). Both hGR1 and zfGR1 were used for XP IFD to test ligand binding of significant NR3C1 agonists from screening assays. As the proof of concept predicted, XP IFD was able to dock all 12 ligands correctly into the binding pockets of both models (Table 38). The side chains of hydrophobic AAs within the LBT can interact with the ligand in different conformations, enhancing stability and increasing selectivity and specificity for nuclear receptors. We found that the AAs primarily involved in ligand binding in both models are Asn^{533} and Arg^{580} (resp. Asn^{564} and Arg^{611}). The primary AAs involved in hydrophic interactions in both models are: Met^{560}, Leu^{563}, Leu^{566}, Met^{646}, Leu^{732}, Cys^{736} and Leu^{753}

(resp. Met^{529}, Leu^{532}, Leu^{535}, Met^{615}, Leu^{701}, Cys^{705} and Leu^{722}). Further, the IF docking score was used for a ranking correlation that demonstrated moderate correlation between ranks of hGR1 and zfGR1 ($p = 0.019$) (Figure 43). Lower IF docking scores with higher correlation suggest high probability of the ligands binding to both receptors. This data suggests comparability between both models and confirms the suitability of zebrafish as a model for this drug screening and for further research on Nr3c1.

In summary, this study provides a reliable homology model for the zebrafish Nr3c1 (zfGR1). Ranked correlation of tested NR3C1 agonists in combination with visualized multiple sequence alignment points towards high conservation of NR3C1 between humans and zebrafish. As a result, it is recommended to conduct experiments on the top 5 ranked ligands in human CMs to verify the tachycardia symptoms observed in zebrafish.

7.5 Outlook

A protocol for screening cardiovascular active compounds was established and executed in this study. The screening for vascular modulators was continued to the primary screening phase, while the heartbeat screening went through filtering, concentration optimization, validation in a second transgenic line and finally the identification of target clusters. Various hits with different targets were assessed for their teratogenicity. Additionally, the expression patterns of *hrh1* and *nr3c1* were analyzed as an initial step in comprehending their involvement in cardiac morphology and function. A reliable *in silico* homology model was created for Nr3c1 to assess protein-ligand docking likelihood and transferability between zebrafish and human data. Despite laying the groundwork for further research there is still much to be done, such as continuing the vascular screening and achieving a better comprehension of the mechanisms of Nr3c1 and Hrh1 in cardiovascular development and function.

To better comprehend these mechanisms, it is necessary to repeat treatment with the primary hits in Tg(*fli1a:eGFP*)^{y7} and test them at different concentrations. This will not only determine dose-dependent effects but also provide insight into the MoA causing the vascular phenotype. The resulting hits should then be validated in Tg(*kdrl:Has.HRAS-mCherry*)$^{S916/+}$ zebrafish, which expresses mCherry in the vasculature under the *kinase insert domain receptor-like* (*kdrl)* promoter. Lastly, the identified hit targets should be further investigated for their role in cardiovascular development.

Research on HRHs in various organisms has revealed that the function of H and its receptors may change from early development to adulthood (255). Therefore, it is crucial to study the impact of

HRH1 up and downregulation in larval and adult zebrafish. To get a complete overview of whole-body expression patterns, the probes for *hrh3a* and *hrh3c* should be generated and analyzed. Further, the expression of the different *hrhs* in the larval heart should be examined by isolating larval hearts and performing RT-qPCR on the extracted samples. This way even low expression levels could be detected. In mammals all four HRHs are present in the heart, however it was shown, that expression of HRHs does not only differ between different mammalian species, but also shows a different distribution in different heart tissues (391). Therefore, cryosections of adult zebrafish hearts and *in-situ* hybridization with the different probes could provide a clearer picture of cardiac hrh expression patterns in zebrafish. Further, the use of MOs followed by a rescue with H and/or P5 treatment and *hrh1* mRNA injections could indicate, whether downregulation of Hrh1 is causative for the observed bradycardia and arrhythmias and if the phenotypes caused by the antagonists are morphological or functional. These observations would then determine the course for further studies. Nevertheless, further investigation on the MoA of Hrh1 is necessary to comprehend the long-term effects of HRH1 antagonists on the developing embryo to determine drug safety for pregnant women.

The homology modeling of hGR1 and zfGR1 showed ranked correlation for NR3C1 agonists. Testing of the top 5 ranked ligands in human CMs could confirm phenotypes of tachycardia and provide valuable insights into the MoA of NR3C1. Further, as mentioned previously, the heart morphology of NR3C1 agonist-treated zebrafish should be assessed via confocal laser scanning microscopy and angles between atrium and ventricle should be assessed to determine, whether the observed phenotype is an AVC extension or may be indicative of a looping defect. Further, as Nr3c1 is a transcription factor, scRNA-seq of the hearts of treated embryos at 24 and 48 hpf could provide valuable information about downstream targets involved in the observed phenotypes. So far GR research focused on knockdown (KD) and KO models in zebrafish (265). Therefore, *nr3c1* should be overexpressed in zebrafish, either by generation of a transgenic overexpression line or via transient plasmid injections encoding for *nr3c1*. These experiments should be followed by treatment of the mutants/injected fish and analysis of HR and heart morphology. Here, the GC prehormone P5 could serve as a positive control. These tests can also help to determine, whether the observed conduction defects are a result of Nr3c1 protein-ligand binding or if an off-target effect may cause the conduction defects. If *nr3c1* is a probable cause of the conduction defects, the overexpression scenarios could help to further understand the pathway that underlies AVBs. In case *nr3c1* is not involved in AVBs in zebrafish, an apoptosis staining such as acridine orange and TUNEL staining could be performed. Acridine orange is a nucleic acid binding-stain that emits green fluorescence when binding to double stranded DNA and red fluorescence when binding to single stranded DNA

or RNA. This way it can be assessed whether the compounds induce apoptosis in the CM and thereby induce the conduction defects. Comprehensive understanding of this pathway could help to develop new therapies for patients to treat AVBs medically instead of with a pacemaker.

8 References

1. Genetic Nomenclature Guide. 1998;

2. Mullins M. Chapter 7 - Genetic Methods Conventions for Naming Zebrafish Genes. In: The zebrafish book A guide for the laboratory use of zebrafish (Danio rerio). 4th ed. Univ. of Oregon Press, Eugene.; 2000.

3. ZFIN Zebrafish Nomenclature Conventions - General Information - Confluence [Internet]. 2019 [cited 2022 Mar 24]. Available from: https://zfin.atlassian.net/wiki/spaces/general/pages/1818394635/ZFIN+Zebrafish+Nomenclature+Conventions

4. WHO. World Health Organization. 2019 [cited 2021 Jul 18]. WHO | The top 10 causes of death. Available from: https://www.who.int/news-room/fact-sheets/detail/the-top-10-causes-of-death

5. Virani SS, Alonso A, Aparicio HJ, Benjamin EJ, Bittencourt MS, Callaway CW, et al. Heart Disease and Stroke Statistics-2021 Update: A Report From the American Heart Association. Circulation. 2021 Feb 23;143(8):e254–743.

6. van der Linde D, Konings EEM, Slager MA, Witsenburg M, Helbing WA, Takkenberg JJM, et al. Birth prevalence of congenital heart disease worldwide: a systematic review and meta-analysis. J Am Coll Cardiol. 2011 Nov 15;58(21):2241–7.

7. Baruteau AE, Pass RH, Thambo JB, Behaghel A, Le Pennec S, Perdreau E, et al. Congenital and childhood atrioventricular blocks: pathophysiology and contemporary management. Eur J Pediatr. 2016 Sep 1;175(9):1235–48.

8. Michaelsson M, Riesenfeld T, Jonzon A. Natural history of congenital complete atrioventricular block. Pacing Clin Electrophysiol PACE. 1997 Aug;20(8 Pt 2):2098–101.

9. Tsao CW, Aday AW, Almarzooq ZI, Alonso A, Beaton AZ, Bittencourt MS, et al. Heart Disease and Stroke Statistics—2022 Update: A Report From the American Heart Association. Circulation. 2022 Feb 22;145(8):e153–639.

10. Roth GA, Mensah GA, Johnson CO, Addolorato G, Ammirati E, Baddour LM, et al. Global Burden of Cardiovascular Diseases and Risk Factors, 1990–2019. J Am Coll Cardiol. 2020 Dec 22;76(25):2982–3021.

11. United Nations. Health [Internet]. United Nations Sustainable Development. [cited 2023 Jan 18]. Available from: https://www.un.org/sustainabledevelopment/health/

12. Wessels A, Sedmera D. Developmental anatomy of the heart: a tale of mice and man. Physiol Genomics. 2003 Nov 11;15(3):165–76.

13. Hirota A, Fujii S, Kamino K. Optical Monitoring of Spontaneous Electrical Activity of 8-somite Embryonic Chick Heart. Jpn J Physiol. 1979;29(5):635–9.

14. Moorman AFM, de Jong F, Denyn MMFJ, Lamers WH. Development of the Cardiac Conduction System. Circ Res. 1998 Apr 6;82(6):629–44.

15. Buijtendijk MFJ, Barnett P, Hoff MJB. Development of the human heart. Am J Med Genet C Semin Med Genet. 2020 Mar;184(1):7–22.

16. Kurian T, Ambrosi C, Hucker W, Fedorov VV, Efimov IR. ANATOMY AND ELECTROPHYSIOLOGY OF THE HUMAN AV NODE. Pacing Clin Electrophysiol PACE. 2010 Jun 1;33(6):754–62.

17. Hussen E, Aakel N, Shaito AA, Al-Asmakh M, Abou-Saleh H, Zakaria ZZ. Zebrafish (Danio rerio) as a Model for the Study of Developmental and Cardiovascular Toxicity of Electronic Cigarettes. Int J Mol Sci. 2024 Jan;25(1):194.

18. Iop L, Iliceto S, Civieri G, Tona F. Inherited and Acquired Rhythm Disturbances in Sick Sinus Syndrome, Brugada Syndrome, and Atrial Fibrillation: Lessons from Preclinical Modeling. Cells. 2021 Nov;10(11):3175.

19. Cardarilli GC, Di Nunzio L, Fazzolari R, Re M, Silvestri F. Improvement of the Cardiac Oscillator Based Model for the Simulation of Bundle Branch Blocks. Appl Sci. 2019 Jan;9(18):3653.

20. Wessels A, Markman MW, Vermeulen JL, Anderson RH, Moorman AF, Lamers WH. The development of the atrioventricular junction in the human heart. Circ Res. 1996 Jan;78(1):110–7.

21. Camenisch TD, Spicer AP, Brehm-Gibson T, Biesterfeldt J, Augustine ML, Calabro A, et al. Disruption of hyaluronan synthase-2 abrogates normal cardiac morphogenesis and hyaluronan-mediated transformation of epithelium to mesenchyme. J Clin Invest. 2000 Aug 1;106(3):349–60.

22. Lakkis MM, Epstein JA. Neurofibromin modulation of ras activity is required for normal endocardial-mesenchymal transformation in the developing heart. Development. 1998 Nov 15;125(22):4359–67.

23. Gruber PJ, Kubalak SW, Pexieder T, Sucov HM, Evans RM, Chien KR. RXR alpha deficiency confers genetic susceptibility for aortic sac, conotruncal, atrioventricular cushion, and ventricular muscle defects in mice. J Clin Invest. 1996 Sep 15;98(6):1332–43.

24. Abu Nahia K, Migdał M, Quinn TA, Poon KL, Łapiński M, Sulej A, et al. Genomic and physiological analyses of the zebrafish atrioventricular canal reveal molecular building blocks of the secondary pacemaker region. Cell Mol Life Sci. 2021;78(19–20):6669–87.

25. Chi NC, Shaw RM, Jungblut B, Huisken J, Ferrer T, Arnaout R, et al. Genetic and Physiologic Dissection of the Vertebrate Cardiac Conduction System. PLoS Biol. 2008 May;6(5):e109.

26. Meijler FL, Janse MJ. Morphology and electrophysiology of the mammalian atrioventricular node. Physiol Rev. 1988 Apr;68(2):608–47.

27. Dobrzynski H, Nikolski VP, Sambelashvili AT, Greener ID, Yamamoto M, Boyett MR, et al. Site of origin and molecular substrate of atrioventricular junctional rhythm in the rabbit heart. Circ Res. 2003 Nov 28;93(11):1102–10.

28. Hucker WJ, Fedorov VV, Foyil KV, Moazami N, Efimov IR. Optical Mapping of the Human Atrioventricular Junction. Circulation. 2008 Mar 18;117(11):1474–7.

29. Martin KE, Waxman JS. Atrial and Sinoatrial Node Development in the Zebrafish Heart. J Cardiovasc Dev Dis. 2021 Feb 9;8(2):15.

30. Campbell NA, Reece JB. Biology. 6th ed. San Francisco: Benjamin Cummings; 2002. 1247 p.

31. Maass K, Shekhar A, Lu J, Kang G, See F, Kim E, et al. Isolation and Characterization of ESC-Derived Cardiac Purkinje Cells. Stem Cells Dayt Ohio. 2015 Apr;33(4):1102–12.

32. Kreuzberg MM, Willecke K, Bukauskas FF. Connexin-Mediated Cardiac Impulse Propagation: Connexin 30.2 Slows Atrioventricular Conduction in Mouse Heart. Trends Cardiovasc Med. 2006 Nov;16(8):266–72.

33. Virágh Sz, Challice CE. The development of the conduction system in the mouse embryo heart: III. The development of sinus muscle and sinoatrial node. Dev Biol. 1980 Nov 1;80(1):28–45.

34. Liu P, Wang Y, Zhang X, Zhang Z, Zhao N, Ou W, et al. Obesity and Cardiac Conduction Block Disease in China. JAMA Netw Open. 2023 Nov 13;6(11):e2342831.

35. Heart Block [Internet]. 2021 [cited 2022 May 1]. Available from: https://www.hopkinsmedicine.org/health/conditions-and-diseases/heart-block

36. Ziacchi M, Spadotto A, Palmisano P, Guerra F, De Ponti R, Zanotto G, et al. Conduction system disease management in patients candidate and/or treated for the aortic valve disease: an Italian Survey promoted by Italian Association of Arrhythmology and Cardiac Pacing (AIAC). Acta Cardiol. 2024 Mar 5;1–7.

37. Barold SS, Hayes DL. Second-Degree Atrioventricular Block: A Reappraisal. Mayo Clin Proc. 2001 Jan 1;76(1):44–57.

38. Kashou AH, Goyal A, Nguyen T, Chhabra L. Atrioventricular Block. In: StatPearls [Internet]. Treasure Island (FL): StatPearls Publishing; 2022 [cited 2022 May 1]. Available from: http://www.ncbi.nlm.nih.gov/books/NBK459147/

39. Barold SS, Herweg B. Centennial of the original description of Mobitz type II second-degree atrioventricular block. J Cardiovasc Electrophysiol [Internet]. 2024 [cited 2024 Apr 5];n/a(n/a). Available from: https://onlinelibrary.wiley.com/doi/abs/10.1111/jce.16199

40. Glikson M, Nielsen JC, Kronborg MB, Michowitz Y, Auricchio A, Barbash IM, et al. 2021 ESC Guidelines on cardiac pacing and cardiac resynchronization therapy: Developed by the Task Force on cardiac pacing and cardiac resynchronization therapy of the European Society of Cardiology (ESC) With the special contribution of the European Heart Rhythm Association (EHRA). Eur Heart J. 2021 Sep 14;42(35):3427–520.

41. Rosen KM. Junctional Tachycardia. Circulation. 1973 Mar;47(3):654–64.

42. Rahman MFF, Yandrapalli S. Atrioventricular Dissociation. In: StatPearls [Internet]. Treasure Island (FL): StatPearls Publishing; 2024 [cited 2024 Apr 5]. Available from: http://www.ncbi.nlm.nih.gov/books/NBK563205/

43. Meyer M, Arnold A, Stein T, Niemöller U, Tanislav C, Erkapic D. Arrhythmias among Older Adults Receiving Comprehensive Geriatric Care: Prevalence and Associated Factors. Clin Pract. 2024 Jan 4;14(1):132–47.

44. Ortiz J, Niwano S, Abe H, Rudy Y, Johnson NJ, Waldo AL. Mapping the conversion of atrial flutter to atrial fibrillation and atrial fibrillation to atrial flutter. Insights into mechanisms. Circ Res. 1994 May;74(5):882–94.

45. Olgin JE, Kalman JM, Fitzpatrick AP, Lesh MD. Role of right atrial endocardial structures as barriers to conduction during human type I atrial flutter. Activation and entrainment mapping guided by intracardiac echocardiography. Circulation. 1995 Oct 1;92(7):1839–48.

46. Yamabe H, Misumi I, Fukushima H, Ueno K, Kimura Y, Hokamura Y. Conduction properties of the crista terminalis and its influence on the right atrial activation sequence in patients with typical atrial flutter. Pacing Clin Electrophysiol PACE. 2002 Feb;25(2):132–41.

47. Diamant MJ, Andrade JG, Virani SA, Jhund PS, Petrie MC, Hawkins NM. Heart failure and atrial flutter: a systematic review of current knowledge and practices. ESC Heart Fail. 2021 Sep 10;8(6):4484–96.

48. Rahman F, Wang N, Yin X, Ellinor PT, Lubitz SA, LeLorier PA, et al. Atrial flutter – clinical risk factors and adverse outcomes in the Framingham Heart Study. Heart Rhythm Off J Heart Rhythm Soc. 2016 Jan;13(1):233–40.

49. Healey JS, Oldgren J, Ezekowitz M, Zhu J, Pais P, Wang J, et al. Occurrence of death and stroke in patients in 47 countries 1 year after presenting with atrial fibrillation: a cohort study. Lancet Lond Engl. 2016 Sep 17;388(10050):1161–9.

50. Marrouche NF, Brachmann J, Andresen D, Siebels J, Boersma L, Jordaens L, et al. Catheter Ablation for Atrial Fibrillation with Heart Failure. N Engl J Med. 2018 Feb 1;378(5):417–27.

51. Tripathi B, Arora S, Mishra A, Kundoor VR, Lahewala S, Kumar V, et al. Short-term outcomes of atrial flutter ablation. J Cardiovasc Electrophysiol. 2017 Nov;28(11):1275–84.

52. LaPointe NMA, Sun JL, Kaplan S. In-hospital management of patients with atrial flutter. Am Heart J. 2010 Mar;159(3):370–6.

53. Saglietto A, Gaita F, De Ponti R, De Ferrari GM, Anselmino M. Catheter Ablation vs. Anti-Arrhythmic Drugs as First-Line Treatment in Symptomatic Paroxysmal Atrial Fibrillation: A Systematic Review and Meta-Analysis of Randomized Clinical Trials. Front Cardiovasc Med. 2021;8:664647.

54. Wilkinson RN, van Eeden FJM. The zebrafish as a model of vascular development and disease. Prog Mol Biol Transl Sci. 2014;124:93–122.

55. Lammert E, Axnick J. Vascular Lumen Formation. Cold Spring Harb Perspect Med. 2012 Apr;2(4):a006619.

56. Carmeliet P, Jain RK. Molecular mechanisms and clinical applications of angiogenesis. Nature. 2011 May 19;473(7347):298–307.

57. Roman BL, Pham VN, Lawson ND, Kulik M, Childs S, Lekven AC, et al. Disruption of acvrl1 increases endothelial cell number in zebrafish cranial vessels. Development. 2002 Jun 15;129(12):3009–19.

58. Xu L, Kanasaki K, Kitada M, Koya D. Diabetic angiopathy and angiogenic defects. Fibrogenesis Tissue Repair. 2012 Aug 1;5(1):13.

59. Koch AE, Distler O. Vasculopathy and disordered angiogenesis in selected rheumatic diseases: rheumatoid arthritis and systemic sclerosis. Arthritis Res Ther. 2007 Aug 15;9(2):S3.

60. Autiero M, Luttun A, Tjwa M, Carmeliet P. Placental growth factor and its receptor, vascular endothelial growth factor receptor-1: novel targets for stimulation of ischemic tissue revascularization and inhibition of angiogenic and inflammatory disorders. J Thromb Haemost JTH. 2003 Jul;1(7):1356–70.

61. Chappell JC, Taylor SM, Ferrara N, Bautch VL. Local guidance of emerging vessel sprouts requires soluble Flt-1. Dev Cell. 2009 Sep;17(3):377–86.

62. Meyer RD, Mohammadi M, Rahimi N. A Single Amino Acid Substitution in the Activation Loop Defines the Decoy Characteristic of VEGFR-1/FLT-1. J Biol Chem. 2006 Jan 13;281(2):867–75.

63. Gerald D, Chintharlapalli S, Augustin HG, Benjamin LE. Angiopoietin-2: An Attractive Target for Improved Antiangiogenic Tumor Therapy. Cancer Res. 2013 Mar 15;73(6):1649–57.

64. Montero-Balaguer M, Swirsding K, Orsenigo F, Cotelli F, Mione M, Dejana E. Stable vascular connections and remodeling require full expression of VE-cadherin in zebrafish embryos. PloS One. 2009 Jun 3;4(6):e5772.

65. Sauteur L, Krudewig A, Herwig L, Ehrenfeuchter N, Lenard A, Affolter M, et al. Cdh5/VE-cadherin promotes endothelial cell interface elongation via cortical actin polymerization during angiogenic sprouting. Cell Rep. 2014 Oct 23;9(2):504–13.

66. Du J, Yang Q, Luo L, Yang D. C1qr and C1qrl redundantly regulate angiogenesis in zebrafish through controlling endothelial Cdh5. Biochem Biophys Res Commun. 2017 29;483(1):482–7.

67. Janning W, Knust E. Genetik: Allgemeine Genetik - Molekulare Genetik - Entwicklungsgenetik. Georg Thieme Verlag; 2008. 531 p.

68. Habeck H, Odenthal J, Walderich B, Maischein HM, Schulte-Merker S. Analysis of a Zebrafish VEGF Receptor Mutant Reveals Specific Disruption of Angiogenesis. Curr Biol. 2002 Aug 20;12(16):1405–12.

69. Roskoski R. Sunitinib: a VEGF and PDGF receptor protein kinase and angiogenesis inhibitor. Biochem Biophys Res Commun. 2007 May 4;356(2):323–8.

70. Vandekeere S, Dewerchin M, Carmeliet P. Angiogenesis Revisited: An Overlooked Role of Endothelial Cell Metabolism in Vessel Sprouting. Microcirc N Y N 1994. 2015 Oct;22(7):509–17.

71. Krueger J, Liu D, Scholz K, Zimmer A, Shi Y, Klein C, et al. Flt1 acts as a negative regulator of tip cell formation and branching morphogenesis in the zebrafish embryo. Dev Camb Engl. 2011 May 15;138(10):2111–20.

72. Betsholtz C. Insight into the physiological functions of PDGF through genetic studies in mice. Cytokine Growth Factor Rev. 2004 Aug;15(4):215–28.

73. Wiens KM, Lee HL, Shimada H, Metcalf AE, Chao MY, Lien CL. Platelet-derived growth factor receptor beta is critical for zebrafish intersegmental vessel formation. PloS One. 2010 Jun 25;5(6):e11324.

74. Lampugnani MG, Orsenigo F, Gagliani MC, Tacchetti C, Dejana E. Vascular endothelial cadherin controls VEGFR-2 internalization and signaling from intracellular compartments. J Cell Biol. 2006 Aug 14;174(4):593–604.

75. Yamashita A, Inada H, Chihara K, Yamada T, Deguchi J, Funabashi H. Improvement of the evaluation method for teratogenicity using zebrafish embryos. J Toxicol Sci. 2014;39(3):453–64.

76. Streisinger G, Walker C, Dower N, Knauber D, Singer F. Production of clones of homozygous diploid zebra fish (Brachydanio rerio). Nature. 1981 May 28;291(5813):293–6.

77. Haffter P, Granato M, Brand M, Mullins MC, Hammerschmidt M, Kane DA, et al. The identification of genes with unique and essential functions in the development of the zebrafish, Danio rerio. Dev Camb Engl. 1996 Dec;123:1–36.

78. Driever W, Solnica-Krezel L, Schier AF, Neuhauss SC, Malicki J, Stemple DL, et al. A genetic screen for mutations affecting embryogenesis in zebrafish. Dev Camb Engl. 1996 Dec;123:37–46.

79. Hwang WY, Peterson RT, Yeh JRJ. Methods for targeted mutagenesis in zebrafish using TALENs. Methods San Diego Calif. 2014 Aug 15;69(1):76–84.

80. Kettleborough RNW, Busch-Nentwich EM, Harvey SA, Dooley CM, de Bruijn E, van Eeden F, et al. A systematic genome-wide analysis of zebrafish protein-coding gene function. Nature. 2013 Apr 25;496(7446):494–7.

81. Patton EE, Zon LI. The art and design of genetic screens: zebrafish. Nat Rev Genet. 2001 Dec;2(12):956–66.

82. Bakkers J. Zebrafish as a model to study cardiac development and human cardiac disease. Cardiovasc Res. 2011 Jul 15;91(2):279–88.

83. Howe K, Clark MD, Torroja CF, Torrance J, Berthelot C, Muffato M, et al. The zebrafish reference genome sequence and its relationship to the human genome. Nature. 2013 Apr;496(7446):498–503.

84. Vilella AJ, Severin J, Ureta-Vidal A, Heng L, Durbin R, Birney E. EnsemblCompara GeneTrees: Complete, duplication-aware phylogenetic trees in vertebrates. Genome Res. 2009 Feb 1;19(2):327–35.

85. Gunnarsson L, Jauhiainen A, Kristiansson E, Nerman O, Larsson DGJ. Evolutionary conservation of human drug targets in organisms used for environmental risk assessments. Environ Sci Technol. 2008 Aug 1;42(15):5807–13.

86. Watkins SC, Maniar S, Mosher M, Roman BL, Tsang M, St Croix CM. High Resolution Imaging of Vascular Function in Zebrafish. PLoS ONE. 2012 Aug 30;7(8):e44018.

87. Liu L, Yang G, Liu S, Wang L, Yang X, Qu H, et al. High-throughput imaging of zebrafish embryos using a linear-CCD-based flow imaging system. Biomed Opt Express. 2017 Nov 16;8(12):5651–62.

88. Gierten J, Pylatiuk C, Hammouda OT, Schock C, Stegmaier J, Wittbrodt J, et al. Automated high-throughput heartbeat quantification in medaka and zebrafish embryos under physiological conditions. Sci Rep. 2020 Feb 6;10(1):2046.

89. Vedder VL, Aherrahrou Z, Erdmann J. Dare to Compare. Development of Atherosclerotic Lesions in Human, Mouse, and Zebrafish. Front Cardiovasc Med. 2020 Jun 30;7:109.

90. Staudt D, Stainier D. Uncovering the molecular and cellular mechanisms of heart development using the zebrafish. Annu Rev Genet. 2012;46:397–418.

91. Bowley G, Kugler E, Wilkinson R, Lawrie A, Eeden F, Chico TJA, et al. Zebrafish as a tractable model of human cardiovascular disease. Br J Pharmacol. 2021 May 10;bph.15473.

92. Zhao Y, Zhang K, Sips P, MacRae CA. Screening drugs for myocardial disease in vivo with zebrafish: an expert update. Expert Opin Drug Discov. 2019 Apr 3;14(4):343–53.

93. Kemmler CL, Riemslagh FW, Moran HR, Mosimann C. From Stripes to a Beating Heart: Early Cardiac Development in Zebrafish. J Cardiovasc Dev Dis. 2021 Feb;8(2):17.

94. Miura GI, Yelon D. Chapter 7 - A Guide to Analysis of Cardiac Phenotypes in the Zebrafish Embryo. In: Detrich HW, Westerfield M, Zon LI, editors. Methods in Cell Biology. Academic Press; 2011. p. 161–80. (The Zebrafish: Cellular and Developmental Biology, Part B; vol. 101).

95. Yelon D, Horne SA, Stainier DY. Restricted expression of cardiac myosin genes reveals regulated aspects of heart tube assembly in zebrafish. Dev Biol. 1999 Oct 1;214(1):23–37.

96. Burkhard SB, Bakkers J. Spatially resolved RNA-sequencing of the embryonic heart identifies a role for Wnt/β-catenin signaling in autonomic control of heart rate. Yelon D, editor. eLife. 2018 Feb 5;7:e31515.

97. Gauvrit S, Bossaer J, Lee J, Collins MM. Modeling Human Cardiac Arrhythmias: Insights from Zebrafish. J Cardiovasc Dev Dis. 2022 Jan;9(1):13.

98. Khodiyar VK, Howe D, Talmud PJ, Breckenridge R, Lovering RC. From zebrafish heart jogging genes to mouse and human orthologs: using Gene Ontology to investigate mammalian heart development. F1000Research. 2013;2:242.

99. Peralta M, González-Rosa JM, Marques IJ, Mercader N. The Epicardium in the Embryonic and Adult Zebrafish. J Dev Biol. 2014 Apr 11;2(2):101–16.

100. van Weerd JH, Christoffels VM. The formation and function of the cardiac conduction system. Dev Camb Engl. 2016 Jan 15;143(2):197–210.

101. Jensen B, Boukens BJD, Postma AV, Gunst QD, van den Hoff MJB, Moorman AFM, et al. Identifying the Evolutionary Building Blocks of the Cardiac Conduction System. PLoS ONE. 2012 Sep 11;7(9):e44231.

102. Chávez MN, Aedo G, Fierro FA, Allende ML, Egaña JT. Zebrafish as an Emerging Model Organism to Study Angiogenesis in Development and Regeneration. Front Physiol. 2016;7:56.

103. Fang L, Miller YI. Emerging applications for zebrafish as a model organism to study oxidative mechanisms and their roles in inflammation and vascular accumulation of oxidized lipids. Free Radic Biol Med. 2012 Oct 1;53(7):1411–20.

104. Fang L, Liu C, Miller YI. Zebrafish models of dyslipidemia: relevance to atherosclerosis and angiogenesis. Transl Res J Lab Clin Med. 2014 Feb;163(2):99–108.

105. Larson JD, Wadman SA, Chen E, Kerley L, Clark KJ, Eide M, et al. Expression of VE-cadherin in zebrafish embryos: a new tool to evaluate vascular development. Dev Dyn Off Publ Am Assoc Anat. 2004 Sep;231(1):204–13.

106. Stainier DY, Fouquet B, Chen JN, Warren KS, Weinstein BM, Meiler SE, et al. Mutations affecting the formation and function of the cardiovascular system in the zebrafish embryo. Dev Camb Engl. 1996 Dec;123:285–92.

107. Huang CJ, Tu CT, Hsiao CD, Hsieh FJ, Tsai HJ. Germ-line transmission of a myocardium-specific GFP transgene reveals critical regulatory elements in the cardiac myosin light chain 2 promoter of zebrafish. Dev Dyn. 2003;228(1):30–40.

108. Ren J, Han P, Ma X, Farah EN, Bloomekatz J, Zeng XXI, et al. Canonical Wnt5b signaling directs outlying Nkx2.5+ mesoderm into pacemaker cardiomyocytes. Dev Cell. 2019 Sep 23;50(6):729-743.e5.

109. van Opbergen CJM, van der Voorn SM, Vos MA, de Boer TP, van Veen TAB. Cardiac Ca2+ signalling in zebrafish: Translation of findings to man. Prog Biophys Mol Biol. 2018 Oct 1;138:45–58.

110. Salgado-Almario J, Vicente M, Vincent P, Domingo B, Llopis J. Mapping Calcium Dynamics in the Heart of Zebrafish Embryos with Ratiometric Genetically Encoded Calcium Indicators. Int J Mol Sci. 2020 Sep 10;21(18):6610.

111. Nemtsas P, Wettwer E, Christ T, Weidinger G, Ravens U. Adult zebrafish heart as a model for human heart? An electrophysiological study. J Mol Cell Cardiol. 2010 Jan 1;48(1):161–71.

112. Liu C, Cao R, Xu Y, Li T, Li F, Chen S, et al. Rare copy number variants analysis identifies novel candidate genes in heterotaxy syndrome patients with congenital heart defects. Genome Med. 2018 May 30;10(1):40.

113. Noël ES, Momenah TS, Al-Dagriri K, Al-Suwaid A, Al-Shahrani S, Jiang H, et al. A Zebrafish Loss-of-Function Model for Human CFAP53 Mutations Reveals Its Specific Role in Laterality Organ Function. Hum Mutat. 2016;37(2):194–200.

114. Covassin LD, Villefranc JA, Kacergis MC, Weinstein BM, Lawson ND. Distinct genetic interactions between multiple Vegf receptors are required for development of different blood vessel types in zebrafish. Proc Natl Acad Sci U S A. 2006 Apr 25;103(17):6554–9.

115. Jin D, Zhu D, Fang Y, Chen Y, Yu G, Pan W, et al. Vegfa signaling regulates diverse artery/vein formation in vertebrate vasculatures. J Genet Genomics Yi Chuan Xue Bao. 2017 Oct 20;44(10):483–92.

116. Abraham S, Yeo M, Montero-Balaguer M, Paterson H, Dejana E, Marshall CJ, et al. VE-Cadherin-mediated cell-cell interaction suppresses sprouting via signaling to MLC2 phosphorylation. Curr Biol CB. 2009 Apr 28;19(8):668–74.

117. Gu G, Na Y, Chung H, Seok SH, Lee HY. Zebrafish Larvae Model of Dilated Cardiomyopathy Induced by Terfenadine. Korean Circ J. 2017 Nov;47(6):960–9.

118. Milan DJ, Peterson TA, Ruskin JN, Peterson RT, MacRae CA. Drugs That Induce Repolarization Abnormalities Cause Bradycardia in Zebrafish. Circulation. 2003 Mar 18;107(10):1355–8.

119. Wiggenhauser LM, Qi H, Stoll SJ, Metzger L, Bennewitz K, Poschet G, et al. Activation of Retinal Angiogenesis in Hyperglycemic pdx1−/− Zebrafish Mutants. Diabetes. 2020 Mar 5;69(5):1020–31.

120. Yabu T, Tomimoto H, Taguchi Y, Yamaoka S, Igarashi Y, Okazaki T. Thalidomide-induced antiangiogenic action is mediated by ceramide through depletion of VEGF receptors, and is antagonized by sphingosine-1-phosphate. Blood. 2005 Jul 1;106(1):125–34.

121. Williams KJ. The introduction of "chemotherapy" using arsphenamine - the first magic bullet. J R Soc Med. 2009 Aug;102(8):343–8.

122. Science History Institute [Internet]. 2016 [cited 2023 Jan 15]. Alexander Fleming. Available from: https://sciencehistory.org/historical-profile/alexander-fleming

123. Li JWH, Vederas JC. Drug Discovery and Natural Products: End of an Era or an Endless Frontier? Science. 2009 Jul 10;325(5937):161–5.

124. Westhoff JH, Steenbergen PJ, Thomas LSV, Heigwer J, Bruckner T, Cooper L, et al. In vivo High-Content Screening in Zebrafish for Developmental Nephrotoxicity of Approved Drugs. Front Cell Dev Biol. 2020;8:583.

125. Terstappen GC, Schlüpen C, Raggiaschi R, Gaviraghi G. Target deconvolution strategies in drug discovery. Nat Rev Drug Discov. 2007 Nov;6(11):891–903.

126. Kola I, Landis J. Can the pharmaceutical industry reduce attrition rates? Nat Rev Drug Discov. 2004;3(8):711–5.

127. Nosengo N. Can you teach old drugs new tricks? Nature. 2016 Jun 1;534(7607):314–6.

128. Rennane S, Baker L, Mulcahy A. Estimating the Cost of Industry Investment in Drug Research and Development: A Review of Methods and Results. Inq J Med Care Organ Provis Financ. 2022 Feb 16;58:00469580211059731.

129. Roessler HI, Knoers NVAM, van Haelst MM, van Haaften G. Drug Repurposing for Rare Diseases. Trends Pharmacol Sci. 2021 Apr 1;42(4):255–67.

130. Patton EE, Zon LI, Langenau DM. Zebrafish disease models in drug discovery: from preclinical modelling to clinical trials. Nat Rev Drug Discov. 2021 Aug;20(8):611–28.

131. Shi M, Sekulovski N, MacLean JA II, Whorton A, Hayashi K. Prenatal Exposure to Bisphenol A Analogues on Female Reproductive Functions in Mice. Toxicol Sci. 2019 Apr 1;168(2):561–71.

132. Guzmán C, Cabrera R, Cárdenas M, Larrea F, Nathanielsz PW, Zambrano E. Protein restriction during fetal and neonatal development in the rat alters reproductive function and accelerates reproductive ageing in female progeny. J Physiol. 2006 Apr 1;572(Pt 1):97–108.

133. Peterson RT, Link BA, Dowling JE, Schreiber SL. Small molecule developmental screens reveal the logic and timing of vertebrate development. Proc Natl Acad Sci U S A. 2000 Nov 21;97(24):12965–9.

134. Kais B, Schneider KE, Keiter S, Henn K, Ackermann C, Braunbeck T. DMSO modifies the permeability of the zebrafish (Danio rerio) chorion-implications for the fish embryo test (FET). Aquat Toxicol Amst Neth. 2013 Sep 15;140–141:229–38.

135. Rammler DH, Zaffaroni A. Biological implications of DMSO based on a review of its chemical properties. Ann N Y Acad Sci. 1967 Mar 15;141(1):13–23.

136. OECD. Guidance Document on Aquatic Toxicity Testing of Difficult Sub-stances and Mixtures. Paris, France: Organization for Economic Cooperation and Develop-ment (OECD); 2000. (OECD Series on Testing and Assessment No. 23,ENV/JM/MONO(2000)6.).

137. Hallare AV, Köhler HR, Triebskorn R. Developmental toxicity and stress protein responses in zebrafish embryos after exposure to diclofenac and its solvent, DMSO. Chemosphere. 2004 Aug;56(7):659–66.

138. Hamm JT, Ceger P, Allen D, Stout M, Maull EA, Baker G, et al. Characterizing sources of variability in zebrafish embryo screening protocols. ALTEX. 2019;36(1):103–20.

139. Vedder VL. Angiogenesis in zebrafish. University of Osnabrueck; 2018.

140. Bussmann J, Lawson N, Zon L, Schulte-Merker S, Zebrafish Nomenclature Committee. Zebrafish VEGF receptors: a guideline to nomenclature. PLoS Genet. 2008 May 30;4(5):e1000064.

141. Drugs.com [Internet]. [cited 2018 Jul 6]. List of VEGF/VEGFR inhibitors. Available from: https://www.drugs.com/drug-class/vegf-vegfr-inhibitors.html

142. Kanada M, Zhang J, Yan L, Sakurai T, Terakawa S. Endothelial cell-initiated extravasation of cancer cells visualized in zebrafish. PeerJ. 2014 Dec 23;2:e688.

143. Engebretsen I, Munkhaugen J, Bugge C, Halvorsen S, Ødegaard KM, Støvring H, et al. Gaps and discontinuation of statin treatment in Norway: potential for optimizing management of lipid lowering drugs. Eur Heart J Open. 2022 Oct 27;2(6):oeac070.

144. Yee HS, Fong NT. Atorvastatin in the Treatment of Primary Hypercholesterolemia and Mixed Dyslipidemias. Ann Pharmacother. 1998 Oct 1;32(10):1030–43.

145. FDA. LIPITOR (Atorvastatin calcium) Safety Datasheet. 2009 [cited 2024 May 3]. 020702s056lbl.pdf. Available from: https://www.accessdata.fda.gov/drugsatfda_docs/label/2009/020702s056lbl.pdf

146. McIver LA, Siddique MS. Atorvastatin. In: StatPearls [Internet]. Treasure Island (FL): StatPearls Publishing; 2022 [cited 2022 Nov 23]. Available from: http://www.ncbi.nlm.nih.gov/books/NBK430779/

147. Administration (TGA) TG. Therapeutic Goods Administration (TGA). Therapeutic Goods Administration (TGA); 2022 [cited 2022 Dec 30]. Prescribing medicines in pregnancy database. Available from: https://www.tga.gov.au/products/medicines/find-information-about-medicine/prescribing-medicines-pregnancy-database

148. Kim MS, Jin SJ, Kim JS, Park HJ, Song HS, Neubert RHH, et al. Preparation, characterization and in vivo evaluation of amorphous atorvastatin calcium nanoparticles using supercritical antisolvent (SAS) process. Eur J Pharm Biopharm Off J Arbeitsgemeinschaft Pharm Verfahrenstechnik EV. 2008 Jun;69(2):454–65.

149. MacDonald JS, Halleck MM. The toxicology of HMG-CoA reductase inhibitors: prediction of human risk. Toxicol Pathol. 2004;32 Suppl 2:26–41.

150. Kong R, Zhu X, Meteleva ES, Polyakov NE, Khvostov MV, Baev DS, et al. Atorvastatin calcium inclusion complexation with polysaccharide arabinogalactan and saponin disodium glycyrrhizate for increasing of solubility and bioavailability. Drug Deliv Transl Res. 2018 Oct 1;8(5):1200–13.

151. Maerz LD, Burkhalter MD, Schilpp C, Wittekindt OH, Frick M, Philipp M. Pharmacological cholesterol depletion disturbs ciliogenesis and ciliary function in developing zebrafish. Commun Biol. 2019 Jan 29;2(1):1–13.

152. Crilly S, Njegic A, Parry-Jones AR, Allan SM, Kasher PR. Using Zebrafish Larvae to Study the Pathological Consequences of Hemorrhagic Stroke. J Vis Exp. 2019 Jun 5;(148):59716.

153. Augustine-Rauch K, Zhang CX, Panzica-Kelly JM. A Developmental Toxicology Assay Platform for Screening Teratogenic Liability of Pharmaceutical Compounds. Birth Defects Res B Dev Reprod Toxicol. 2016;107(1):4–20.

154. K. AAR. Predictive Teratology: Teratogenic Risk-Hazard Identification Partnered in the Discovery Process. Curr Drug Metab. 2008 Oct 31;9(9):971–7.

155. Uguz F. Selective serotonin reuptake inhibitors and the risk of congenital anomalies: a systematic review of current meta-analyses. Expert Opin Drug Saf. 2020 Dec;19(12):1595–604.

156. Colvin L, Walters BN. The Use of Angiotensin Converting Enzyme Inhibitors during the First Trimester of Pregnancy. J Pharmacovigil. 2016;2(3).

157. Hernandez RK, Werler MM, Romitti P, Sun L, Anderka M, National Birth Defects Prevention Study. Nonsteroidal antiinflammatory drug use among women and the risk of birth defects. Am J Obstet Gynecol. 2012 Mar;206(3):228.e1-8.

158. Dathe K, Schaefer C. The Use of Medication in Pregnancy. Dtsch Ärztebl Int. 2019 Nov;116(46):783–90.

159. Huybrechts KF, Bröms G, Christensen LB, Einarsdóttir K, Engeland A, Furu K, et al. Association Between Methylphenidate and Amphetamine Use in Pregnancy and Risk of Congenital Malformations: A Cohort Study From the International Pregnancy Safety Study Consortium. JAMA Psychiatry. 2018 Feb 1;75(2):167–75.

160. Halpern DG, Weinberg CR, Pinnelas R, Mehta-Lee S, Economy KE, Valente AM. Use of Medication for Cardiovascular Disease During Pregnancy: JACC State-of-the-Art Review. J Am Coll Cardiol. 2019 Feb 5;73(4):457–76.

161. Barrow P. Review of embryo-fetal developmental toxicity studies performed for pharmaceuticals approved by FDA in 2016 and 2017. Reprod Toxicol. 2018 Sep 1;80:117–25.

162. Flint OP. In vitro tests for teratogens: desirable endpoints, test batteries and current status of the micromass teratogen test. Reprod Toxicol Elmsford N. 1993;7 Suppl 1:103–11.

163. Webster WS, Brown-Woodman PD, Ritchie HE. A review of the contribution of whole embryo culture to the determination of hazard and risk in teratogenicity testing. Int J Dev Biol. 1997 Apr;41(2):329–35.

164. Braunbeck T, Boettcher M, Hollert H, Kosmehl T, Lammer E, Leist E, et al. Towards an alternative for the acute fish LC(50) test in chemical assessment: the fish embryo toxicity test goes multi-species -- an update. ALTEX. 2005;22(2):87–102.

165. Lammer E, Carr GJ, Wendler K, Rawlings JM, Belanger SE, Braunbeck T. Is the fish embryo toxicity test (FET) with the zebrafish (Danio rerio) a potential alternative for the fish acute toxicity test? Comp Biochem Physiol Toxicol Pharmacol CBP. 2009 Mar;149(2):196–209.

166. Panzica-Kelly JM, Zhang CX, Danberry TL, Flood A, DeLan JW, Brannen KC, et al. Morphological score assignment guidelines for the dechorionated zebrafish teratogenicity assay. Birth Defects Res B Dev Reprod Toxicol. 2010 Oct;89(5):382–95.

167. Brannen KC, Panzica-Kelly JM, Danberry TL, Augustine-Rauch KA. Development of a zebrafish embryo teratogenicity assay and quantitative prediction model. Birth Defects Res B Dev Reprod Toxicol. 2010;89(1):66–77.

168. Augustine-Rauch K, Zhang CX, Panzica-Kelly JM. In vitro developmental toxicology assays: A review of the state of the science of rodent and zebrafish whole embryo culture and embryonic stem cell assays. Birth Defects Res Part C Embryo Today Rev. 2010 Jun;90(2):87–98.

169. Jarque S, Rubio-Brotons M, Ibarra J, Ordoñez V, Dyballa S, Miñana R, et al. Morphometric analysis of developing zebrafish embryos allows predicting teratogenicity modes of action in higher vertebrates. Reprod Toxicol. 2020 Sep 1;96:337–48.

170. Chung R, Ghosh AK, Banerjee A. Cardiotoxicity: precision medicine with imprecise definitions. Open Heart. 2018 Jul;5(2):e000774.

171. Cardinale DM, Zaninotto M, Cipolla CM, Passino C, Plebani M, Clerico A. Cardiotoxic effects and myocardial injury: the search for a more precise definition of drug cardiotoxicity. Clin Chem Lab Med CCLM. 2021 Jan 1;59(1):51–7.

172. Ferdinandy P, Baczkó I, Bencsik P, Giricz Z, Görbe A, Pacher P, et al. Definition of hidden drug cardiotoxicity: paradigm change in cardiac safety testing and its clinical implications. Eur Heart J. 2019 Jun 7;40(22):1771–7.

173. López-Sendón J, Álvarez-Ortega C, Zamora Auñon P, Buño Soto A, Lyon AR, Farmakis D, et al. Classification, prevalence, and outcomes of anticancer therapy-induced cardiotoxicity: the CARDIOTOX registry. Eur Heart J. 2020 May 7;41(18):1720–9.

174. Zakaria ZZ, Benslimane FM, Nasrallah GK, Shurbaji S, Younes NN, Mraiche F, et al. Using Zebrafish for Investigating the Molecular Mechanisms of Drug-Induced Cardiotoxicity. BioMed Res Int. 2018 Sep 27;2018:1–10.

175. Huang C, Zhang X, Ramil JM, Rikka S, Kim L, Lee Y, et al. Juvenile Exposure to Anthracyclines Impairs Cardiac Progenitor Cell Function and Vascularization Resulting in Greater Susceptibility to Stress-Induced Myocardial Injury in Adult Mice. Circulation. 2010 Feb 9;121(5):675–83.

176. Pardo Sanz A, Zamorano JL. 'Cardiotoxicity': time to define new targets? Eur Heart J. 2020 May 7;41(18):1730–2.

177. Westerfield M. The zebrafish book. A guide for the laboratory use of zebrafish (Danio rerio). 4th ed. Univ. of Oregon Press, Eugene.; 2000.

178. Lawson ND, Weinstein BM. In vivo imaging of embryonic vascular development using transgenic zebrafish. Dev Biol. 2002 Aug 15;248(2):307–18.

179. Thompson MA, Ransom DG, Pratt SJ, MacLennan H, Kieran MW, Detrich HW, et al. The cloche and spadetail genes differentially affect hematopoiesis and vasculogenesis. Dev Biol. 1998 May 15;197(2):248–69.

180. Kimmel CB, Ballard WW, Kimmel SR, Ullmann B, Schilling TF. Stages of embryonic development of the zebrafish. Dev Dyn Off Publ Am Assoc Anat. 1995 Jul;203(3):253–310.

181. Poureetezadi SJ, Donahue EK, Wingert RA. A Manual Small Molecule Screen Approaching High-throughput Using Zebrafish Embryos. JoVE J Vis Exp. 2014 Nov 8;(93):e52063.

182. Wittbrodt JN, Liebel U, Gehrig J. Generation of orientation tools for automated zebrafish screening assays using desktop 3D printing. BMC Biotechnol. 2014 May 1;14:36.

183. Pandey G, Westhoff JH, Schaefer F, Gehrig J. A Smart Imaging Workflow for Organ-Specific Screening in a Cystic Kidney Zebrafish Disease Model. Int J Mol Sci. 2019 Mar 14;20(6):1290.

184. Schindelin J, Arganda-Carreras I, Frise E, Kaynig V, Longair M, Pietzsch T, et al. Fiji: an open-source platform for biological-image analysis. Nat Methods. 2012 Jun 28;9(7):676–82.

185. Vedder VL, Reinberger T, Haider SMI, Eichelmann L, Odenthal N, Abdelilah-Seyfried S, et al. pyHeart4Fish: Chamber-specific heart phenotype quantification of zebrafish in high-content screens. Front Cell Dev Biol. 2023 Apr 11;11:1143852.

186. Virtanen P, Gommers R, Oliphant TE, Haberland M, Reddy T, Cournapeau D, et al. SciPy 1.0: fundamental algorithms for scientific computing in Python. Nat Methods. 2020 Mar;17(3):261–72.

187. Trinh LA, McCutchen MD, Bonner-Fraser M, Fraser SE, Bumm LA, McCauley DW. Fluorescent in situ hybridization employing the conventional NBT/BCIP chromogenic stain. BioTechniques. 2007 Jun;42(6):756–9.

188. Thisse C, Thisse B. High-resolution in situ hybridization to whole-mount zebrafish embryos. Nat Protoc. 2008 Jan;3(1):59–69.

189. Breuer M. Characterizing the function and role of three dihydropteridine reductase homologs, Qdpra, Qdprb1 and Qdprb2 in the embryonic development of Danio rerio [Internet]. [Heidelberg, Germany]: Ruprecht-Karls-University of Heidelberg; 2018. Available from: https://archiv.ub.uni-heidelberg.de/volltextserver/24357/1/Dissertation%20Complete_MaximilianBreuer.pdf

190. Gupta T, Mullins MC. Dissection of Organs from the Adult Zebrafish. JoVE J Vis Exp. 2010 Mar 4;(37):e1717.

191. Fischer AH, Jacobson KA, Rose J, Zeller R. Cryosectioning Tissues. Cold Spring Harb Protoc. 2008 Aug 1;2008(8):pdb.prot4991.

192. McCurley AT, Callard GV. Characterization of housekeeping genes in zebrafish: male-female differences and effects of tissue type, developmental stage and chemical treatment. BMC Mol Biol. 2008 Nov 12;9(1):102.

193. Livak KJ, Schmittgen TD. Analysis of relative gene expression data using real-time quantitative PCR and the 2(-Delta Delta C(T)) Method. Methods San Diego Calif. 2001 Dec;25(4):402–8.

194. Schrödinger Release 2022-3. New York: Schrödinger, LLC; 2021.

195. Lu C, Wu C, Ghoreishi D, Chen W, Wang L, Damm W, et al. OPLS4: Improving Force Field Accuracy on Challenging Regimes of Chemical Space. J Chem Theory Comput. 2021 Jul 13;17(7):4291–300.

196. Protein Data Bank | Nucleic Acids Research | Oxford Academic [Internet]. [cited 2022 Sep 15]. Available from: https://academic.oup.com/nar/article/28/1/235/2384399

197. Berman HM, Westbrook J, Feng Z, Gilliland G, Bhat TN, Weissig H, et al. The Protein Data Bank. Nucleic Acids Res. 2000 Jan 1;28(1):235–42.

198. Edman K, Hosseini A, Bjursell MK, Aagaard A, Wissler L, Gunnarsson A, et al. Ligand Binding Mechanism in Steroid Receptors: From Conserved Plasticity to Differential Evolutionary Constraints. Structure. 2015 Dec;23(12):2280–90.

199. Madhavi Sastry G, Adzhigirey M, Day T, Annabhimoju R, Sherman W. Protein and ligand preparation: parameters, protocols, and influence on virtual screening enrichments. J Comput Aided Mol Des. 2013 Mar 1;27(3):221–34.

200. Marchler-Bauer A, Bryant SH. CD-Search: protein domain annotations on the fly. Nucleic Acids Res. 2004 Jul 1;32(Web Server issue):W327-331.

201. Jacobson MP, Pincus DL, Rapp CS, Day TJF, Honig B, Shaw DE, et al. A hierarchical approach to all-atom protein loop prediction. Proteins Struct Funct Bioinforma. 2004;55(2):351–67.

202. Greenwood JR, Calkins D, Sullivan AP, Shelley JC. Towards the comprehensive, rapid, and accurate prediction of the favorable tautomeric states of drug-like molecules in aqueous solution. J Comput Aided Mol Des. 2010 Jun 1;24(6):591–604.

203. Schrödinger Release 2022-3: LigPrep. New York: Schrödinger, LLC; 2021.

204. Jumper J, Evans R, Pritzel A, Green T, Figurnov M, Ronneberger O, et al. Highly accurate protein structure prediction with AlphaFold. Nature. 2021 Aug;596(7873):583–9.

205. Varadi M, Anyango S, Deshpande M, Nair S, Natassia C, Yordanova G, et al. AlphaFold Protein Structure Database: massively expanding the structural coverage of protein-sequence space with high-accuracy models. Nucleic Acids Res. 2022 Jan 7;50(D1):D439–44.

206. Smith TF, Waterman MS. Identification of common molecular subsequences. J Mol Biol. 1981 Mar 25;147(1):195–7.

207. Altschul SF, Gish W, Miller W, Myers EW, Lipman DJ. Basic local alignment search tool. J Mol Biol. 1990 Oct 5;215(3):403–10.

208. Martins WS, Del Cuvillo JB, Useche FJ, Theobald KB, Gao GR. A multithreaded parallel implementation of a dynamic programming algorithm for sequence comparison. In: Biocomputing 2001. Mauna Lani, Hawaii: WORLD SCIENTIFIC; 2000. p. 311–22.

209. The UniProt Consortium. UniProt: the universal protein knowledgebase in 2021. Nucleic Acids Res. 2021 Jan 8;49(D1):D480–9.

210. Goldstein T, Studer C, Baraniuk R. FASTA: A Generalized Implementation of Forward-Backward Splitting [Internet]. arXiv; 2016 Jan [cited 2022 Sep 21]. Report No.: arXiv:1501.04979. Available from: http://arxiv.org/abs/1501.04979

211. Bridgham JT, Ortlund EA, Thornton JW. An epistatic ratchet constrains the direction of glucocorticoid receptor evolution. Nature. 2009 Sep 24;461(7263):515–9.

212. Sun Z, Liu Q, Qu G, Feng Y, Reetz MT. Utility of B-Factors in Protein Science: Interpreting Rigidity, Flexibility, and Internal Motion and Engineering Thermostability. Chem Rev. 2019 Feb 13;119(3):1626–65.

213. Mulnaes D, Gohlke H. TopScore: Using Deep Neural Networks and Large Diverse Data Sets for Accurate Protein Model Quality Assessment. J Chem Theory Comput. 2018 Nov 13;14(11):6117–26.

214. Ramachandran GN, Ramakrishnan C, Sasisekharan V. Stereochemistry of polypeptide chain configurations. J Mol Biol. 1963 Jul 1;7(1):95–9.

215. Nelson DL, Cox MM, Lehninger AL, Nelson DL. Lehninger Biochemie: mit 131 Tabellen. 4., vollst. überarb. und erw. Aufl., Übers. der 5. amerikan. Aufl., korr. Nachdr. Berlin Heidelberg: Springer; 2011. 1667 p. (Springer-Lehrbuch).

216. Mannige RV. An exhaustive survey of regular peptide conformations using a new metric for backbone handedness (h). PeerJ. 2017 May 16;5:e3327.

217. Anderson RJ, Weng Z, Campbell RK, Jiang X. Main-chain conformational tendencies of amino acids. Proteins Struct Funct Bioinforma. 2005;60(4):679–89.

218. Corpet F. Multiple sequence alignment with hierarchical clustering. Nucleic Acids Res. 1988 Nov 25;16(22):10881–90.

219. Biggadike K, Bledsoe RK, Hassell AM, Kirk BE, McLay IM, Shewchuk LM, et al. X-ray Crystal Structure of the Novel Enhanced-Affinity Glucocorticoid Agonist Fluticasone Furoate in the Glucocorticoid Receptor−Ligand Binding Domain. J Med Chem. 2008 Jun 1;51(12):3349–52.

220. Farid R, Day T, Friesner RA, Pearlstein RA. New insights about HERG blockade obtained from protein modeling, potential energy mapping, and docking studies. Bioorg Med Chem. 2006 May 1;14(9):3160–73.

221. Sherman W, Day T, Jacobson MP, Friesner RA, Farid R. Novel Procedure for Modeling Ligand/Receptor Induced Fit Effects. J Med Chem. 2006 Jan 1;49(2):534–53.

222. Kaushik AC, Kumar S, Wei DQ, Sahi S. Structure Based Virtual Screening Studies to Identify Novel Potential Compounds for GPR142 and Their Relative Dynamic Analysis for Study of Type 2 Diabetes. Front Chem. 2018;6.

223. Friesner RA, Murphy RB, Repasky MP, Frye LL, Greenwood JR, Halgren TA, et al. Extra Precision Glide: Docking and Scoring Incorporating a Model of Hydrophobic Enclosure for Protein−Ligand Complexes. J Med Chem. 2006 Oct 1;49(21):6177–96.

224. Kainkaryam RM, Woolf PJ. Pooling in high-throughput drug screening. Curr Opin Drug Discov Devel. 2009 May;12(3):339–50.

225. Avdesh A, Chen M, Martin-Iverson MT, Mondal A, Ong D, Rainey-Smith S, et al. Regular Care and Maintenance of a Zebrafish (Danio rerio) Laboratory: An Introduction. J Vis Exp JoVE. 2012 Nov 18;(69):4196.

226. Christou M, Kavaliauskis A, Ropstad E, Fraser TWK. DMSO effects larval zebrafish (Danio rerio) behavior, with additive and interaction effects when combined with positive controls. Sci Total Environ. 2020 Mar 20;709:134490.

227. Thaler R, Spitzer S, Karlic H, Klaushofer K, Varga F. DMSO is a strong inducer of DNA hydroxymethylation in pre-osteoblastic MC3T3-E1 cells. Epigenetics. 2012 Jun 1;7(6):635–51.

228. Tannenbaum J, Bennett BT. Russell and Burch's 3Rs Then and Now: The Need for Clarity in Definition and Purpose. J Am Assoc Lab Anim Sci JAALAS. 2015 Mar;54(2):120–32.

229. Russell WMS, Burch RL. The principles of humane experimental technique. Methuen; 1959.

230. Gandin V, Fernandes AP, Rigobello MP, Dani B, Sorrentino F, Tisato F, et al. Cancer cell death induced by phosphine gold(I) compounds targeting thioredoxin reductase. Biochem Pharmacol. 2010 Jan 15;79(2):90–101.

231. Furst DE. Mechanism of action, pharmacology, clinical efficacy and side effects of auranofin. An orally administered organic gold compound for the treatment of rheumatoid arthritis. Pharmacotherapy. 1983;3(5):284–98.

232. Messori L, Marcon G. Gold complexes in the treatment of rheumatoid arthritis. Met Ions Biol Syst. 2004;41:279–304.

233. Open Targets Platform [Internet]. [cited 2022 Apr 4]. Available from: https://platform.opentargets.org/

234. Drugs and Supplements - Drugs and Supplements - Mayo Clinic [Internet]. [cited 2022 Apr 4]. Available from: https://www.mayoclinic.org/drugs-supplements

235. Li C, Chen L, Song M, Fang Z, Zhang L, Coffie JW, et al. Ferulic acid protects cardiomyocytes from TNF-α/cycloheximide-induced apoptosis by regulating autophagy. Arch Pharm Res. 2020 Aug;43(8):863–74.

236. Li Y, Li S, Chen M, Xiao J, Fang H. Synergistic effect of pyrvinium pamoate and posaconazole against Cryptococcus neoformans in vitro and in vivo. Front Cell Infect Microbiol. 2022;12:1074903.

237. Schultz CW, Nevler A. Pyrvinium Pamoate: Past, Present, and Future as an Anti-Cancer Drug. Biomedicines. 2022 Dec;10(12):3249.

238. van den Boorn JG, Picavet DI, van Swieten PF, van Veen HA, Konijnenberg D, van Veelen PA, et al. Skin-depigmenting agent monobenzone induces potent T-cell autoimmunity toward pigmented cells by tyrosinase haptenation and melanosome autophagy. J Invest Dermatol. 2011 Jun;131(6):1240–51.

239. Turnbull RS. Benzydamine Hydrochloride (Tantum) in the management of oral inflammatory conditions. J Can Dent Assoc. 1995 Feb;61(2):127–34.

240. Passali D, Barat V, Cadevall O, Freire HM, Grattagliano I, Gutu I, et al. International Delphi-based consensus on the appropriate use and effect of Benzydamine hydrochloride in the treatment of sore throat. BMC Prim Care. 2022 Nov 23;23:296.

241. Blackwell GJ, Flower RJ, Vane JR. Some characteristics of the prostaglandin synthesizing system in rabbit kidney microsomes. Biochim Biophys Acta. 1975 Jul 22;398(1):178–90.

242. Modéer T, Yucel-Lindberg T. Benzydamine reduces prostaglandin production in human gingival fibroblasts challenged with interleukin-1 beta or tumor necrosis factor alpha. Acta Odontol Scand. 1999 Feb;57(1):40–5.

243. Krzeszowski W, Wilczyński J, Grzesiak M, Nowakowska D. Prenatal Sonographic Diagnosis of Premature Constriction of the Fetal Ductus Arteriosus After Maternal Self-Medication With Benzydamine Hydrochloride. J Ultrasound Med. 2015;34(3):531–5.

244. Smyj R, Wang XP, Han F. Chapter 7 - Pimozide. In: Brittain HG, editor. Profiles of Drug Substances, Excipients and Related Methodology. Academic Press; 2012. p. 287–311.

245. Zhu X, Ding S, Li H, Zhang Z, Xu L, Wu J, et al. Disruption of histamine/H1R signaling pathway represses cardiac differentiation and maturation of human induced pluripotent stem cells. Stem Cell Res Ther. 2020 Mar 4;11(1):27.

246. Garbarg M, Barbin G, Bischoff S, Pollard H, Schwartz JC. Evidence for a specific decarboxylase involved in histamine synthesis in an ascending pathway in rat brain. Agents Actions. 1974 Aug;4(3):181.

247. O'Mahony L, Akdis M, Akdis CA. Regulation of the immune response and inflammation by histamine and histamine receptors. J Allergy Clin Immunol. 2011 Dec 1;128(6):1153–62.

248. Peitsaro N, Sundvik M, Anichtchik OV, Kaslin J, Panula P. Identification of zebrafish histamine H1, H2 and H3 receptors and effects of histaminergic ligands on behavior. Biochem Pharmacol. 2007 Apr 15;73(8):1205–14.

249. Panula P, Chen YC, Baronio D, Lewis S, Sundvik M. The Histamine System in Zebrafish Brain: Organization, Receptors, and Behavioral Roles. In Berlin, Heidelberg: Springer; 2021. p. 1–12.

250. Hill SJ, Ganellin CR, Timmerman H, Schwartz JC, Shankley NP, Young JM, et al. International Union of Pharmacology. XIII. Classification of Histamine Receptors. Pharmacol Rev. 1997 Sep 1;49(3):253–78.

251. Branco ACCC, Yoshikawa FSY, Pietrobon AJ, Sato MN. Role of Histamine in Modulating the Immune Response and Inflammation. Mediators Inflamm. 2018 Aug 27;2018:e9524075.

252. Eckel L, Gristwood RW, Nawrath H, Owen DA, Satter P. Inotropic and electrophysiological effects of histamine on human ventricular heart muscle. J Physiol. 1982 Sep;330:111–23.

253. Overington JP, Al-Lazikani B, Hopkins AL. How many drug targets are there? Nat Rev Drug Discov. 2006 Dec;5(12):993–6.

254. Wang J, Al-Ouran R, Hu Y, Kim SY, Wan YW, Wangler MF, et al. MARRVEL: Integration of Human and Model Organism Genetic Resources to Facilitate Functional Annotation of the Human Genome. Am J Hum Genet. 2017 Jun 1;100(6):843–53.

255. Neumann J, Kirchhefer U, Dhein S, Hofmann B, Gergs U. The Roles of Cardiovascular H2-Histamine Receptors Under Normal and Pathophysiological Conditions. Front Pharmacol. 2021;12.

256. The histaminergic system regulates wakefulness and orexin/hypocretin neuron development via histamine receptor H1 in zebrafish. [cited 2023 May 24]; Available from: https://faseb.onlinelibrary.wiley.com/doi/10.1096/fj.11-188268

257. Reichmann F, Rimmer N, Tilley CA, Dalla Vecchia E, Pinion J, Al Oustah A, et al. The zebrafish histamine H3 receptor modulates aggression, neural activity and forebrain functional connectivity. Acta Physiol Oxf Engl. 2020 Dec;230(4):e13543.

258. Lewis S. Expression and effects of social defeat on histamine receptor expression in wild-type and hdc –/– zebrafish gut and brain. 2021.

259. Larkin MA, Blackshields G, Brown NP, Chenna R, McGettigan PA, McWilliam H, et al. Clustal W and Clustal X version 2.0. Bioinforma Oxf Engl. 2007 Nov 1;23(21):2947–8.

260. Facchinello N, Skobo T, Meneghetti G, Colletti E, Dinarello A, Tiso N, et al. nr3c1 null mutant zebrafish are viable and reveal DNA-binding-independent activities of the glucocorticoid receptor. Sci Rep. 2017 Jun 29;7(1):4371.

261. Taves MD, Gomez-Sanchez CE, Soma KK. Extra-adrenal glucocorticoids and mineralocorticoids: evidence for local synthesis, regulation, and function. Am J Physiol-Endocrinol Metab. 2011 Jul;301(1):E11–24.

262. Evans DH, Claiborne JB, editors. The physiology of fishes. 3rd ed. Boca Raton, FL: CRC, Taylor & Francis; 2006. 601 p. (Marine biology series).

263. Nicolaides NC, Galata Z, Kino T, Chrousos GP, Charmandari E. The human glucocorticoid receptor: Molecular basis of biologic function. Steroids. 2010 Jan 1;75(1):1–12.

264. Pratt WB. The role of heat shock proteins in regulating the function, folding, and trafficking of the glucocorticoid receptor. J Biol Chem. 1993 Oct 15;268(29):21455–8.

265. Dinarello A, Licciardello G, Fontana CM, Tiso N, Argenton F, Valle LD. Glucocorticoid receptor activities in the zebrafish model: a review. J Endocrinol. 2020 Dec 1;247(3):R63–82.

266. Lieberman BA, Bona BJ, Edwards DP, Nordeen SK. The constitution of a progesterone response element. Mol Endocrinol Baltim Md. 1993 Apr;7(4):515–27.

267. Oakley RH, Cidlowski JA. The biology of the glucocorticoid receptor: New signaling mechanisms in health and disease. J Allergy Clin Immunol. 2013 Nov 1;132(5):1033–44.

268. Lapp HE, Bartlett AA, Hunter RG. Stress and glucocorticoid receptor regulation of mitochondrial gene expression. J Mol Endocrinol. 2019 Feb 1;62(2):R121–8.

269. Schaaf MJM, Champagne D, van Laanen IHC, van Wijk DCWA, Meijer AH, Meijer OC, et al. Discovery of a Functional Glucocorticoid Receptor β-Isoform in Zebrafish. Endocrinology. 2008 Apr 1;149(4):1591–9.

270. Lewis-Tuffin LJ, Jewell CM, Bienstock RJ, Collins JB, Cidlowski JA. Human Glucocorticoid Receptor β Binds RU-486 and Is Transcriptionally Active. Mol Cell Biol. 2007 Mar;27(6):2266–82.

271. Otto C, Reichardt HM, Schütz G. Absence of glucocorticoid receptor-beta in mice. J Biol Chem. 1997 Oct 17;272(42):26665–8.

272. Chatzopoulou A, Schoonheim PJ, Torraca V, Meijer AH, Spaink HP, Schaaf MJM. Functional analysis reveals no transcriptional role for the glucocorticoid receptor β-isoform in zebrafish. Mol Cell Endocrinol. 2017 May 15;447:61–70.

273. Napier C, Pearce SHS. Current and emerging therapies for Addison's disease. Curr Opin Endocrinol Diabetes Obes. 2014 Jun;21(3):147–53.

274. Oakley RH, Cidlowski JA. Glucocorticoid Signaling in the Heart: A Cardiomyocyte Perspective. J Steroid Biochem Mol Biol. 2015 Sep;153:27–34.

275. Wei L, MacDonald TM, Walker BR. Taking glucocorticoids by prescription is associated with subsequent cardiovascular disease. Ann Intern Med. 2004 Nov 16;141(10):764–70.

276. Lin RCY, Wang XL, Morris BJ. Association of Coronary Artery Disease With Glucocorticoid Receptor N363S Variant. Hypertension. 2003 Mar;41(3):404–7.

277. Walker BR. Glucocorticoids and Cardiovascular Disease. Eur J Endocrinol. 2007 Nov 1;157(5):545–59.

278. Willi RA, Faltermann S, Hettich T, Fent K. Active Glucocorticoids Have a Range of Important Adverse Developmental and Physiological Effects on Developing Zebrafish Embryos. ACS Publ. 2017 Dec 22;

279. Rouillard AD, Gundersen GW, Fernandez NF, Wang Z, Monteiro CD, McDermott MG, et al. The harmonizome: a collection of processed datasets gathered to serve and mine knowledge about genes and proteins. Database. 2016 Jan 1;2016:baw100.

280. Kuleshov MV, Jones MR, Rouillard AD, Fernandez NF, Duan Q, Wang Z, et al. Enrichr: a comprehensive gene set enrichment analysis web server 2016 update. Nucleic Acids Res. 2016 Jul 8;44(W1):W90-97.

281. Wang J, Liu Z, Bellen HJ, Yamamoto S. Navigating MARRVEL, a Web-Based Tool that Integrates Human Genomics and Model Organism Genetics Information. JoVE J Vis Exp. 2019 Aug 15;(150):e59542.

282. Hu Y, Comjean A, Rodiger J, Liu Y, Gao Y, Chung V, et al. FlyRNAi.org-the database of the Drosophila RNAi screening center and transgenic RNAi project: 2021 update. Nucleic Acids Res. 2021 Jan 8;49(D1):D908–15.

283. Vandevyver S, Dejager L, Libert C. Comprehensive overview of the structure and regulation of the glucocorticoid receptor. Endocr Rev. 2014 Aug;35(4):671–93.

284. Kumar R, Thompson EB. Transactivation functions of the N-terminal domains of nuclear hormone receptors: protein folding and coactivator interactions. Mol Endocrinol Baltim Md. 2003 Jan;17(1):1–10.

285. Bledsoe RK, Montana VG, Stanley TB, Delves CJ, Apolito CJ, McKee DD, et al. Crystal structure of the glucocorticoid receptor ligand binding domain reveals a novel mode of receptor dimerization and coactivator recognition. Cell. 2002 Jul 12;110(1):93–105.

286. Whirledge S, Cidlowski JA. Glucocorticoids and Reproduction: Traffic Control on the Road to Reproduction. Trends Endocrinol Metab. 2017 Jun 1;28(6):399–415.

287. Schaaf MJM, Chatzopoulou A, Spaink HP. The zebrafish as a model system for glucocorticoid receptor research. Comp Biochem Physiol A Mol Integr Physiol. 2009 May;153(1):75–82.

288. He Y, Yi W, Suino-Powell K, Zhou XE, Tolbert WD, Tang X, et al. Structures and mechanism for the design of highly potent glucocorticoids. Cell Res. 2014 Jun;24(6):713–26.

289. Hemmerling M, Nilsson S, Edman K, Eirefelt S, Russell W, Hendrickx R, et al. Selective Nonsteroidal Glucocorticoid Receptor Modulators for the Inhaled Treatment of Pulmonary Diseases. J Med Chem. 2017 Oct 26;60(20):8591–605.

290. Wiederstein M, Sippl MJ. ProSA-web: interactive web service for the recognition of errors in three-dimensional structures of proteins. Nucleic Acids Res. 2007 May 8;35(Web Server):W407–10.

291. Stephenson A, Adams JW, Vaccarezza M. The vertebrate heart: an evolutionary perspective. J Anat. 2017;231(6):787–97.

292. Vornanen M, Hassinen M. Zebrafish heart as a model for human cardiac electrophysiology. Channels Austin Tex. 2016;10(2):101–10.

293. Ren B, Deng Y, Mukhopadhyay A, Lanahan AA, Zhuang ZW, Moodie KL, et al. ERK1/2-Akt1 crosstalk regulates arteriogenesis in mice and zebrafish. J Clin Invest. 2010 Apr;120(4):1217–28.

294. Liu Y, Asnani A, Zou L, Bentley VL, Yu M, Wang Y, et al. Visnagin protects against doxorubicin-induced cardiomyopathy through modulation of mitochondrial malate dehydrogenase. Sci Transl Med. 2014 Dec 10;6(266):266ra170.

295. Asimaki A, Kapoor S, Plovie E, Arndt AK, Adams E, Liu Z, et al. Identification of a New Modulator of the Intercalated Disc in a Zebrafish Model of Arrhythmogenic Cardiomyopathy. Sci Transl Med. 2014 Jun 11;6(240):240ra74.

296. Ravens U. Ionic basis of cardiac electrophysiology in zebrafish compared to human hearts. Prog Biophys Mol Biol. 2018 Oct;138:38–44.

297. Stoletov K, Fang L, Choi SH, Hartvigsen K, Hansen LF, Hall C, et al. Vascular lipid accumulation, lipoprotein oxidation, and macrophage lipid uptake in hypercholesterolemic zebrafish. Circ Res. 2009 Apr 24;104(8):952–60.

298. Postlethwait J, Amores A, Cresko W, Singer A, Yan YL. Subfunction partitioning, the teleost radiation and the annotation of the human genome. Trends Genet. 2004 Oct 1;20(10):481–90.

299. Gao M, Xin G, Qiu X, Wang Y, Liu G. Establishment of a rat model with diet-induced coronary atherosclerosis. J Biomed Res. 2017 Jan;31(1):47–55.

300. Huang S, Huang M, Tian S, Meng Z, Yan S, Teng M, et al. Imazalil and its metabolite imazalil-M caused developmental toxicity in zebrafish (Danio rerio) embryos via cell apoptosis mediated by metabolic disorders. Pestic Biochem Physiol. 2022 Jun 1;184:105113.

301. He MF, Gao XP, Li SC, He ZH, Chen N, Wang YB, et al. Anti-angiogenic effect of auranofin on HUVECs in vitro and zebrafish in vivo. Eur J Pharmacol. 2014 Oct 5;740:240–7.

302. Papaioannou M, Mylonas I, Kast RE, Brüning A. Disulfiram/copper causes redox-related proteotoxicity and concomitant heat shock response in ovarian cancer cells that is augmented by auranofin-mediated thioredoxin inhibition. Oncoscience. 2014;1(1):21–9.

303. Chirullo B, Sgarbanti R, Limongi D, Shytaj IL, Alvarez D, Das B, et al. A candidate anti-HIV reservoir compound, auranofin, exerts a selective "anti-memory" effect by exploiting the baseline oxidative status of lymphocytes. Cell Death Dis. 2013 Dec 5;4(12):e944.

304. Szabo KT, DiFebbo ME, Phelan DG. The effects of gold-containing compounds on pregnant rabbits and their fetuses. Vet Pathol. 1978 Aug;15 Suppl 5:97–102.

305. Gao XP, Feng F, Zhang XQ, Liu XX, Wang YB, She JX, et al. Toxicity assessment of 7 anticancer compounds in zebrafish. Int J Toxicol. 2014;33(2):98–105.

306. Newman TAC, Carleton CR, Leeke B, Hampton MB, Horsfield JA. Embryonic oxidative stress results in reproductive impairment for adult zebrafish. Redox Biol. 2015 Dec;6:648–55.

307. Gao XY, Li K, Jiang LL, He MF, Pu CH, Kang D, et al. Developmental toxicity of auranofin in zebrafish embryos. J Appl Toxicol. 2017;37(5):602–10.

308. Van der Veken B, De Meyer GRY, Martinet W. Axitinib attenuates intraplaque angiogenesis, haemorrhages and plaque destabilization in mice. Vascul Pharmacol. 2018 Jan;100:34–40.

309. Moreno Pedro R., Purushothaman K-Raman, Sirol Marc, Levy Andrew P., Fuster Valentin. Neovascularization in Human Atherosclerosis. Circulation. 2006 May 9;113(18):2245–52.

310. Kahanek N, Gelbard C, Hebert A. Desonide: a review of formulations, efficacy and safety. Expert Opin Investig Drugs. 2008 Jul 1;17(7):1097–104.

311. Liu B, Zhou H, Zhang T, Gao X, Tao B, Xing H, et al. Loss of endothelial glucocorticoid receptor promotes angiogenesis via upregulation of Wnt/β-catenin pathway. Angiogenesis. 2021 Aug;24(3):631–45.

312. Gull K, Dawson PJ, Davis C, Byard EH. Microtubules as target organelles for benzimidazole anthelmintic chemotherapy. Biochem Soc Trans. 1987 Feb;15(1):59–60.

313. Jordan MA, Wilson L. Microtubules as a target for anticancer drugs. Nat Rev Cancer. 2004 Apr;4(4):253–65.

314. Sultana T, Jan U, Lee JI. Double Repositioning: Veterinary Antiparasitic to Human Anticancer. Int J Mol Sci. 2022 Apr 13;23(8):4315.

315. Yoon J, Kwack WG, Shim WS, Lee JK, Jang DK, Gu N, et al. Quantitation of plasma and biliary cefpiramide concentrations in human samples using high-performance liquid chromatography. Biomed Chromatogr. 2020;34(12):e4957.

316. Briggs GG, Freeman RK, Yaffe SJ. Drugs in pregnancy and lactation: a reference guide to fetal and neonatal risk. 8th ed. Philadelphia: Wolters Kluwer - Lippincott Williams & Wilkins; 2008.

317. Parichy DM, Elizondo MR, Mills MG, Gordon TN, Engeszer RE. Normal table of postembryonic zebrafish development: Staging by externally visible anatomy of the living fish. Dev Dyn. 2009;238(12):2975–3015.

318. Maciuca AM, Munteanu AC, Mihaila M, Badea M, Olar R, Nitulescu GM, et al. A Study on Repositioning Nalidixic Acid via Lanthanide Complexation: Synthesis, Characterization, Cytotoxicity and DNA/Protein Binding Studies. Pharmaceuticals. 2022 Aug;15(8):1010.

319. Yang J, Hartjes KA, Nelson TJ, Xu X. Cessation of contraction induces cardiomyocyte remodeling during zebrafish cardiogenesis. Am J Physiol - Heart Circ Physiol. 2014 Feb 1;306(3):H382–95.

320. Murakoshi M, Saiki K, Urayama K, Sato TN. An Anthelmintic Drug, Pyrvinium Pamoate, Thwarts Fibrosis and Ameliorates Myocardial Contractile Dysfunction in a Mouse Model of Myocardial Infarction. PLOS ONE. 2013 Apr 11;8(11):e79374.

321. Barat R, Srinatha A, Pandit JK, Ridhurkar D, Balasubramaniam J, Mittal N, et al. Niridazole Biodegradable Inserts for Local Long-Term Treatment of Periodontitis: Possible New Life for an Orphan Drug. Drug Deliv. 2006 Jan 1;13(5):365–73.

322. Vardanyan RS, Hruby VJ. 38 - Antihelmintic Drugs. In: Vardanyan RS, Hruby VJ, editors. Synthesis of Essential Drugs. Amsterdam: Elsevier; 2006. p. 583–93.

323. Otubanjo OA, Mosuro AA. An in vivo evaluation of induction of abnormal sperm morphology by some anthelmintic drugs in mice. Mutat Res. 2001 Oct 18;497(1–2):131–8.

324. El-Beheiry AH, Kamel MN, Gad A. Niridazole and fertility in bilharzial men. Arch Androl. 1982 Jun;8(4):297–300.

325. Hof H, Ströder J. Antibacterial activity of GO 10213, a nitroimidazole derivative. Antimicrob Agents Chemother. 1986 May;29(5):953–4.

326. Wade WG, Addy M. Comparison of in vitro activity of niridazole, metronidazole and tetracycline against subgingival bacteria in chronic periodontitis. J Appl Bacteriol. 1987 Nov;63(5):455–7.

327. Hatt PY, Swynghedauw B, Hayat JC. Myocardial effects of niridazole. Ann N Y Acad Sci. 1969 Oct 6;160(2):799–810.

328. Dennis AT, Wang L, Wan H, Nassal D, Deschenes I, Ficker E. Molecular Determinants of Pentamidine-Induced hERG Trafficking Inhibition. Mol Pharmacol. 2012 Feb;81(2):198–209.

329. Sanguinetti MC, Tristani-Firouzi M. hERG potassium channels and cardiac arrhythmia. Nature. 2006 Mar 23;440(7083):463–9.

330. Oliver EA, Schwartz L, Warren LH. Occupational leukoderma: Preliminary report. J Am Med Assoc. 1939 Sep 2;113(10):927.

331. Boissy RE, Manga P. On the Etiology of Contact/Occupational Vitiligo. Pigment Cell Res. 2004;17(3):208–14.

332. van den Boorn JG, Konijnenberg D, Tjin EPM, Picavet DI, Meeuwenoord NJ, Filippov DV, et al. Effective Melanoma Immunotherapy in Mice by the Skin-Depigmenting Agent Monobenzone and the Adjuvants Imiquimod and CpG. PLoS ONE. 2010 May 13;5(5):e10626.

333. Kammeyer A, Willemsen KJ, Ouwerkerk W, Bakker WJ, Ratsma D, Pronk SD, et al. Mechanism of action of 4-substituted phenols to induce vitiligo and antimelanoma immunity. Pigment Cell Melanoma Res. 2019 Jul;32(4):540–52.

334. Zenker M, Klinge J, Krüger C, Singer H, Scharf J. Severe pulmonary hypertension in a neonate caused by premature closure of the ductus arteriosus following maternal treatment with diclofenac: a case report. J Perinat Med. 1998;26(3):231–4.

335. Chen IC, Chen HL, Liu YC, Wu YH, Lo SH, Hsu JH, et al. Unique Pulmonary Hypertension in Young Children: A Case Series Study. Children. 2022 Jul 17;9(7):1064.

336. Vonk Noordegraaf A, Westerhof BE, Westerhof N. The Relationship Between the Right Ventricle and its Load in Pulmonary Hypertension. J Am Coll Cardiol. 2017 Jan 17;69(2):236–43.

337. Nakajima H, Chiba A, Fukumoto M, Morooka N, Mochizuki N. Zebrafish Vascular Development: General and Tissue-Specific Regulation. J Lipid Atheroscler. 2021;10(2):145.

338. González-Rosa JM. Zebrafish Models of Cardiac Disease: From Fortuitous Mutants to Precision Medicine. Circ Res. 2022 Jun 10;130(12):1803–26.

339. Trinidad F, Rubonal F, Rodriguez de Castro I, Pirzadeh I, Gerrah R, Kheradvar A, et al. Effect of Blood Flow on Cardiac Morphogenesis and Formation of Congenital Heart Defects. J Cardiovasc Dev Dis. 2022 Sep;9(9):303.

340. Nielsen GL, Sørensen HT, Larsen H, Pedersen L. Risk of adverse birth outcome and miscarriage in pregnant users of non-steroidal anti-inflammatory drugs: population based observational study and case-control study. BMJ. 2001 Feb 3;322(7281):266–70.

341. Dathe K, Frank J, Padberg S, Hultzsch S, Beck E, Schaefer C. Fetal adverse effects following NSAID or metamizole exposure in the 2nd and 3rd trimester: an evaluation of the German Embryotox cohort. BMC Pregnancy Childbirth. 2022 Aug 26;22(1):666.

342. Committee on Safety of Medicines-Medicines Control Agency. Cardiac arrhythmias with pimozide (Orap) Current Problems in Pharmacovigilance. 1995;(21:1).

343. Mothi M, Sampson S. Pimozide for schizophrenia or related psychoses. Cochrane Database Syst Rev. 2013 Nov 5;(11):CD001949.

344. el-Sherif N, Turitto G. The long QT syndrome and torsade de pointes. Pacing Clin Electrophysiol PACE. 1999 Jan;22(1 Pt 1):91–110.

345. Stäubli M, Studer H. The effects of amiodarone on the electrocardiogram of the guinea-pig are not explained by interaction with thyroid hormone metabolism alone. Br J Pharmacol. 1986 Jun;88(2):405–10.

346. Perret G, Yin YL, Nicolas P, Pussard E, Vassy R, Uzzan B, et al. Amiodarone decreases cardiac beta-adrenoceptors through an antagonistic effect on 3,5,3' triiodothyronine. J Cardiovasc Pharmacol. 1992 Apr;19(4):473–8.

347. Berti P, Materazzi G, Bogazzi F, Ambrosini CE, Martino E, Miccoli P. Combination of minimally invasive thyroid surgery and local anesthesia associated to iopanoic acid for patients with amiodarone-induced thyrotoxicosis and severe cardiac disorders: a pilot study. Langenbecks Arch Surg. 2007 Nov;392(6):709–13.

348. Lindenmeyer M, Spörri S, Stäubli M, Studer A, Studer H. Does amiodarone affect heart rate by inhibiting the intracellular generation of triiodothyronine from thyroxine? Br J Pharmacol. 1984 May;82(1):275–80.

349. Chenard BL, Shalaby IA, Koe BK, Ronau RT, Butler TW, Prochniak MA, et al. Separation of alpha 1 adrenergic and N-methyl-D-aspartate antagonist activity in a series of ifenprodil compounds. J Med Chem. 1991 Oct;34(10):3085–90.

350. Tajima N, Karakas E, Grant T, Simorowski N, Diaz-Avalos R, Grigorieff N, et al. Activation of NMDA receptors and the mechanism of inhibition by ifenprodil. Nature. 2016 Jun;534(7605):63–8.

351. Kobayashi T, Washiyama K, Ikeda K. Inhibition of G protein-activated inwardly rectifying K+ channels by ifenprodil. Neuropsychopharmacol Off Publ Am Coll Neuropsychopharmacol. 2006 Mar;31(3):516–24.

352. Mizusawa H, Sakakibara E. [Effects of 2-(4-benzyl-piperidino)-1-(4-hydroxyphenyl)-1-propanol (ifenprodil) on the cardiovascular system in vivo]. Nihon Yakurigaku Zasshi Folia Pharmacol Jpn. 1975 Sep;71(6):597–608.

353. Borchard U, Hafner D, Hirth C. Electrophysiological actions of histamine and H1-, H2-receptor antagonists in cardiac tissue. Agents Actions. 1986 Apr;18(1–2):186–90.

354. Bernstein JA. Azelastine hydrochloride: a review of pharmacology, pharmacokinetics, clinical efficacy and tolerability. Curr Med Res Opin. 2007 Oct;23(10):2441–52.

355. Trybus E, Król T, Trybus W. The Multidirectional Effect of Azelastine Hydrochloride on Cervical Cancer Cells. Int J Mol Sci. 2022 May 24;23(11):5890.

356. Kar S, Krishnan A, Preetha K, Mohankar A. A review of antihistamines used during pregnancy. J Pharmacol Pharmacother. 2012;3(2):105–8.

357. Einis W. Über die Wirkung des Pituitrins und ß-Imidazoläthylamins (Histamins) auf die Herzaktion: Inaugural-Dissertation. Springer-Verlag; 2013. 26 p.

358. Kimura ET, Young PR, Richards RK. Pharmacologic properties of N-p-chloro-benzhydryl-N′-methyl homopiperazine dihydrochloride (homochlorcyclizine; SA-97), a serotonin antagonist. J Allergy. 1960 May 1;31(3):237–47.

359. Campaigne E. 3.15 - Thiophenes and their Benzo Derivatives: (iii) Synthesis and Applications. In: Katritzky AR, Rees CW, editors. Comprehensive Heterocyclic Chemistry. Oxford: Pergamon; 1984. p. 863–934.

360. Martínez-Romero M, Jonquet C, O'Connor MJ, Graybeal J, Pazos A, Musen MA. NCBO Ontology Recommender 2.0: an enhanced approach for biomedical ontology recommendation. J Biomed Semant. 2017 Jun 7;8(1):21.

361. Vardanyan R, Hruby V. Chapter 16 - Antihistamine Drugs. In: Vardanyan R, Hruby V, editors. Synthesis of Best-Seller Drugs. Boston: Academic Press; 2016. p. 247–63.

362. Shawky RM, Seifeldin NS. The relation between antihistamine medication during early pregnancy & birth defects. Egypt J Med Hum Genet. 2015 Oct 1;16(4):287–90.

363. Etwel F, Faught LH, Rieder MJ, Koren G. The Risk of Adverse Pregnancy Outcome After First Trimester Exposure to H1 Antihistamines: A Systematic Review and Meta-Analysis. Drug Saf. 2017 Feb;40(2):121–32.

364. Greferath U, Kambourakis M, Barth C, Fletcher EL, Murphy M. Characterization of histamine projections and their potential cellular targets in the mouse retina. Neuroscience. 2009 Jan 23;158(2):932–44.

365. Uhlén M, Fagerberg L, Hallström BM, Lindskog C, Oksvold P, Mardinoglu A, et al. Tissue-based map of the human proteome. Science. 2015 Jan 23;347(6220):1260419.

366. Tiligada K, Zampeli E, Sander K, Stark H. Histamine H 3 and H 4 receptors as novel drug targets. Expert Opin Investig Drugs. 2009 Oct 1;18:1519–31.

367. Zhang C, Yu Y, Ma L, Fu P. Histamine H3 Receptor Promotes Cell Survival via Regulating PKA/CREB/CDKN1A Signal Pathway in Hepatocellular Carcinoma. OncoTargets Ther. 2020 May 4;13:3765–76.

368. Wei Z, Wang L, Zhang M, Xuan J, Wang Y, Liu B, et al. A pharmacogenetic study of risperidone on histamine H3 receptor gene (HRH3) in Chinese Han schizophrenia patients. J Psychopharmacol (Oxf). 2012 Jun 1;26(6):813–8.

369. Godlewski G, Malinowska B, Buczko W, Schlicker E. Inhibitory H3 receptors on sympathetic nerves of the pithed rat: activation by endogenous histamine and operation in spontaneously hypertensive rats. Naunyn Schmiedebergs Arch Pharmacol. 1997 Jan 1;355(2):261–6.

370. Singh D, Piccinno A, Borrill Z, Poli G, Acerbi D, Meuleners L, et al. Tolerability of high cumulative doses of the HFA modulite beclomethasone dipropionate/formoterol combination inhaler in asthmatic patients. Pulm Pharmacol Ther. 2008 Jun 1;21(3):551–7.

371. Del Rosso JQ, Kircik L. A Comprehensive Review of Clocortolone Pivalate 0.1% Cream. J Clin Aesthetic Dermatol. 2012 Jul;5(7):20–4.

372. Hsu HJ, Liang MR, Chen CT, Chung B chu. Pregnenolone stabilizes microtubules and promotes zebrafish embryonic cell movement. Nature. 2006 Jan;439(7075):480–3.

373. Desonide (Topical Application Route) Side Effects - Mayo Clinic [Internet]. [cited 2023 Jan 20]. Available from: https://www.mayoclinic.org/drugs-supplements/desonide-topical-application-route/side-effects/drg-20073898?p=1

374. Gallina D, Zelinka C, Fischer AJ. Glucocorticoid receptors in the retina, Müller glia and the formation of Müller glia-derived progenitors. Dev Camb Engl. 2014 Sep;141(17):3340–51.

375. Natsaridis E, Perdikaris P, Fokos S, Dermon CR. Neuronal and Astroglial Localization of Glucocorticoid Receptor GRα in Adult Zebrafish Brain (Danio rerio). Brain Sci. 2023 Jun;13(6):861.

376. Haynes EM, Ulland TK, Eliceiri KW. A Model of Discovery: The Role of Imaging Established and Emerging Non-mammalian Models in Neuroscience. Front Mol Neurosci [Internet]. 2022 [cited 2023 Jun 18];15. Available from: https://www.frontiersin.org/articles/10.3389/fnmol.2022.867010

377. Remington LA. Chapter 4 - Retina. In: Remington LA, editor. Clinical Anatomy and Physiology of the Visual System (Third Edition). Saint Louis: Butterworth-Heinemann; 2012. p. 61–92.

378. Cruz-Topete D, Oakley RH, Carroll NG, He B, Myers PH, Xu X, et al. Deletion of the Cardiomyocyte Glucocorticoid Receptor Leads to Sexually Dimorphic Changes in Cardiac Gene Expression and Progression to Heart Failure. J Am Heart Assoc. 2019 Aug 6;8(15):e011012.

379. Whirledge S, DeFranco DB. Glucocorticoid Signaling in Health and Disease: Insights From Tissue-Specific GR Knockout Mice. Endocrinology. 2018 Jan 1;159(1):46–64.

380. Sainte-Marie Y, Cat AND, Perrier R, Mangin L, Soukaseum C, Peuchmaur M, et al. Conditional glucocorticoid receptor expression in the heart induces atrio-ventricular block. FASEB J. 2007;21(12):3133–41.

381. Cole TJ, Blendy JA, Monaghan AP, Krieglstein K, Schmid W, Aguzzi A, et al. Targeted disruption of the glucocorticoid receptor gene blocks adrenergic chromaffin cell development and severely retards lung maturation. Genes Dev. 1995 Jul 1;9(13):1608–21.

382. Pepin MC, Pothier F, Barden N. Impaired type II glucocorticoid-receptor function in mice bearing antisense RNA transgene. Nature. 1992 Feb;355(6362):725–8.

383. Peal DS, Mills RW, Lynch SN, Mosley JM, Lim E, Elllinor PT, et al. Novel Chemical Suppressors of Long QT Syndrome Identified by an in vivo Functional Screen. Circulation. 2011 Jan 4;123(1):23–30.

384. Fischbach PS, Frias PA, Strieper MJ, Campbell RM. Natural History and Current Therapy for Complete Heart Block in Children and Patients with Congenital Heart Disease. Congenit Heart Dis. 2007 Jul;2(4):224–34.

385. James TN, St. Martin E, Willis PW, Lohr TO. Apoptosis as a Possible Cause of Gradual Development of Complete Heart Block and Fatal Arrhythmias Associated With Absence of the AV Node, Sinus Node, and Internodal Pathways. Circulation. 1996 Apr;93(7):1424–38.

386. Ambrosi A, Wahren-Herlenius M. Congenital heart block: evidence for a pathogenic role of maternal autoantibodies. Arthritis Res Ther. 2012 Apr 26;14(2):208.

387. Pujades-Rodriguez M, Morgan AW, Cubbon RM, Wu J. Dose-dependent oral glucocorticoid cardiovascular risks in people with immune-mediated inflammatory diseases: A population-based cohort study. PLoS Med. 2020 Dec;17(12):e1003432.

388. MacLeod C, Hadoke PWF, Nixon M. Glucocorticoids: Fuelling the Fire of Atherosclerosis or Therapeutic Extinguishers? Int J Mol Sci. 2021 Jan;22(14):7622.

389. Roden DM. Drug-Induced Prolongation of the QT Interval. N Engl J Med. 2004 Mar 4;350(10):1013–22.

390. Tennstedt S. In silico Identifizierung und Untersuchung von Agonisten und Antagonisten des Androgenrezeptors. [Halle]: Martin-Luther-Universität Halle-Wittenberg; 2011.

391. Matsuda N, Jesmin S, Takahashi Y, Hatta E, Kobayashi M, Matsuyama K, et al. Histamine H_1 and H_2 Receptor Gene and Protein Levels Are Differentially Expressed in the Hearts of Rodents and Humans. J Pharmacol Exp Ther. 2004 May;309(2):786–95.

392. Sievers F, Wilm A, Dineen D, Gibson TJ, Karplus K, Li W, et al. Fast, scalable generation of high-quality protein multiple sequence alignments using Clustal Omega. Mol Syst Biol. 2011 Jan;7(1):539.

9 Supplements

9.1 Prestwick Chemical Library® Version 2019

Supplementary Table 1: Significant ISV Modulators

Chemical name	*Formula*	*Appr by*	*Therapeutic class*	*Target type*	*Target name*	*Target mechanism*	*Metabolism tissue*
Acetaminophen	C8H9NO2	FDA BBW Hepatotoxicity	Central Nervous System	Enzyme	Cyclooxygenases, Vanilloid receptor; Anandamide amidohydrolase	inhibitor, opener	Liver
Acitretin	C21H26O3	FDA	Dermatology	Nuclear receptors	Retinoid receptor	agonist	
Adapalene	C28H28O3	FDA	Dermatology	Nuclear receptors	Retinoic acid receptor (RAR) subtypes RARbeta and RARgamma		Liver
Altrenogest	C21H26O2	EMA	Endocrinology	Nuclear receptors			Liver
Azlocillin sodium salt	C20H22N5NaO6S	FDA	Metabolism, Infectiology	Enzyme	Bacterial transpeptidase; Penicillin-binding protein	inhibitor	n. a.
Demecarium bromide	C32H52Br2N4O4	FDA	Ophthalmology	Enzyme	acetylcholinesterase	inhibitor	
Desonide	C24H32O6	FDA	Dermatology	GPCR	Glucocorticoid receptor	agonist	
Ethopropazine hydrochloride	C19H25ClN2S	FDA	Central Nervous System	Receptor	Cholinergic receptors; Muscarinic acetylcholine receptor M1	antagonist	
Fluvastatin sodium salt	C24H25FNNaO4	FDA	Cardiovascular	Enzyme	HMG-CoA reductase	inhibitor	Liver
Ilbutilide fumarate	C44H76N4O10S2	FDA	Cardiovascular	Ion channel	Na+	blocker	Liver
Nilvadipine	C19H19N3O6	EMA	Cardiovascular	Ion channel	Voltage-gated L-type Ca2+ channel	blocker	Liver
Nisoldipine	C20H24N2O6	FDA	Cardiovascular	Ion channel	Voltage-gated L-type Ca2+ channel	blocker	Liver
Oxibendazole	C12H15N3O3	EMA	Metabolism		Tubulin beta-4B chain		Liver
Simvastatin	C25H38O5	FDA	Cardiovascular	Enzyme	HMG-CoA reductase	inhibitor	Liver
Suprofen	C14H12O3S	FDA	Central Nervous System Metabolism	Enzyme	Cyclooxygenase	inhibitor	
Tolcapone	C14H11NO5	FDA	Central Nervous System	Enzyme	Catechol O-methyltransferase	inhibitor	
Tolterodine tartrate	C26H37NO7	FDA	Neuromuscular	GPCR	Muscarinic M2 / M3 receptors	antagonist	Liver

(BBW) Black box warning; (n.a.) not applicable; (GPCR) G-protein coupled receptor

Supplementary Table 2: Significant DA and DV Modulators

Chemical name	*Formula*	*Appr by*	*Therapeutic class*	*Target type*	*Target name*	*Target mechanism*	*Metabolism tissue*
Acitretin	C21H26O3	FDA	Dermatology	Nuclear receptors	Retinoid receptor	agonist	Liver
Alfacalcidol	C27H44O2	FDA	Metabolism	Enzyme	Farnesyl pyrophosphate synthase		Liver
Altrenogest	C21H26O2	EMA	Endocrinology	Nuclear receptors			Liver
Azelastine hydrochloride	C22H25Cl2N3O	FDA	Immunology	GPCR	Histaminergic H1 receptor	antagonist	
Cefpiramide	C25H24N8O7S2	FDA	Infectiology	Enzyme	Transpeptidase Bacterial penicillin-binding protein	inhibitor	
Cephalothin sodium salt	C16H15N2NaO6S2	FDA	Infectiology Metabolism	Enzyme	Bacterial transpeptidase Bacterial penicillin-binding protein	Inhibitor	
Clidinium bromide	C22H26BrNO3	FDA	Antispastic	GPCR	Muscarinic receptors	antagonist	Liver
Dasabuvir	C26H27N3O5S	FDA	Infectiology	Enzyme	NS5B palm polymerase	inhibitor	
Demecarium bromide	C32H52Br2N4O4	FDA	Ophthalmology	Enzyme	Acetylcholinesterase Cholinesterase	inhibitor	
Diclofenac sodium	C14H10Cl2NNaO2	FDA	Central Nervous System Metabolism	Enzyme	Cyclooxygenase		Liver
Diphenylpyraline hydrochloride	C19H24ClNO	EMA	Allergology Central Nervous System	GPCR	Histaminergic H1 receptor		
Etanidazole	C7H10N4O4	EMA	Antineoplastic Chemosensitizer	DNA			
Flunisolide	C24H31FO6	FDA	Anti-inflammatory	Nuclear receptors	Glucocorticoid receptor	agonist	Liver
Fluvastatin sodium salt	C24H25FNNaO4	FDA	Cardiovascular	Enzyme	HMG-CoA reductase	inhibitor	Liver
Furazolidone	C8H7N3O5	FDA	Metabolism	DNA			Liver
Ibutilide fumarate	C44H76N4O10S2	FDA	Cardiovascular	Ion channel	Na+	blocker	Liver
Irinotecan hydrochloride trihydrate	C33H45ClN4O9	FDA	Antineoplastic	DNA			
Lomerizine hydrochloride	C27H31ClF2N2O3	EMA	Central Nervous System Cardiovascular	Ion channel	Ca2+ channel	blocker	
Mepenzolate bromide	C21H26BrNO3	FDA	Antispastic Antiulcer	GPCR	Muscarinic receptors	antagonists	
Nalidixic acid sodium salt	C12H11N2NaO3	FDA	Infectiology Metabolism	DNA	Bacterial DNA gyrase		Liver
Nelfinavir mesylate	C33H49N3O7S2	FDA	Infectiology Oncology	Enzyme	HIV-1 protease	inhibitor	Liver
Nevirapine	C15H14N4O	FDA	Infectiology	Enzyme	Non-nucleoside reverse transcriptase	inhibitor	Liver
Nilvadipine	C19H19N3O6	EMA	Cardiovascular	Ion channel	Voltage-gated L-type Ca2+ channel	blocker	Liver
Nisoldipine	C20H24N2O6	FDA	Cardiovascular	Ion channel	Voltage-gated L-type Ca2+ channel	blocker	Liver
Oxibendazol	C12H15N3O3	EMA	Metabolism	Protein	Tubulin beta-4B chain		Liver

Papaverine hydrochloride	C20H22ClNO4	EMA	Cardiovascular Gastroenterology Respiratory	Enzyme	Phosphodiesterases	inhibitor	Liver
Raltitrexed	C21H22N4O6S	EMA	Antineoplastic	Enzyme	Thymidylate synthase		
Rasagiline	C12H13N	FDA	Central Nervous System	Enzyme	Monoamine oxidase B	inhibitor	Liver
Sertindole	C24H26ClFN4O	EMA	Central Nervous System	GPCR	Dopaminergic D2 / 5-HT2 receptors	antagonist	
Simvastatin	C25H38O5	FDA	Cardiovascular	Enzyme	HMG-CoA reductase	inhibitor	Liver
Temozolomide	C6H6N6O2	FDA	Oncology	DNA			Liver
Tolterodine tartrate	C26H37NO7	FDA	Neuromuscular	GPCR	Muscarinic M2 / M3 receptors	antagonist	Liver
Tylosin	C46H77NO17	EMA	Infectiology Metabolism	Ribosome	50S unit	inhibitor	
Warfarin	C19H16O4	FDA	Hematology	Enzyme	Vitamin K epoxide reductase	inhibitor	Liver

(n.a.) not applicable; (GPCR) G-protein coupled receptor

Supplementary Table 3: Significant Heartbeat Hits of the Prestwick Chemical Library®

Chemical name	*Formula*	*Appr by*	*Therapeutic class*	*Target type*	*Target name*	*Target mechanism*	*Metabolism tissue*
Ticlopidine hydrochloride	C14H15Cl2NS	FDA	Hematology	GPCR	Purinergic P2Y12 receptor		Liver
Fulvestrant	C32H47F5O3S	FDA	Endocrinology, 'Oncology	Nuclear receptor	Estrogen receptor		Liver
Edrophonium chloride	C10H16ClNO	FDA	Diagnostic, 'Neuromuscular	Enzyme	Cholinesterase	inhibitor	n.i.
Haloperidol	C21H23ClFNO2	FDA	Central Nervous System	GPCR	Dopaminergic receptors	antagonist	n.i.
Picotamide monohydrate	C21H22N4O4	EMA	Hematology	Receptor	Eicosenoid receptor	antagonist	n.i.
Bromocryptine mesylate	C33H44BrN5O8S	FDA	Central Nervous System	GPCR	D2-like dopamine receptor/ Dopamine/ CYP3A4	agonist	Liver
Azilsartan kamedoxomil	C30H24N4O8	FDA	Cardiovascular	GPCR	Angiotensin II Receptor	antagonist	n.i.
Astemizole	C28H31FN4O	EMA	Allergology	GPCR	Histaminergic H1 receptor		Liver
Terfenadine	C32H41NO2	EMA	Allergology	GPCR	Histaminergic H1 receptor		n.i.
Nicergoline	C24H26BrN3O3	EMA	Cardiovascular	GPCR	Adrenergic Alpha receptors	agonist	Liver
Dihydroergotamine tartrate	C70H80N10O16	FDA - BBW	Central Nervous System	GPCR	Serotoninergic 5-HT1d receptor		n.i.
Ivermectin	C48H74O14	FDA	Infectiology, 'Metabolism	Ionotropic receptor	Glutamate receptors	agonist	Liver
Levamisole hydrochloride	C11H13ClN2S	FDA	Immunology 'Infectiology 'Metabolism	Enzyme	Alkaline phosphatase	inhibitor	Liver
Tiratricol, 3,3',5-triiodothyroacetic acid	C14H9I3O4	EMA	Endocrinology	Nuclear receptor	Thyroid hormone receptor		Liver
Tibolone	C21H28O2	EMA	Endocrinology	Nuclear receptors			Liver

Scopolamine-N-oxide hydrobromide	C17H22BrNO5	FDA	Neuromuscular	GPCR	Muscarinic receptors	antagonist	n.i.
Ethacrynic acid	C13H12Cl2O4	FDA	Metabolism	Carrier	Solute carrier family 12 member 1		n.i.
Triprolidine hydrochloride	C19H23ClN2	FDA	Allergology, 'Central Nervous System	GPCR	Histaminergic H1 receptor		n.i.
Dyclonine hydrochloride	C18H28ClNO2	FDA	Neuromuscular	Ion channel	Voltage-gated Na+ channel		n.i.
Fendiline hydrochloride	C23H26ClN	EMA	Cardiovascular	Ion channel	Ca2+ channel	activator	n.i.
Homochlorcyclizine dihydrochloride	C19H25Cl3N2	Japan	Allergology, 'Central Nervous System	GPCR	Histamine H1 receptor	antagonist	n.i.
Benzydamine hydrochloride	C19H24ClN3O	EMA	Central Nervous System, 'Metabolism	Enzyme	Prostaglandin synthetase; Cyclooxygenase	inhibitor	n.i.
Econazole nitrate	C18H16Cl3N3O4	FDA	Infectiology 'Metabolism	Enzyme	Cytochrome P450 51		n.i.
Clemastine fumarate	C25H30ClNO5	FDA	Allergology, 'Central Nervous System	GPCR	Histaminergic H1 receptor		n.i.
Pimozide	C28H29F2N3O	FDA	Central Nervous System	GPCR	Dopaminergic receptors; Serotonin 2a (5-HT2a) receptor	antagonist	Liver
Mebeverine hydrochloride	C25H36ClNO5	EMA	Neuromuscular	GPCR	Muscarinic receptors	antagonist	Liver
Ifenprodil tartrate	C25H33NO8	EMA	Cardiovascular	GPCR	Adrenergic receptors	antagonist	n.i.
Flunarizine dihydrochloride	C26H28Cl2F2N2	EMA	Central Nervous System	Ion channel	Ca2+ channel		Liver
Clofilium tosylate	C28H44ClNO3S	EMA	Cardiovascular	Ion channel	K+		n.i.
Methapyrilene hydrochloride	C14H20ClN3S	EMA	Allergology, 'Central Nervous System	GPCR	Histaminergic H1 receptor		n.i.
Hycanthone	C20H24N2O2S	FDA	Infectiology	DNA			n.i.
Betamethasone	C22H29FO5	FDA	Endocrinology	Nuclear receptor	Glucocorticoid receptor		Liver
Bepridil hydrochloride	C24H35ClN2O	FDA	Cardiovascular	Ion channel	Ca2+ channel	blocker	n.i.
Amethopterin (R,S)	C20H22N8O5	EMA	Immunology, 'Metabolism, 'Oncology	Enzyme	Dihydrofolate reductase		Liver, Intracellular
Nafronyl oxalate	C26H35NO7	EMA	Cardiovascular, 'Neuromuscular	GPCR	Serotoninergic 5-HT receptors	antagonist	Liver
Amiodarone hydrochloride	C25H30ClI2NO3	FDA - BBW	Cardiovascular	Ion channel	Na+, HERG	blocker	n.i.
Amlodipine	C20H25ClN2O5	FDA	Cardiovascular	Ion channel	Voltage-gated L-type Ca2+ channel	blocker	n.i.
Suloctidil	C20H35NOS	EMA	Neuromuscular	Enzyme	Transferase, Phosphodiesterase		n.i.
Nebivolol hydrochloride	C22H26ClF2NO4	FDA	Cardiovascular		Beta-1/2 adrenergic receptor	antagonist	Liver
Meclozine dihydrochloride	C25H29Cl3N2	FDA	Allergology 'Central Nervous System	GPCR	Histaminergic H1 receptor	antagonist	Liver
Efavirenz	C14H9ClF3NO2	FDA	Infectiology 'Metabolism	Enzyme	Reverse transcriptase	inhibitor	Liver
Niridazole	C6H6N4O3S	EMA	Infectiology 'Metabolism	DNA			n.i.

Brompheniramine maleate	C20H23BrN2O4	FDA	Allergology	GPCR	Histaminergic H1 receptor	antagonist	n.i.
Propafenone hydrochloride	C21H28ClNO3	FDA - BBW	Cardiovascular	GPCR	Adrenergic Beta receptors; Sodium channel alpha subunit	antagonist/ blocker	n.i.
Pregnenolone	C21H32O2	OTC	Endocrinology				n.i.
Pentamidine isethionate	C23H36N4O10S2	FDA	Infectiology	DNA	minor groove of AT-rich DNA regions		n.i.
Atropine sulfate monohydrate	C34H50N2O11S	FDA	Ophthalmology	GPCR	Muscarinic receptors	antagonist	Liver
Azelastine hydrochloride	C22H25Cl2N3O	FDA	Immunology	GPCR	Histaminergic H1 receptor	antagonist	n.i.
Temozolomide	C6H6N6O2	FDA	Oncology	DNA			Liver
Zafirlukast	C31H33N3O6S	FDA	Respiratory	GPCR	Cysteinyl leukotriene receptor		n.i.
Carbadox	C11H10N4O4	FDA Vet	Infectiology				n.i.
(-)-Emtricitabine	C8H10FN3O3S	FDA	Infectiology				Liver
Levetiracetam	C8H14N2O2	FDA	Central Nervous System				n.i.
Pinaverium bromide	C26H41Br2NO4	EMA	Neuromuscular				Liver
Loratadine		Clin Ther. 1997 Nov-Dec 19(6):1278-93	Antihistaminic				n.i.
Opipramol dihydrochloride	C23H31Cl2N3O	EMA	Central Nervous System	GPCR	Sigma receptors	agonist	n.i.
Ibutilide fumarate	C44H76N4O10S2	FDA	Cardiovascular	Ion channel	Na+		Liver
Chlorcyclizine hydrochloride	C18H22Cl2N2	EMA	Allergology 'Central Nervous System	GPCR	Histaminergic H1 receptor		n.i.
Diphenylpyraline hydrochloride	C19H24ClNO	EMA	Allergology 'Central Nervous System	GPCR	Histaminergic H1 receptor		n.i.
Flumethasone	C22H28F2O5	FDA	Metabolism				n.i.
Monensin sodium salt	C36H61NaO11	EMA	Infectiology	Membrane			Liver
Dronedarone hydrochloride	C31H45ClN2O5S	FDA - BBW	Cardiovascular	Ion channel	Potassium/sodium hyperpolarization-activated cyclic nucleotide-gated channel 4 / Voltage-gated L-type calcium channel/ Sodium channel alpha subunit/ Inward rectifier potassium channel 2	blocker	n.i.
Fenoprofen calcium salt dihydrate	C30H30CaO8	FDA - BBW	Metabolism	Enzyme	Cyclooxygenase		Liver
Diethylstilbestrol	C18H20O2	FDA	Endocrinology 'Oncology	Nuclear receptor	Estrogen receptor alpha	agonist	n.i.

Alclometasone dipropionate	C28H37ClO7	FDA	Metabolism	Nuclear receptors	Glucocorticoid receptor		n.i.
Fluocinonide	C26H32F2O7	FDA - BBW	Metabolism		Glucocorticoid receptor	agonist	n.i.
Clobetasol propionate	C25H32ClFO5	FDA - BBW	Metabolism		Glucocorticoid receptor	agonist	n.i.
Cycloheximide	C15H23NO4	no	Infectiology		80S Ribosome	inhibitor	n.i.
Cloperastine hydrochloride	C20H25Cl2NO	EMA	Respiratory	GPCR	Histaminergic receptors	antagonist	n.i.
Dienestrol	C18H18O2	FDA	Endocrinology	Nuclear receptor	Estrogen receptor alpha	agonist	n.i.
Carbinoxamine maleate salt	C20H23ClN2O5	FDA	Allergology 'Metabolism	GPCR	Histaminergic H1 receptor		n.i.
Trimipramine maleate salt	C24H30N2O4	FDA - BBW	Central Nervous System	Carrier	5-HT uptake	inhibitor	Liver
Chloropyramine hydrochloride	C16H21Cl2N3	EMA	Allergology	GPCR	Histaminergic H1 receptor		n.i.
Cefsulodin sodium salt	C22H19N4NaO8S2	EMA	Metabolism 'Infectiology	Enzyme	Bacterial transpeptidase	inhibitor	n.i.
Deflazacort	C25H31NO6	EMA	Immunology 'Metabolism	Nuclear receptor	Glucocorticoid receptor		n.i.
Ethaverine hydrochloride	C24H30ClNO4	Taiwan	Central Nervous System				n.i.
Butacaine	C18H30N2O2	EMA	Dermatology	Ion channel	Voltage-gated Na+ channel		n.i.
Cefoxitin sodium salt	C16H16N3NaO7S2	FDA	Metabolism 'Infectiology	Enzyme	Bacterial transpeptidase	inhibitor	None
Indoprofen	C17H15NO3	EMA	Central Nervous System 'Metabolism	Enzyme	Cyclooxygenase		n.i.
Ethopropazine hydrochloride	C19H25ClN2S	FDA	Central Nervous System	Receptor	Cholinergic receptors	antagonist	n.i.
Procyclidine hydrochloride	C19H30ClNO	FDA	Central Nervous System	GPCR	Muscarinic receptors	antagonist	n.i.
(-) -Levobunolol hydrochloride	C17H26ClNO3	FDA	Ophthalmology	GPCR	Adrenergic beta receptors	antagonist	n.i.
Paroxetine Hydrochloride	C19H21ClFNO3	FDA	Central Nervous System	Carrier	Serotonin transporter		Liver
Beclomethasone dipropionate	C28H37ClO7	FDA	Metabolism	Nuclear receptor	Glucocorticoid receptor	agonist	Liver
Ciclesonide	C32H44O7	FDA	Respiratory	Nuclear receptor	Glucocorticoid receptor	agonist	n.i.
Ethynodiol diacetate	C24H32O4	FDA	Endocrinology	Nuclear receptors	Progesterone receptors	agonist	n.i.
Monobenzone	C13H12O2	FDA	Dermatology	Cell			Liver
Nimodipine	C21H26N2O7	FDA	Cardiovascular	Ion channel	Voltage-gated L-type Ca2+ channel		Liver
Nilutamide	C12H10F3N3O4	FDA	Oncology	Nuclear receptor	Androgen Receptor		n.i.
S(-)Eticlopride hydrochloride	C17H26Cl2N2O3	EMA	Central Nervous System	GPCR	Dopaminergic receptors	antagonist	n.i.
Canrenone	C22H28O3	EMA	Endocrinology, Cardiovascular	Nuclear receptors	Aldosterone, Mineralocorticoid receptor	antagonist	n.i.
Enilconazole	C14H14Cl2N2O	FDA	Metabolism	Enzyme	Ergosterol synthesis	inhibitor	n.i.
Indatraline hydrochloride	C16H16Cl3N	EMA	Central Nervous System				n.i.

Naftopidil dihydrochloride	C24H30Cl2N2O3	EMA	Cardiovascular	GPCR	Alpha-1d adrenergic receptor	antagonist	n.i.
Nandrolone	C18H26O2	FDA	Endocrinology 'Hematology				Liver
Pramipexole dihydrochloride	C10H19Cl2N3S	FDA	Central Nervous System	GPCR	Dopaminergic receptors, D2-like dopamine receptor	agonist	n.i.
Norgestimate	C23H31NO3	FDA	Endocrinology	Nuclear receptor	Progesterone receptor	agonist	Liver
Chlormadinone acetate	C23H29ClO4	EMA	Endocrinology 'Oncology	Nuclear receptor	Progesterone receptor	modulator	n.i.
Fluticasone propionate	C25H31F3O5S	FDA	Cardiovascular 'Metabolism	Nuclear receptors	Glucocorticoid receptor	agonist	Liver
Alfaxalone	C21H32O3	EMA	Central Nervous System	Ionotropic receptor	GABAa receptor	allosteric inhibitor	n.i.
Isradipine	C19H21N3O5	FDA	Cardiovascular	Ion channel	Voltage-gated L-type Ca2+ channel	blocker	Liver
Nomegestrol acetate	C23H30O4	EMA	Endocrinology	Nuclear receptor	Progesterone receptor		n.i.
Pyrvinium pamoate	C75H70N6O6	FDA	Metabolism	Not identified			n.i.
Prednicarbate	C27H36O8	FDA	Metabolism	Nuclear receptors	Glucocorticoid receptor	agonist	n.i.
Iopanoic acid	C11H12I3NO2	FDA	Diagnostic				Liver
Pivmecillinam hydrochloride	C21H34ClN3O5S	EMA	Metabolism 'Infectiology	Enzyme	Peptidoglycan synthesis	inhibitor	n.i.
Ioxaglic acid	C24H21I6N5O8	FDA	Diagnostic				n.i.
Estriol	C18H24O3	EMA	Endocrinology	Nuclear receptor	Estrogen receptor		Liver
Meropenem	C17H25N3O5S	FDA	Infectiology 'Metabolism	Enzyme	Peptidoglycan synthesis	inhibitor	Liver
Clocortolone pivalate	C27H36ClFO5	FDA	Endocrinology	Nuclear receptors	Glucocorticoid receptor	agonist	n.i.
Anastrozole	C17H19N5	FDA	Oncology	Coenzyme	Cytochrome P450 19A1		Liver
Amcinonide	C28H35FO7	FDA	Metabolism	Nuclear receptors	Glucocorticoid receptor	agonist	n.i.
Fluocinolone acetonide	C24H30F2O6	FDA	Metabolism				n.i.
Tripelennamine hydrochloride	C16H22ClN3	FDA	Allergology	GPCR	Histaminergic H1 receptor		n.i.
Telmisartan	C33H30N4O2	FDA	Cardiovascular	GPCR	Angiotensin II receptor type 1		Liver
Montelukast	C35H36ClNO3S	FDA BBW	Respiratory	GPCR	Cysteinyl leukotriene receptor 1		n.i.
Trimebutine	C22H29NO5	EMA	Neuromuscular	GPCR	Muscarinic receptors	antagonist	n.i.
Ipriflavone	C18H16O3	EMA	Metabolism	Not identified	Allows osteoblasts to build up bone mass		n.i.
Ezetimibe	C24H21F2NO3	FDA	Metabolism 'Gastroenterology 'Cardiovascular	Protein	Niemann-Pick C1-like protein 1	inhibitor	Liver
(R)-Duloxetine hydrochloride	C18H20ClNOS	FDA					Liver
Donepezil hydrochloride	C24H30ClNO3	FDA	Central Nervous System	Enzyme	Acetylcholinesterase		Liver
1,8-Dihydroxyanthraquinone	C14H8O4	EMA	Gastroenterology	Ionotropic receptor	Serotoninergic 5-HT3 receptor	antagonist	n.i.

Ethoxzolamide	C9H10N2O3S2	FDA	Ophthalmology 'Gastroenterology 'Central Nervous System	Enzyme	Carbonic anhydrase I	inhibitor	n.i.
Perospirone hydrochloride	C23H31ClN4O2S	EMA	Central Nervous System	GPCR	Monoamines receptors; Serotonin-dopamine antagonists	antagonist	n.i.
Dofetilide	C19H27N3O5S2	FDA BBW	Cardiovascular	Ion channel	K+, hERG	Blocker	n.i.
Flumethasone pivalate	C27H36F2O6	FDA	Dermatology	Nuclear receptors	Glucocorticoid receptor	agonist	n.i.
Lomerizine hydrochloride	C27H31ClF2N2O3	EMA	Central Nervous System 'Cardiovascular	Ion channel	Ca2+ channel	blocker	n.i.
Desonide	C24H32O6	FDA	Dermatology	Nuclear receptors			n.i.

(BBW) Black box warning; (EMA) European Medicines Agency; (FDA) Food and Drug Administration; (n.a.) not applicable; (n.i.) no information; (OTC) Over the counter medication; (GPCR) G-protein coupled receptor

9.1.1 Primary Screening for Vascular Hits

Supplementary Table 4: Preliminary Hits for Vascular Modulators

Common name	Formula	ISV Diameter	DA Diameter	DV Diameter	Appr. by	ATC Codes	Therapeutic class	Structure
Azlocillin sodium s	C20H22N5NaO6S	-2.156	-1.091	0.029	FDA	J01CA09	Metabolism Infectiology	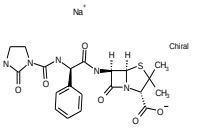
Desonide	C24H32O6	-2.076	-0.67	0.306	FDA	S01BA11	Dermatology	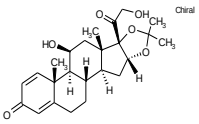
Oxibendazole	C12H15N3O3	-1.745	-0.144	0.252	EMA	n.a.	Metabolism	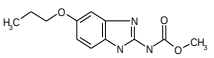
Flunisolide	C24H31FO6	-0.61	0.897	2.202	FDA	R01AD04	Endocrino-logy	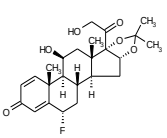
Azelastine HCl	C22H25Cl2N3O	-2.598	-1.948	-1.341	FDA	R06AX19; S01GX07; R01AC03	Immuno-logy	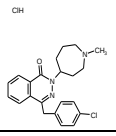

Diphenylpyraline HCl	C19H24ClNO	-3.549	-2.581	-0.159	EMA	R06AA07	Allergology Central Nervous System	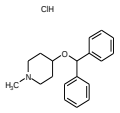
Furazolidone	C8H7N3O5	-0.344	0.321	2.147	FDA	G01AX06	Metabolism	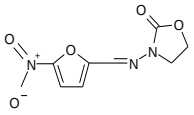
Rasagiline	C12H13N	0.977	2.564	-1.294	FDA	N04BD02	Central Nervous System	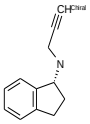
Nalidixic acid sodium salt	C12H11N2NaO3	-0.41	-1.718	-1.469	FDA	J01MB02	Infectiology Metabolism	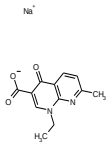
Cephalothin sodium salt	C16H15N2NaO6S2	-0.091	-2.913	-0.51	FDA	J01DB03	Infectiology Metabolism	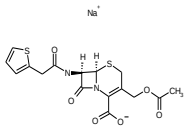
Cefpiramide	C25H24N8O7S2	-0.163	1.837	-0.458	FDA	J01DD11	Infectiology	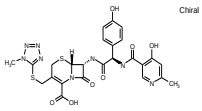

9.1.1 Primary Screen for Heart Rate Modulators

Supplementary Table 5: Heart Rate Hits Identified from the PDL

Chemical name	*Formula*	*Appr by*	*Therapeutic class*	*Target type*	*Target name*	*Target mechanism*	*Metabolism: tissue*
Alclometasone dipropionate	C28H37ClO7	FDA	Metabolism	Nuclear receptors	Glucocorticoid receptor		n.i.
Azelastine hydrochloride	C22H25Cl2N3O	FDA	Immunology	GPCR	Histaminergic H1 receptor	antagonist	n.i.
Beclomethasone dipropionate	C28H37ClO7	FDA	Metabolism				Liver
Benzydamine hydrochloride	C19H24ClN3O	EMA	Central Nervous System, 'Metabolism	Enzyme	Prostaglandin synthetase; Cyclooxygenase	inhibitor	n.i.
Chloropyramine hydrochloride	C16H21Cl2N3	EMA	Allergology	GPCR	Histaminergic H1 receptor		n.i.
Clocortolone pivalate	C27H36ClFO5	FDA	Endocrinology	Nuclear receptors	Glucocorticoid receptor	agonist	n.i.
Cycloheximide	C15H23NO4	no	Infectiology		80S Ribosome	inhibitor	n.i.
Diphenylpyraline hydrochloride	C19H24ClNO	EMA	Allergology 'Central Nervous System	GPCR	Histaminergic H1 receptor		n.i.
Flumethasone pivalate	C27H36F2O6	FDA	Dermatology	Nuclear receptors	Glucocorticoid receptor	agonist	n.i.
Fluticasone propionate	C25H31F3O5S	FDA	Cardiovascular 'Metabolism	Nuclear receptors	Glucocorticoid receptor	agonist	Liver

Homochlorcyclizine dihydrochloride	C19H25Cl3N2	Japan	Allergology, 'Central Nervous System	GPCR	Histamine H1 receptor	antagonist	n.i.
Ifenprodil tartrate	C25H33NO8	EMA	Cardiovascular	GPCR	Adrenergic receptors	antagonist	n.i.
Iopanoic acid	C11H12I3NO2	FDA	Diagnostic				Liver
Methapyrilene hydrochloride	C14H20ClN3S	EMA	Allergology, 'Central Nervous System	GPCR	Histaminergic H1 receptor		n.i.
Monobenzone	C13H12O2	FDA	Dermatology	Cell			Liver
Niridazole	C6H6N4O3S	EMA	Infectiology 'Metabolism	DNA			n.i.
Pentamidine isethionate	C23H36N4O10S2	FDA	Infectiology	DNA	minor groove of AT-rich DNA regions		n.i.
Pimozide	C28H29F2N3O	FDA	Central Nervous System	GPCR	Dopaminergic receptors; Serotonin 2a (5-HT2a) receptor	antagonist	Liver
Prednicarbate	C27H36O8	FDA	Metabolism	Nuclear receptors	Glucocorticoid receptor	agonist	n.i.
Pregnenolone	C21H32O2	OTC	Endocrinology	n. a.	n. a.	n. a.	n.i.
Pyrvinium pamoate	C75H70N6O6	FDA	Metabolism	Not identified			n.i.
Tripelennamine hydrochloride	C16H22ClN3	FDA	Allergology	GPCR	Histaminergic H1 receptor		n.i.

(EMA) European Medicines Agency; (FDA) Food and Drug Administration; (n.a.) not applicable; (n.i.) no information; (OTC) Over the counter medication; (GPCR) G-protein coupled receptor

Supplementary Table 6: Heart Rate Hits with Various Targets

Chemical name	*Formula*	*Appr by*	*Therapeutic class*	*Target type*	*Target name*	*Target mechanism*	*Metabolism: tissue*
Benzydamine hydrochloride	C19H24ClN3O	EMA	Central Nervous System, 'Metabolism	Enzyme	Prostaglandin synthetase; Cyclooxygenase	inhibitor	n.i.
Cycloheximide	C15H23NO4	no	Infectiology		80S Ribosome	inhibitor	n.i.
Ifenprodil tartrate	C25H33NO8	EMA	Cardiovascular	GPCR	Adrenergic receptors	antagonist	n.i.
Iopanoic acid	C11H12I3NO2	FDA	Diagnostic				Liver
Monobenzone	C13H12O2	FDA	Dermatology	Cell			Liver
Niridazole	C6H6N4O3S	EMA	Infectiology 'Metabolism	DNA			n.i.
Pentamidine isethionate	C23H36N4O10S2	FDA	Infectiology	DNA	minor groove of AT-rich DNA regions		n.i.
Pimozide	C28H29F2N3O	FDA	Central Nervous System	GPCR	Dopaminergic receptors; Serotonin 2a (5-HT2a) receptor	antagonist	Liver
Pregnenolone	C21H32O2	OTC	Endocrinology	n. a.	n. a.	n. a.	n.i.

Pyrvinium pamoate	C75H70N6O6	FDA	Metabolism	Not identified	n.i.

(EMA) European Medicines Agency; (FDA) Food and Drug Administration; (n.a.) not applicable; (n.i.) no information; (OTC) Over the counter medication; (GPCR) G-protein coupled receptor

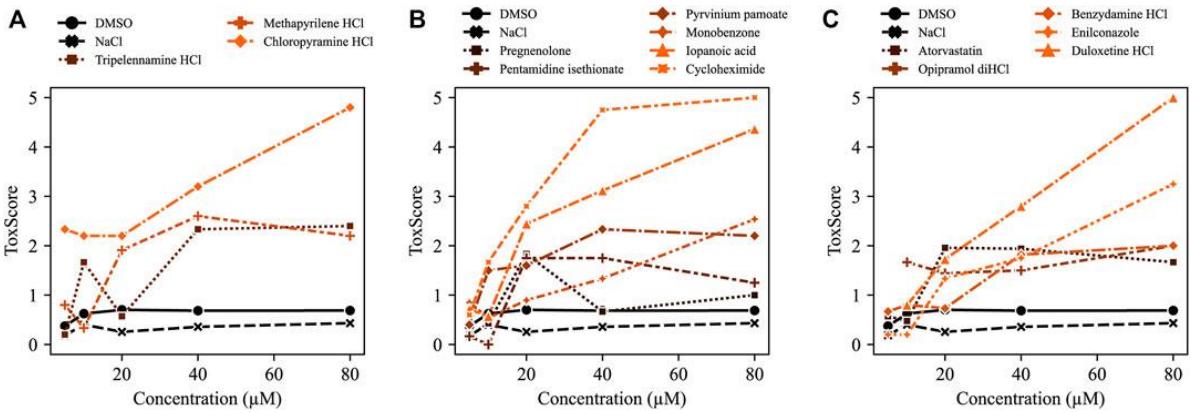

Supplementary Figure 1: ToxScore for Various Compounds

ToxScores increased dose-dependently for most compounds in treated zebrafish. **A**, Two of three HRH1 antagonists have not reached their highest ToxScore at 80 µM. **B**, Various compounds displayed high ToxScores at higher concentrations. **C**, Hydrochlorides showed similar ToxScores to other compounds, indicating no role for the hydrochlorides themselves in the observed phenotypes. Severity of the ToxScore at 80 µM is indicated by the color gradient: black (low ToxScore), orange (high ToxScore). Figure was taken with permission from Vedder *et al.* (185).

9.2 Hrh1

Supplementary Table 7: Hrh1 Antagonists With Significant Effects in the Primary Screening

Chemical name	*Heart rate z-score*	*N*	*Formula*	*Appr by*	*Therapeutic class*	*Target mechanism*
Astemizole	-7.190	3	C28H31FN4O	EMA	Allergology	antagonist
Terfenadine	-5.761	5	C32H41NO2	EMA	Allergology	antagonist
Meclozine dihydrochloride	-3.976	4	C25H29Cl3N2	FDA	Allergology Central Nervous System	antagonist
Diphenylpyraline hydrochloride	-3.549	3	C19H24ClNO	EMA	Allergology Central Nervous System	antagonist
Chloropyramine hydrochloride	-2.971	5	C16H21Cl2N3	EMA	Allergology	antagonist
Clemastine fumarate	-2.762	4	C25H30ClNO5	FDA	Allergology Central Nervous System	antagonist

Azelastine hydrochloride	-2.598	5	C22H25Cl2N3O	FDA	Immunology	antagonist
Tripelennamine hydrochloride	-2.358	5	C16H22ClN3	FDA	Allergology	antagonist
Methapyrilene hydrochloride	-2.210	6	C14H20ClN3S	EMA	Allergology Central Nervous System	antagonist
Brompheniramine maleate	-2.122	5	C20H23BrN2O4	FDA	Allergology	antagonist
Triprolidine hydrochloride	-2.068	5	C19H23ClN2	FDA	Allergology Central Nervous System	antagonist
Chlorcyclizine hydrochloride	-2.061	4	C18H22Cl2N2	EMA	Allergology Central Nervous System	antagonist
Homochlorcyclizine dihydrochloride	-1.853	10	C19H25Cl3N2	Japan	Allergology Central Nervous System	antagonist
Carbinoxamine maleate salt	-1.800	4	C20H23ClN2O5	FDA	Allergology Metabolism	antagonist
Astemizole	-7.190	5	C28H31FN4O	EMA	Allergology	antagonist

(EMA) European Medicines Agency; (FDA) Food and Drug Administration; (n.a.) not applicable; (n.i.) no information; (OTC) Over the counter medication; (GPCR) G-protein coupled receptor

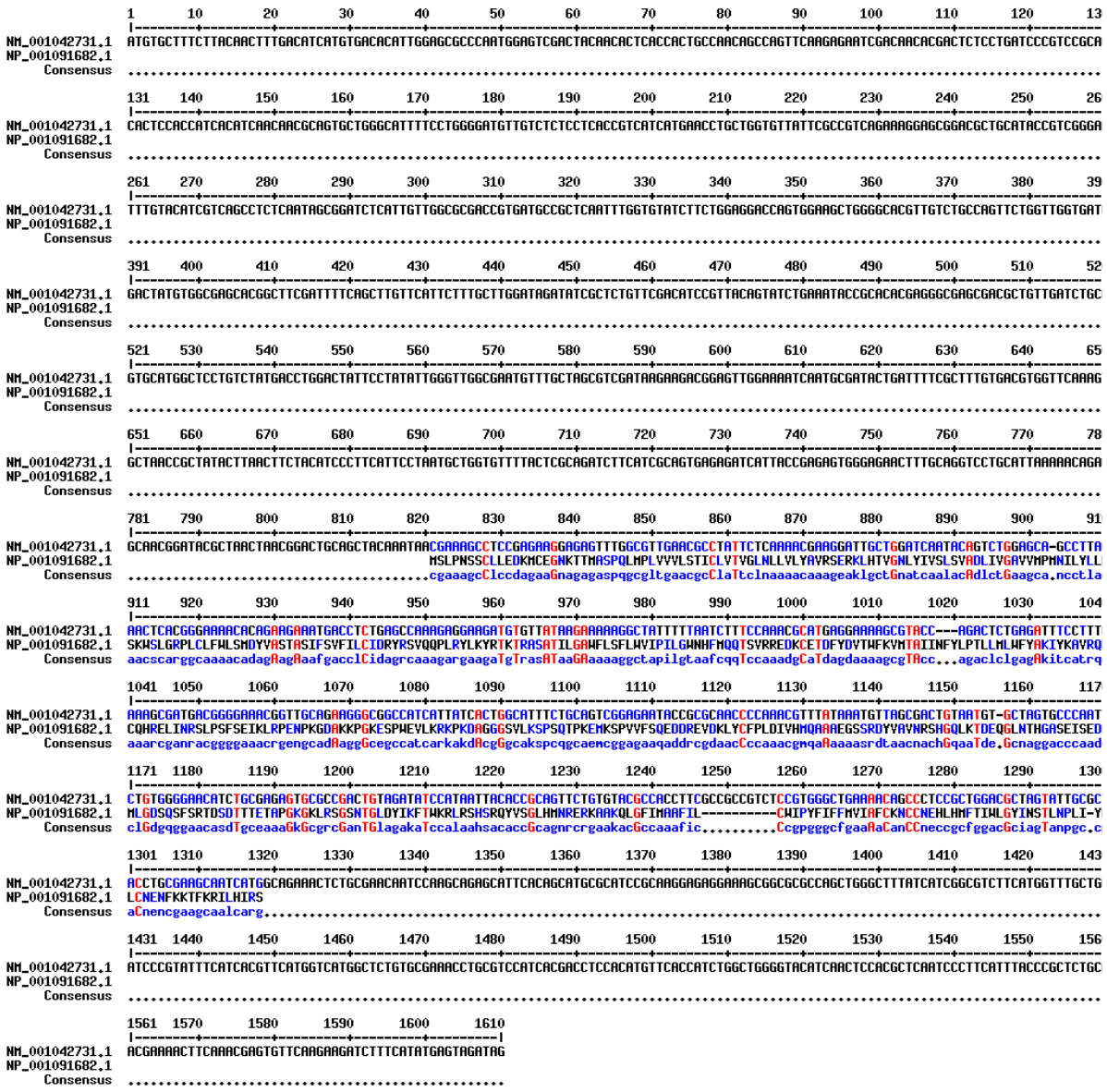

Supplementary Figure 2: MultAlin Multiple Sequence Alignment of HRH1 and Hrh1

Multiple sequence alignment was performed with the MultAlin (218) multiple sequence viewer. The human FASTA sequence (NP_001091682.1) was aligned against the zebrafish Hrh1 (NM_001042731). Red = Conserved sequences; Blue and black = Not conserved sequences

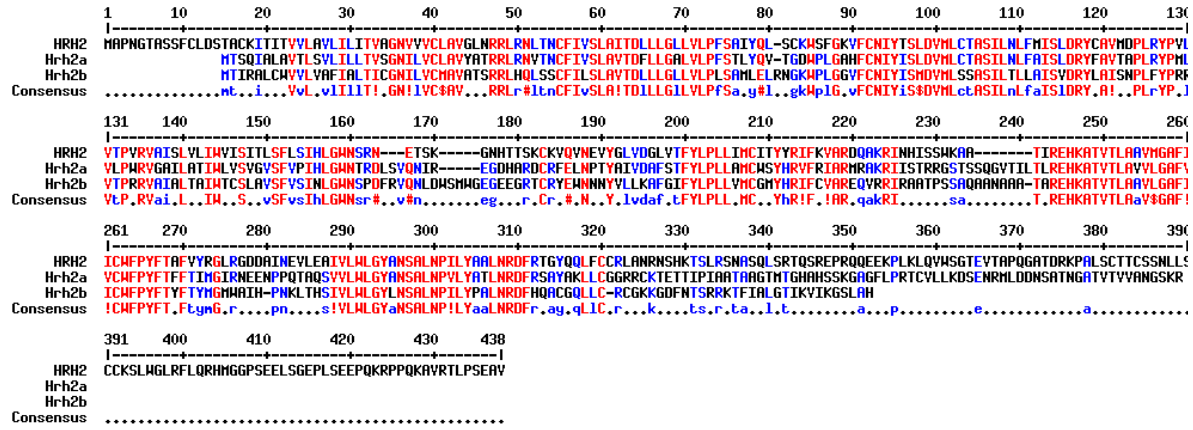

Supplementary Figure 3: MultAlin HRH2 and Hrh2a-b Multiple Sequence Alignment

Multiple sequence alignment was performed with the MultAlin (218) multiple sequence viewer. The human FASTA sequence (NP_001380389.1) was aligned against the zebrafish Hrh2a (NP_001038803.2) and Hrh2b (NP_001103208.1).

Red = Conserved sequences; Blue and black = Not conserved sequences

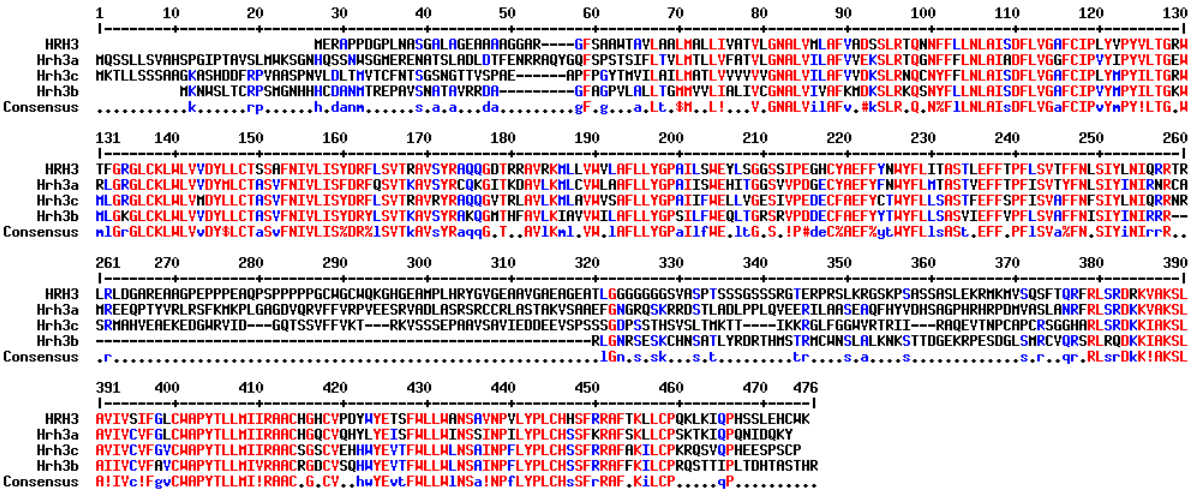

Supplementary Figure 4: HRH3 and Hrh3a-c MultAlin Multiple Sequence Alignment

Multiple sequence alignment was performed with the MultAlin (218) multiple sequence viewer. The human HRH3 FASTA sequence (NP_009163.2) was aligned against the zebrafish Hrh3a (NP_001020689.1), Hrh3b (XP_002667517.2) and Hrh3c (ENSDART00000164061.2).

Red = Conserved sequences; Blue and black = Not conserved sequences

9.3 Nr3c1

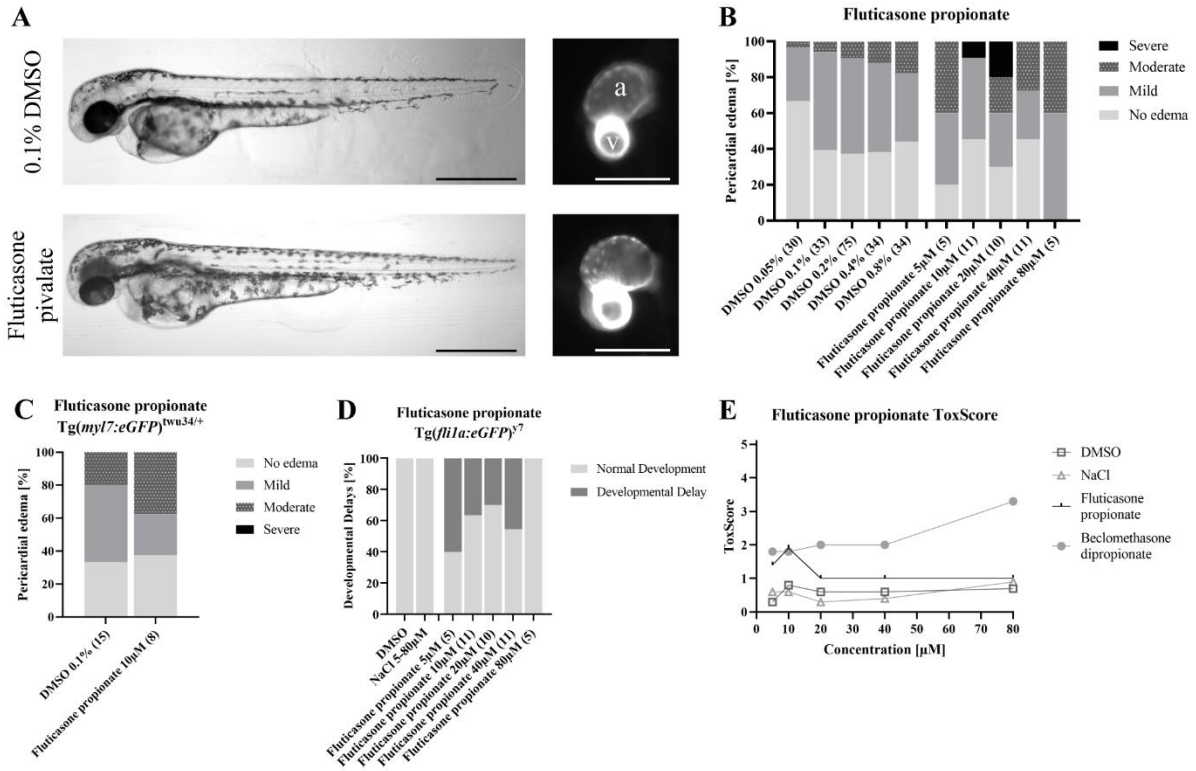

Supplementary Figure 5: Fluticasone Pivalate (FCP)

Phenotype overview for fluticasone pivalate (FCP)-treated zebrafish 2 dpf. **A**, Morphology of FCP-treated embryos. **B**, FCP-treatment induced pericardial edemas in Tg(*fli1a:eGFP*)^{y7} at all concentrations. **C**, in Tg(*myl7:eGFP*)$^{twu34/+}$ zebrafish FCP induced more moderate pericardial edemas. **D**, FCP caused developmental delay all concentrations except 80 µM. **E**, ToxScore derived from cardiac arrest, developmental delays, heart rate and pericardial edemas. Beclomethasone dipropionate was used as a reference to the other NR3C1 agonists tested in this study.

Supplementary Table 8: NR3C1-Regulated Gene Orthologues Based on MARRVEL[2]

Human target gene (Gene aliases)	*Zebrafish orthologues*	*ZFIN Identifier*	*DIOPT Score*	*Confidence*
ACO2 *(ACONM, HEL-S-284, ICRD, OCA8, OPA9)*	aco2	ZDB-GENE-030131-1390	11/15	High
ADM *(AM, PAMP)*	adma	ZDB-GENE-120221-5	12/15	Moderate
ADRA1B *(ADRA1, ALPHA1BAR)*	adra1ba	ZDB-GENE-120510-1	14/15	Moderate
ADRB1 *(ADRB1R, B1AR, BETA1AR, FNSS2, RHR)*	adrb1	ZDB-GENE-081022-145	12/15	Moderate

ATP2A2 *(ATP2B, DAR, DD, SERCA2)*	atp2a2b	ZDB-GENE-030131-867	14/15	High
BBC3 *(JFY-1, JFY1, PUMA)*	bbc3	ZDB-GENE-070119-4	2/15	Moderate
BDKRB2 *(B2R, BK-2, BK2, BKR2, BRB2)*	bdkrb2	ZDB-GENE-060515-1	9/15	High
CAV1 *(BSCL3, CGL3, LCCNS, MSTP085, PPH3, VIP21)*	cav1	ZDB-GENE-030131-2415	15/15	High
CCL2 *(GDCF-2, HC11, HSMCR30, MCAF, MCP-1, MCP1, SCYA2, SMC-CF)*	ccl35.2; ccl38.1; ccl38a.4; ccl38a.5	ZDB-GENE-140718-1; ZDB-GENE-041014-320; ZDB-GENE-041014-163; ZDB-GENE-041014-167	5/15; 5/15; 5/15; 5/15	Moderate; Moderate; High; Moderate
CCND1 *(BCL1, D11S287E, PRAD1, U21B31)*	ccnd1	ZDB-GENE-980526-176	13/15	High
CD14	tmco6	ZDB-GENE-070410-47	1/15	Low
CDKN1A *(CAP20, CDKN1, CIP1, MDA-6, P21, SDI1, WAF1, p21CIP1)*	cdkn1a	ZDB-GENE-070705-7	9/15	High
CEBPB *(C/EBP-beta, IL6DBP, NF-IL6, TCF5)*	cebpb	ZDB-GENE-020111-3	13/15	High
CITED2 *(ASD8, MRG-1, MRG1, P35SRJ, VSD2)*	cited2	ZDB-GENE-041010-141	11/15	High
CP *(CP-2)*	cp	ZDB-GENE-010522-1	14/15	High
CRYAB *(CMD1II, CRYA2, CTPP2, CTRCT16, HEL-S-101, HSPB5, MFM2)*	cryaba	ZDB-GENE-991119-2	11/15	High
CCN2 *(CTGF, HCS24, IGFBP8, NOV2)*	ccn2a	ZDB-GENE-030131-102	15/15	High

CXCL2 *(CINC-2a, GRO2, GROb, MGSA-b, MIP-2a, MIP2, MIP2A, SCYB2)*	cxcl8a	ZDB-GENE-081104-317	5/15	Moderate
CYP1B1 *(ASGD6, CP1B, CYPIB1, GLC3A, P4501B1)*	cyp1b1	ZDB-GENE-030902-1	14/15	Moderate
CYP2A6 *(CPA6, CYP2A, CYP2A3, CYPIIA6, P450C2A, P450PB)*	si:zfos-411a11.2	ZDB-GENE-131119-33	8/15	Moderate
CCN1 *(CYR61, GIG1, IGFBP10)*	ccn1	ZDB-GENE-040426-3	14/15	Moderate
EGFR *(ERBB, ERBB1, HER1, NISBD2, PIG61, mENA)*	egfra	ZDB-GENE-030918-1	10/15	High
FN1 *(CIG, ED-B, FINC, FN, FNZ, GFND, GFND2, LETS, MSF, SMDCF)*	fn1a	ZDB-GENE-000426-1	13/15	High
FOSL2 *(FRA2)*	fosl2	ZDB-GENE-070209-164	15/15	High
HMOX1 *(HMOX1D, HO-1, HSP32, bK286B10)*	hmox1a	ZDB-GENE-030131-3102	12/15	High
HSPB1 *(CMT2F, HEL-S-102, HMN2B, HS.76067, HSP27, HSP28, Hsp25, SRP27)*	hspb1	ZDB-GENE-030326-4	15/15	High
ID1 *(ID, bHLHb24)*	id1	ZDB-GENE-990415-96	13/15	Moderate
IRS1 *(HIRS-1)*	irs1	ZDB-GENE-030131-872	15/15	Moderate
KCNH2 *(ERG-1, ERG1, H-ERG, HERG, HERG1, Kv11.1, LQT2, SQT1)*	kcnh2a	ZDB-GENE-070912-699	9/15	High
KDR *(CD309, FLK1, VEGFR, VEGFR2)*	kdr	ZDB-GENE-041001-112	15/15	High

KLF4 *(EZF, GKLF)*	klf4	ZDB-GENE-111014-1	7/15	High
KRT18 *(CK-18, CYK18, K18)*	krt18a.1	ZDB-GENE-030411-6	14/15	Moderate
METRN *(C16orf23, c380A1.2)*	metrn	ZDB-GENE-050102-1	15/15	High
NR3C1 *(GCCR, GCR, GCRST, GR, GRL)*	Nr3c1	ZDB-GENE-050522-503	15/15	High
NRP1 *(BDCA4, CD304, NP1, NRP, VEGF165R)*	nrp1a	ZDB-GENE-030519-2	14/15	Moderate
PER1 *(PER, RIGUI, hPER)*	per1a	ZDB-GENE-011220-1	10/15	High
PKD1 *(PBP, PC1, Pc-1, TRPP1)*	pkd1a	ZDB-GENE-100707-1	8/15	High
PLAT *(T-PA, TPA)*	plat	ZDB-GENE-081104-181	13/15	High
PLAU *(ATF, BDPLT5, QPD, UPA, URK, u-PA)*	plaua	ZDB-GENE-090313-278	11/15	Moderate
SERPINA3 *(AACT, ACT, GIG24, GIG25)*	serpina1l	ZDB-GENE-040721-3	6/15	Moderate
SERPINE1 *(PAI, PAI-1, PAI1, PLANH1)*	serpine1	ZDB-GENE-070912-60	15/15	High
SLC29A1 *(ENT1)*	slc29a1a	ZDB-GENE-050913-138	13/15	High
TBX3 *(TBX3-ISO, UMS, XHL)*	tbx3a	ZDB-GENE-070209-80	15/15	High
THBS1 *(THBS, THBS-1, TSP, TSP-1, TSP1)*	thbs1b	ZDB-GENE-020708-1	15/15	High
TJP1 *(ZO-1)*	tjp1a	ZDB-GENE-031001-2	11/15	High
VCL *(CMD1W, CMH15, HEL114, MV, MVCL)*	vcla	ZDB-GENE-050506-61	12/15	Moderate

Supplementary Table 9: Gene-Associated Cardiac Disease Phenotypes in Mammals (MARRVEL[2])

Human target gene	*Zebrafish orthologues*	*Gene-associated cardiac disease phenotypes in mammals**	*Confidence*
ATP2A2	atp2a2b	**In mice:** Abnormal: Blood circulation; cardiac muscle relaxation; cardiac output; cardiovascular system physiology; left atrium morphology; left ventricle morphology; left ventricle pressure; heart shape; myocardial fiber physiology Decreased: Cardiac output; cardiac stroke volume; HR; left ventricle systolic pressure; systemic arterial blood pressure; systemic arterial systolic blood pressure; ventricle myocardium compact layer thickness Increased: Atrium dilation; **left and right ventricle dilation**; HS; left ventricle hypertrophy; left ventricle size; heart weight; left ventricle diastolic pressure; response of heart to induced stress; interventricular septum thickness; ventricular wall thickness Others: Atrial septal defect; cardiac fibrosis; cardiac hypertrophy; cardiac interstitial fibrosis; congestive heart failure; ventricular septal defect	High
BDKRB2	bdkrb2	Decreased: HR; systemic arterial systolic blood pressure	High
CAV1	cav1	Abnormal: Myocardium layer morphology Decreased: Interventricular septum thickness; ventricular wall thickness Increased: **HR**; heart weight; interventricular septum thickness; ventricular wall thickness Others: Dilated cardiomyopathy; cardiac fibrosis; cardiac hypertrophy; cardiac interstitial fibrosis; cardiomyopathy; congestive heart failure; **dilated left and right ventricle**; heart inflammation; left and right ventricle hypertrophy	High
CCND1	ccnd1	Abnormal: Interventricular septum morphology Decreased: Ventricular wall thickness	High

CDKN1A	cdkn1a	Abnormal: Heart echocardiography feature; heart morphology; ventricle wall thickness; myocardium compact layer morphology Increased: HS; atrium size Others: Atrial septal defect; ventricular septal defect	High
CITED2	cited2	Abnormal: atrioventricular cushion morphology; blood flow velocity; cardiac neural crest cell morphology; cardiac OFT development; direction of heart looping; heart and great artery attachment; atrium and ventricle morphology; heart development; left ventricle morphology; heart morphology; heart position or orientation; interventricular septum morphology; truncus arteriosus septation Decreased: Atrioventricular cushion size; cardiac neural crest cell number Others: Absent cardiac neural crest cells; absent coronary sinus; atrial septal defect; atrioventricular valve regurgitation; dextrocardia; double outlet right ventricle; interrupted aortic arch; mesocardiac; ostium primum atrial septal defect; ventricular septal defect	High
CP	cp	Increased: Heart weight	High
CRYAB	cryaba	**In humans**: Cardiomyopathy; dilated cardiomyopathy; hypertrophic cardiomyopathy; mitral regurgitation	High
EGFR	egfra	Abnormal: Left ventricle morphology; heart valve physiology; **impulse conducting system conduction**; semilunar valve morphology Increased: Cardiac stroke volume; left ventricle size; **HR**; left ventricle diastolic and systolic pressure; increased pulse pressure; prolonged PR interval; prolonged QRS complex duration; prolonged QT interval; prolonged RR interval; prolonged ST segment Others: Cardiac fibrosis; cardiac hypertrophy; congestive heart failure; left ventricle hypertrophy	High
FN1	fn1a	Abnormal: Atrioventricular cushion morphology: cardiac jelly morphology; cardiac OFT development; endocardium	High

		morphology; heart development; heart morphology; distended pericardium Increased: Myocardium thickness	
HMOX1	hmox1a	Abnormal: **Cardiac muscle contractility**; cardiovascular system physiology; response to myocardial infarction Increased: **Right ventricle dilation**; CM apoptosis; right ventricle weight; myocardial infarction size; myocardium necrosis Others: Cardiac fibrosis; Dilated heart	High
HSPB1	hspb1	Increased: Heart weight	High
KCNH2	kcnh2a	Abnormal: Bulbus cordis morphology; cardiac OFT development; cardiovascular system physiology; heart development; heart looping; heart morphology Decreased: HR Others: Irregular heartbeat	High
KDR	kdr	Abnormal: Heart development; interventricular septum morphology; absent atrioventricular cushions Decreased: HS Others: Congestive heart failure; heart hemorrhage; pericardial effusion	High
NR3C1	nr3c1	**In humans:** Stroke **In mice:** Abnormal: Heart echocardiography feature; myocardial fiber physiology Increased: Left ventricle dilation; HS; heart weight; left ventricle weight; mean systemic arterial blood pressure; systemic arterial systolic blood pressure; ventricular wall thickness Others: Cardiac fibrosis; cardiac hypertrophy; congestive heart failure; heart inflammation;	High
PKD1	pkd1a	Abnormal: Myocardial trabeculae morphology	High

		Increased: Heart weight; myocardium thickness Decreased: Myocardium thickness Others: Aortic aneurysm; aortic dissection; atrial septal defect; common atrioventricular valve; double outlet right ventricle; failure of atrioventricular cushion closure; Left and right ventricle hypertrophy; hemopericardium; ventricular septal defect	
PLAT	plat	Abnormal: Heart morphology Increased: HS Others: Cardiac interstitial fibrosis; Left ventricle hypertrophy	High
SERPINE1	serpine1	Abnormal: Blood circulation Others: Cardiac fibrosis; heart inflammation	High
SLC29A1	slc29a1a	Abnormal: Sinus arrhythmia Decreased: HR Increased: Prolonged RR interval	High
TBX3	tbx3a	Abnormal: P wave; QRS complex; cardiac jelly morphology; cardiovascular development; fetal AVC morphology; heart development; heart looping; **impulse conducting system conduction**; inferior vena cava morphology; SAN morphology; sinus arrhythmia; vitelline vasculature morphology Decreased: HR Absent: P wave; PR interval; atrioventricular cushions Increased: Cardiac muscle contractility; HR variability Others: **AVB**; delayed heart looping; failure of heart looping; irregular heartbeat; **pericardial edema**; prolonged QRS complex duration; shortened PR interval; sinus bradycardia; ventricular septal defect	High
THBS1	thbs1b	Abnormal: Heart morphology; ventricle morphology Decreased: HR Increased: HS; systemic arterial diastolic blood pressure	High
ADM	adma	Abnormal: Myocardial trabeculae morphology Decreased: HS	Moderate

		Increased: Cardiomyocyte apoptosis; ventricular wall thickness Others: Cardiac hypertrophy; disorganized myocardium; pericardial effusion	
ADRA1B	adra1ba	Abnormal: Cardiac muscle contractility; cardiovascular system physiology; left ventricle morphology; HS; myocardial fiber physiology; systemic arterial blood pressure Decreased: Cardiac output; cardiac stroke volume; HR; heart weight; systemic arterial systolic blood pressure; HS Increased: Cardiac muscle contractility; left ventricle developed pressure; response of heart to induced stress Others: Congestive heart failure	Moderate
ADRB1	adrb1	Decreased: HR	Moderate
BBC3	bbc3	Abnormal: Heart left ventricle pressure Decreased: Myocardial infarction size Increased: Left ventricle developed pressure	Moderate
CCN1	ccn1	Abnormal: Heart development; interventricular septum morphology; mitral valve morphology Others: Complete atrioventricular septal defect; failure of atrioventricular cushion closure; ostium primum atrial septal defect; patent cardiac foramen ovale	Moderate
NRP1	nrp1a	Increased: Atrium dilation Others: Ventricular septal defect	Moderate
PLAU	plaua	Others: Left ventricle hypertrophy; ventricle muscle contractility; cardiac interstitial fibrosis	Moderate
VCL	vcla	Abnormal: Cardiac muscle relaxation; cardiovascular system morphology; cardiovascular system physiology; heart development; heart electrocardiography waveform feature; heart position or orientation; **impulse conducting system conduction;** pericardial cavity morphology Absent: Atrioventricular cushions; heart valves Decreased: HS; myocardium thickness Increased: Left ventricle dilation; heart weight	Moderate

	Others: Cardiac fibrosis; cardiac hypertrophy; congestive heart failure; delayed heart development; dilated cardiomyopathy; **heart block**; irregular heartbeat; prolonged QRS complex duration; ventricular tachycardia

*Data does not include vascular phenotypes.

Supplementary Table 10: Gene-Associated Cardiac Disease Phenotypes in Zebrafish (MARRVEL2)

Human target gene	*Zebrafish orthologues*	*Gene-associated cardiac disease phenotypes in zebrafish (none reported in mammals)**	*Confidence*
FOSL2	fosl2	Decreased: Ventricular muscle tissue growth Others: Hypertrophic ventricular muscle tissue growth	High
TJP1	tjp1a	Increased: Pericardial edema	High

*Data does not include vascular phenotypes.

9.3.1 Protein Modeling of hGR1 and zfGR1

Supplementary Table 11: PDB IDs Used for *In Silico* Protein-Ligand Interactions

PBD	*Protein*	*Ligand*	*Resolution [Å]*	*Downloaded on*	*Reference*
4UDD	NR3C1	Desisobutyrylciclesonide	1.8	14/09/2022	(198)
4P6W	NR3C1	Mometasone furoate	1.95	15/09/2022	(288)
5NFP	NR3C1	Budesonide	2.1	15/09/2022	(289)
4UDC	NR3C1	Dexamethasone	2.5	15/09/2022	(198)
3CLD	NR3C1	Fluticasone furoate	2.84	15/09/2022	(219)
3GN8	AncGR2	Dexamethasone	2.5	19/09/2022	(211)

Supplementary Table 12: Schrödinger BLAST Homology Search Results

Name	*E-value*	*Score*	*Identity [%]*	*Positive [%]*	*Gaps [%]*	*Description*
7KW7_F	0	1632	49.42	64.22	8.37	Chain F, Glucocorticoid receptor [Homo sapiens]
3GN8_A	$5.51E^{-154}$	1102	85.89	94.36	0	X-ray Crystal Structure of AncGR2 in Complex with Dexamethasone [Homo sapiens]
3GN8_B	$5.51E^{-154}$	1102	85.89	94.36	0	X-ray Crystal Structure of AncGR2 in Complex with Dexamethasone [Homo sapiens]
6W9K_A	$5.51E^{-154}$	1102	85.89	94.36	0	Structure of the Ancestral Glucocorticoid Receptor 2 ligand binding domain in complex with Prednisolone and PGC1a coregulator fragment [synthetic construct]
6W9M_A	$6.44E^{-154}$	1102	85.89	94.36	0	Structure of the Ancestral Glucocorticoid Receptor 2 ligand binding domain in complex with vamorolone and SHP coregulator fragment [synthetic construct]
6NWK_A	$6.48E^{-154}$	1102	85.89	94.36	0	Structure of the Ancestral Glucocorticoid Receptor 2 ligand binding domain in complex with dexamethasone and PGC1a coregulator fragment [Homo sapiens]
6NWL_A	$6.48E^{-154}$	1102	85.89	94.36	0	Structure of the Ancestral Glucocorticoid Receptor 2 ligand binding domain in complex with hydrocortisone and PGC1a coregulator fragment [Homo sapiens]
6W9L_A	$6.48E^{-154}$	1102	85.89	94.36	0	Structure of the Ancestral Glucocorticoid Receptor 2 ligand binding domain in complex with deacetylated deflazacort and PGC1a coregulator fragment [synthetic construct]
4E2J_A	$2.63E^{-153}$	1098	85.83	94.33	0	X-Ray Crystal Structure of the Ancestral Glucocorticoid Receptor 2 ligand binding domain in complex with mometasone furoate and TIF-2 coactivator fragment [Neolamprologus pulcher]
4E2J_B	$2.63E^{-153}$	1098	85.83	94.33	0	X-Ray Crystal Structure of the Ancestral Glucocorticoid Receptor 2 ligand binding domain in complex with mometasone furoate and TIF-2 coactivator fragment [Neolamprologus pulcher]

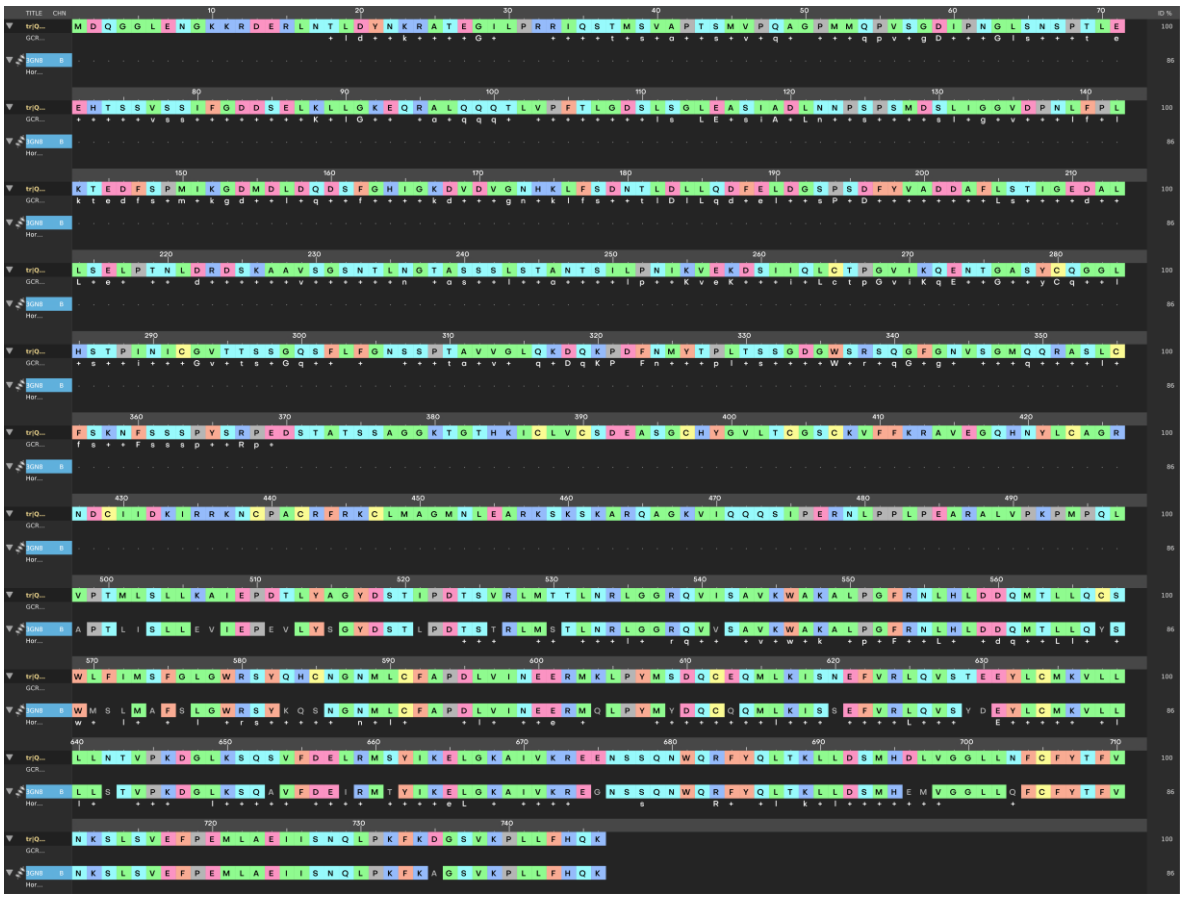

Supplementary Figure 6: Schrödinger Multiple Sequence Alignment for 3D Protein Modeling
Multiple sequence alignment was performed with the Schrödinger® Multiple Sequence Viewer/Editor. FASTA sequence Q1XHK0 of zebrafish Nr3c1 (top sequence) was aligned against the AncGR2 PDB sequence (lower sequence) to generate a 3D homology model.

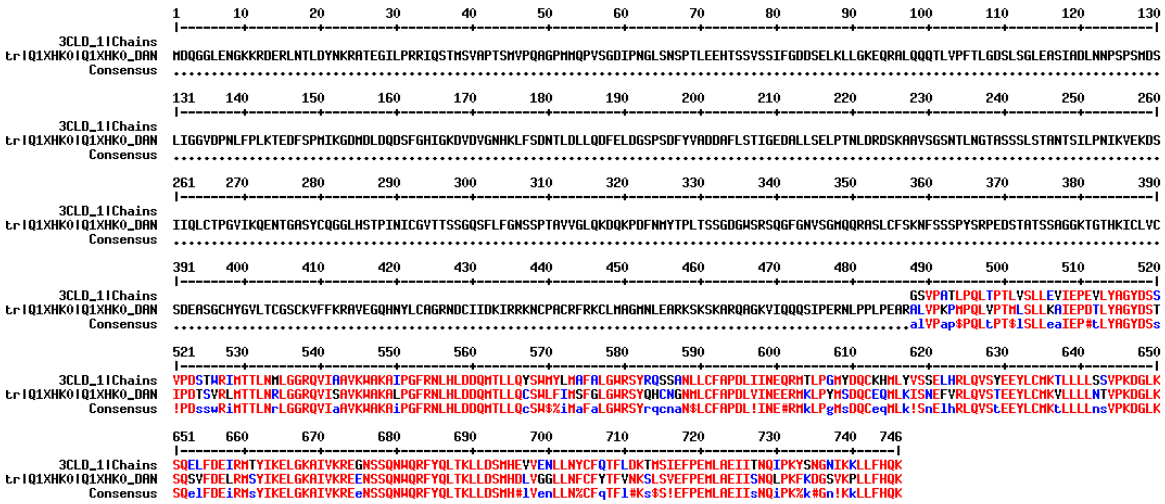

Supplementary Figure 7: MultAlin Multiple Sequence Alignment of Human and Zebrafish

Multiple sequence alignment was performed with the MultAlin (218) multiple sequence viewer. FASTA sequence Q1XHK0 of zebrafish Nr3c1 (middle sequence) was aligned against the hGR1 3CLD PDB sequence (top sequence).

Red = Conserved sequences; Blue and black = Not conserved sequences

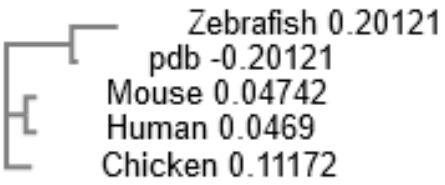

Supplementary Figure 8: ClustalO Phylogenetic Tree of NR3C1

Sequence alignment for the phylogenetic tree was performed with Clustal Omega (392). FASTA sequence Q1XHK0 of zebrafish Nr3c1 was aligned against AncGR2 (PDB: 3GN8_A), chicken GR (NP_001032915.1), human NR3C1 (NP_000167.1) and mouse Nr3c1 (AAI64545.1).

9.4 Scripts

9.4.1 Fiji Macros

9.4.1.1 Vessel Measurements Using Point Selection on Fluorescence Maximum Projections

Filename: AngioScript.ijm

Creator: Adapted from Jochen Gehrig; published by Pandey et al. 2019 (183)

```
// Vessel measurements
// This macro should be run after clicking 24 points in a given order as depicted on reference figure
// on a fluorescently labelled zebrafish vessels oriented laterally with head toward the left

macro "length [1]"{
getSelectionCoordinates(x, y);
len1 = sqrt((x[0]-x[1])*(x[0]-x[1])+(y[0]-y[1])*(y[0]-y[1])); //DA
len2 = sqrt((x[2]-x[1])*(x[2]-x[1])+(y[2]-y[1])*(y[2]-y[1])); //DV

len3 = sqrt((x[3]-x[4])*(x[3]-x[4])+(y[3]-y[4])*(y[3]-y[4])); //Left ISV1 bottom
len4 = sqrt((x[5]-x[6])*(x[5]-x[6])+(y[5]-y[6])*(y[5]-y[6])); //Left ISV1 middle
len5 = sqrt((x[7]-x[8])*(x[7]-x[8])+(y[7]-y[8])*(y[7]-y[8])); //Left ISV1 top
len6 = sqrt((x[9]-x[10])*(x[9]-x[10])+(y[9]-y[10])*(y[9]-y[10])); //Left ISV2 bottom
len7 = sqrt((x[11]-x[12])*(x[11]-x[12])+(y[11]-y[12])*(y[11]-y[12])); //Left ISV2 middle
len8 = sqrt((x[13]-x[14])*(x[13]-x[14])+(y[13]-y[14])*(y[13]-y[14])); //Left ISV2 top
len9 = sqrt((x[15]-x[16])*(x[15]-x[16])+(y[15]-y[16])*(y[15]-y[16])); //Left ISV3 bottom
len10 = sqrt((x[17]-x[18])*(x[17]-x[18])+(y[17]-y[18])*(y[17]-y[18])); //Left ISV3 middle
len11 = sqrt((x[19]-x[20])*(x[19]-x[20])+(y[19]-y[20])*(y[19]-y[20])); //Left ISV3 top
len12 = sqrt((x[21]-x[22])*(x[21]-x[22])+(y[21]-y[22])*(y[21]-y[22])); //Left ISV4 bottom
len13 = sqrt((x[23]-x[24])*(x[23]-x[24])+(y[23]-y[24])*(y[23]-y[24])); //Left ISV4 middle
len14 = sqrt((x[25]-x[26])*(x[25]-x[26])+(y[25]-y[26])*(y[25]-y[26])); //Left ISV4 top

len15 = sqrt((x[27]-x[28])*(x[27]-x[28])+(y[27]-y[28])*(y[27]-y[28])); //Right ISV1 bottom
len16 = sqrt((x[29]-x[30])*(x[29]-x[30])+(y[29]-y[30])*(y[29]-y[30])); //Right ISV1 middle
len17 = sqrt((x[31]-x[32])*(x[31]-x[32])+(y[31]-y[32])*(y[31]-y[32])); //Right ISV1 top
len18 = sqrt((x[33]-x[34])*(x[33]-x[34])+(y[33]-y[34])*(y[33]-y[34])); //Right ISV2 bottom
```

```
len19 = sqrt((x[35]-x[36])*(x[35]-x[36])+(y[35]-y[36])*(y[35]-y[36])); //Right ISV2 middle
len20 = sqrt((x[37]-x[38])*(x[37]-x[38])+(y[37]-y[38])*(y[37]-y[38])); //Right ISV2 top
len21 = sqrt((x[39]-x[40])*(x[39]-x[40])+(y[39]-y[40])*(y[39]-y[40])); //Right ISV3 bottom
len22 = sqrt((x[41]-x[42])*(x[41]-x[42])+(y[41]-y[42])*(y[41]-y[42])); //Right ISV3 middle
len23 = sqrt((x[43]-x[44])*(x[43]-x[44])+(y[43]-y[44])*(y[43]-y[44])); //Right ISV3 top
len24 = sqrt((x[45]-x[46])*(x[45]-x[46])+(y[45]-y[46])*(y[45]-y[46])); //Right ISV4 bottom
len25 = sqrt((x[47]-x[48])*(x[47]-x[48])+(y[47]-y[48])*(y[47]-y[48])); //Right ISV4 middle
len26 = sqrt((x[49]-x[50])*(x[49]-x[50])+(y[49]-y[50])*(y[49]-y[50])); //Right ISV4 top

row = Table.size;

        imageDir = getInfo("image.directory");
        Table.set("Image_Folder", row, imageDir);

        imageName = getInfo("image.filename");
        Table.set("Image_Name", row, imageName);

        Table.set("DA", row, len1);
        Table.set("DV", row, len2);

        Table.set("Left_ISV1_bottom", row, len3);
        Table.set("Left_ISV1_middle", row, len4);
        Table.set("Left_ISV1_top", row, len5);
        Table.set("Left_ISV2_bottom", row, len6);
        Table.set("Left_ISV2_middle", row, len7);
        Table.set("Left_ISV2_top", row, len8);
```

```
Table.set("Left_ISV3_bottom", row, len9);
Table.set("Left_ISV3_middle", row, len10);
Table.set("Left_ISV3_top", row, len11);
Table.set("Left_ISV4_bottom", row, len12);
Table.set("Left_ISV4_middle", row, len13);
Table.set("Left_ISV4_top", row, len14);

Table.set("Right_ISV1_bottom", row, len15);
Table.set("Right_ISV1_middle", row, len16);
Table.set("Right_ISV1_top", row, len17);
Table.set("Right_ISV2_bottom", row, len18);
Table.set("Right_ISV2_middle", row, len19);
Table.set("Right_ISV2_top", row, len20);
Table.set("Right_ISV3_bottom", row, len21);
Table.set("Right_ISV3_middle", row, len22);
Table.set("Right_ISV3_top", row, len23);
Table.set("Right_ISV4_bottom", row, len24);
Table.set("Right_ISV4_middle", row, len25);
Table.set("Right_ISV4_top", row, len26);

print (len1);  //DA
print (len2);     //DV
print (len3);     //Left ISV1 bottom
print (len4);     //Left ISV1 middle
print (len5);      //Left ISV1 top
print (len6);     //Left ISV2 bottom
```

```
        print (len7);     //Left ISV2 middle
        print (len8);      //Left ISV2 top
        print (len9);      //Left ISV3 bottom
        print (len10); //Left ISV3 middle
        print (len11); //Left ISV3 top
        print (len12); //Left ISV4 bottom
        print (len13); //Left ISV4 middle
        print (len14); //Left ISV4 top

        print (len15); //Right ISV1 bottom
        print (len16); //Right ISV1 middle
        print (len17); //Right ISV1 top
        print (len18); //Right ISV2 bottom
        print (len19); //Right ISV2 middle
        print (len20); //Right ISV2 top
        print (len21); //Right ISV3 bottom
        print (len22); //Right ISV3 middle
        print (len23); // Right ISV3 top
        print (len24); //Right ISV4 bottom
        print (len25); //Right ISV4 middle
        print (len26); //Right ISV4 top

run("Open Next");
        run("Select None");
}
```

9.4.1.2 White Balance RGB to Selected Region

Filename: White Balance RGB to Selected Region.ijm

Creator: Vytas Bindokas; Oct 2006, Univ. of Chicago; modified by Patrice Mascalchi, 2014, Univ. of Cambridge UK

```
setTool(0);
waitForUser("Draw a region over background");
run("Set Measurements...", "  mean redirect=None decimal=3");
if (selectionType==-1) exit("you must draw a region first");

ti = getTitle;
run("Select None");
//setBatchMode(true);

run("Duplicate...", "title=rgbstk-temp");
origBit = bitDepth;
if (bitDepth() != 24) exit("Active image is not RGB");
run("RGB Stack");
run("Restore Selection");

val = newArray(3);
for (s=1;s<=3;s++) {
        setSlice(s);
        run("Measure");
        val[s-1] = getResult("Mean");
}
```

```
run("Select None");


run("16-bit");
run("32-bit");
Array.getStatistics(val, min, max, mean);


for (s=1; s<=3; s++) {
	setSlice(s);
	dR = val[s-1] - mean;
	if (dR < 0) {
		run("Add...", "slice value="+ abs(dR));
	} else if (dR > 0) {
		run("Subtract...", "slice value="+ abs(dR));
	}
}


run("16-bit");
run("Convert Stack to RGB");


rename(ti + "-corrected");
//closeWin("Results");
closeWin("rgbstk-temp");


setBatchMode("exit and display");
run("Tile");				// Can be removed
```

```
// -------------------------------------------------------------------------------------
// close any window without returning any error
function closeWin(name) {
	if (isOpen(name)) {
	    selectWindow(name);
	    run("Close");
	}
}
```

9.4.2 Perl Scripts

9.4.2.1 Setup of Fiji Macro to Prepare Images for Heartbeat Analysis

Filename: HeartBeat_image_preProc_modified.pl

Creator: Jochen Gehrig (88)

```
use strict;

print "Choose experimental folder:\nUSAGE: x:\\a\\b\\c\n(right_click -> paste)";
my $choice = <STDIN>;

chomp $choice;

(my $parentdir = $choice);
chdir($parentdir);
opendir(DIR1, $parentdir) or die "can't opendir $parentdir: $!";
```

```
my @listdir = readdir (DIR1);

my @experiment_folders;
my @wells;

open OUT, ">$parentdir/macro.ijm" or die $!,"\n" ;

print "$parentdir\n";
print OUT "setBatchMode(true)\n";
print OUT qq(run("Set Measurements...", "center redirect=None decimal=0"););

foreach my $folder (@listdir){

                        if ($folder !~ /\./ig) {

                        print "$folder\n";

                        mkdir("$folder/Jpeg", 0777) || print $!;
                        mkdir("$folder/Tiff", 0777) || print $!;

                        my $experiment = $parentdir."\\".$folder;
                        push @experiment_folders, ($experiment);
                        }
}

foreach my $exp_folder (@experiment_folders) {
```

```
my @tags = split (/\\/, $exp_folder);
        my $tag = $tags[-1];

        print OUT "\n\nfiles$tag = newArray(";

        chdir($exp_folder);
        opendir(DIR3, $exp_folder) or die "can't opendir $exp_folder: $!";
        my @listfiles = readdir (DIR3);

        my @wellarray;
        my %wellhash;

        foreach my $file (@listfiles){
                #print "$file\n";
                my ($a, $b, $c, $d, $e, $f, $g, $h, $i, $j, $k, $l, $m, $n) = split ("--", $file);
#WE00001a---A001b--PO01c--LO001d--CO6e--SL001f--PX00040g--PW0080h--IN0010i--
TM209j--X014463k--Y011163l--Z219000m--T0785469733n.tif
                #WE00001a---A001b--PO01c--LO001d--CO6e--SL001f--PX32500g--
PW0080h--IN0010i--TM210j--X014463k--Y011163l--Z205426m--T1537283210n
                if ($e =~ /CO6/ig){
                my ($b1, $b2) = split ("-", $b);
                #print "a:$a, b:$b, c:$c, d:$d, e:$e, f:$f, g:$g, i:$i, j:$j, k:$k, l:$l, m:$m,
n:$n\n";
                my ($i1, $i2) = split ("\.tif", $n);
                #print $i1,"\n";
                my $e1 = $e."--";
```

```
                $wellhash{$a."--".$b."--".$c."--".$d."--".$e1} = ($i1);#"filehandle";
                }
        }

        while( my( $k, $v ) = each %wellhash ){
                print "$k -> $v\n";
                push @wellarray, ("\'$k\'->$v");
                push @wellarray, (', ');
                }
        pop @wellarray;
        #my @sortedwellarray = sort @wellarray;
        while (my $entry = shift @wellarray){
                my ($e1, $e2) = split ("->", $entry);
                print OUT qq($e1);
        }

        (my $exp_folder2 = $exp_folder) =~  s/\\/\\\\/g;

        print OUT ");\n";
        print OUT "for (i=0; i<files$tag.length;i++){\n";
        print OUT qq(
        run("Image Sequence...", "open=$exp_folder2\\\\ number=1000 starting=1 increment=1 scale=100 file=\"+files$tag\[i\]+\" sort");

        a = getInfo("image.filename");
```

```
run("Duplicate...", "title=b duplicate range=1-130");

run("Gaussian Blur...", "sigma=200 stack");

run("Calculator Plus", "i1=a i2=b operation=[Divide: i2 = (i1/i2) x k1 + k2] k1=8000 k2=0");


selectWindow("b");

run("Image Sequence... ", "format=JPEG name="+files$tag\[i\]+"SL start=1 digits=3 save=$exp_folder2\\\\Jpeg\\\\");

run("Image Sequence... ", "format=TIFF name="+files$tag\[i\]+"SL start=1 digits=3 save=$exp_folder2\\\\Tiff\\\\");


run("Close All");


})

}
```

9.4.2.2 Creation of Folders Labeled According to Well Number and Sorting of the Images into Respective Folders

Filename: process_filename.pl

Creator: Syed Haider Ijlal Muhammad

```
#!/usr/bin/perl


use warnings;

use strict;


my $c = ("ABCDEFGH");

my @c = split("", $c);
```

```
foreach my $c (@c){
	for(my $i=1;$i<=12;$i++){

		my $file;
		my $folder;

		if($i<=9){
			$folder = $c."0".$i;
			$file = $c."00".$i;
		}
		else {
			$folder = $c.$i;
			$file = $c."0".$i;

		}

		print "Folder: $folder\n";
		print "File: $file\n";

		print "mkdir E:\\Plate_A\\VV20210708P04V26\\Heartbeat\\210708110131_BFHB__Myl7_HitVal102_2x\\Tiff\\$folder\n";
		system("mkdir E:\\Plate_A\\VV20210708P04V26\\Heartbeat\\210708110131_BFHB__Myl7_HitVal102_2x\\Tiff\\$folder");
```

```
        print "move E:\\Plate_A\\VV20210708P04V26\\Heartbeat\\210708110131_BFHB__Myl7_HitVal102_2x\\Tiff\\*${file}*CO6* E:\\Plate_A\\VV20210708P04V26\\Heartbeat\\210708110131_BFHB__Myl7_HitVal102_2x\\Tiff\\$folder\n";
        system("move E:\\Plate_A\\VV20210708P04V26\\Heartbeat\\210708110131_BFHB__Myl7_HitVal102_2x\\Tiff\\*${file}*CO6* E:\\Plate_A\\VV20210708P04V26\\Heartbeat\\210708110131_BFHB__Myl7_HitVal102_2x\\Tiff\\$folder");
    }
}
```

9.4.3 MATLAB Scripts

9.4.3.1 Reformatting of Image Names into Video-Labeled jpeg

Filename: BatchRenameImagesForHeartbeatAnalysis.m

Creator: Jochen Gehrig

```
%get main folder
string_to_folder = strcat(uigetdir(),'\');
d = dir(string_to_folder);
isub = [d(:).isdir]; %# returns logical vector
nameFolds = {d(isub).name}';
nameFolds(ismember(nameFolds,{'.','..'})) = [];
framerate = input('Enter desired framerate: ');

for i =1:length(nameFolds)
   foldername = sprintf('%s%s', string_to_folder, nameFolds{i});
   %define folder
```

```
    cd(foldername);
    allimages = dir('*.jpg');
    for j =1:length(allimages)
        filename = allimages(j).name;
        Timestamp = datestr(((j-1)*1/framerate)/(24*3600), 'yy.mm.dd_HH.MM.SS,FFF');
        newfilename = strcat(foldername,'\',nameFolds{i},'.avi','_',Timestamp,'.jpg');
        movefile(filename, newfilename);
    end
end
```

10 Acknowledgements

I want to extend my heartfelt thanks and gratitude to the wonderful people who have played a significant role in my academic journey. First and foremost, I would like to thank my late academic supervisor and advisor Prof. Dr. rer. nat. Jeanette Erdmann for giving me the opportunity to complete my PhD in the Institute for Cardiogenetics and for the support she provided during this extensive project. I would also like to express my deepest appreciation to Dr. Zouhair Aherrahrou for initiating and mentoring this thesis, for various discussions that helped me to progress in this project. Further, I would like to thank my referees Prof. Dr. med. Malte Spielmann and Prof. Dr. *rer. nat*. Stefan Schulte-Merker for picking up the baton after the sudden loss of Jeanette Erdmann and devoting their time to examine this thesis.

Let's not forget Lisa Diner and Nadine Odenthal, M.Sc. They have been my rock throughout the screening process and beyond, offering both technical and emotional support. Thank you both for all you did for me! And thank you to all the other lab technicians and staff scientists who have been instrumental in my journey: Maren Behrensen, Sandra Wrobel, Petra Bruse, and Anette Liebers. Your help and assistance have made a world of difference.

A massive thank you also to Syed Ilal Muhammad, M.Sc. and Dr. *rer. nat*. Tobias Reinberger. Without their computational skills, I would still be grappling with data analysis today. Especially, a big thank you to Tobias, who took over the bioinformatical part of developing *pyHeart4Fish* with me. He has turned all my wishes for *pyHeart4Fish* into a reality. The tool brought my analysis to the next level and will undoubtedly benefit the entire zebrafish community.

I would like to extend a warm thank you to Prof. Dr. *rer. nat*. Salim Seyfried for welcoming me to the Institute for Biochemistry and Biology, Department Animal Physiology, University of Potsdam, Potsdam, Germany as a visiting scientist to finalize my PhD.

Another special thank you goes to Dr. Maximillian Breuer, who is not only a fantastic Co-Chair of the Environmental Sustainability Committee of the International Zebrafish Society but was an exceptional instructor and mentor during my time in the Institute for Biochemistry and Biology, Department Animal Physiology, University of Potsdam and beyond. Your willingness to make time for me and discuss my wild ideas and listen to any issues is sincerely appreciated.

Further, I would like to thank our collaborator Charlie Kruse and the Fish Facility Team of the Fraunhofer Institute for Marine Biology EMB Lübeck, Germany for providing us with the zebrafish facility and technical support.

I also want to thank the fantastic team from ACQUIFER, particularly Bettina Trauernicht and Jochen Gehrig. Your assistance has gone above and beyond mere technical support.

Another warm thank you goes to my current PI, Prof. Dr. Lilianna Solnica-Krezel, who not only welcomed me as a PostDoc into her lab, but also supported me in the process of finalizing writing my thesis. Thank you for your support and patience!

Finally, I want to express my deepest appreciation to my family. Your unwavering support during the challenges of pursuing my PhD amidst the pandemic has meant the world to me. I know, I have rambled a lot about things you didn't understand, but your listening ears helped a lot.